Université de Lille

UCCS
UNITÉ DE CATALYSE ET CHIMIE DU SOLIDE

DOCTORAL THESIS

Université de Lille

Photocatalytic Conversion of Methane and Reduction of CO_2 with H_2O

PhD Candidate: Mr Xiang YU

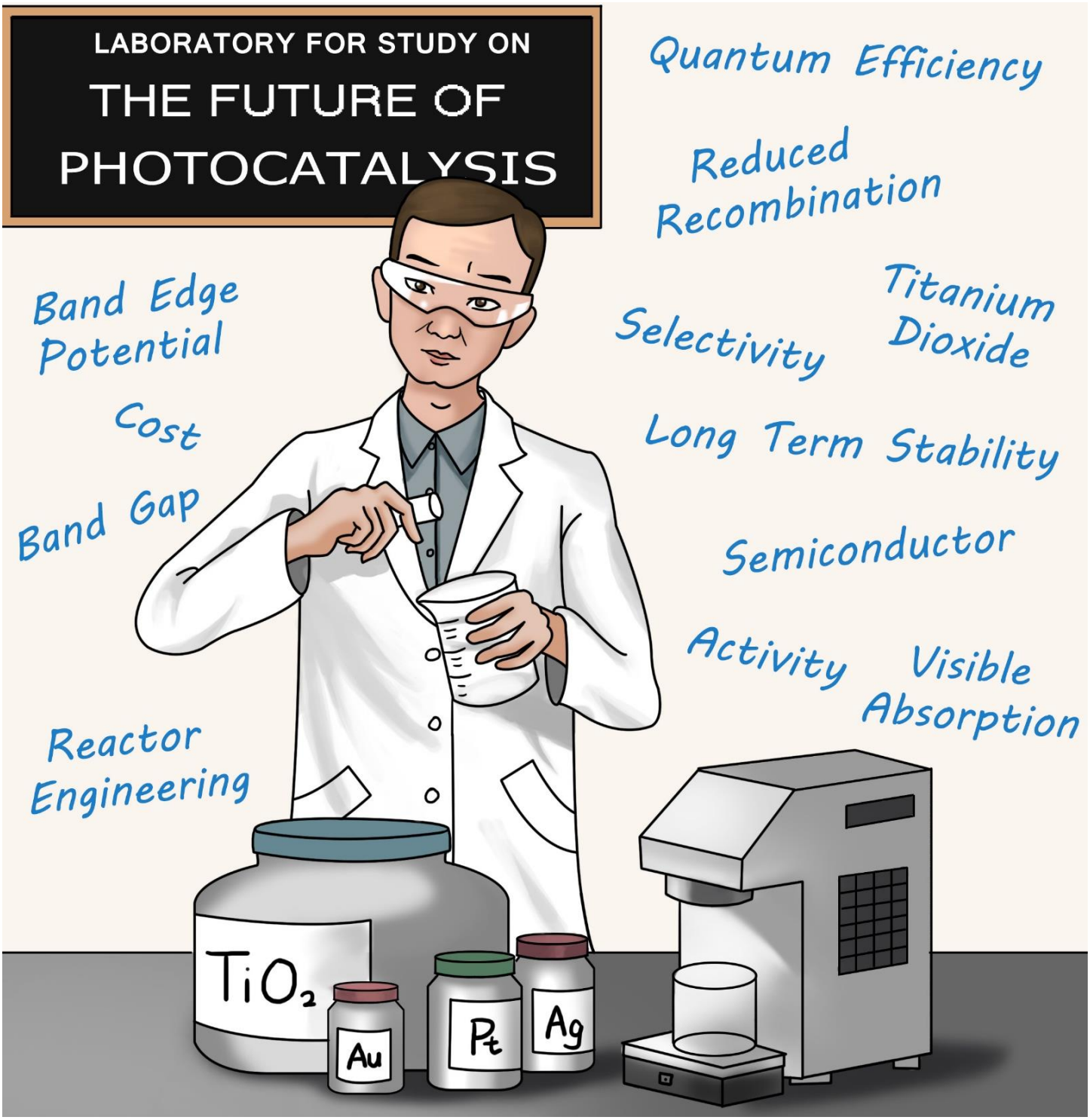

THÈSE DE DOCTORAT

PRÉSENTÉE PAR

Xiang YU

POUR L'OBTENTION DU TITRE DE

DOCTEUR DE L' UNIVERSITÉ DE LILLE

Ecole Doctorale: Sciences de la Matière du Rayonnement et de l'Environnement

Spécialité: Chimie organique, minerale, industrielle

Conversion photocatalytique du méthane et réduction du CO_2 avec H_2O

Soutenue le 26 sep 2019 devant le jury composé de:

Dr. Cuong PHAM-HUU, Directeur de recherche, CNRS, Rapporteur

Prof. Pedro H. C. CAMARGO, Professeur, Université ode Helsinki, Rapporteur

Dr. Jean-Pierre DATH, Direction R&D, TOTAL, Examinateur Invité

Dr. Céline PAGIS, Ingénieure de recherche, IFP Energies Nouvelles, Examinatrice invitée

Dr. Andrei Y. KHODAKOV, Directeur de recherche, CNRS, Examinateur

Dr. Vitaly V. ORDOMSKY, Chargé de recherche, CNRS, Directeur de thèse

Contents

Abstract

This dissertation focuses on the photocatalytic and photochemical conversion of methane and carbon dioxide. The reaction, catalytic performances, structures of the catalysts and reaction mechanisms have been investigated and discussed in detail.

Photocatalysis is one of the key technologies for clean energy and environmental applications. The number of applications based on photocatalysis has increased dramatically for the past two decades. Photocatalysis is extremely important for transformation of inert and thermodynamically stable molecules like methane or CO_2.

Photocatalytic activation of C-H bonds is an emerging field. Methane is a promising source of energy with a huge reserve and is considered to be one of the alternatives to non-renewable petroleum resources because it can be converted to valuable hydrocarbon feedstocks and hydrogen through appropriate reactions. However, due to its high stability, high energy is usually consumed for its conversion, which remains a problem to be solved. Methane conversion and reaction mechanism occurring on metal-heteropolyacid-titania nanocomposites were investigated in Chapters 3 and 4.

Oxidation of methane has been carried out for more than a century. Since oxygen is a very reactive molecule, methane can react very rapidly with molecular oxygen and is prone to total oxidation till CO_2. Therefore, it is difficult to obtain a desired product with high yield and high selectivity. We report here direct and selective photocatalytic highly-selective oxidation of methane to carbon monoxide under ambient conditions. The composite catalysts on the basis of zinc, tungstophosphoric acid and titania exhibit exceptional performance in this reaction, high carbon monoxide selectivity and quantum efficiency of 7.1% at 362 nm. The reaction is consistent with the Mars-Van Krevelen type sequence and involves formation of the surface methoxy-carbonates as intermediates and zinc oxidation-reduction cycling.

In the past few decades, extensive research has focused on the direct conversion of methane to alcohols or higher hydrocarbons. The current processes of converting methane to alcohols or olefins are complex and expensive, because they require an intermediate step of reforming methane to syngas. Although the direct conversion of methane to more valuable products has significant environmental and potential commercial value, there is no

commercial scale process available. We uncovered highly selective (>90%) quantitative photochemical direct conversion of methane to ethane at ambient temperature over silver-heteropolyacid-titania nanocomposites. The ethane yield from methane reaches 9 % on the optimized materials. High quantum efficiency, high selectivity and significant yield of ethane combined with excellent stability are major advantages of methane quantitative synthesis from methane using the photochemical looping approach.

The rise in atmospheric carbon dioxide and the depletion of fossil fuel reserves have raised serious concerns about the subsequent impact of CO_2 on the global climate and future energy supply. The use of abundant solar energy to convert carbon dioxide into fuel, such as carbon monoxide, methane or methanol, solves both problems simultaneously and provides a convenient method of energy storage. Chapter 5 addresses a new efficient catalyst for selective CO_2 to CO conversion. The zinc containing phosphotungstic acid-titania nanocomposites exhibited exceptional high activity reaching 50 µmol CO/g·h and selectivity (73%) in the CO_2 photocatalytic reduction to CO in the presence of water. The in-situ IR experiments suggest that reaction involves zinc bicarbonates containing hydroxyl groups. The decomposition of these zinc bicarbonate species under irradiation leads to the selective production of carbon monoxide and oxygen.

In photocatalytic reactions, the difference in catalyst morphology usually has a significant effect on the photocatalytic performance. Chapter 6 studied the effect of monoclinic bismuth vanadate ($BiVO_4$) crystals with controlled ratio of {010} and {110} facets for photocatalytic reduction of CO_2 by H_2O. The reaction under irradiation is significantly enhanced by selective photo-deposition of Cu and Co co-catalysts over different facets providing Z-scheme charge flow.

Keywords: Photocatalysis, methane activation, CO_2 reduction, zinc, silver, heteropolyacid, titania, bismuth vanadate

Resumé

Cette thèse porte sur les conversions photocatalytique et photochimique du méthane et du dioxyde de carbone en produits à haute valeur ajoutée. La réaction, les performances catalytiques, la structure des catalyseurs et les mécanismes réactionnels ont été étudiés et discutés en détail.

La photocatalyse est l'une des technologies clés pour les applications liées à l'énergie propre et à l'environnement. Le nombre d'applications basées sur la photocatalyse a considérablement augmenté au cours des deux dernières décennies. La photocatalyse est extrêmement importante pour la transformation de molécules inertes et thermodynamiquement stables telles que le méthane ou le CO_2.

L'activation photocatalytique des liaisons C-H est un domaine émergent. Le méthane est une source d'énergie prometteuse avec une énorme réserve et est considéré comme l'une des solutions de remplacement des ressources pétrolières non renouvelables, car il peut être converti en hydrocarbures et en hydrogène par le biais de réactions appropriées. Cependant, en raison de sa grande stabilité, une grande quantité d'énergie est habituellement consommée pour sa conversion, ce qui reste un problème à résoudre. La conversion du méthane et le mécanisme réactionnel qui se produisent sur les nanocomposites métal-hétéropolyacide-oxyde de titane ont été étudiés aux chapitres 3 et 4.

L'oxydation du méthane est effectuée depuis plus d'un siècle. Étant donné que l'oxygène est une molécule très réactive, le méthane peut réagir très rapidement avec l'oxygène moléculaire en produisant le CO_2. Par conséquent, il est difficile d'obtenir un produit souhaité avec un rendement élevé et une sélectivité importante. Nous avons observé l'oxydation photocatalytique directe et très sélective du méthane en monoxyde de carbone dans les conditions ambiantes. Les catalyseurs composites à base de zinc, d'acide tungstophosphorique et d'oxyde de titane présentent des performances exceptionnelles dans cette réaction, une sélectivité élevée en monoxyde de carbone et un rendement quantique de 7.1% à 362 nm. La réaction se réalise selon le mécanisme de type Mars-Van Krevelen et implique la formation de méthoxy-carbonates de surface en tant qu'intermédiaires et un cycle d'oxydation et de réduction du zinc.

Au cours des dernières décennies, des recherches approfondies ont été dédiées à la conversion directe du méthane en alcools ou en hydrocarbures supérieurs. Le procédé actuel de conversion du méthane en alcools ou en oléfines est complexe et coûteux car ils nécessitent une étape intermédiaire de reformage du méthane en gaz de synthèse. Bien que la conversion directe du méthane en produits à haute valeur ajoutée ait un potentiel environnemental et commercial important, il n'existe aucun procédé à l'échelle commerciale. Nous avons découvert une conversion photochimique directe quantitative hautement sélective (>90%) du méthane en éthane à température ambiante sur un nanocomposite argent-hétéropolyacide-oxyde de titane. Le rendement en éthane atteint 9% sur les matériaux optimisés. Une efficacité quantique élevée, une sélectivité élevée et un rendement significatif en éthane, associés à une excellente stabilité, sont les principaux avantages de la synthèse quantitative de méthane à partir de méthane en utilisant l'approche de boucle photochimique.

L'augmentation du taux de dioxyde de carbone dans l'atmosphère et l'épuisement des réserves de combustibles fossiles ont suscité de vives inquiétudes quant à l'impact ultérieur sur le climat mondial et l'approvisionnement futur en énergie. L'utilisation d'une énergie solaire abondante pour convertir le dioxyde de carbone en molécules plateformes, tel que le monoxyde de carbone, le méthane ou le méthanol, peut résoudre simultanément ces deux problèmes et constitue un moyen pratique de stockage d'énergie. Le chapitre 5 porte sur l'efficacité du nouveau catalyseur pour la conversion sélective de CO_2 en CO. Les nanocomposites acide de phosphotungstique-oxyde de titane contenant du zinc ont présenté une activité exceptionnelle atteignant 50 μmol CO/g·h et une sélectivité (73%) dans la réduction photocatalytique du CO_2 en CO en présence d'eau. Les expériences infrarouges in situ suggèrent que la réaction implique des bicarbonates de zinc contenant des groupes hydroxyle. La décomposition sous irradiation de ces espèces de bicarbonate de zinc conduit à la production sélective de monoxyde de carbone et d'oxygène.

Lors des réactions photocatalytiques, la différence de morphologie du catalyseur a généralement un effet significatif sur les performances photocatalytiques. Le chapitre 6 a étudié l'effet des cristaux monocliniques de vanadate de bismuth ($BiVO_4$) avec un rapport contrôlé de facettes {010} et {110} sur la réduction photocatalytique de CO_2 par H_2O. La

réaction sous irradiation est considérablement améliorée par la photodéposition sélective de co-catalyseurs de Cu et Co sur différentes facettes, fournissant un flux de charge selon le Z-schéma.

Mots clés: Photocatalyse, activation du méthane, réduction du CO_2, zinc, argent, hétéropolyacide, oxyde de titane, vanadate de bismuth

Chapter 1. General Introduction

1.1 Introduction

As a renewable energy source, solar energy has the advantages of being clean, universal, and durable, and the disadvantages of dispersion, instability, and low density. Specifically, solar energy does not pollute the environment, the sun shines on the earth, there is no geographical restriction. The solar radiation energy reaching the earth's surface every year is equivalent to 130 trillion tons of coal, and this energy transfer can be maintained for hundreds of millions of years without interruption[1, 2, 3]. Solar energy is the largest energy system that human beings can develop and utilize today. At present, the more mature routes of solar energy use are “photothermal conversion” and “photoelectric conversion”. The former is mainly applied to solar water heaters, while the latter is mainly used in storage lighting. Although many technologies for utilizing solar energy for chemical reactions are still in the laboratory development stage, more and more studies have shown that photocatalytic technology will have a lot of room for development in the future. Moreover, in recent years, with the rapid development of various nano-semiconductor materials, the implementationof photocatalytic technology into real life applications is getting faster and faster. It is foreseeable that photocatalysis will become a reliable technology to promote the healthy development of human society in the near future[4, 5, 6].

1.2 Overview of semiconductor photocatalysis

1.2.1 The basic principle of semiconductor photocatalysis

Semiconductor is a material with electrical conductivity between conductor (such as metals) and insulator (such as ceramic). The conductivity of a semiconductor usually increases with the increase of the temperature, which is opposite to that of a metal[7]. The unique electronic property of a semiconductor is characterized by its valence band (VB) and conduction band (CB). The VB of a semiconductor is formed by the interaction of the highest occupied molecular orbital (HOMO), while the CB is formed by the interaction of the lowest

unoccupied molecular orbital (LUMO). There is no electron state between the top of the VB and the bottom of CB. The energy range between CB and VB is called the forbidden bandgap (also called energy gap or bandgap), which is usually denoted as E_g. The band structure, including the bandgap and the positions of VB and CB, is one of the important properties for a semiconductor photocatalyst, because it determines the light absorption property as well as the redox capability of a semiconductor[5, 8, 9]. As shown in Figure 1-1, the photocatalytic reaction initiates from the generation of electron-hole pairs upon light irradiation. When a semiconductor photocatalyst absorbs photons with energy equal to or greater than its E_g, the electrons in VB will be excited to CB, leaving the holes in VB. This electron−hole pair generation process in TiO_2 can be expressed as follows[8, 10, 11, 12]:

$$TiO_2 + h\nu \longrightarrow e^{-}(TiO_2) + h^{+}(TiO_2)$$

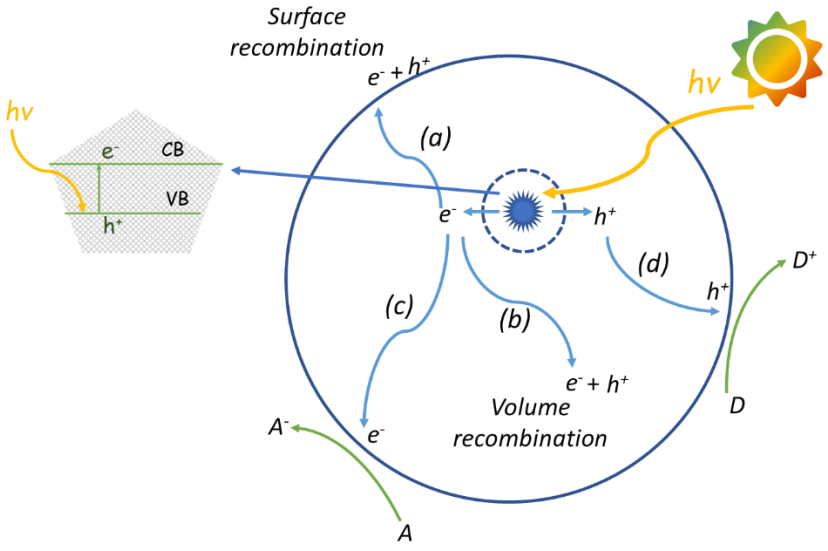

Figure 1-1 Proposed mechanism of photocatalytic reactions on semiconductor photocatalyst.

These photogenerated electron-hole pairs may further be involved in the following three possible processes: (i) successfully migrate to the surface of semiconductor; (ii) be captured by the defect sites in bulk and/or on the surface region of semiconductor; and (iii) recombine and release the energy in the form of heat or photon. The last two processes are generally

viewed as deactivation processes because the photogenerated electrons and holes do not contribute to the photocatalytic reaction. Only the photogenerated charges that reached the surface of semiconductor could be available for photocatalytic reactions. The defect sites in the bulk and on the surface of semiconductor may serve as recombination centers for the photogenerated electrons and holes, which will decrease the efficiency of the photocatalytic reaction[13].

In fact, semiconductor photocatalysis is often more complex than the three-step process mentioned above. It involves many elementary reactions such as excitation, separation, transfer, recombination of the photogenerated electron-hole pairs, migration of the surface charge and so on. Litter and coworkers[14] reported TiO_2 as a model photocatalyst, according to the pulsed photolysis experiments, the mechanism of photocatalysis was described in detail. Figure 1-2 shows that the typical photocatalytic reaction, the steps of each reaction, and the time scale of each reaction[15, 16, 17].

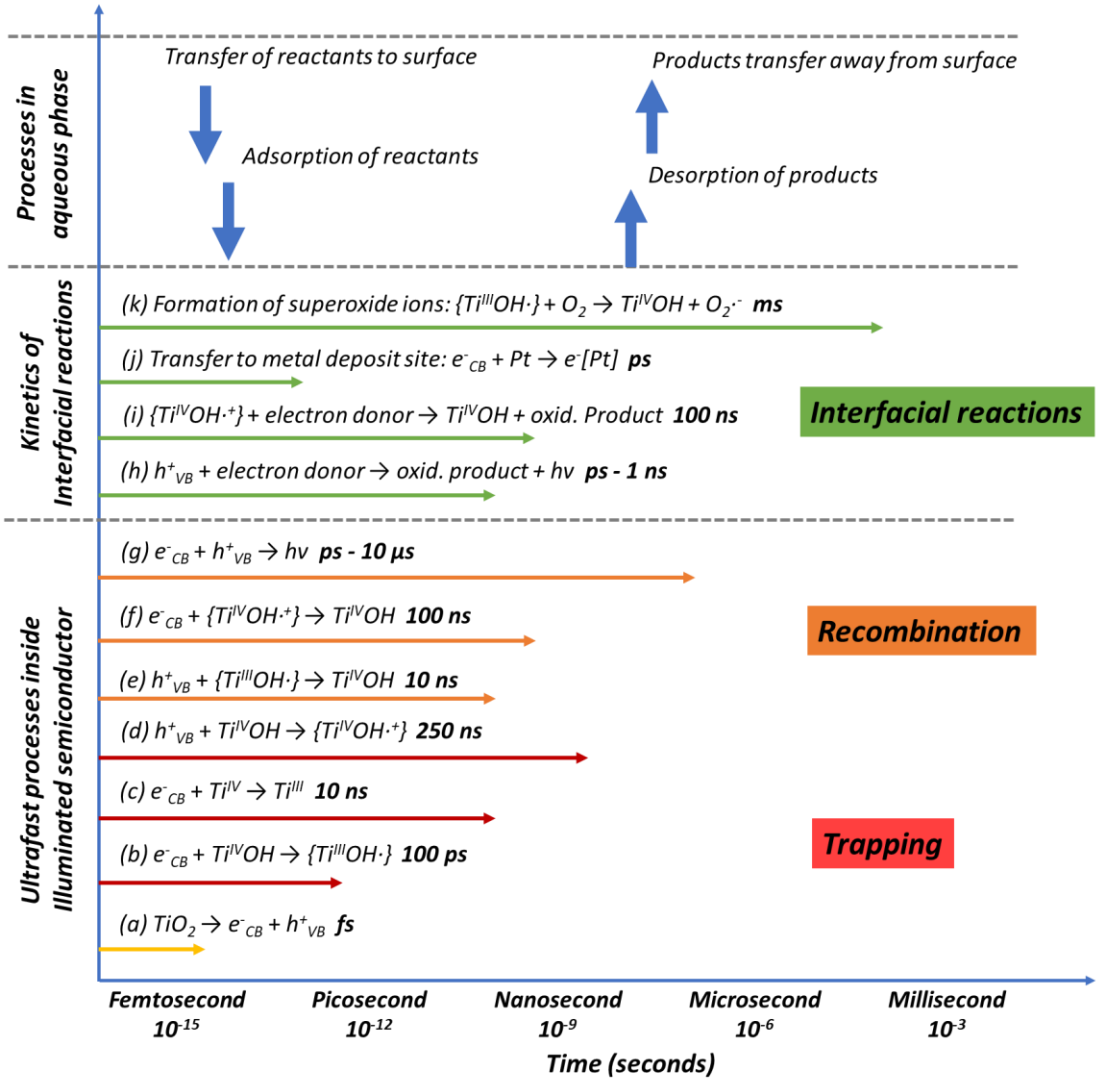

Figure 1-2 Elementary reactions in the TiO_2-based photocatalysis with corresponding time scales.

In the photocatalytic reaction, the energy band structure of the photocatalytic material determines the properties of the photogenerated electron-hole pair. Photogenerated electron-hole pairs are generated and transferred under light irradiation. The excited carriers and the reaction of reactants are closely related to the band structure of semiconductor materials. Therefore, the band structure of semiconductor photocatalyst is of great significance for the study of photocatalysis. Theoretical analysis shows that the ability of semiconductors to induce the transfer of electrons to the surface of the catalyst depends on two aspects: (i) semiconductor energy band position; (ii) redox potential of adsorbed reactants on the catalyst

surface. The reduction potential of the electron-accepting reactant adsorbed on the surface of the catalyst is thermodynamically lower than the conduction band position of the semiconductor, in order to provide electrons and holes. Several semiconductor band edge positions are shown in Figure 1-3. The left side of the figure is relative to the standard hydrogen electrode (NHE pH = 0), on the right is the oxidation-reduction electrode potential of the relevant reactant[18].

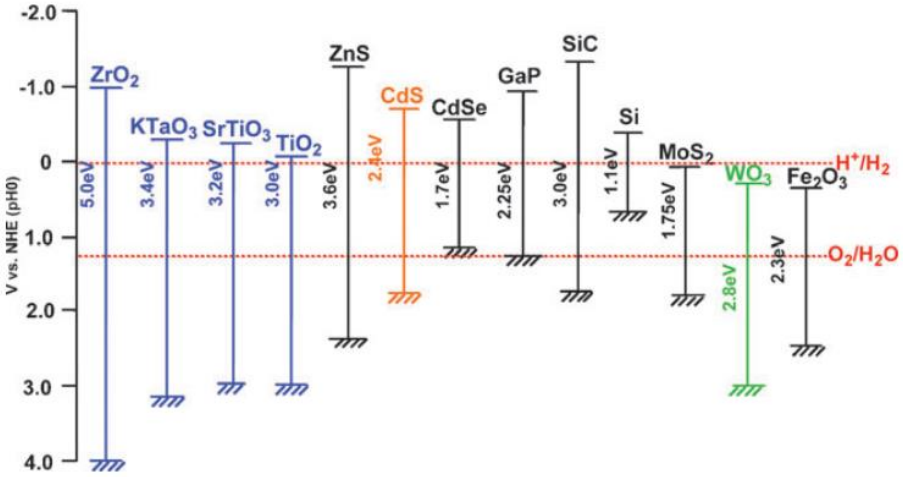

Figure 1-3 Band edge positions of semiconductor photocatalysts relative to the energy levels of various redox couples in water.

1.2.2 Application of photocatalytic technology

As a new technology developed in the recent decades, photocatalytic reactions have always attracted the increasing attention of scientists because of their unique advantages. Since photocatalysis can utilize solar energy as a clean energy source, traditional catalytic reactions generally require relatively harsh conditions such as high temperature and high pressure. Photocatalytic reactions can be carried out not only in mild conditions but also with high selectivity[19]. After decades of efforts, photocatalytic reactions have been rapidly developed and applied in many fields, including water treatment, organic synthesis, photocatalytic hydrogen production, reduction of carbon dioxide, and conversion of methane[20, 21, 22].

Photocatalysis can be widely used in different fields because the light is one of the most

widely used energy sources in daily life and it can be used for the excitation of semiconductors by generation of electrons and holes for reduction and oxidation reactions, respectively. The application of photocatalytic reactions in different fields is is shown in Figure 1-4. Photocatalytic reactions often exhibit higher selectivity compared to the relevant thermocatalytic processes.

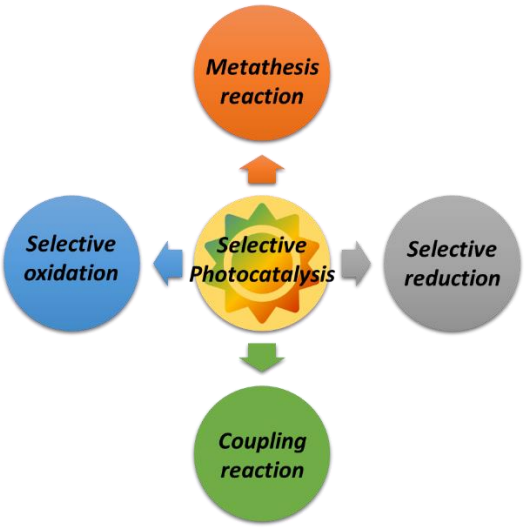

Figure 1-4 Selectivity enhancement in photocatalytic reaction.

1.3 Photocatalytic activation of methane

1.3.1 Importance of the methane utilization

As prices fluctuate sharply and crude oil reserves decline, natural gas is attracting more and more attention as an important source of clean fossil energy and chemical raw materials. In particular, large reserves of shale gas, coalbed methane, and methane hydrate have been recently discovered[23]. Energy-intensive reactions inevitably activate stable alkanes and convert them into other valuable products. Fuel processing involves hydrocarbons such as methane, ethane, propane, butane and higher hydrocarbons, or liquid alcohols such as methanol, ethanol and butanol[24, 25]. Developing an effective and cost-effective way to convert methane into a more useful product is a major challenge in the current situation.

Different strategies of methane conversions have been summarized briefly in Figure 1-

5.

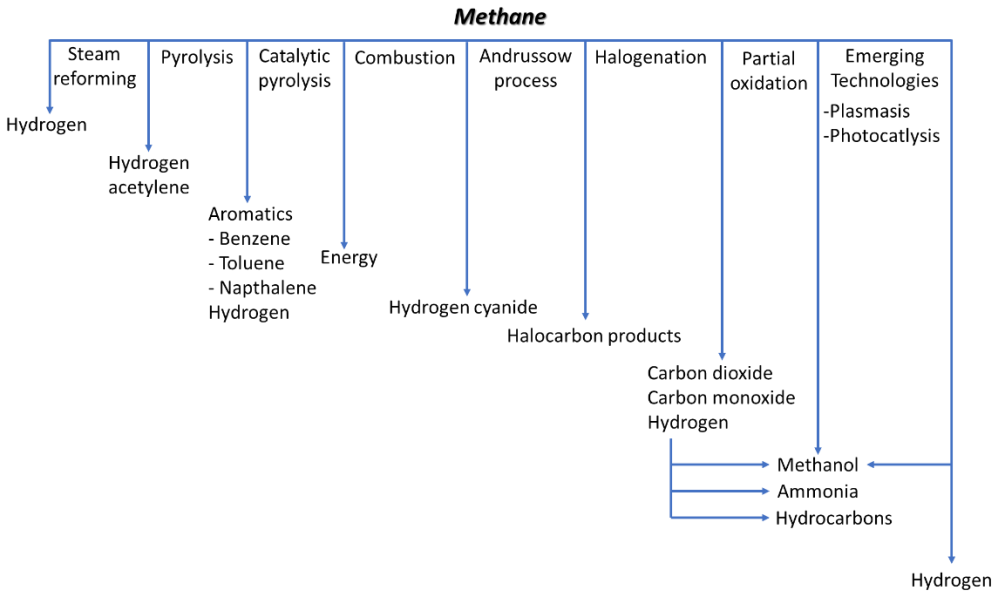

Figure 1-5 Methane and its end products[26].

Methane can be converted into a variety of products of interest.There are two main routes for transforming methane into valuable fuels and chemicals (Figure 1-6). The first one is the indirect conversion route, or synthesis gas (syngas, H_2/CO) route, which is the current commercial route for large-scale transformation of methane. This route converts methane into syngas through steam reforming of methane (SRM) and utilizes the obtained syngas in downstream processes such as Fischer-Tropsch synthesis or methanol synthesis. Another one is the direct conversion route, in which methane is converted directly into liquid oxygenates or higher hydrocarbons. The indirect route is the industrialized route for methane conversion and is economically competitive on large scales, but it is an energy-intensive process because high operating temperatures (700-1100°C) are required to drive the endothermic SRM reaction. In the process, about 60%-70% of the cost of the overall process is associated with the reforming process. In order to reduce the reforming cost, direct routes have been attracting the attention of many scientists. Therefore, innovative catalysts and reaction systems should be developed to reduce the reaction temperature of methane conversion.

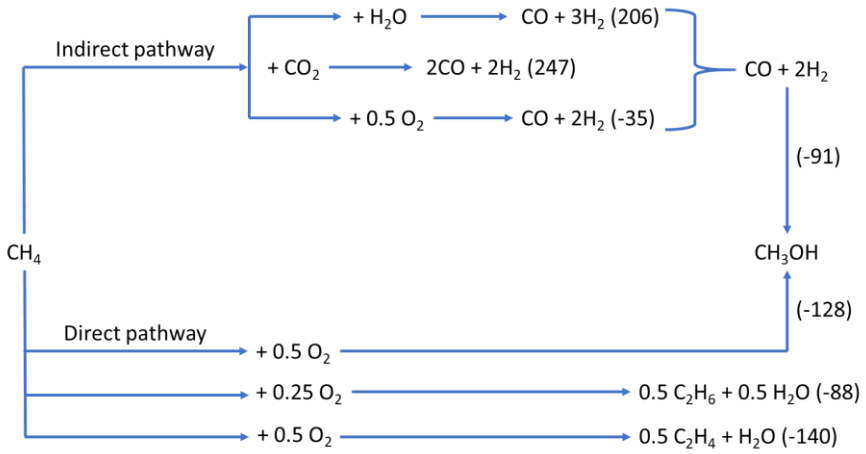

Figure 1-6 Methane conversion in direct and indirect routes. The numbers within parentheses represent enthalpy changes (DH) in kJ mol^{-1} at 25°C[27].

1.3.2 Research progress of photocatalytic methane conversion

1.3.3.1 Methane coupling

Photocatalytic non-oxidative coupling of methane (NOCM) was first discovered in 1998[28]. This reaction is thermodynamically unfavorable at low reaction temperatures. Thus, it was a surprise to find that this reaction could proceed at around room temperature (310 K) over silica, alumina, and silica–alumina photocatalysts under UV irradiation. The reaction test was carried out in a closed quartz reactor (Figure 1-7a) for 18 h under UV irradiation from a 250 W Xe lamp. The catalyst was 1 g and only methane (100 mmol) was introduced as the reactant. After the 18 h photo reaction, the highest yield of C_2–C_6 products obtained from the methane coupling and the consecutive reactions was achieved on silica–alumina (5.9 C%), where the main product was ethane (60%). It is worth noting here that the ethane yield on these photocatalysts was much higher than the one calculated from the thermodynamic equilibrium constant (ca. 0.0004% at 314 K). Thus, it is confirmed that the photocatalyst selectively promoted the forward reaction, methane activation, than the reverse reaction, activation of ethane and/or hydrogen, in the photocatalytic NOCM. This would be one of the advantages of the photocatalytic systems.

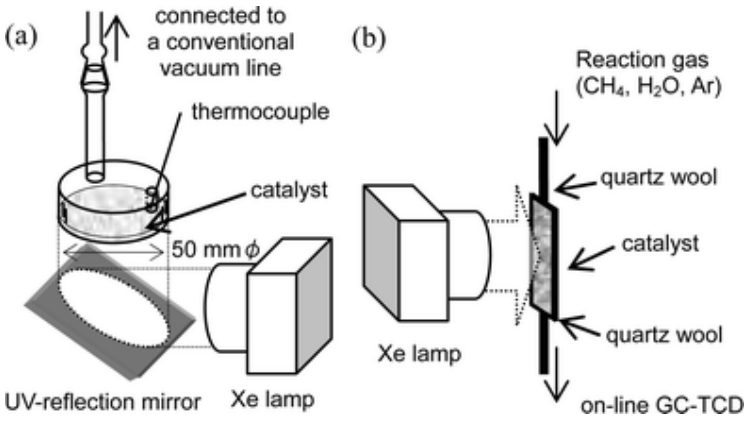

Figure 1-7 Schematic drawing of the photoreactor made of quartz. (a) A closed reactor (typically, the bottom was ca. 20 cm^2, volume was ca. 30–50 cm^3), (b) a flow reactor (typically 10 cm^2 * 1 mm).

Chen and coworkers[29, 30] report a series of metal-modified zeolite catalyst for photoactivation of methane C-H bond. Zn^+-modified ZSM-5 zeolite catalyst exhibits superior photocatalytic activity for selective C-H activation of an alkane molecule. An optimized catalyst converts 24% of methane upon irradiation for 8 hours by a high-pressure mercury lamp with a selectivity larger than 99% for ethane and hydrogen products. The experiments suggest a two-stage catalytic process that requires light of wavelengths shorter than 390 nm to transfer electrons from the zeolite framework to the Zn^{2+} centers, and light of visible wavelengths to promote the Zn^+ reactivity towards methane. Using visible light of different wavelengths, we have found that the minimum energy required to drive the electron from the Zn^+ site to activate methane corresponds to a wavelength of about 700 nm. A schematic energy diagram for the whole processes involved in the photocatalytic reaction is given in Figure 1-8a. Quantum chemical calculations give rise to the optimized structure of the initially adsorbed methane molecule linked to a Zn^+ cation in the pore of zeolite ZSM-5 (Figure 1-8b).

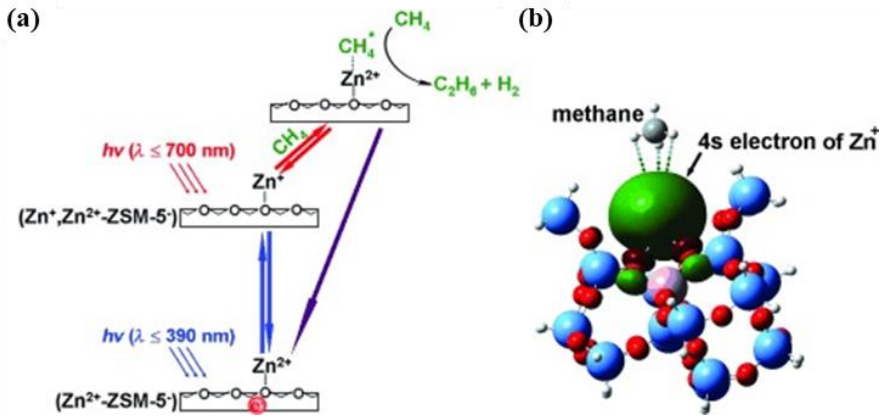

Figure 1-8 (a) Schematic energy diagram for the processes of the photocatalytic reaction. (b) The B3LYP hybrid exchange-correlation optimized geometry of the adsorbed methane molecule attracted by the Zn^{+} active site (red: O, blue: Si, pink: Al, gray: C, white: H, and green: the 4s electron of Zn^{+}).

One year later, they describe a Ga^{3+}-modified EST10 zeolite catalyst (EST-10 = titanosilicate) in which the photogenerated hydroxyl radical and the extraframework metal ion interact with the methane molecule to split the H_3C-H bond in a synergistic way under UV irradiation ($\lambda < 350$ nm). They think that the combination of both oxygen-centered and metal-centered active sites in the material significantly enhances its photoactivity for methane C-H bond activation, leading to efficient non-oxidative coupling of methane at room temperature (Figure 1-9). An average methane conversion rate of around 29.8 μmol h^{-1} g^{-1} was achieved after UV irradiation for 5 h.

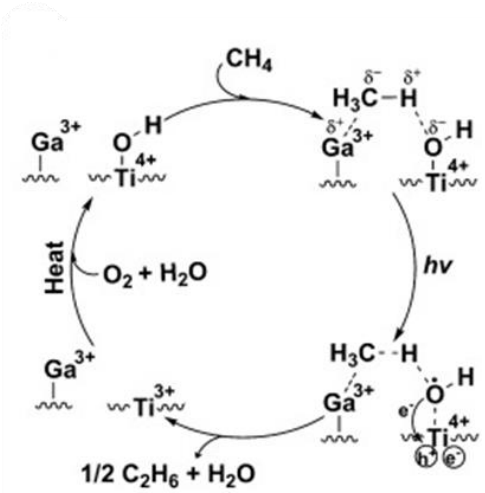

Figure 1-9 Reaction mechanism involved in the photo-driven methane activation reaction.

1.3.3.2 Methane conversion with O_2

Photocatalytic conversion of methane in the presence of oxygen was reported in 1978 at room temperature under UV irradiation[31]. It was proposed that the hole sites O^- that were produced on the photocatalysts such as TiO_2, V/SiO_2, and P/SiO_2 under UV irradiation ($O^{2-} + h^+ \rightarrow O^-$) would play the important role to attack the methane molecules to generate methyl radicals as the first step.

Similar to the case of thermal catalytic reaction, the complete oxidation of methane to CO_2 and H_2O could not be avoided in the photocatalytic system when using molecular oxygen and a semiconductor photocatalyst, such as TiO_2. It is a challenge to convert methane to more useful oxygenated compounds such as methanol, formaldehyde, and carbon monoxide. So far, the photocatalytic methane conversion through partial oxidation of methane (POM) has been the most popular way to obtain the oxygenated compounds. The most intensively studied photocatalysts for the POM are vanadia-based photocatalysts, molybdenum-based photocatalysts[32] and others[33, 34].

Vanadia-based photocatalysts. V/SiO_2 (V = 2%) produced only a trace amount of ethane and formaldehyde at room temperature under UV irradiation in the photocatalytic partial oxidation of methane (POM)[31]. The major product was CO_2. Yoshida and co-workers tested the activity of V/SiO_2 for the POM under UV irradiation at 493 K. It was confirmed that the high photoactivity for formaldehyde formation (1.8–2.6% yield) with high selectivity (80–92%) was obtained when the loading amount of V was very low, ca. 0.01–0.1 mol%. When the loading amount of V increased, the total oxidation to CO_x proceeded more easily, resulting in a lower activity and selectivity to formaldehyde. In the photoreaction at higher temperature (>673 K), both the conversion of methane and the selectivity to formaldehyde decreased, which would be due to the reduced lifetime of the photoexcitation state and the increase in the thermally catalyzed consecutive oxidation of formaldehyde to CO_2, respectively. A large specific surface area seems to be an important factor contributing to the high activity of vanadia-based photocatalysts. Under UV

irradiation at 493 K[35], with the same amount of V loading, a mesoporous silica-supported photocatalyst was reported to show much higher activity to produce formaldehyde than the amorphous silica-supported version[36]. The yield and selectivity of formaldehyde product were ca. 0.3% and 95.4%, respectively. In all cases mentioned above, the four-coordinated species having the V=O bond on the surface (highly dispersed and isolated vanadium oxide surface species) were proposed to be the active sites for selective formation of formaldehyde. The high surface area of the support would favor high dispersion of the vanadium oxide species resulting in both a high photocatalytic activity and a high selectivity for the formaldehyde formation.

Molybdenum-based photocatalysts. Although the TiO_2 and MoO_3 photocatalysts only produced CO_2, the TiO_2-supported MoO_3 yields both CO and CO_2 in an almost equal amount in a closed reactor under UV irradiation around room temperature[37]. The activity of TiO_2-supported MoO_3 is much higher than that of either TiO_2 or MoO_3, suggesting the synergic interaction between TiO_2 and MoO_3. The photoexcited electrons and holes would migrate through the conjugation between them, which would assist the local separation and prevent their recombination, and thus, would give a high activity. Photocatalytic POM to methanol was reported on a MoO_3/SiO_2 catalyst[38]. The reaction was carried out in a circulated closed system. A low yield of methanol was detected under UV irradiation at 313 K without any CO_x molecule formation. However, MoO_3/SiO_2 was turned to blue after photoirradiation for a long time, suggesting the reduction of MoO_3. When the photoreaction was carried out at a higher temperature (373 K), the color of the catalyst did not change, suggesting facile oxidation of the reduced sites by oxygen at this temperature. The addition of Cu^{2+} to the MoO_3/SiO_2 catalyst also enhanced the methanol formation, from 2 mmol h^{-1} to 6 mmol h^{-1}. It was proposed that the increase in the formation rate under UV irradiation was possibly caused by the longer lifetime of the active O^- centres photo-formed by the charge transfer from O 2p to the valence d orbital of Cu^{2+}. In addition, silica-supported $CuMoO_4$ exhibited absorption in the visible region and gave a high methanol formation (2.8 mmol h^{-1}) under visible irradiation. So far, it is still difficult to obtain both high activity and high selectivity for the photocatalytic POM by using molecular oxygen. This is because of the high reactivity

of the oxidant. In many cases, the addition of mild thermal energy seemed to be effective in promoting the photocatalytic reaction.

Others photocatalysts. Yi and coworkers[39] show that Ag decorated ZnO can activate methane under ambient conditions when the particle size of zinc oxide is reduced down to the nanoscale, it exhibits high activity for methane oxidation under simulated sunlight illumination. The function of nano-silver decoration lies at least in: (i) as electron sink reducing the recombination of electrons and holes in the surface of ZnO; (ii) as a photo-sensitizer extending the utilization of the visible light. They revealed that the methane photo-oxidation, in all likelihood, proceeds via a two-step process (Figure 1-10): first, CH_4 reacts with O_2 and produces H_2O and HCHO ($CH_4 + O_2 \rightarrow HCHO + H_2O$), and then the intermediate product HCHO further reacts with O_2 and produces H_2O and CO_2 ($HCHO + O_2 \rightarrow CO_2 + H_2O$).

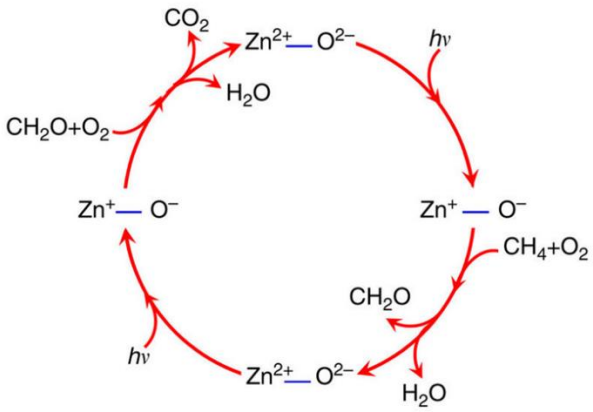

Figure 1-10 Schematic illustration for the photocatalytic CH_4 reaction processes under ambient conditions[39].

1.3.3.3 Methane conversion with H_2O

Other oxidants milder than molecular oxygen have also been examined in photocatalytic conversion of methane to obtain organic products and/or hydrogen. Here, the photocatalytic methane conversion by using water molecules as the oxidant will be introduced[21, 40, 41, 42, 43, 44, 45, 46].

Photocatalytic methanol formation. Photocatalytic conversion of methane to methanol

by using water as an oxidant was reported to occur on WO_3 doped with lanthanum under either UV or visible irradiation at 343 K[45]. Methane conversion was ca. 4% and the main products were hydrogen and methanol at 1 MPa. The observed side products were ethane, oxygen, formic acid, and CO_2. The conversion depended on the concentration of dissolved methane in water. The reaction occurred only above 343 K at atmospheric pressure (0.1 MPa), but it occurred at a lower temperature (323 K) at 10 MPa. The addition of hydrogen peroxide increased the conversion of methane. It was proposed that the hydroxyl radical would react with methane to give a methyl radical, which would further react with the additional water to produce methanol and hydrogen. Conversion of methane to methanol by using a visible laser (514 nm) and a WO_3 catalyst was reported to occur at room temperature[47]. The products observed were methanol, O_2, and CO_2. The maximum yield of methanol was ca. 32 mg dm^{-3} when the laser power was 1.5 W and the catalyst amount was 0.3 g. The addition of H_2O_2 has no effect in enhancing the methanol yield, but the addition of an electron capture agent like Fe^{3+} could optimize the yield. Here Fe^{3+} would inhibit the generation of O^{-2} and CO_2 by capturing the conduction band electron to produce Fe^{2+}. This keeps the concentration of methanol and oxygen constant over a prolonged period. Recently, bismuth-based photocatalyst was found to catalyze methane conversion to methanol[48]. Bi_2WO_6, $BiVO_4$, and coupled Bi_2WO_6/TiO_2-P25, have been synthesized by a facile hydrothermal method, characterized, and evaluated for the first time in the selective photooxidation of methane to methanol. The obtained $BiVO_4$ is, among the others, the most promising photocatalyst for this reaction, displaying higher CH_3OH selectivity and being more stable than the others. When Bi_2WO_6 was coupled with TiO_2, the methane conversion increased; however, overoxidation of CH_4 to CO_2 predominates. Andreu and coworkers[49] designed Bi- and V-containing beta zeolites prepared by incipient wetness impregnation have been used. While the zeolite proves to be photoactive under UVC irradiation toward the total oxidation process, the formation of V_2O_5 on the surface is an effective alternative for modifying the acid−base surface properties, thus significantly decreasing the undesired CO_2 formation. Additionally, the addition of small Bi amounts favors the formation of a $BiVO_4/V_2O_5$ heterojunction, which acts as a visible light photocatalyst while at the same time, leading to higher selectivity

to methanol at the expense of ethylene formation (Figure 1-11).

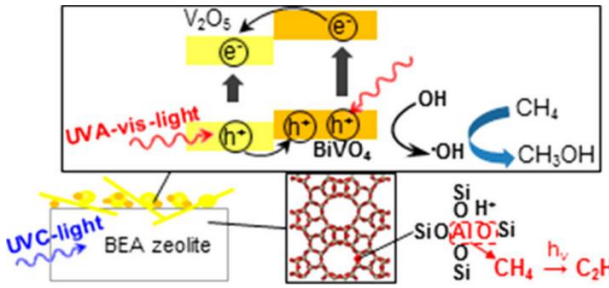

Figure 1-11 Schematic illustration for the photocatalytic oxidation of methane to methanol.

Photocatalytic SRM. Pt/TiO_2 photocatalyst was found to promote the photocatalytic steam reforming of methane (SRM) at around room temperature[50, 51]. Under these conditions, both the SRM and consecutive water–gas shift reaction occurred simultaneously. High activity was obtained on Pt/TiO_2 photocatalysts having large surface area of anatase TiO_2 and enough loading amount (40.1 wt;%) of metallic Pt nanoparticles. H_2 and CO_2 were observed as the main products upon photoirradiation, as shown in Fig. 9. Trace amounts of C_2H_6 and CO were observed as minor products. After an induction period, the molar ratio of H_2 to CO_2 in the outlet gas became close to four (Figure 1-12), confirming that the photocatalytic SRM proceeded as the main reaction. In this system, H_2O and CH_4 would be activated to form the surface reaction intermediates, $[CH_2O]_n$.

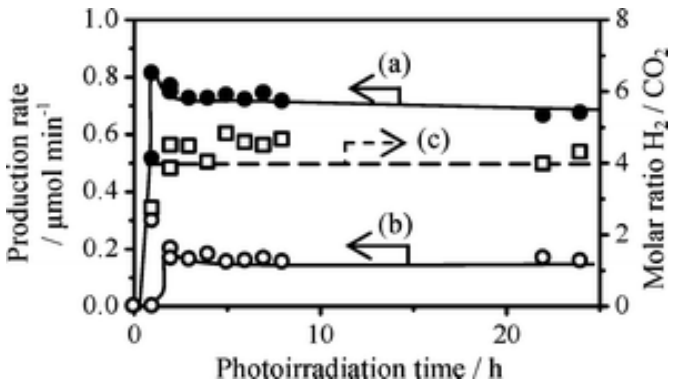

Figure 1-12 Time course of the production rate for (a) H_2 and (b) CO_2, and that of (c) the molar ratio of H_2 to CO_2 over Pt (0.1)/TiO_2 in the flow of CH_4 (50%) and H_2O (1.4%).

Total flow rate was 50 mL min^{-1}.

Platinum-loaded lanthanum-doped sodium tantalate, Pt/$NaTaO_3$: La was found to show higher activity for the photocatalytic SRM than the other catalysts[51]. By-products were hardly observed in this case. In this system, the highest H_2 production rate observed was 4.5 mmol min^{-1} (6.6 mL h^{-1}), corresponding to 0.6% methane conversion. over Pt (0.03 wt%)/$NaTaO_3$: La upon photoirradiation of maximum intensity (116 mW cm^{-2}) from the Xe lamp. This photocatalytic SRM system can produce H_2 from renewable resources (biomethane and water) and natural energy (photoenergy such as solar energy).

As mentioned above, methane can be converted in various ways. We introduced some photocatalytic reaction systems for the methane conversion, i.e., the direct methane conversion to hydrocarbons (NOCM), the partial oxidation (POM), the steam reforming (SRM), and others. These photocatalytic reaction systems provide us with many possibilities to activate methane (Table 1-1).

Table 1-1 State of the art methane chemical utilization reactions.

Entry	Reactions	Chemical equations
Methane only		
1	Pyrolysis	$CH_4 \rightarrow C + 2H_2$
2	Non-oxidative coupling of methane (NOCM)	$2CH_4 \rightarrow C_2H_6 + H_2$
3	Aromatization	$6CH_4 \rightarrow C_6H_6 + 9H_2$
Methane and oxygen		
4	Total oxidation	$CH_4 + 2O_2 \rightarrow CO_2 + 2H_2O$
5	Oxidative coupling of methane (OCM)	$4CH_4 + O_2 \rightarrow 2C_2H_6 + 2H_2O$
6	Partial oxidation of methane (POM)	$2CH_4 + O_2 \rightarrow 2CO + 4H_2$ $2CH_4 + O_2 \rightarrow 2CH_3OH$
Methane and water		
7	Methane to methanol	$CH_4 + H_2O \rightarrow CH_3OH + H_2$
8	Steam reforming of methane (SRM)	$CH_4 + H_2O \rightarrow CO + 3H_2$
9	SRM + Water–gas shift reaction	$CH_4 + 2H_2O \rightarrow CO_2 + 4H_2$

1.4 Research progress of photocatalytic CO_2 reduction

1.4.1 Titanium dioxide-based photocatalysts

Although the TiO_2 semiconductor material has a bandgap energy of more than 3.0 eV, which makes it a UV-absorbing semiconductor material, it has low cost, high catalytic activity, high chemical stability, strong anti-oxidation capability, non-toxicity, and no secondary pollution. So it has become the most widely used photocatalytic material. In 1979, Japanese researcher Fujishima and Honda reported for the first time the synthesis of formic acid, methanol, formaldehyde and other organic compounds by photocatalytic reduction of CO_2 in semiconductor suspensions, in which TiO_2 exhibited excellent photocatalytic activity[52]. Since then, photocatalysts for the photocatalytic reduction of CO_2 on the basis of TiO_2 have attracted a great deal of attention and have attracted a great deal of research interest[53, 54, 55, 56].

1.4.1.1 Metal- and non-metal dopping of TiO_2

The doping of TiO_2 mainly includes the doping with metal and non-metal elements. Metal doping can introduce defect sites or change crystallinity in the semiconductor lattice, thus affecting the recombination of electron-hole pairs. The non-metal doping mainly introduces new valence bands, which narrows the gap width to absorb visible light, thereby increasing the catalyst's absorption of sunlight. Both the doping methods may affect the adsorption behavior of the reaction species on the surface of the catalyst and they have a significant influence on the photocatalytic activity of the TiO_2.

In 1990, Verwey and coworkers[57] first discovered that the catalytic properties of the semiconductors changed after the semiconductors were doped with different valence metal. For photocatalytic reduction of CO_2, Cu-based catalysts have been considered to have high selectivity for reducing CO_2. Experiments show that Cu-doped TiO_2 photocatalyst can significantly improve the effect of photocatalytic reduction of CO_2[58]. Richardson and coworkers[59] reported that the activity of photocatalytic reduction of CO_2 to methanol with Cu and Mn co-doped TiO_2 catalysts prepared by the sol-gel method has been further

improved comparing with a single metal-doped catalyst. Kočí and coworkers[60] synthesized Ag-doped TiO_2 catalysts under reversed micelles using sol-gel method. Under the appropriate Ag content, the methanol and methane generation rates have been significantly improved. Marta and coworkers[61] also used the sol-gel method to dope Mg in TiO_2. The introduction of Mg increased the density of Ti^{3+} and oxygen vacancies on the TiO_2 surface, which promoted the separation of photogenerated electrons and holes.

Ultraviolet light often used for excitation, is one of the main reasons restricting the photocatalytic application of semiconductor TiO_2. Extending the light absorption range of TiO_2 to the visible light region and realizing the direct use of visible light photocatalytic reduction of CO_2 in solar energy will be a major advance in photocatalytic research. According to the semiconducting energy band theory, the conduction band position of a semiconductor mainly depends on the energy level of the d orbit of the metal ion (Ti^{4+}) in the semiconductor, and the valence band energy level mainly depends on the energy level of the p orbital of the nonmetal ion (O^{2-}). Therefore, the valence band position of the catalyst can be adjusted to change the forbidden band to promote the absorption of visible light by introducing non-metal ions (B, N, S, C, halogens, etc.) instead of part of the oxygen in TiO_2 (Figure 1-13).

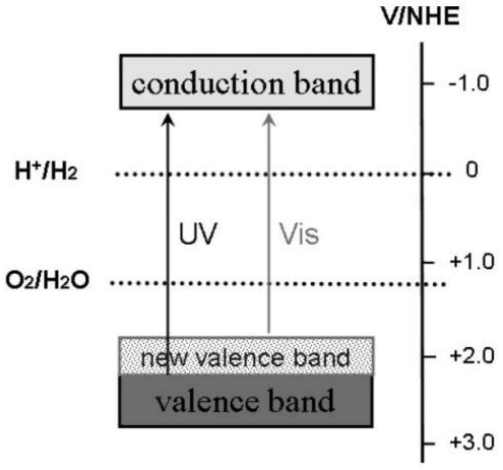

Figure 1-13 New valence band formation by doping of nonmetal ions.

1.4.2 Non-titanium-based photocatalysts

A large number of semiconductor materials have been developed and applied to catalyze various photocatalytic reactions under visible or ultraviolet light. Classifying the main semiconductor photocatalysts into five categories based on their electronic structure. (i) d^0 metal oxide photocatalysts (Ti^{4+}, Zr^{4+}, Nb^{5+}, Ta^{5+}, V^{5+}, Mo^{6+} and W^{6+}), (ii) d^{10} metal oxide photocatalysts (Ga^{3+}, Ge^{4+}, In^{3+}, Sn^{4+}, and Sb^{5+}), (iii) layered double hydroxides, (iv) MOFs materials.

1.4.2.1 d^0 metal oxide photocatalysts (Ti^{4+}, Zr^{4+}, Nb^{5+}, Ta^{5+}, V^{5+}, Mo^{6+} and W^{6+})

Other cations are introduced by solution or hydrothermal methods to synthesize the corresponding titanate-based semiconductor materials. These materials show some catalytic activity in the photocatalytic reduction of CO_2 through the modification of promoter or compounding with other semiconductors[62, 63, 64]. Guan and coworkers[62] prepared $K_2Ti_6O_{13}$ by the solid solution method, then $Cu/ZnO/K_2Ti_6O_{13}$ was obtained by impregnation method, and finally photo-deposition Pt to obtain $Pt\text{-}Cu/ZnO/K_2Ti_6O_{13}$ catalyst. In the experiment, focused sunlight was used to irradiate the catalyst for photocatalytic reduction of CO_2. The main products were methanol, formaldehyde and formic acid. The total production rate of hydrocarbon reached 17 μmol/gcat/h. Kudo and coworkers prepared a layered perovskite structure of $ALa_4Ti_4O_{15}$ (A=Ca, Sr, and Ba) by complexation-polymerization and modified the catalyst with Ag. It was found that $Ag\text{-}BaLa_4Ti_4O_{15}$ had the highest catalytic activity, and the main product of the reduction was CO, and the product molar ratio is $(H_2 + CO)$: O_2 = 2: 1 (Figure 1-14a). This is in accordance with the stoichiometry, which shows that the production of CO is mainly from the photocatalytic reduction of CO_2. Further characterization found that Ag is mainly deposited on the side of the layered material, the photocatalytic reduction reaction occurs mainly on the side, and the oxidation reaction mainly occurs on the front side (Figure 1-14b).

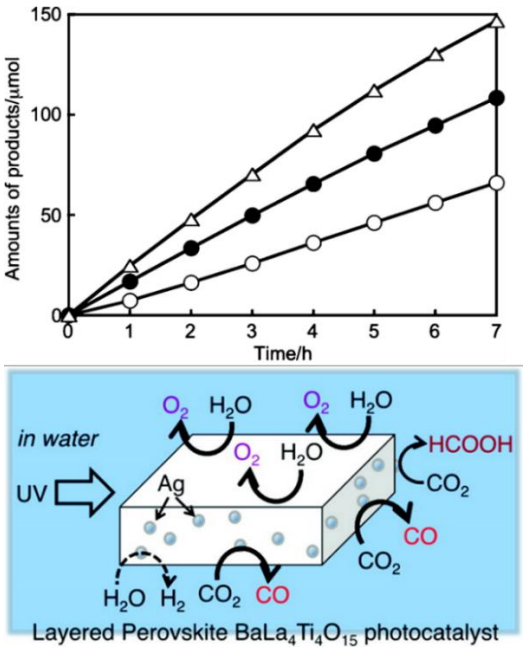

Figure 1-14 (a) CO_2 reduction over $BaLa_4Ti_4O_{15}$ photocatalyst with Ag (2wt%) cocatalyst loaded by a liquid-phase reduction method; (b) Mechanism of photocatalytic CO_2 reduction over $BaLa_4Ti_4O_{15}$ with Ag cocatalysts loaded.

Alkaline and alkaline-earth metal niobate have been shown to have good photocatalytic activity in photo-degraded pure water, but their less applied in photocatalytic reduction of CO_2. In 2011, Zou and coworkers first applied the niobate salt semiconductor material to the photocatalytic reduction of CO_2. $NaNbO_3$ nanowires prepared by the hydrothermal method have significantly improved the activity of photocatalytic reduction of CO_2 to produce CH_4 comparing with the $NaNbO_3$ particles prepared by the solid solution method. A further study by Ye and coworkers found that the crystalline structure and electronic structure of $NaNbO_3$ material have a significant effect on photocatalytic activity[65, 66]. The cubic phase c-$NaNbO_3$ has a higher photocatalytic activity than the orthorhombic phase o-$NaNbO_3$ (Figure 1-15). Further characterization and theoretical calculations found that the band gap of the cubic phase c-$NaNbO_3$ is narrower than the orthorhombic phase o-$NaNbO_3$ and has a wider absorption range. Its unique crystal structure makes the electrons in the c-$NaNbO_3$ more easily excited by light and transferred to the surface. These properties make the c-$NaNbO_3$ have higher photocatalytic activity.

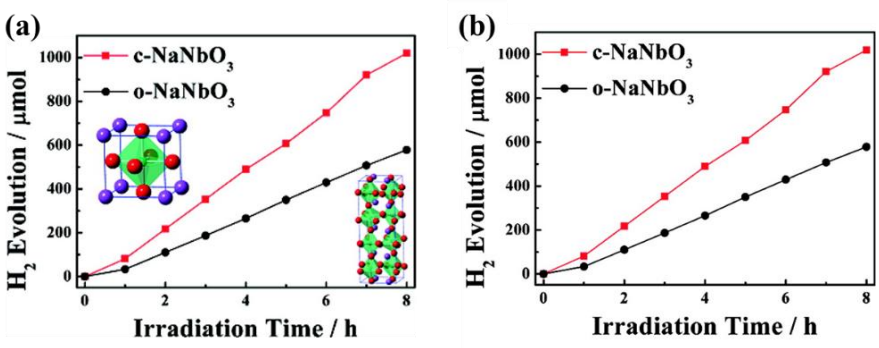

Figure 1-15 (a) Photocatalytic H_2 evolution from the aqueous methanol solution; (b) CH_4 evolution in gas-phase CO_2 reduction over c-$NaNbO_3$ and o-$NaNbO_3$ samples (with loading 0.5 wt % Pt).

Tantalate catalysts have some applications in the photocatalytic reduction of CO_2. In particular, $InTaO_4$ semiconductor materials with visible absorption ability have received more attention[67, 68, 69, 70]. The band gap of $InTaO_4$ is 2.6 eV, and the valence band structure is shown in Figure 1-16. Its conduction band position is relatively high, and photo-generated electrons have a relatively high reduction capacity, which can well reduce CO_2 to generate CH_3OH; its valence band is in a suitable position, and it can also oxidize water to generate oxygen. After $InTaO_4$ is modified with nitrogen or NiO, the visible light photocatalytic activity of CO_2 will be further improved. Teramura and coworkers prepared $ATaO_3$ (A = Li, Na, K) catalyst by solid solution method, in which $LiTaO_3$ had the highest activity of photocatalytic reduction of CO_2 to CO, and it had better ability to separate photogenerated carriers[71]. Lv and coworkers prepared NiO_x-Ta_2O_5-rG composite photocatalytic material by one-step hydrothermal method. After graphene modification, the activity of the photocatalytic reduction of CO_2 to CH_3OH has been significantly improved[72].

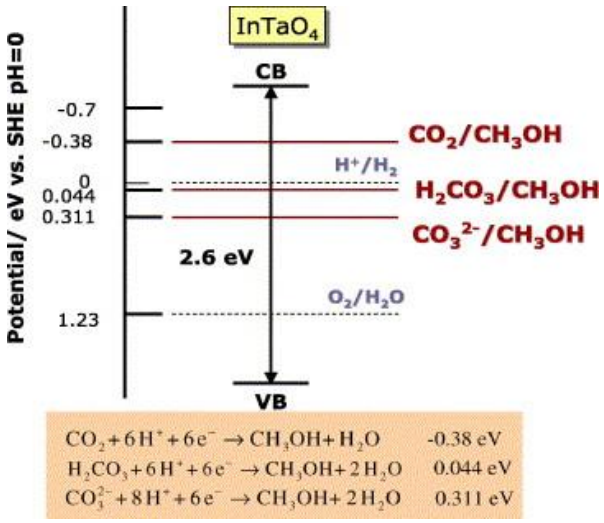

Figure 1-16 Band structure of $InTaO_4$.

Bi_2WO_6 is a typical visible light semiconductor material. During the photocatalytic reduction of CO_2, different synthesis methods were used to prepare Bi_2WO_6 in order to obtain higher photocatalytic activity. In 2011, Zou and coworkers prepared ultra-thin Bi_2WO_6 nanosheets by hydrothermal method using oleylamine. The activity of photocatalytic reduction of CO_2 to CH_4 was about 20 times higher than that of Bi_2WO_6 prepared by solid solution method (Figure 1-17a)[73]. Huang and coworkers prepared Bi_2WO_6 hollow spheres by anion exchange method. The activity of photocatalytic reduction of CO_2 to CH_3OH was about 13 times higher than Bi_2WO_6 prepared by solid solution method (Figure 1-17b)[74].

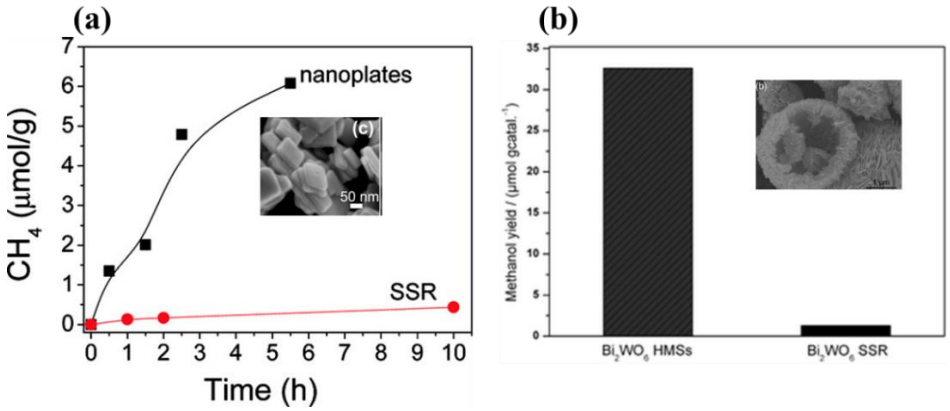

Figure 1-17 (a) CH_4 generation over Bi_2WO_6 nanoplates and the SSR sample as a function of visible-light irradiation times ($\lambda > 420$ nm); (b) Methanol yields on the Bi_2WO_6

photocatalysts under visible light irradiation for 2 h.

1.4.2.2 d^{10} metal oxide photocatalysts (Ga^{3+}, Ge^{4+}, In^{3+}, Sn^{4+}, and Sb^{5+})

Zou's group and Ye's group have many in-depth studies on photocatalytic materials such as Zn_2GeO_4[75, 76, 77], $ZnGa_2O_4$[77, 79], Zn_2SnO_4[80], $In_2Ge_2O_7$[81]. By controlling the material's morphology such as crystal face, composition, promoter modification and non-metal doping, the series of materials showed good catalytic activity in photocatalytic reduction of CO_2.

Zou and coworkers prepared an ultra-long and ultra-thin Zn_2GeO_4 nanoribbon material[82]. Comparing with the activity of Zn_2GeO_4 prepared by solid solution method, Zn_2GeO_4 nanoribbon has exhibited significantly improved photocatalytic reduction of CO_2, and the activity has been greatly improved after the promoter modification of Pt and RuO_2 (Figure 1-18). Then they synthesize a hexagonal prismatic Zn2GeO4 nanorod catalyst by low-temperature hydrothermal method. It also confirmed that this material is superior to the solid solution method for the photocatalytic reduction of CO_2 to CH_4 and CO. The study believes that the main reason for its better activity is that the material has fewer defect sites, a larger surface area, and a unique surface microstructure. Ye and coworkers synthesized a Zn_2GeO_4 catalyst with both micropores and mesoporous structures under room temperature conditions by a simple ion exchange method.

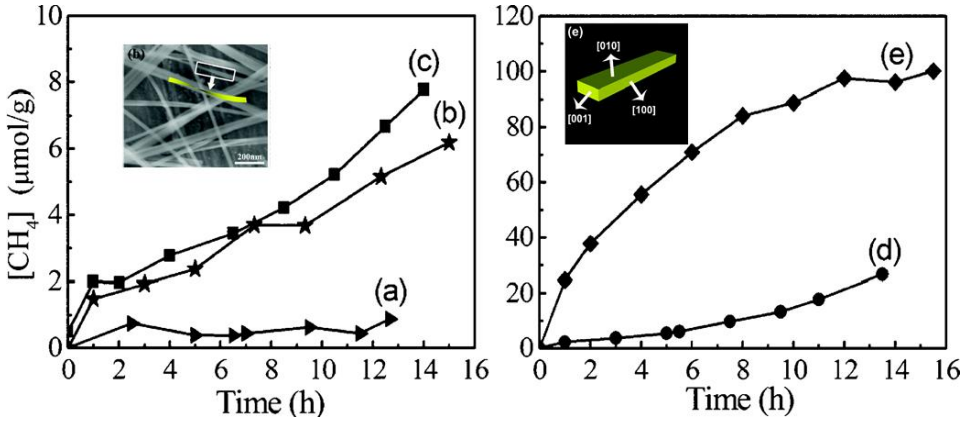

Figure 1-18 CH_4 generation over (a) the SSR sample, (b) nanoribbons, (c) 1wt %Pt-loaded nanoribbons, (d) 1 wt % RuO_2-loaded nanoribbons, and (e) 1 wt % RuO_2 + 1 wt % Pt-coloaded nanoribbons as a function of light irradiation time.

$ZnGa_2O_4$ also shows good activity in photocatalytic reduction of CO_2. Zou and coworkers prepared mesoporous $Zn(Ga_{1-x}Al_x)_2O_4$ precursor by sol-gel method and ion exchange method, and then high-temperature ammonia treatment to obtain mesoporous $ZnAl_2O_4$-ZnGaNO photocatalyst[78]. The rate of photocatalytic reduction of CO_2 to CH_4 is 9.2 μmol $g^{-1}h^{-1}$, which is 7.7 times higher than that of ZnGaNO or N-doped TiO_2 catalysts. And then, they controlled the exposed crystal facet of $ZnGa_2O_4$ and synthesized a $ZnGa_2O_4$ nanocubic with exposed {100} facets by ion exchange hydrothermal method without surfactant. The study found that the {100} facets has a higher hole migration rate, which is accelerating the water oxidation reaction, and more hydrogen ions generate on the catalyst surface. Thus, the reduction of CO_2 is promoted.

Zn_2SnO_4[80], $In_2Ge_2O_7$[81], Ga_2O_3[82, 83] also have been applied in the photocatalytic reduction of CO_2. Zou and coworkers synthesized octahedrons Zn_2SnO_4 with hexagonal nanosheet interlaced on the surface under hydrothermal conditions using L-tryptophan. The special structure of the material contributes to the scattering of light in the catalyst and increases the absorption of light by the catalyst, on the other hand, the surface of the material is roughened by the nanosheets, which not only improves the separation of the photogenerated carriers, but also facilitates the product diffusion. The catalyst was applied for the photocatalytic reduction of CO_2 to produce CH_4. Its activity was significantly higher than that of irregular particles and no nanosheets structure Zn_2SnO_4 catalysts (Figure 1-19). They also prepared $In_2Ge_2O_7$ nanowires with good crystallinity by solvothermal method. The main product of photocatalytic reduction of CO_2 by this catalyst is CO, while the main product of other germanate semiconductors (Zn_2GeO_4) is CH_4.

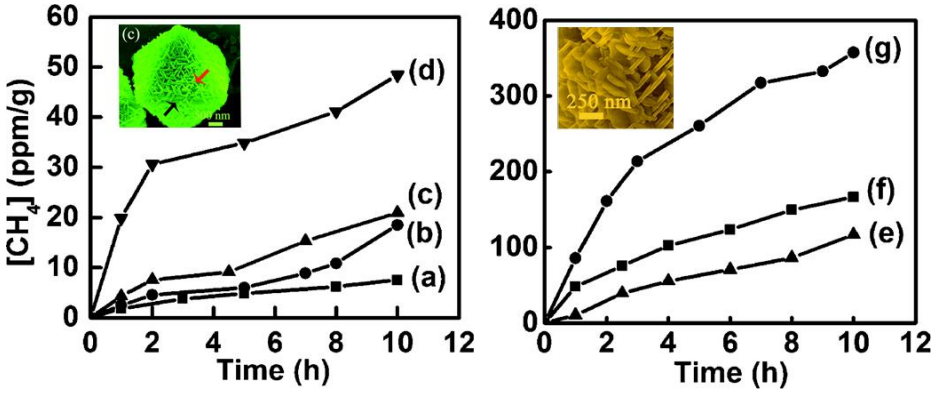

Figure 1-19 CH_4 generation over Zn_2SnO_4 (a) the bulky, (b) atactic particle, (c) micro-octahedron, (d) nanoplate/micro-octahedrons, (e) 1 wt % RuO_2 + 1 wt % Pt-coloaded atacticparticle, (f) 1wt % RuO_2+1wt % Pt-coloaded micro-octahedron, (g) 1wt % RuO_2+1wt % Pt-coloaded nanoplate/micro-octahedrons.

1.4.2.3 Layered double hydroxides

Layered Double Hydroxide (LDH) is a general term for hydrotalcite (HT) and Hydrotalcite-Like Compounds (HTLCs). LDHs are a class of ionic solids characterized by a layered structure with the generic layer sequence $[AcBZAcB]_n$, where c represents layers of metal cations, A and B are layers of hydroxide (HO^-) anions, and Z are layers of other anions and neutral molecules (such as water). Lateral offsets between the layers may result in longer repeating periods. The intercalated anions (Z) are weakly bound, often exchangeable, their intercalation properties have scientific and commercial interest. The basicity of LDHs allows the material to have the ability to adsorb activated CO_2, which has a certain research potential in the photocatalytic reduction of CO_2[84, 85, 86, 87].

Ahmed and coworkers[88] first prepared Zn-Al LDHs catalysts and applied them to the photocatalytic reduction of CO_2 by hydrogen. The main product of the reaction is CO, and its formation rate is: 620 nmol $h^{-1}g^{-1}_{cat}$. And then, Cu was introduced into Zn-Ga LDHs to obtain Zn-Cu-Ga photocatalysts. The main product of photocatalytic reduction of CO_2 is CH_3OH, and the formation rate is 170 nmol $h^{-1}g^{-1}_{cat}$. Corma and coworkers[89] prepared Zn-Ti LDHs materials and utilized 185 nm deep UV light to catalyze the reduction of CO_2. When H_2 was used as a reducing agent, the CO_2 conversion is around 40%, and the main

product is CH_4. When H_2O was used as a reducing agent, the conversion is around 2.2%, and the formation rate of CH_4 is 77 μmol $h^{-1}g^{-1}_{cat}$. This result is much higher than the general photocatalytic reduction of CO_2. The main reason is that deep ultraviolet light can directly activate H_2O and CO_2 molecules without catalysts.

1.4.2.4 MOFs

Metal-organic frameworks (MOFs) are compounds consisting of metal ions or clusters coordinated to organic ligands to form one-, two-, or three-dimensional structures. The framework metal and framework organic ligands of MOFs materials can be controlled, and the framework metal and organic ligands can serve as active sites for catalytic reactions. Therefore, it has a very good potential for research in photocatalysis. Lin and coworkers[90] prepared a $Zr_6O_4(OH)_4(bpdc)_6$ metal-organic framework material (UiO-67) by a hybrid-matching synthesis. Then, the complex $[Re^I(CO)_3(dcbpy)Cl](H_2L_4)$ was introduced into UiO-67, and the material was used in the photocatalytic reduction of CO_2 to CO (Figure 1-20a). Wang and coworkers[91] prepared Co-ZIF-9 metal-organic framework material, which has a good ability to adsorb CO_2 (Figure 1-20b). The application of MOFs materials in photocatalysis has just begun. Because of its unique advantages, it is believed that MOFs will make a greater progress in photocatalysis[92, 93, 94, 95].

Figure 1-20 Mechanism of photocatalytic CO_2 reduction over (a) UiO-67, (b) Co-ZIF-9.

1.5 Conclusion

As mentioned above, photocatalysis has a number of advantages. In photocatalytic

systems, the reaction could proceed beyond the thermodynamic barrier to give selected products under mild conditions. The low temperature process would be beneficial for some reasons. Since other molecules used to reduce the activation energy would not be required, newly designed photocatalytic reaction systems might occur without consumption of extra energy and chemicals, and without undesirable emissions. It is also important that the photocatalysis can convert the solar energy to chemical compounds having high potential such as hydrogen.

However, most of the reported photocatalytic methane conversions give a low product yield and a low energy efficiency, which are still very far from our demands. Thus, while we must further improve the performance of these photocatalytic systems, and we must consider the place where the photocatalytic reaction systems can be applied efficiently. The photocatalytic conversion of methane has not been deeply studied to date. There should still be many undiscovered photocatalysts and photocatalytic systems. Even the known photocatalytic systems have enough potential to be improved. It is expected that further development would bring the photocatalytic system for methane conversion closer to being a real application.

One significant problem in the photocatalytic redox reactions is the separation of the separation of the reagents and products. Heterogeneous photocatalytic reduction of carbon dioxide on semiconductors is not yet ready for implementation in real-life solar fuel applications. However, with the current pace of development in the field, an emerging understanding of the mechanism and new materials should make the promise of this process even closer in the near future.

1.5.1 Photocatalytic conversion of methane

The selective oxidation of methane to fuels and chemicals has attracted great attention from researchers around the world. Photocatalytic conversion of methane has not been generally studied to date. There should be many undiscovered photocatalysts and photocatalytic systems. Even known photocatalytic systems have sufficient potential for improvement.

Methane conversion involves multiple steps due to its high stability. Thus, several catalytic methods have been explored, including homogeneous, heterogeneous, and photocatalytic processes to selectively oxidize methane to methanol and other chemicals such as ethane, ethylene, and formaldehyde[26, 96, 97]. High reaction temperatures (>700 °C), low selectivity to target products, and often abundant CO_2 production are major drawbacks of conventional thermocatalytic technologies. Photocatalysis, which uses sunlight, has been shown to be very promising for water decomposition and environmental remediation. In some photocatalytic systems, the reaction can exceed the thermodynamic barrier and the selected product is obtained under mild conditions.

We introduced some photocatalytic reaction systems for the methane conversion, *i.e.*, the partial oxidation (POM) and oxidative coupling of methane (OCM). Direct methane conversion to hydrocarbons (NOCM), the steam reforming (SRM), the dry reforming (DRM) and representative achievements are highlighted in Table 1-2. Most of the reported photocatalytic methane conversion products have low yields and low energy efficiency, but they are still far from meeting our requirements. Therefore, although we must further develop the performance of these photocatalytic systems, we must consider where the photocatalytic reaction system can be effectively applied.

Table 1-2 Representative studies of photocatalytic conversion of methane.

Catalyst	Reactants	Products	Ref.
$2CH_4 \rightarrow C_2H_6 + H_2$			
FSM-16	CH_4	C_2, C_3 total yield: 0.1 C%	25
Ga_2O_3	CH_4	C_2, C_3 total yield: 0.49 C%	26
Ag-ZnO	CH_4+O_2	C_2H_6 quantum yield: 8%	39
Ga-ETS-10	CH_4	C_2H_6: 29.8 μmol g^{-1} h^{-1}	30
Zn^+- ZSM-5	CH_4	C_2H_6: 3 μmol g^{-1} h^{-1}	29
Au-ZnO	CH_4	C_2H_6: 11.3 μmol g^{-1} h^{-1}	98
Ga/ TiO_2-SiO_2 microarray	CH_4	C_2H_6: 5 μmol g^{-1} h^{-1}	99

Au-HPW/TiO_2	CH_4	C_2H_6 yield: 9%	Chap. 4
$CH_4 + H_2O \rightarrow CO + 3H_2$			
0.03 wt %Rh/$K_2Ti_6O_{13}$	CH_4+H_2O	H_2: 1.875 μmol g^{-1} min^{-1}	102
Ni/SiO_2	CH_4+CO_2	H_2: 17.1 mmol g^{-1} min^{-1} CO: 19.9 mmol g^{-1} min^{-1}	103
2% Rh/TiO_2	CH_4+H_2O	H_2: 116 μmol g^{-1} min^{-1}	104
Pt/$NaTaO_3$:La	CH_4+H_2O	H_2: 0.26 μmol g^{-1} min^{-1}	105
$CH_4 + H_2O \rightarrow CH_3OH + H_2$			
$BiVO_4$ bipyramids	CH_4+H_2O	CH_3OH: 111.9 μmol g^{-1} h^{-1}	100
0.33_{metal}wt %FeO_x/TiO_2	CH_4+H_2O+H_2O_2	CH_3OH: 1056 μmol g^{-1} in 3 h	101
Cu/PCN	CH_4+H_2O	C_2H_5OH: 106 μmol g^{-1} h^{-1}	107
$2CH_4 + 3O_2 \rightarrow 2CO + 4H_2O$			
Zn-HPW/TiO_2	CH_4+Air	CO: 420 μmol g^{-1} h^{-1}	Chap.3[106]

1.5.2 Photocatalytic Reduction of CO_2

At present, the product formation rate of photocatalytic reduction of carbon dioxide on semiconductors rarely exceeds several tens of $\mu molg^{-1}h^{-1}$. This means that the efficiency of the process is generally lower than that of natural photosynthesis or photocatalysis to produce H_2. Recent developments have focused on new photocatalytic materials and new nanoscale structures that provide large surface area, improved charge separation and directed electron transfer. The mechanism of this process is also the subject of many studies, usually based on a combination of experimental and computational methods which are summarized in Table 1-3. These studies attempt to answer unresolved questions about the chemical pathways for CO_2 reduction that determine the selectivity of the overall reaction.

The overview of the physical, optical, and electronic properties of $BiVO_4$, in particular that of the monoclinic scheelite structure has shown the promise of $BiVO_4$ as a visible light-active photocatalyst. while crystal facet engineering of $BiVO_4$ with exposed {010} and {110} facets promotes spatial separation of photogenerated electrons and holes on the two surfaces

and enlargement of {010} increases the charge transfer efficiency. The construction of p-n heterojunctions and Z-scheme heterojunctions provides more efficient charge separation and rapid charge transfer, which facilitates higher photocatalytic activity. In the coming decades, $BiVO_4$ may become a potential material for photocatalytic applications. It is undeniable that the charge kinetics of photocatalysts, which involve multiple steps and mechanisms, are indeed a complicated field of study. While existing mechanisms are primarily based on theoretical and experimental data from various characterization tools, a deeper understanding of charge dynamics is often limited by characterization techniques and realistic experimental conditions[108, 109].

Table 1-3 Representative studies of photocatalytic CO_2 reduction.

Catalyst	Reaction Medium	Products	Ref.
$2CO_2 + 3H_2O \rightarrow CO + CH_4 + 3O_2$			
Pt/TiO_2 NPs	H_2O	CH_4: 60 μmol g^{-1} h^{-1}	110
Pt/TiO_2 on glass beads	H_2O vapor	CH_4: 0.3 μmol g^{-1} h^{-1}	111
Pt/TiO_2 NRs	H_2O vapor	CH_4: 6 μmol g^{-1} h^{-1}	112
Pt/Ti-MCM-48	H_2O vapor	CH_4: 12.3 μmol g^{-1} h^{-1}	113
Pt/N-doped meso-TiO_2	H_2O vapor	CH_4: 2.8 μmol g^{-1} h^{-1}	114
Pt/TiO_2-SiO_2 composite	H_2O vapor	CH_4: 9.7 μmol g^{-1} h^{-1} CO: 1.8 μmol g^{-1} h^{-1}	115
Pt/$KNbO_3$	H_2O vapor	CH_4: 70 ppm g^{-1} h^{-1}	116
Pt/$NaNbO_3$	H_2O vapor	CH_4: 4.86 μmol g^{-1} h^{-1}	117
Pt/Zn_2GeO_4	H_2O vapor	CH_4: 28.9 ppm g^{-1} h^{-1}	118
Pt/$In_2Ge_2O_7$ hybrid NWs	H_2O vapor	CO: 0.95 μmol g^{-1} h^{-1}	119
Pt/g-C_3N_4	H_2O vapor	CH_4: 0.13 μmol g^{-1} h^{-1}	120
Pt/Red phosphor/g-C_3N_4	H_2O vapor	CH_4: 295 μmol g^{-1} h^{-1}	121
Pt/In_2O_3/C_3N_4	H_2O vapor	CH_4: 1990 ppm g^{-1} h^{-1}	122
Pt/$NaNbO_3$/C_3N_4	H_2O vapor	CH_4: 6.4 μmol g^{-1} h^{-1}	123
Ag/Brookite TiO_2	0.2 m $KHCO_3$ solution	CH_3OH: 266.7 μmol g^{-1} h^{-1}	124

Ag/TiO_2	H_2O/CH_3OH vapor	CO: 87 μmol g^{-1} h^{-1} CH_4: 10 μmol g^{-1} h^{-1}	125
Ag/CdS	TEOA solution	CO: 258 μmol g^{-1} h^{-1}	126
$Ag/KCaSrTa_5O_{15}$	H_2O	CO: 8.1 μmol g^{-1} h^{-1}	127
$Ag/SrLa_4Ti_4O_{15}$	H_2O	CO: 23.7 μmol g^{-1} h^{-1}	128
Rh/TiO_2	H_2	CO: 5.1 μmol g^{-1} h^{-1}	130
Pd/TiO_2	H_2O	CH_4: 0.6 μmol g^{-1} h^{-1}	131
Cu-PbS QD sensitized TiO_2	H_2O	CH_4: 0.82 μmol g^{-1} h^{-1} C_2H_6: 0.31μmol g^{-1} h^{-1} CO: 0.58 μmol g^{-1} h^{-1}	135
Cu-CdS QD sensitized TiO_2	H_2O	CH_4: 27.5 μmol g^{-1} h^{-1} C_2H_6: 17.5 μmol g^{-1} h^{-1} C_3H_8: 10.0 μmol g^{-1} h^{-1}	136
Cu/MOF-525	Solution MeCN/ TEOA = 4:1)	CO: 200.6 μmol g^{-1} h^{-1} CH_4: 36.67 μmol g^{-1} h^{-1}	138
$MgO-TiO_2$	H_2O vapor	CO: 1.3 μmol g^{-1} h^{-1}	143
Cu_2O/I-doped TiO_2	H_2O vapor	CO: 1.9 μmol g^{-1} h^{-1}	147
CuO/TiO_2-SiO_2	H_2O vapor	CO: 20.3 μmol g^{-1} h^{-1}	148
Zn-HPW/TiO_2	H_2O vapor	CO: 50 μmol g^{-1} h^{-1}	Chap. 5
$CuO_x/CoO_x/BiVO_4$	H_2O vapor	Hydrocarbons: 11 μmol g^{-1} h^{-1}	Chap. 6
$CO_2 + 3H_2O \rightarrow CH_3OH + 2O_2 + H_2$ $2CO_2 + 3H_2O \rightarrow CH_3CHO + 3O_2 + H_2$			
Ag/Brookite TiO_2	0.2 m $KHCO_3$ solution	CH_3OH: 266.7 μmol g^{-1} h^{-1}	124
Rh/TiO_2	H_2O	CH_3OH: 0.4 μmol g^{-1} h^{-1} HCOOH: 1.62 μmol g^{-1} h^{-1}	129
Pd/g-C_3N_4	H_2O	CO: 20.3 μmol g^{-1} h^{-1} C_2H_5OH: 2.18 μmol g^{-1} h^{-1}	132
Cu/TiO_2	1 M $KHCO_3$ solution	CH_3OH: 194 μmol g^{-1} h^{-1}	133
Cu-TiO_2/SBA-15	0.1 M NaOH solution	CH_3OH: 627 μmol g^{-1} h^{-1}	134
Cu/GO	H_2O	CH_3OH: 2.94 μmol g^{-1} h^{-1} CH_3CHO: 3.88 μmol g^{-1} h^{-1}	137
RuO_2-$Cu_xAg_yIn_zZn_kS_m$	$NaHCO_3$ solution	CH_3OH: 118.5 μmol g^{-1} h^{-1}	139
NiO-$InNbO_4$	0.2 M $KHCO_3$ solution	CH_3OH: 1.57 μmol g^{-1} h^{-1}	140

$NiO-InTaO_4$	0.2 M NaOH solution	CH_3OH: 21 μmol g^{-1} h^{-1}	141
$NiO-InTaO_4$	H_2O vapor	CH_3CHO: 0.3 μmol g^{-1} h^{-1}	142
$Co_3O_4-InNbO_4$	0.2 m $KHCO_3$ solution	CH_3OH: 1.5 μmol g^{-1} h^{-1}	140
Cu_2O-TiO_2	1 M $KHCO_3$ solution	CH_3OH: 224 μmol g^{-1} h^{-1}	144
Cu_2O-TiO_2	0.2 M NaOH solution	CH_3OH: 19.75 μmol g^{-1} h^{-1}	145
Cu_2O-TiO_2	H_2O vapor	CH_3OH: 0.45 μmol g^{-1} h^{-1}	146
$CuO-TiO_2$	1 M $KHCO_3$ solution	CH_3OH: 442.5 μmol g^{-1} h^{-1}	133
MoS_2-TiO_2	1 M $NaHCO_3$ solution	CH_3OH: 10.6 μmol g^{-1} h^{-1}	149

1.6 Objective of thesis

This thesis aims to:

✓ Develop and propose new efficient materials, catalysts and processes to utilize methane and carbon dioxide with high selectivities and yields to valuable products. In particular, this thesis focuses on the methane selective photocatalytic oxidation to CO and methane selective photochemical coupling to ethane. We are also considering in this work the CO_2 photocatalytic reduction to CO and CO_2 reduction to hydrocarbons.

✓ Evaluation of the mechanism of the reaction and optimize its catalytic performance based on it.

1.7 References

1. Fahrenbruch A, Bube R. Fundamentals of solar cells: photovoltaic solar energy conversion. *Elsevier* (2012).

2. Cook TR, Dogutan DK, Reece SY, Surendranath Y, Teets TS, Nocera DG. Solar energy supply and storage for the legacy and nonlegacy worlds. *Chem. Rev.* **110**, 6474-6502 (2010).

3. Mishra A, Bäuerle P. Small molecule organic semiconductors on the move: promises for future solar energy technology. *Angew. Chem. Int. Ed.,* **51**, 2020-2067 (2012).

4. Kubacka A, Fernandez-Garcia M, Colon G. Advanced nanoarchitectures for solar photocatalytic applications. *Chem. Rev.* **112**, 1555-1614 (2011).

5. Daghrir R, Drogui P, Robert D. Modified TiO_2 for environmental photocatalytic applications: a review. *Ind. Eng. Chem. Res.* **52**, 3581-3599 (2013).

6. Pan X, Yang M-Q, Fu X, Zhang N, Xu Y-J. Defective TiO_2 with oxygen vacancies: synthesis, properties and photocatalytic applications. *Nanoscale* **5**, 3601-3614 (2013).

7. Yacobi BG. Semiconductor materials: an introduction to basic principles. *Springer Science & Business Media* (2003).

8. Ni M, Leung MK, Leung DY, Sumathy K. A review and recent developments in photocatalytic water-splitting using TiO_2 for hydrogen production. *Renew. Sus. Energ. Rev.* **11**, 401-425 (2007).

9. Ahmad H, Kamarudin S, Minggu L, Kassim M. Hydrogen from photo-catalytic water splitting process: A review. *Renew. Sus. Energ. Rev.* **43**, 599-610 (2015).

10. Gabor NM, Zhong Z, Bosnick K, Park J, McEuen PL. Extremely efficient multiple electron-hole pair generation in carbon nanotube photodiodes. *Science* **325**, 1367-1371 (2009).

11. Conibeer G. Third-generation photovoltaics. *Mater. Today* **10**, 42-50 (2007).

12. Pelaez M*, et al.* A review on the visible light active titanium dioxide photocatalysts for environmental applications. *Appl. Catal. B* **125**, 331-349 (2012).

13. Ma Y, Wang X, Jia Y, Chen X, Han H, Li C. Titanium dioxide-based nanomaterials for photocatalytic fuel generations. *Chem. Rev.* **114**, 9987-10043 (2014).

14. Litter MI. Heterogeneous photocatalysis: transition metal ions in photocatalytic systems. *Appl. Catal. B* **23**, 89-114 (1999).

15. Turchi CS, Ollis DF. Photocatalytic degradation of organic water contaminants: mechanisms involving hydroxyl radical attack. *J. Catal.* **122**, 178-192 (1990).

16. Dalrymple OK, Stefanakos E, Trotz MA, Goswami DY. A review of the mechanisms and modeling of photocatalytic disinfection. *Appl. Catal. B* **98**, 27-38 (2010).

17. Lee H, Choi W. Photocatalytic oxidation of arsenite in TiO_2 suspension: kinetics and mechanisms. *Environ. Sci. Technol.* **36**, 3872-3878 (2002).

18. Indrakanti VP, Kubicki JD, Schobert HH. Photoinduced activation of CO_2 on Ti-based heterogeneous catalysts: Current state, chemical physics-based insights and outlook. *Energy Environ. Sci.* **2**, 745-758 (2009).

19. Chen F, Zhao J, Hidaka H. Highly selective deethylation of rhodamine B: Adsorption and photooxidation pathways of the dye on the TiO_2/SiO_2 composite photocatalyst. *Int. J. Photoenergy* **5**, 209-217 (2003).

20. Schneider J, Bahnemann D, Ye J, Puma GL, Dionysiou DD. Photocatalysis: fundamentals and perspectives. *Royal Society of Chemistry* (2016).

21. Bagheri S, Julkapli NM. *Nanocatalysts in Environmental Applications*. Springer (2018).

22. Dionysiou DD, Puma GL, Ye J, Schneider J, Bahnemann D. Photocatalysis: applications. *Royal Society of Chemistry* (2016).

23. Labinger JA, Bercaw JE. Understanding and exploiting C–H bond activation. *Nature* **417**, 507 (2002).

24. Joensen F, Rostrup-Nielsen JR. Conversion of hydrocarbons and alcohols for fuel cells. *J. Power Sources* **105**, 195-201 (2002).

25. Tijm P, Waller F, Brown D. Methanol technology developments for the new millennium. *Appl. Catal. A* **221**, 275-282 (2001).

26. Karoshi G, Kolar P, Shah SB, Gilleskie G. Value-addition of methane via selective catalytic oxidation. *Biofuels* **5**, 175-188 (2014).

27. Zhang Q, He D, Zhu Q. Recent progress in direct partial oxidation of methane to methanol. *J. Nat. Gas Chem.* **12**, 81-89 (2003).

28. Kato Y, Yoshida H, Hattori T. Photoinduced non-oxidative coupling of methane over silica-alumina and alumina around room temperature. *Chem. Commun.* 2389-2390 (1998).

29. Li L*, et al.* Efficient Sunlight-Driven Dehydrogenative Coupling of Methane to Ethane over a Zn^{+}-Modified Zeolite. A*ngew. Chem. Int. Ed.* **123**, 8449-8453 (2011).

30. Li L, Cai YY, Li GD, Mu XY, Wang KX, Chen JS. Synergistic Effect on the Photoactivation of the Methane CH Bond over Ga^{3+}-Modified ETS-10. *Angew. Chem. Int. Ed.,* **51**, 4702-4706 (2012).

31. Kaliaguine S, Shelimov B, Kazansky V. Reactions of methane and ethane with hole centers O^{-}. *J. Catal.* **55**, 384-393 (1978).

32. Wada K, Yoshida K, Watanabe Y. Selective photooxidation of light alkanes to oxygenates using supported molybdenum oxide catalysts. *Faraday Trans.* **91**, 1647-1654 (1995).

33. Wei J, Yang J, Wen Z, Dai J, Li Y, Yao B. Efficient photocatalytic oxidation of methane over β-Ga_2O_3/activated carbon composites. *RSC Adv.* **7**, 37508-37521 (2017).

34. Chen G*, et al.* Recent Advances in the Synthesis, Characterization and Application of Zn^{+}-containing Heterogeneous Catalysts. *Adv. Sci.* **3**, (2016).

35. Wada K, Yamada H, Watanabe Y, Mitsudo T-a. Selective photo-assisted catalytic oxidation of methane and ethane to oxygenates using supported vanadium oxide catalysts. *Faraday Trans.* **94**, 1771-1778 (1998).

36. López HH, Martínez A. Selective Photo-Assisted Oxidation of Methane into Formaldehyde on Mesoporous VOx/SBA-15 Catalysts. *Catal. Lett.* **83**, 37-41 (2002).

37. Thampi KR, Kiwi J, Grätzel M. Room temperature photo-activation of methane on TiO_2 supported molybdena. *Catal. Lett.***1**, 109-116 (1988).

38. Ward MD, Brazdil JF, Mehandru S, Anderson AB. Methane photoactivation on copper molybdate: an experimental and theoretical study. *J. Phy. Chem.* **91**, 6515-6521 (1987).

39. Chen X, Li Y, Pan X, Cortie D, Huang X, Yi Z. Photocatalytic oxidation of methane over silver decorated zinc oxide nanocatalysts. *Nat. Commun.* **7**, 12273 (2016).

40. Gondal M, Hameed A, Yamani Z, Arfaj A. Photocatalytic transformation of methane into methanol under UV laser irradiation over WO_3, TiO_2 and NiO catalysts. *Chem. Phys. Lett.* **392**, 372-377 (2004).

41. Hameed A, Ismail IM, Aslam M, Gondal M. Photocatalytic conversion of methane into methanol: Performance of silver impregnated WO_3. *Appl. Catal. A* **470**, 327-335 (2014).

42. Villa K, Murcia-López S, Andreu T, Morante JR. Mesoporous WO_3 photocatalyst for the partial

oxidation of methane to methanol using electron scavengers. *Appl. Catal. B* **163**, 150-155 (2015).

43. Villa K, Murcia-López S, Morante JR, Andreu T. An insight on the role of La in mesoporous WO_3 for the photocatalytic conversion of methane into methanol. *Appl. Catal. B* **187**, 30-36 (2016).

44. Villa K, Murcia-López S, Andreu T, Morante JR. On the role of WO_3 surface hydroxyl groups for the photocatalytic partial oxidation of methane to methanol. *Catal. Commun.* **58**, 200-203 (2015).

45. Taylor CE. Methane conversion via photocatalytic reactions. *Catal. Today* **84**, 9-15 (2003).

46. Hu Y, Nagai Y, Rahmawaty D, Wei C, Anpo M. Characteristics of the photocatalytic oxidation of methane into methanol on V-containing MCM-41 catalysts. *Catal. Lett.* **124**, 80 (2008).

47. Gondal M, Hameed A, Suwaiyan A. Photo-catalytic conversion of methane into methanol using visible laser. *Appl. Catal. A* **243**, 165-174 (2003).

48. Murcia-López Sn, Villa K, Andreu T, Morante JR. Partial oxidation of methane to methanol using bismuth-based photocatalysts. *ACS Catal.* **4**, 3013-3019 (2014).

49. Murcia-López Sn*, et al.* Controlled photocatalytic oxidation of methane to methanol through surface modification of beta zeolites. *ACS Catal.* **7**, 2878-2885 (2017).

50. Yoshida H*, et al.* Hydrogen production from methane and water on platinum loaded titanium oxide photocatalysts. *J. Phys. Chem. C* **112**, 5542-5551 (2008).

51. Yoshida H, Kato S, Hirao K, Nishimoto J, Hattori T. Photocatalytic steam reforming of methane over platinum-loaded semiconductors for hydrogen production. *Chem. Lett.* **36**, 430-431 (2007).

52. Inoue T, Fujishima A, Konishi S, Honda K. Photoelectrocatalytic reduction of carbon dioxide in aqueous suspensions of semiconductor powders. *Nature* **277**, 637-638 (1979).

53. Zhang Z, Wang CC, Zakaria R, Ying JY. Role of particle size in nanocrystalline TiO_2-based photocatalysts. *J. Phys. Chem. B* **102**, 10871-10878 (1998).

54. Akpan UG, Hameed BH. Parameters affecting the photocatalytic degradation of dyes using TiO_2-based photocatalysts: a review. *Journal Hazard. Mater.* **170**, 520-529 (2009).

55. Yang X, Cao C, Erickson L, Hohn K, Maghirang R, Klabunde K. Synthesis of visible-light-active TiO_2-based photocatalysts by carbon and nitrogen doping. *J. Catal.* **260**, 128-133 (2008).

56. Zhang Y-Q, Ma D-K, Zhang Y-G, Chen W, Huang S-M. N-doped carbon quantum dots for TiO_2-based photocatalysts and dye-sensitized solar cells. *Nano Energy* **2**, 545-552 (2013).

57. Ileperuma O, Tennakone K, Dissanayake W. Photocatalytic behaviour of metal doped titanium

dioxide: Studies on the photochemical synthesis of ammonia on Mg/TiO_2 catalyst systems. *Appl. Catal.* **62**, L1-L5 (1990).

58. Nasution HW, Purnama E, Kosela S, Gunlazuardi J. Photocatalytic reduction of CO_2 on copper-doped Titania catalysts prepared by improved-impregnation method. *Catal. Commun.* **6**, 313-319 (2005).

59. Richardson P, Perdigoto ML, Wang W, Lopes RJ. RETRACTED: manganese-and copper-doped titania nanocomposites for the photocatalytic reduction of carbon dioxide into methanol. *Elsevier* (2012).

60. Kočí K*, et al.* Effect of silver doping on the TiO_2 for photocatalytic reduction of CO_2. *Appl. Catal. B* **96**, 239-244 (2010).

61. Manzanares M, Fàbrega C, Ossó JO, Vega LF, Andreu T, Morante JR. Engineering the TiO_2 outermost layers using magnesium for carbon dioxide photoreduction. *Appl. Catal. B* **150**, 57-62 (2014).

62. Guan G, Kida T, Harada T, Isayama M, Yoshida A. Photoreduction of carbon dioxide with water over $K_2Ti_6O_{13}$ photocatalyst combined with Cu/ZnO catalyst under concentrated sunlight. *Appl. Catal. A* **249**, 11-18 (2003).

63. Iizuka K, Wato T, Miseki Y, Saito K, Kudo A. Photocatalytic reduction of carbon dioxide over Ag cocatalyst-loaded $ALa_4Ti_4O_{15}$ (A= Ca, Sr, and Ba) using water as a reducing reagent. *J. Am. Chem. Soc.* **133**, 20863-20868 (2011).

64. Lee W-H, Liao C-H, Tsai M-F, Huang C-W, Wu JC. A novel twin reactor for CO_2 photoreduction to mimic artificial photosynthesis. *Appl. Catal. B* **132**, 445-451 (2013).

65. Li P, Ouyang S, Xi G, Kako T, Ye J. The effects of crystal structure and electronic structure on photocatalytic H_2 evolution and CO_2 reduction over two phases of perovskite-structured $NaNbO_3$. *J. Phys. Chem. C* **116**, 7621-7628 (2012).

66. Li P, Ouyang S, Zhang Y, Kako T, Ye J. Surface-coordination-induced selective synthesis of cubic and orthorhombic $NaNbO_3$ and their photocatalytic properties. *J. Mater. Chem. A* **1**, 1185-1191 (2013).

67. Lee D-S, Chen H-J, Chen Y-W. Photocatalytic reduction of carbon dioxide with water using $InNbO_4$ catalyst with NiO and Co_3O_4 cocatalysts. *J. Phys. Chem. Solids* **73**, 661-669 (2012).

68. Pan P-W, Chen Y-W. Photocatalytic reduction of carbon dioxide on $NiO/InTaO_4$ under visible light irradiation. *Catal. Commun.* **8**, 1546-1549 (2007).

69. Tsai C-W, Chen HM, Liu R-S, Asakura K, Chan T-S. Ni@NiO core–shell structure-modified nitrogen-doped $InTaO_4$ for solar-driven highly efficient CO_2 reduction to methanol. *J. Phys. Chem. C* **115**, 10180-10186 (2011).

70. Liou P-Y*, et al.* Photocatalytic CO_2 reduction using an internally illuminated monolith photoreactor. *Energy Environ. Sci.* **4**, 1487-1494 (2011).

71. Teramura K, Okuoka S-i, Tsuneoka H, Shishido T, Tanaka T. Photocatalytic reduction of CO_2 using H_2 as reductant over $ATaO_3$ photocatalysts (A= Li, Na, K). *Appl. Catal. B* **96**, 565-568 (2010).

72. Lv X-J, Fu W-F, Hu C-Y, Chen Y, Zhou W-B. Photocatalytic reduction of CO_2 with H_2O over a graphene-modified $NiOx–Ta_2O_5$ composite photocatalyst: coupling yields of methanol and hydrogen. *RSC Adv.* **3**, 1753-1757 (2013).

73. Zhou Y*, et al.* High-yield synthesis of ultrathin and uniform Bi_2WO_6 square nanoplates benefitting from photocatalytic reduction of CO_2 into renewable hydrocarbon fuel under visible light. *ACS Appl. Mater. Inter.* **3**, 3594-3601 (2011).

74. Cheng H*, et al.* An anion exchange approach to Bi_2WO_6 hollow microspheres with efficient visible light photocatalytic reduction of CO_2 to methanol. *Chem. Commun.* **48**, 9729-9731 (2012).

75. Liu Q*, et al.* High-yield synthesis of ultralong and ultrathin Zn_2GeO_4 nanoribbons toward improved photocatalytic reduction of CO_2 into renewable hydrocarbon fuel. *J. Am. Chem. Soc.* **132**, 14385-14387 (2010).

76. Yan S, Wan L, Li Z, Zou Z. Facile temperature-controlled synthesis of hexagonal Zn_2GeO_4 nanorods with different aspect ratios toward improved photocatalytic activity for overall water splitting and photoreduction of CO_2. *Chem. Commun.* **47**, 5632-5634 (2011).

77. Zhang N*, et al.* Ion-exchange synthesis of a micro/mesoporous Zn_2GeO_4 photocatalyst at room temperature for photoreduction of CO_2. *Chem. Commun.* **47**, 2041-2043 (2011).

78. Yan S, Yu H, Wang N, Li Z, Zou Z. Efficient conversion of CO_2 and H_2O into hydrocarbon fuel over $ZnAl_2O_4$-modified mesoporous ZnGaNO under visible light irradiation. *Chem. Commun.* **48**, 1048-1050 (2012).

79. Yan S*, et al.* An Ion-Exchange Phase Transformation to $ZnGa_2O_4$ Nanocube Towards Efficient

Solar Fuel Synthesis. *Adv. Funct. Mater.* **23**, 758-763 (2013).

80. Li Z*, et al.* Hexagonal nanoplate-textured micro-octahedron Zn_2SnO_4: combined effects toward enhanced efficiencies of dye-sensitized solar cell and photoreduction of CO_2 into hydrocarbon fuels. *Cryst. Growth Des.* **12**, 1476-1481 (2012).

81. Liu Q, Zhou Y, Ma Y, Zou Z. Synthesis of highly crystalline $In_2Ge_2O_7$ (En) hybrid sub-nanowires with ultraviolet photoluminescence emissions and their selective photocatalytic reduction of CO_2 into renewable fuel. *RSC Adv.* **2**, 3247-3250 (2012).

82. Tsuneoka H, Teramura K, Shishido T, Tanaka T. Adsorbed Species of CO_2 and H_2 on Ga_2O_3 for the Photocatalytic Reduction of CO_2. *J. Phys. Chem. C* **114**, 8892-8898 (2010).

83. Park H-a, Choi JH, Choi KM, Lee DK, Kang JK. Highly porous gallium oxide with a high CO_2 affinity for the photocatalytic conversion of carbon dioxide into methane. *J. Mater. Chem.* **22**, 5304-5307 (2012).

84. Gunjakar JL, Kim TW, Kim HN, Kim IY, Hwang S-J. Mesoporous layer-by-layer ordered nanohybrids of layered double hydroxide and layered metal oxide: highly active visible light photocatalysts with improved chemical stability. *J. Am. Chem. Soc.* **133**, 14998-15007 (2011).

85. Silva CG, Bouizi Y, Fornés V, García H. Layered double hydroxides as highly efficient photocatalysts for visible light oxygen generation from water. *J. Am. Chem. Soc.* **131**, 13833-13839 (2009).

86. Shao M, Han J, Wei M, Evans DG, Duan X. The synthesis of hierarchical Zn–Ti layered double hydroxide for efficient visible-light photocatalysis. *Chem. Eng. J.* **168**, 519-524 (2011).

87. Zhao Y*, et al.* Layered double hydroxide nanostructured photocatalysts for renewable energy production. *Adv. Energy Mater.* **6**, 1501974 (2016).

88. Ahmed N, Shibata Y, Taniguchi T, Izumi Y. Photocatalytic conversion of carbon dioxide into methanol using zinc–copper–M (III)(M= aluminum, gallium) layered double hydroxides. *J. Catal.* **279**, 123-135 (2011).

89. Sastre F, Corma A, García H. 185 nm Photoreduction of CO_2 to Methane by Water. Influence of the Presence of a Basic Catalyst. *J. Am. Chem. Soc.* **134**, 14137-14141 (2012).

90. Wang C, Xie Z, deKrafft KE, Lin W. Doping metal–organic frameworks for water oxidation, carbon dioxide reduction, and organic photocatalysis. *J. Am. Chem. Soc.* **133**, 13445-13454 (2011).

91. Wang S, Yao W, Lin J, Ding Z, Wang X. Cobalt imidazolate metal–organic frameworks photosplit CO_2 under mild reaction conditions. *Angew. Chem. Int. Ed.,* **53**, 1034-1038 (2014).

92. Wang D, Huang R, Liu W, Sun D, Li Z. Fe-based MOFs for photocatalytic CO_2 reduction: role of coordination unsaturated sites and dual excitation pathways. *ACS Catal.* **4**, 4254-4260 (2014).

93. Gascon J, Hernández-Alonso MD, Almeida AR, Van Klink GP, Kapteijn F, Mul G. Isoreticular MOFs as efficient photocatalysts with tunable band gap: an operando FTIR study of the photoinduced oxidation of propylene. *ChemSusChem* **1**, 981-983 (2008).

94. Sun D, Liu W, Qiu M, Zhang Y, Li Z. Introduction of a mediator for enhancing photocatalytic performance via post-synthetic metal exchange in metal–organic frameworks (MOFs). *Chem. Commun.* **51**, 2056-2059 (2015).

95. Chen Y, Wang D, Deng X, Li Z. Metal–organic frameworks (MOFs) for photocatalytic CO_2 reduction. *Catal. Sci. Technol.* **7**, 4893-4904 (2017).

96. Tang P, Zhu Q, Wu Z, Ma D. Methane activation: the past and future. *Energy Environ. Sci.* **7**, 2580-2591 (2014).

97. Wang B, Albarracín-Suazo S, Pagán-Torres Y, Nikolla E. Advances in methane conversion processes. *Catal. Today* **285**, 147-158 (2017).

98. Meng LS, Chen ZY, Ma ZY, He S, Hou YD, Li HH, Yuan RS, Huang XH, Wang XX, Wang XC, Long JL. Gold plasmon-induced photocatalytic dehydrogenative coupling of methane to ethane on polar oxide surfaces. *Energ. Environ. Sci.* **11**, 294-298 (2018).

99. Wu, SQ, Tan XJ, Lei JY, Chen HJ, Wang LZ, Zhang JL. Ga-Doped and Pt-Loaded Porous TiO_2–SiO_2 for Photocatalytic Nonoxidative Coupling of Methane. *J. Am. Chem. Soc.* **141**, 6592-6600, (2019).

100. Zhu, W., Shen, M., Fan, G., Yang, A., Meyer, J.R., Ou, Y., Yin, B., Fortner, J., Foston, M., Li, Z. Facet-dependent enhancement in the activity of bismuth vanadate microcrystals for the photocatalytic conversion of methane to methanol. *ACS Appl. Nano Mater.* **1**, 6683–6691 (2018).

101. Xie, J., Jin, R., Li, A., Bi, Y., Ruan, Q., Deng, Y., Zhang, Y., Yao, S., Sankar, G., Ma, D. Highly selective oxidation of methane to methanol at ambient conditions by titanium dioxide-supported iron species. *Nat. Catal.* **1**, 889–896 (2018).

102. Shimura, K., Kawai, H., Yoshida, T., and Yoshida, H. (2012). Bifunctional rhodium cocatalysts

for photocatalytic steam reforming of methane over alkaline titanate. ACS Catal. 2, 2126–2134.

103. Wang, Y., Yao, L., Wang, S., Mao, D., and Hu, C. Low-temperature catalytic CO_2 dry reforming of methane on Ni-based catalysts: a review. *Fuel Process. Technol.* **169**, 199–206 (2018).

104. Lustemberg, P.G., Palomino, R.M., Gutierrez, R.A., Grinter, D.C., Vorokhta, M., Liu, Z., Ramırez, P.J., Matolın, V., GandugliaPirovano, M.V., Senanayake. Direct conversion of methane to methanol on Ni-ceria surfaces: metal-support interactions and water-enabled catalytic conversion by site blocking. *J. Am. Chem. Soc.* **140**, 7681– 7687 (2018).

105. Shimura, K., Yoshida, T., Yoshida, H. Photocatalytic activation of water and methane over modified gallium oxide for hydrogen production. *J. Phys. Chem. C* **114**, 11466-11474 (2010).

106. Yu X, De Waele V, Löfberg A, Ordomsky V, Khodakov AY. Selective photocatalytic conversion of methane into carbon monoxide over zinc-heteropolyacid-titania nanocomposites. *Nat. Commun.,* **10**, 700 (2019).

107. Zhou Y, Zhang L, Wang W. Direct functionalization of methane into ethanol over copper modified polymeric carbon nitride via photocatalysis. *Nat. Commun.,* **10**, 506 (2019).

108. Tan HL, Amal R, Ng YH. Alternative strategies in improving the photocatalytic and photoelectrochemical activities of visible light-driven $BiVO_4$: a review. *J. Mater. Chem. A* **5**, 16498-16521 (2017).

109. Malathi A, Madhavan J, Ashokkumar M, Arunachalam P. A review on $BiVO_4$ photocatalyst: activity enhancement methods for solar photocatalytic applications. *Appl. Catal. A* **555**, 47-74 (2018).

110. Y Wang, Q Lai, F Zhang, X Shen, M Fan, Y He, S Ren, High efficiency photocatalytic conversion of CO_2 with H_2O over Pt/TiO_2 nanoparticles. *RSC Adv.*, **4**, 44442 (2014).

111. O Ozcan, F Yukruk, EU Akkaya, D Uner, Dye sensitized CO_2 reduction over pure and platinized TiO_2. *Top. Catal.* **44**, 523 (2007).

112. J. Pan, X. Wu, L. Wang, G. Liu, G. Q. Lu, H.-M. Cheng, Synthesis of anatase TiO_2 rods with dominant reactive {010} facets for the photoreduction of CO_2 to CH_4 and use in dye-sensitized solar cells. *Chem. Commun.*, **47**, 8361 (2011).

113. M. Anpo, H. Yamashita, K. Ikeue, Y. Fujii, S. G. Zhang, Y. Ichihashi, D. R. Park, Y. Suzuki, K. Koyano, T. Tatsumi, Photocatalytic reduction of CO_2 with H_2O on Ti-MCM-41 and Ti-MCM-48 mesoporous zeolite catalysts. *Catal. Today*, **44**, 327 (1998).

114. X. Li, Z. Zhuang, W. Li, H. Pan, Photocatalytic reduction of CO_2 over noble metal-loaded and nitrogen-doped mesoporous TiO_2. *Appl. Catal., A,* **31**, 429–430 (2012).

115. C. Dong, C. Lian, S. Hu, Z. Deng, J. Gong, M. Li, H. Liu, M. Xing, J. Zhang, Size-dependent activity and selectivity of carbon dioxide photocatalytic reduction over platinum nanoparticles. *Nat. Commun.* **9**, 1252 (2018).

116. H. Shi, Z. Zou, Photophysical and photocatalytic properties of $ANbO_3$ (A=Na, K) photocatalysts. *J. Phys. Chem. Solids*, **73**, 788 (2012).

117. P. Li, S. Ouyang, G. Xi, T. Kako, J. Ye, The Effects of Crystal Structure and Electronic Structure on Photocatalytic H_2 Evolution and CO_2 Reduction over Two Phases of Perovskite-Structured $NaNbO_3$. *J. Phys. Chem. C*, **116**, 7621 (2012).

118. N. Zhang, S. Ouyang, P. Li, Y. Zhang, G. Xi, T. Kako, J. Ye, Ion-exchange synthesis of a micro/mesoporous Zn_2GeO_4 photocatalyst at room temperature for photoreduction of CO_2. *Chem. Commun*, **47**, 2041 (2011).

119. Q. Liu, Y. Zhou, Y. Ma, Z. Zou, Synthesis of highly crystalline $In_2Ge_2O_7$(En) hybrid sub-nanowires with ultraviolet photoluminescence emissions and their selective photocatalytic reduction of CO_2 into renewable fuel. *RSC Adv.*, **2**, 3247 (2012).

120. W.-J. Ong, L.-L. Tan, S.-P. Chai, S.-T. Yong, Heterojunction engineering of graphitic carbon nitride (g-C_3N_4) via Pt loading with improved daylight-induced photocatalytic reduction of carbon dioxide to methane. *Dalton Trans.*, **44**, 1249 (2015).

121. Y.-P. Yuan, S.-W. Cao, Y.-S. Liao, L.-S. Yin, C. Xue, Red phosphor/g-C_3N_4 heterojunction with enhanced photocatalytic activities for solar fuels production. *Appl. Catal., B*, **164**, 140–141 (2013).

122. S.-W. Cao, X.-F. Liu, Y.-P. Yuan, Z.-Y. Zhang, Y.-S. Liao, J. Fang, S. C. J. Loo, T. C. Sum, C. Xue, Solar-to-fuels conversion over In_2O_3/g-C_3N_4 hybrid photocatalysts. *Appl. Catal., B*, **147**, 940 (2014).

123. H. Shi, G. Chen, C. Zhang, Z. Zou, Polymeric g-C_3N_4 Coupled with $NaNbO_3$ Nanowires toward Enhanced Photocatalytic Reduction of CO_2 into Renewable Fuel. *ACS Catal.*, **4**, 3637 (2014).

124. T. Ohno, T. Higo, N. Murakami, H. Saito, Q. Zhang, Y. Yang, T. Tsubota, Photocatalytic reduction of CO_2 over exposed-crystal-face-controlled TiO2 nanorod having a brookite phase with co-catalyst loading. *Appl. Catal., B*, **309**, 152–153 (2014).

125. C. Zhao, A. Krall, H. Zhao, Q. Zhang, Y. Li, Ultrasonic spray pyrolysis synthesis of Ag/TiO_2 nanocomposite photocatalysts for simultaneous H_2 production and CO_2 reduction. *Int. J. Hydrogen Energy* **37**, 9967 (2012).

126. Z. Zhu, J. Qin, M. Jiang, Z. Ding, Y. Hou, Enhanced selective photocatalytic CO_2 reduction into CO over Ag/CdS nanocomposites under visible light. *Appl. Surf. Sci.,* **391**, 572 (2017).

127. T. Takayama, K. Tanabe, K. Saito, A. Iwase, A. Kudo, The $KCaSrTa_5O_{15}$ photocatalyst with tungsten bronze structure for water splitting and CO_2 reduction. *Phys. Chem. Chem. Phys.*, **16**, 24417 (2014).

128. K. Iizuka, T. Wato, Y. Miseki, K. Saito, A. Kudo, Photocatalytic Reduction of Carbon Dioxide over Ag Cocatalyst-Loaded $ALa_4Ti_4O_{15}$ (A = Ca, Sr, and Ba) Using Water as a Reducing Reagent. *J. Am. Chem. Soc.*, **133**, 20863 (2011).

129. F. Solymosi, I. Tombácz, Photocatalytic reaction of H_2O+CO_2 over pure and doped Rh/TiO_2. *Catal. Lett.*, **27**, 61 (1994).

130. Y. Kohno, H. Hayashi, S. Takenaka, T. Tanaka, T. Funabiki, S. Yoshida, Photo-enhanced reduction of carbon dioxide with hydrogen over Rh/TiO_2. *J. Photochem. Photobiol., A*, **126**, 117 (1999).

131. N. M. Dimitrijevic, I. A. Shkrob, D. J. Gosztola, T. Rajh, Dynamics of Interfacial Charge Transfer to Formic Acid, Formaldehyde, and Methanol on the Surface of TiO_2 Nanoparticles and Its Role in Methane Production. *J. Phys. Chem. C*, **116**, 878 (2012)

132. S. Bai, X. Wang, C. Hu, M. Xie, J. Jiang, Y. Xiong, Two-dimensional g-C_3N_4: an ideal platform for examining facet selectivity of metal co-catalysts in photocatalysis. *Chem. Commun*, **50**, 6094 (2014).

133. Slamet, H. W. Nasution, E. Purnama, S. Kosela, J. Gunlazuardi, Photocatalytic reduction of CO_2 on copper-doped Titania catalysts prepared by improved-impregnation method. *Catal. Commun.*, **6**, 313 (2005).

134. H.-C. Yang, H.-Y. Lin, Y.-S. Chien, J. C.-S. Wu, H.-H. Wu, Mesoporous TiO_2/SBA-15, and Cu/TiO_2/SBA-15 Composite Photocatalysts for Photoreduction of CO_2 to Methanol. *Catal. Lett.*, **131**, 381 (2009).

135. C. Wang, R. L. Thompson, P. Ohodnicki, J. Baltrus, C. Matranga, Size-dependent photocatalytic

reduction of CO_2 with PbS quantum dot sensitized TiO_2 heterostructured photocatalysts. *J. Mater. Chem.*, **21**, 13452 (2011).

136. H. Park, H.-H. Ou, A. J. Colussi, M. R. Hoffmann, Artificial Photosynthesis of C1–C3 Hydrocarbons from Water and CO_2 on Titanate Nanotubes Decorated with Nanoparticle Elemental Copper and CdS Quantum Dots. *J. Phys. Chem. A*, **119**, 4658 (2015).

137. I. Shown, H.-C. Hsu, Y.-C. Chang, C.-H. Lin, P. K. Roy, A. Ganguly, C.-H. Wang, J.-K. Chang, C.-I. Wu, L.-C. Chen, K.-H. Chen, Highly Efficient Visible Light Photocatalytic Reduction of CO_2 to Hydrocarbon Fuels by Cu-Nanoparticle Decorated Graphene Oxide. *Nano Lett.*, **14**, 6097 (2014).

138. H. Zhang, J. Wei, J. Dong, G. Liu, L. Shi, P. An, G. Zhao, J. Kong, X. Wang, X. Meng, J. Zhang, J. Ye, Efficient Visible-Light-Driven Carbon Dioxide Reduction by a Single-Atom Implanted Metal–Organic Framework. *Angew. Chem.*, **128**, 14522 (2016).

139. J.-Y. Liu, B. Garg, Y.-C. Ling, $Cu_xAg_yIn_zZn_kS_m$ solid solutions customized with RuO_2 or $Rh_{1.32}Cr_{0.6}6O_3$ co-catalyst display visible light-driven catalytic activity for CO_2 reduction to CH3OH. *Green Chem.*, **13**, 2029 (2011).

140. D.-S. Lee, H.-J. Chen, Y.-W. Chen, Photocatalytic reduction of carbon dioxide with water using InNbO4 catalyst with NiO and Co_3O_4 cocatalysts. *J. Phys. Chem. Solids*, **73**, 661 (2012).

141. Z.-Y. Wang, H.-C. Chou, J. C. S. Wu, D. P. Tsai, G. Mul, CO2 photoreduction using NiO/$InTaO_4$ in optical-fiber reactor for renewable energy. *Appl. Catal., A*, **380**, 172 (2010).

142. P.-Y. Liou, S.-C. Chen, J. C. S. Wu, D. Liu, S. Mackintosh, M. Maroto-Valer, R. Linforth, Photocatalytic CO_2 reduction using an internally illuminated monolith photoreactor. *Energy Environ. Sci.*, **4**, 1487 (2011).

143. S. Xie, Y. Wang, Q. Zhang, W. Fan, W. Deng, Y. Wang, Photocatalytic reduction of CO_2 with H_2O: significant enhancement of the activity of Pt–TiO_2 in CH_4 formation by addition of MgO. *Chem. Commun.*, **49**, 2451 (2013).

144. Slamet, H. W. Nasution, E. Purnama, S. Kosela, J. Gunlazuardi, Photocatalytic reduction of CO_2 on copper-doped Titania catalysts prepared by improved-impregnation method. *Catal. Commun.*, **6**, 313 (2005).

145. I. H. Tseng, W.-C. Chang, J. C. S. Wu, Photoreduction of CO_2 using sol–gel derived titania and titania-supported copper catalysts. *Appl. Catal., B*, **37,** 37 (2002).

146. J. C. S. Wu, H.-M. Lin, C.-L. Lai, Photo reduction of CO_2 to methanol using optical-fiber photoreactor. *Appl. Catal., A*, **296**, 194 (2005).

147. Q. Zhang, T. Gao, J. M. Andino, Y. Li, Copper and iodine co-modified TiO_2 nanoparticles for improved activity of CO_2 photoreduction with water vapor. *Appl. Catal., B*, **257**, 123–124 (2012).

148. W.-N. Wang, J. Park, P. Biswas, Rapid synthesis of nanostructured Cu–TiO_2–SiO_2 composites for CO_2 photoreduction by evaporation driven self-assembly. *Catal. Sci. Technol.*, **1**, 593 (2011).

149. W. Tu, Y. Li, L. Kuai, Y. Zhou, Q. Xu, H. Li, X. Wang, M. Xiao, Z. Zou, Construction of unique two-dimensional MoS_2–TiO_2 hybrid nanojunctions: MoS_2 as a promising cost-effective cocatalyst toward improved photocatalytic reduction of CO_2 to methanol. *Nanoscale*, **9**, 9065 (2017).

Chapter 2. Experimental

2.1 Catalyst preparation

2.1.1 Chemicals

Titanium (IV) oxide (P25, TiO_2, 99.5%), phosphotungstic acid hydrate ($H_3O_{40}PW_{12}\cdot xH_2O$, M_w = 2880.05), phosphomolybdic acid hydrate ($H_3[P(Mo_3O_{10})_4] \cdot xH_2O$, M_w = 1825.25), tungstosilicic acid hydrate ($H_4[Si(W_3O_{10})_4] \cdot xH_2O$, M_w = 2878.17), zinc nitrate hexahydrate ($Zn(NO_3)_2\cdot 6H_2O$, ≥99.0%), iron(III) nitrate nonahydrate ($FeNO_3)_3\cdot 9H_2O$, ≥98%), ammonium metavanadate(V) (NH_4VO_3, 99%), ammonium tungstate ($(NH_4)_{10}H_2(W_2O_7)_6$, ≥99.99%), manganese(II) nitrate hydrate ($Mn(NO_3)_2\cdot xH_2O$, 99.99%), cobalt(II) nitrate hexahydrate ($Co(NO_3)_3\cdot 6H_2O$, 98%), cerium(III) nitrate hexahydrate ($Ce(NO_3)_3\cdot 6H_2O$, 99%), gallium(III) nitrate hydrate ($Ga(NO_3)_3\cdot xH_2O$, 99.9%), bismuth(III) nitrate pentahydrate ($Bi(NO_3)_3 \cdot 5H_2O$, ≥98.0%), bismuth(III) oxide (Bi_2O_3, 99.999%) copper(II) nitrate trihydrate ($Cu(NO_3)_2\cdot 3H_2O$, 99-104%), ammonium metavanadate (NH_4VO_3, ≥99.0%), vanadium(V) oxide (V_2O_5, 99.99%), silver nitrate ($AgNO_3$, ≥99.0%), palladium(II) nitrate hydrate ($Pd(NO_3)_2\cdot xH_2O$, 99.9%), ruthenium(III) chloride hydrate ($RuCl_3 \cdot xH_2O$, 38.0-42.0% Ru basis), lead(II) nitrate ($Pb(NO_3)_2$, ≥99.0%), gold(III) chloride hydrate ($HAuCl_4 \cdot aq$, ~50% Au basis), nitric acid (HNO_3, 70%), ammonia solution 28-30%, sodium chloride (NaCl, ≥99.5%), sodium hydroxide (NaOH, ≥98%), sodium dodecylbenzenesulfonate ($CH_3(CH_2)_{11}C_6H_4SO_3Na$, technical grade) and dimethyl carbonate (DMC, ≥99.0%) were purchased from Sigma-Aldrich and used without further purification. ^{13}C labelled carbon dioxide ($^{13}CO_2$, 99 atom % ^{13}C - <3 atom % ^{18}O) was purchased from Cortecnet.

Supports

Commercial amorphous silica (CARIACT Q-10, Fuji Silysia) and TiO_2 (P25) together with the synthetized g-C_3N_4 and $BiVO_4$ were used as supports for the preparation of metal-heteropolyacid nanocomposites. g-C_3N_4 was fabricated by calcining the urea. The powder of urea was calcined in a muffle furnace for 2 h at 550 °C with a ramping rate of 10 °C min^{-1} in air. After cooling down to room temperature, the final light-yellow g-C_3N_4 was obtained.

Monoclinic $BiVO_4$ crystals were synthesized by a hydrothermal method. Briefly, the precursors NH_4VO_3 (0.015 mol) and $Bi(NO_3)_3 \cdot 5H_2O$ (0.015 mol) were dissolved in an aqueous nitric acid solution (2 M), and the pH value of the solution was adjusted to 2.0 with ammonia solution (14.84 M) under continuous stirring. An orange precipitate appears over time. After that, the suspension was transferred to a Teflon-lined stainless steel autoclave with a capacity of 100 mL and treated by hydrothermal at 473 K for 24 h. After the autoclave was cooled down to room temperature, the yellow powdery sample was separated by filtration, washed with deionized water for several times, and then dried at 353 K in air for overnight. Finally, the sample was calcined at 773 K in air for 2 h. The final yellow $BiVO_4$ was obtained.

2.1.2 Synthesis of the metal-heteropolyacid/TiO_2 composite catalysts

TiO_2 (P25) constituted by 20% rutile and 80% anatase was used as catalytic support. The metal-HPW/TiO_2 catalysts were prepared by the two-step impregnation. For example, for preparation of Zn-HPW/TiO_2, first, a fixed amount of TiO_2 was suspended in an anhydrous ethanol solution of phosphotungstic acid hydrate ($H_3[P(W_3O_{10})_4]$ xH_2O, HPW), ungstosilicic acid hydrate ($H_4[Si(W_3O_{10})_4] \cdot xH_2O$, HSiW) and phosphomolybdic acid hydrate ($H_3[P(Mo_3O_{10})_4] \cdot xH_2O$,HPMo). The ratio of HPW to TiO_2 varied from 0.15 to 1.2. The HPW/TiO_2 (HPW/TiO_2 ratio=0.3) sample was obtained by stirring and drying at 353 K for 12 h. Second, the Zn-HPW/TiO_2 catalyst was prepared by incipient wetness impregnation of the support with aqueous solutions of zinc nitrate hexahydrate ($Zn(NO_3)_2 \cdot 6H_2O$). For the other metal-HPW/TiO_2 catalysts, the aqueous solutions of $Fe(NO_3)_3 \cdot 9H_2O$, NH_4VO_3, $Co(NO_3)_3 \cdot 6H_2O$, $Ce(NO_3)_3 \cdot 6H_2O$, $Ga(NO_3)_3 \cdot xH_2O$, $Cu(NO_3)_2 \cdot 3H_2O$, $Bi(NO_3)_3 \cdot 5H_2O$, $RuCl_3 \cdot xH_2O$, $HAuCl_4$, $AgNO_3$ and $Pd(NO_3)_2 \cdot xH_2O$ were used. The concentrations of the impregnating solutions were calculated in order to obtain about 6 wt. % metal in the final catalysts. After the second impregnation, the catalysts were dried overnight in an oven at 373 K. Then, they were calcined in air at 300 °C for 3 h with the 2 °C/min temperature ramping. The catalysts were denoted as M-HPW/TiO_2, and M = V, Fe, Ga, Ce, Co, Cu, Zn, Bi, Au,

Ru, Ag and Pd.

Preparation of the silver salt of HPW deposited on TiO_2 ($AgPW/TiO_2$)

First, a fixed amount of phosphotungstic acid hydrate ($H_3[P(W_3O_{10})_4]$ xH_2O, HPW) was mixed with silver nitrate ($AgNO_3$) aqueous solution. The preparation process was performed at ambient temperature under stirring. The obtained Ag salt was evaporated overnight in the oven at 353K to dryness. Then, the $AgPW/TiO_2$ sample was prepared by incipient wetness impregnation of the TiO_2(P25) support with aqueous solutions of Ag salt. After the impregnation, the samples were dried overnight in an oven at 373 K.

2.1.3 Synthesis of $BiVO_4$ base catalysts

2.1.3.1 Synthesis of monoclinic $BiVO_4$ crystal with controllable exposed facets

Monoclinic $BiVO_4$ crystal was synthesized by a hydrothermal method. In brief, the precursors NH_4VO_3 (0.015 mol) and $Bi(NO_3)_3 \cdot 5H_2O$ (0.015 mol) were dissolved in an aqueous nitric acid solutions (2 M), and the pH value of the solution was adjusted to 2.0 with ammonia solution (14.84 M) under continuous stirring. An orange precipitate appears over time. After that, NaCl was added into the suspension and stirring was continued for 30 minutes. After about 5 h aging, the suspension was transferred to a Teflon-lined stainless steel autoclave with a capacity of 100 mL and treated under hydrothermal conditions at 473 K for 24 h. After the autoclave was cooled down to room temperature, the yellow powdery sample was separated by filtration, washed with deionized water for several times, and then dried at 353 K in air for overnight. Finally, the sample was calcined at 773 K in air for 2 h. The samples were denoted as $BiVO_4$ - x M, and x represents the concentration of NaCl in the suspension[1, 2, 3].

2.1.3.2 Synthesis of monoclinic $BiVO_4$ crystal with predominantly exposed {010} and {110} facets

Synthesis of $BiVO_4$-010

The precursor $Bi(NO_3)_3 \cdot 5H_2O$ (0.015 mol) was dissolved into an aqueous nitric acid

solutions (4 M). And the precursors NH_4VO_3 (0.015 mol) was dissolved into another aqueous sodium hydroxide solution (2 M). Afterwards, sodium dodecyl benzene sulfonate (0.002 mol) was added to the above solutions separately. After stirring for 30 minutes, the above two solutions were mixed under continuous stirring. The pH value of mixed solutions was adjusted to 7.0 with sodium hydroxide solution (2 M). After about 1 h stirring, the mixed solution was transferred into Teflon-lined stainless steel autoclave and hydrothermally treated at 473 K for 1.5 h. The yellow powdery was recovered by filtration, washed with deionized water for several times, and then dried at 353 K in air for overnight. This sample was denoted as $BiVO_4$-010[4].

Synthesis of $BiVO_4$-110

The $BiVO_4$-110 sample was synthesized using solid-liquid state reaction by mixing equal amount of Bi_2O_3 (0.005 mol) and V_2O_5 (0.005 mol) in an aqueous nitric acid solution (1 M). The suspension was stirred for four days at room temperature. The yellow powdery was separated by filtration, washed with deionized water for several times and dried at 353 K in air for overnight. This sample was denoted as $BiVO_4$-110[5].

2.1.3.3 Selective photo-deposition of metal oxides in monoclinic $BiVO_4$ crystal

Photo-reduction and photo-oxidation procedures have been used for deposition of co-catalysts. 1.0 g $BiVO_4$ powder and a calculated amount of metal precursors were added in 40 mL deionized water containing a sacrificial agent. After about 20 minutes ultrasonic dispersion, the aqueous suspension under irradiation with a 300 W Xe lamp for 5 h under continuous stirring with the protection of nitrogen. Then the suspension was filtered, washed with deionized water for several times and dried at 353 K in air for overnight.

5 wt% of metal in the form of metal oxides (WO_x, FeO_x, ZnO_x, CuO_x and CoO_x)were deposited over $BiVO_4$-0.20M by photo-reduction procedure using 20 wt% of methanol as sacrificial agent and $(NH_4)_{10}(H_2W_{12}O_{42})\cdot 4H_2O$, $Fe(NO_3)_3\cdot 9H_2O$, $Zn(NO_3)_2\cdot 6H_2O$ and $Cu(NO_3)_2\cdot 3H_2O$ as precursors, respectively. The obtained samples were denoted as $WO_x/BiVO_4$, $FeO_x/BiVO_4$, $ZnO_x/BiVO_4$ and $CuO_x/BiVO_4$.

5 wt% of metal in the form of metal oxides MnO_x, PbO_2 and CoO_x have been deposited

over $CuO_x/BiVO_4$ by photo-oxidation technique using $NaIO_3$ (0.1 M) as the electron acceptor and $Mn(NO_3)_2{\cdot}xH_2O$, $Pd(NO_3)_2{\cdot}xH_2O$ and $Co(NO_3)_3{\cdot}6H_2O$ as precursor, respectively. The obtained samples were denoted as $MnO_x/CuO_x/BiVO_4$, $PbO_2/CuO_x/BiVO_4$ and $CoO_x/CuO_x/BiVO_4$.

For comparison, the reference sample $CoO_x/CuO_x/BiVO_4$(imp) has been synthesized by impregnation of $Cu(NO_3)_2{\cdot}3H_2O$ and $Co(NO_3)_3{\cdot}6H_2O$ over $BiVO_4$-0.20M with subsequent calcination at 673 K.

2.2 Catalyst Characterization

The X-ray powder diffraction (XRD) experiments were conducted using a Bruker AXS D8 diffractometer with Cu Kα radiation (λ = 0.1538 nm). The XRD patterns were collected in the 5−80° (2θ) range. The diffuse reflectance UV-visible spectra of the catalysts were recorded on a Perkin-Elmer Lambda 650 S UV/VIS spectrometer equipped with an integrating sphere covered with $BaSO_4$ as a reference.

The textural properties of the samples were studied by N_2 physisorption on a Micromeritics Tristar 3020 apparatus.

The photoluminescence (PL) spectroscopy measurements were performed on a LabRam HR (Horiba scientific). For excitation, 325 nm or 532 nm radiation from a diode-pumped solid-state 300 μW laser was used. The spectrophotometer has an entrance slit of 100 μm, and is equipped with a 300 lines/mm^{-1} grating that permits to achieve a spectral resolution of 3.8 cm^{-1} per pixel. The luminescence light was detected with a CCD camera operating at 138 K.

The scanning electron microscope (SEM) measurements were carried out using JEOL scanning electron microscope with 30 Kv accelerating voltage.

The transmission electron microscope (TEM) observations were performed on a Tecnai instrument, equipped with a LaB6 crystal, operating at 200 kV. The point resolution was around 0.24 nm. Prior to the analysis, the samples were dispersed by ultrasound in ethanol solution for 5 min, and a drop of solution was deposited onto a carbon membrane onto a 300

mesh-copper grid. High quality analytical explorations using the double corrected Cold FEG ARM Jeol 200 (field emission gun) microscope were carried out using the 100 mm Centurio detector for the energy dispersive X rays (EDX) equipping this TEM. The point-to-point resolution reached was of the order of 78 pm under the parallel TEM mode and 0.9 Å under the STEM (Scanning TEM) mode. Z-sensitive high angle annular dark field, HAADF–scanning transmission electron microscopy (STEM imaging, and EDX elemental maps were performed using scanning speed 20 μs/px for imaging and 0.05 μs/px for EDX (256x256px maps), with a 0.1 nm probe size and a current of 120pA. All spectra were recorded under a vacuum of 10^{-8} Torr and recalibrated afterwards with the binding energy of the Al 2p at 74.6 eV.

The fourier-transform infrared (FTIR) spectra have been collected using a Thermo iS10 spectrometer at a 4 cm^{-1} resolution (0.96 cm^{-1} data spacing). The spectra were analyzed and presented (including integration, differentiation and determination of peak positions) using a specialized Thermo software (Omnic).

2.3 Photocatalytic tests

2.3.1 Equipment for photocatalytic conversion of methane

The photocatalytic conversion of methane was carried out in a homemade stainless-steel batch reactor (volume, ~250 mL) with a quartz window on the top of the reactor (Figure 2-1a). The light source was 400 W Xe lamp (Newport). The Quantum Efficiency (QE) was determined by using a Hamamatsu spot light sources LC8-06 Hg-Xe lamps emitting between 240 and 600 nm and equipped with a quartz light-guide to deliver a stable and uniform illumination of the sample. The spectral range of the irradiation where selected by using Hamamatsu optical filter. The irradiance measured by an optical power meter (Newport PMKIT) were 94 and 38 mW cm^{-2} in the ranges of >382 nm and 280-400 nm, respectively. All the photocatalytic tests were performed at ambient temperature. The following typical procedure was used. First, 0.1 g of solid catalyst was placed on a quartz glass holder on the bottom of reactor. Then, for selective photocatalytic conversion of methane into carbon

monoxide system, the reactor was filled with CH_4. The methane pressure was increased up to 0.3 MPa. The reactor contained 0.3 MPa of CH_4 and 0.1 MPa of air (78% N_2 and 21% O_2). And for photocatalytic oxidation coupling of methane system, the reactor was evacuated by vacuum pump and filled with CH_4. The methane pressure was increased up to 0.3 MPa. Before starting a photocatalytic reaction, the reactor was kept in the dark for 1 h to ensure an adsorption-desorption equilibrium between the photocatalyst and reactants. Subsequently, the reactor was irradiated by a 400 W Xe lamp. The photocatalytic reaction time was varied from 1 to 50 h.

The reaction products (C_2H_6, C_3H_8, CO and CO_2) were analyzed by gas chromatography (GC, PerkinElmer Clarus® 580). The reaction system was connected to an online GC injection valve, and the gaseous products were directly introduced to the GC for analysis. The GC was equipped with a PoraBOND Q, a ShinCarbon ST 100/120, columns, a flame ionization detector (FID) and a thermal conductivity detector (TCD). Helium was used as carrier gas.

2.3.2 Equipment for photocatalytic CO_2 reduction

The photocatalytic reduction of CO_2 in water was carried out in a homemade stainless-steel batch reactor (~250 mL) with a quartz window on the top of the reactor. The light source was 400 W Xe lamp (Newport). The catalyst was placed on a quartz glass holder in the middle of reactor (Figure 2-1b). 15 ml of liquid water was added at the bottom of reactor. The reaction has been conducted at ambient temperature and 0.2 MPa of CO_2. Before start of the photocatalytic reaction, the reactor was kept in the dark for 1 h to ensure an adsorption-desorption equilibrium between the photocatalyst and the reactants. Subsequently, the reactor was irradiated by a 400 W Xe lamp. The spectral range of the irradiation was selected using Hamamatsu optical filter. The photocatalytic reaction time was typically 7 h.

The gas phase reaction products (CO, CH_4, C_2H_6 and C_3H_8) were analyzed by on-line gas chromatography (GC, PerkinElmer Clarus® 580). Liquid products such as HCHO and CH_3OH were analyzed by off-line GC analysis. The GC was equipped with a PoraBOND Q and ShinCarbon ST 100/120 columns with detection by flame ionization detector (FID) and

a thermal conductivity detector (TCD).

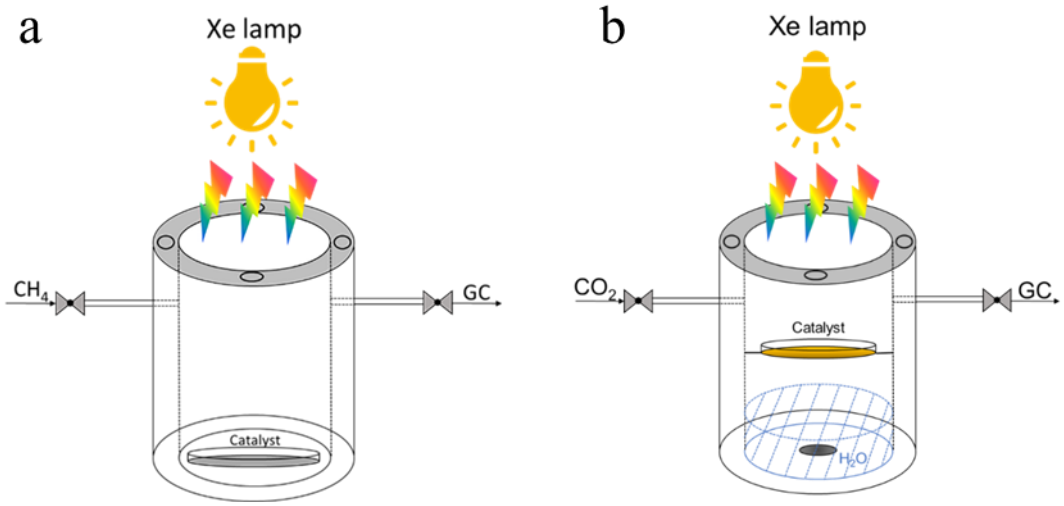

Figure 2-1 The schema of (a) photocatalytic conversion of methane and (b) photocatalytic CO_2 reduction reactor.

2.3.3 $^{13}CO_2$ labeling experiment

The isotopic $^{13}CO_2$ labeling experiments were performed in the homemade stainless-steel batch reactor. First, 0.1 g of solid catalyst was placed on a quartz glass holder on the bottom of reactor. Then, the reactor was sequentially filled with O_2, which was regulated to 0.1 MPa, CH_4 and $^{13}CO_2$. The reactor contained 0.3 MPa of CH_4, 0.1 MPa of O_2 and 0.004 MPa isotopic $^{13}CO_2$. The reactor was kept at ambient temperature. Before starting a photocatalytic reaction, the reactor was kept in the dark for 1 h to ensure an adsorption-desorption equilibrium between the photocatalyst and reactants. The gas phase was analyzed by mass spectrometry. In particular, the (m/z=29)/(m/z=45) ratio was recorded to determine the contribution of $^{13}CO_2$ (m/z=45) cracking to $^{13}CO^+$ (m/z=29) within the ion source of the mass spectrometer. Subsequently, the reactor was irradiated by a 400 W Xe lamp for 14 h. After reaction, the isotopic products (^{13}CO and $^{13}CO_2$) were again analyzed by recording (m/z=29)/(m/z=45) ratio and compared to the value obtained before reaction. Any increase in the (m/z=29)/(m/z=45) ratio would be indicative of the formation of ^{13}CO in the reactor vessel through the conversion of $^{13}CO_2$. The gas from the reaction vessel was slowly released

in a 10 ml/min He flux and analyzed using an online mass spectrometer (Omnistar GSD300 from Pfeiffer Vacuum).

2.4 Measurement of quantum efficiency

We measured quantum efficiency (QE) at 362 nm for the photocatalytic conversion of CH_4 over the 6 wt. % Zn-HPW/TiO_2 and the photocatalytic oxidation coupling of CH_4 over the 6 wt. % Ag-HPW/TiO_2. The quantum efficiency (η) for the formation of a product was calculated using the following equation[6]:

$$\eta = \frac{R(electron) * N_A}{I(W/cm^2) * S(cm^2) * t(s)/E_\lambda(J)} * 100\%$$

Where N_A, I, S, t represents the Avogadro's constant, light irradiance on the sample, irradiation area and reaction time, respectively. E_λ is given by hc/λ (λ = 362 nm). R(electron) represents the amounts of electrons used in the formation of the product. For the photocatalytic conversion of CH_4, R_{CO}(electron) are the amounts of electrons used for the formations of CO. R_{CO}(electron) = 6n(CO), where n is the amount of CO product. For the photocatalytic oxidation coupling of CH_4, R_{C2}(electron) and R_{C3}(electron) are the amounts of electrons used for the formations of C_2H_6 and C_3H_8, respectively. R(electron) = R_{C2}(electron) + R_{C3}(electron) = 2n(C_2H_6) + 3n(C_3H_8), where n(C_2H_6) and n(C_3H_8) are the amount of C_2H_6 product and C_3H_8 product, respectively.

2.5 Reference

1. Li R*, et al.* Spatial separation of photogenerated electrons and holes among {010} and {110} crystal facets of BiVO 4. *Nat. Commun.* **4**, 1432 (2013).

2. Tan HL, Amal R, Ng YH. Alternative strategies in improving the photocatalytic and photoelectrochemical activities of visible light-driven $BiVO_4$: a review. *J. Mater. Chem. A* **5**, 16498-16521 (2017).

3. Malathi A, Madhavan J, Ashokkumar M, Arunachalam P. A review on $BiVO_4$ photocatalyst: activity enhancement methods for solar photocatalytic applications. *Appl. Catal. A* **555**, 47-74 (2018).

4. Zhang L, Chen D, Jiao X. Monoclinic structured $BiVO_4$ nanosheets: hydrothermal preparation, formation mechanism, and coloristic and photocatalytic properties. *J. Phys. Chem. B* **110**, 2668-2673 (2006).

5. Tan HL, Wen X, Amal R, Ng YH. $BiVO_4$ {010} and {110} relative exposure extent: governing factor of surface charge population and photocatalytic activity. *J. Phy. Chem. Lett.* **7**, 1400-1405 (2016).

6. Xie S*, et al.* Visible light-driven C− H activation and C–C coupling of methanol into ethylene glycol. *Nat. Commun.* **9**, 1181 (2018).

Chapter 3. Selective Photocatalytic Conversion of Methane into Carbon Monoxide over Zinc-Heteropolyacid-Titania Nanocomposites

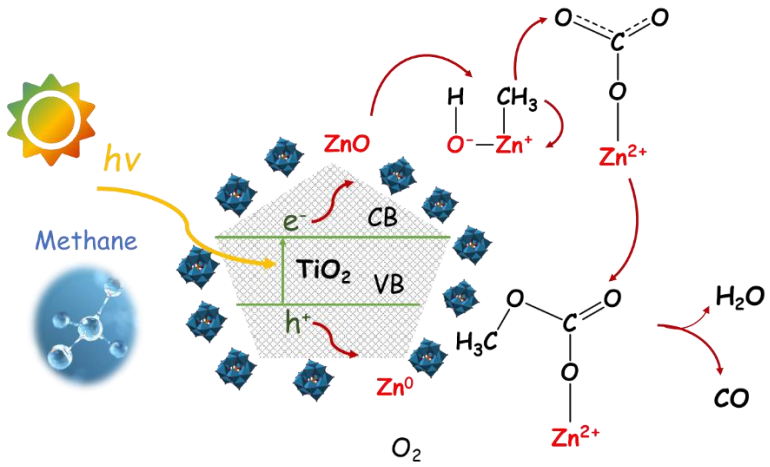

Abstract

Chemical utilization of vast fossil and renewable feedstocks of methane remains one of the most important challenges of modern chemistry. Herein, we report direct and selective methane photocatalytic oxidation at ambient conditions into carbon monoxide, which is an important chemical intermediate and a platform molecule. The composite catalysts on the basis of zinc, tungstophosphoric acid and titania exhibit exceptional performance in this reaction, high carbon monoxide selectivity and quantum efficiency of 7.1% at 362 nm. In-situ Fourier Transform Infrared and X-ray Photoelectron Spectroscopy suggest that the catalytic performance can be attributed to zinc species highly dispersed on tungstophosphoric acid /titania, which undergo reduction and oxidation cycles during the reaction according to the Mars-Van Krevelen sequence. The reaction proceeds via intermediate formation of surface methoxy carbonates.

3.1 Introduction

In recent years, methane has become increasingly abundant due to the development of shale gas fields and other cost efficient or renewable feedstocks such as biogas. Methane is also considered as one of the greenhouse gases with a global warming potential 50 times higher than carbon dioxide[1]. Methane activation is a formidable challenge for catalysis [2, 3, 4,5]. High reaction temperatures (>700°C), low selectivity and abundant CO_2 production are major drawbacks of the conventional thermocatalytic technologies.

Photocatalysis, which uses sunlight, has been shown to be very promising for water decomposition and environmental remediation. Photocatalysis has been also considered as one of pathways to break the thermodynamic barrier[6, 7, 8, 9, 10, 11, 12, 13, 14, 15]. Only a few examples of methane photocatalytic conversion are available in the literature. Earlier reports have shown that methane can be converted by photocatalytic steam reforming ($CH_4 + 2H_2O \rightarrow 4H_2 + CO_2$)[8, 9, 10, 11, 12, 13] or can undergo photocatalytic total oxidation ($CH_4 + 2O_2 \rightarrow CO_2 + 2H_2O$)[9]. A limited number of papers[16, 17] have also addressed combined photo-thermocatalytic[18] or plasma-enhanced[19] methane dry reforming, which represents an interesting route for production of carbon monoxide and hydrogen. A few reports[20, 21, 22, 23] also suggest that methane photo-oxidation can produce methanol, though extremely low yields have been achieved.

Carbon monoxide is a very important compound and a building block in chemical industry. It is utilized as a feedstock in the production of chemicals ranging from acetic acid to polycarbonates and polyurethanes. Syngas, which is a mixture of carbon monoxide and hydrogen, is a valuable feedstock for manufacturing methanol, hydrocarbon fuels, oxo-alcohols and aldehydes. CO is also an important reducing agent and it is used for manufacturing pure metals and in particular iron, cobalt and nickel.

Herein, we report direct selective photocatalytic conversion of methane into carbon monoxide under ambient conditions with only marginal CO_2 production:

$$2CH_4 + 3O_2 \xrightarrow{h\nu} 2CO + 4H_2O \qquad (1)$$

$$2CH_4 + O_2 \xrightarrow{h\nu} 2CO + 4H_2 \qquad (2)$$

A series of catalysts were developed on the basis of metals, $H_3PW_{12}O_{40}$ heteropolyacids (HPW) and TiO_2 (P25). The Zn-HPW/TiO_2 system exhibits exceptional photocatalytic activity in selective carbon monoxide production from methane. Zinc species seem to play an important role in methane activation[6, 24]. Importantly, methane activation and reaction are carried out at ambient temperature. High carbon monoxide yields (up to 3–4% in a single batch experiment), high quantum efficiency (QE = 7.1% at 362 nm) and extended catalyst stability make it potentially interesting in the future for practical applications. To the best of our knowledge, the present work presents the first example of utilizing photocatalysis for methane selective oxidation into carbon monoxide. The conducted in-situ investigation of the reaction mechanism is indicative of zinc reduction by methane with important modifications of the catalyst structure. Exposure to oxygen leads to subsequent regeneration of the composite catalyst according to Mars–van Krevelen mechanism[25, 26, 27].

3.2 Result

3.2.1 Catalytic performance of the metal HPW/TiO_2 composites

CO, CO_2 and trace amounts of hydrogen were detected on TiO_2, HPW, HPW/TiO_2 composites containing different metals after light irradiation (Figure 3-1a). No methanol was detected. Addition of noble or transition metals (Ag, Pd, V, Fe, Ga, Ce, Co, Cu and Zn) to HPW/TiO_2 strongly affects the rate and selectivity of methane oxidation. Much higher activity was observed over the catalysts containing noble metals (Figure 3-1a), but accompanied by significant carbon dioxide production. Among the transition metals, higher CO selectivity was observed on the zinc and copper catalysts.

Compared to the Cu-based catalyst, Zn-HPW/TiO_2 demonstrated a very high activity. Importantly, addition of zinc specifically promotes the carbon monoxide formation rate, which increases almost twenty times from 0.02 mmol g^{-1} h^{-1} over pristine HPW/TiO_2 to 0.429 mmol g^{-1} h^{-1} over the catalyst doped with Zn. Remarkably, the CO selectivity reaches more than 84% on Zn-HPW/TiO_2. Clearly, the Zn-HPW/TiO_2 catalyst has the highest potential for methane selective photocatalytic oxidation. The experiments without irradiation

(dark) yielded no products, confirming that the reaction is indeed driven by light. In order to evaluate the influence of UV, visible and IR light, we conducted photocatalytic experiments on selected spectral ranges ($280 < \lambda < 400$ nm and $\lambda > 380$, Table 3-1). The Zn-HPW/TiO_2 catalyst exhibits very mild activity under visible irradiation, while the reaction rate increases 20 times, when the reactor is exposed to UV.

Methane partial oxidation to CO can be compared with methane dry reforming. Methane dry reforming usually involves both thermo- and photo-catalysis. Note that in our work, methane photooxidation to carbon monoxide occurs with high selectivity at ambient temperature, while in previous reports[16,17], methane dry reforming was conducted at relatively high temperatures in order to obtain noticeable conversion.

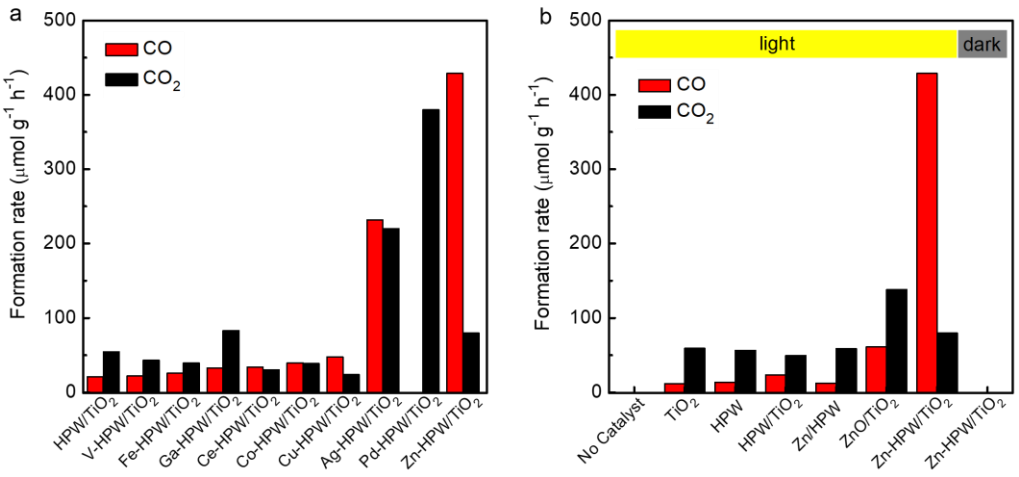

Figure 3-1 Methane photocatalytic oxidation on different catalysts. a Metal-HPW/TiO_2 composite, b TiO_2, HPW, and Zn containing catalysts. Reaction conditions: catalyst, 0.1 g; gas phase pressure, CH_4 0.3 MPa, Air 0.1 MPa; irradiation time, 6 h.

Table 3-1 Catalytic performances for photocatalytic CH_4 conversion measured under irradiation at different spectral ranges.

Spectral range of irradiation (nm)	Formation rate (μmol g^{-1} h^{-1})		Irradiance (mW cm^{-2})	Formation rate to power ratio (μmol g^{-1} h^{-1} mW^{-1} cm^2)
	CO	CO_2		
>382	11	5.9	94	0.12
280-400	208	48	38	5.5

Reaction conditions: catalyst, 0.1 g; Gas phase pressure, CH_4 0.3 Mpa, Air 0.1 Mpa; irradiation time, 6h; light source, Hamamatsu LC8-06 Hg-Xe stabilized irradiation lamps with a spectral irradiance in the range 240-600; Cut-off filter: Vis-IR $\lambda > 382$ nm; UV light, $\lambda = 280$-400 nm.

The exceptional photocatalytic activity of the Zn-HPW/TiO_2 catalyst seems to be related to zinc species. It is reasonable to suggest that the overall reaction rate on Zn-HPW/TiO_2 can be affected by zinc content. Figure 3-2a illustrates the catalytic behavior of Zn-HPW/TiO_2 with different Zn loadings. Addition of even small amounts of zinc results in a major increase in the rate of methane conversion. Note that the presence of zinc principally increases the rate of CO production, while the rate of methane oxidation to CO_2 is only slightly affected. Thus, formation of CO_2 might be explained by the activity of HPW/TiO_2, whereas the Zn species seem active and selective in methane photo-oxidation to CO. Note that the major increase in CO is only observed when the Zn content is higher than 2-3 wt. %. The highest zinc dispersion can be obviously obtained at lower zinc content, at the amount of Zn^{2+} ions, which can neutralize the acid sites in HPW. This amount corresponds to about 2 wt. % Zn.

Another catalyst parameter, which may affect the catalytic performance is the HPW/TiO_2 ratio in the composite. Figure 3-2a shows the performance of Zn-HPW/TiO_2 catalysts with different ratio of HPW to TiO_2, while the molar ratio of Zn to HPW was kept at 2. The HPW/TiO_2 ratio in the composite Zn-HPW/TiO_2 catalysts does not noticeably affect the rate of CO_2 formation, while the effect of this ratio on the rate of CO formation is more significant. Note that only the CO production rate is strongly influenced by the concentration of highly dispersed Zn species. It is expected that higher HPW/TiO_2 ratio could enhance zinc dispersion, because of possible localization of zinc ions in the cationic sites of HPW. Some small decrease in the rate of CO production at higher HPW/TiO_2 ratio can be due to the formation of larger HPW clusters, which would affect the electron transfer from TiO_2 to the Zn species.

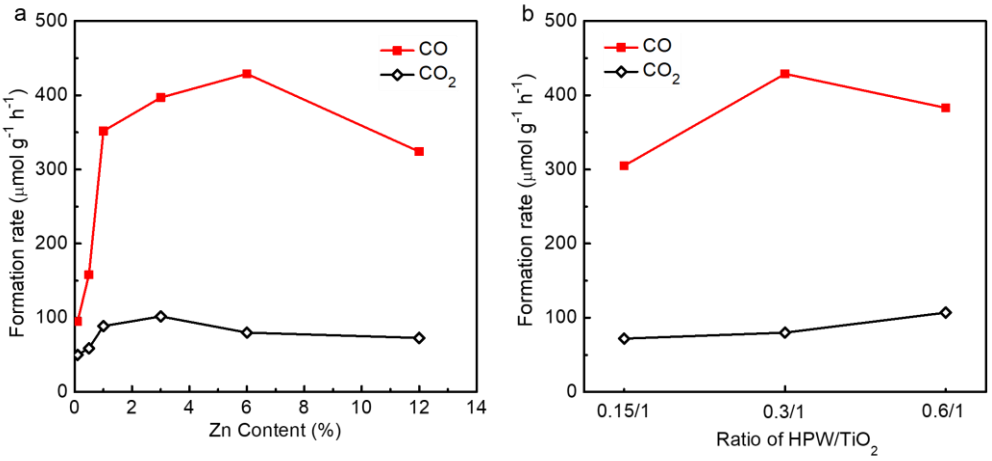

Figure 3-2 Carbon monoxide and carbon dioxide production over Zn-HPW/TiO_2 catalysts. an influence of different Zn loadings, b influence of HPW/TiO_2 ratio. Reaction conditions: catalyst, 0.1 g; gas phase pressure, CH_4 0.3 MPa, Air 0.1 MPa; irradiation time, 6 h.

Further, photocatalytic methane oxidation was investigated on HPW and TiO_2 with and without zinc (Figure 3-1b). TiO_2, HPW, and HPW/TiO_2 exhibit 10-20 times lower activity compared to Zn-HPW/TiO_2. Methane photo-oxidation on TiO_2, HPW, and HPW/TiO_2 primarily results in CO_2, while CO was the major product over Zn-HPW/TiO_2. This could suggest different mechanisms of methane photo-oxidation on these catalysts. The lattice oxygen activated by photo-generated hole could be the main active species for the activation of methane and oxygen and subsequent oxidation of the CH_3 radicals to CO_2 over those semiconductors without zinc[9].

Promotion of TiO_2 or HPW with Zn results only in a slight increase in the methane oxidation rate, whereas CO_2 remains the major reaction product. The mediocre catalytic performance of those composites can be due to the following phenomena. First, Zn/TiO_2 contains relatively large ZnO crystallites. In addition, because of poor zinc dispersion, the uncovered TiO_2 surface leads to an important contribution of TiO_2 to methane total oxidation to CO_2. HPW plays a crucial role in enhancement of zinc dispersion. Indeed, TEM images (Figure 3c) suggest the presence of extremely small Zn clusters in the composite Zn-HPW/TiO_2 catalyst. In addition, HPW could be efficient in transfer of holes and electrons

from TiO_2 to Zn sites[28].

Thus, a major increase in CO production from methane only occurred when the composite catalyst contained together three components: TiO_2, HPW, and Zn. The observed strong effect of Zn on the catalytic performance might be therefore due to the intimate contact between Zn, HPW and TiO_2. It is expected that the interaction of ZnO with the $H_3PW_{12}O_{40}$ acid results in formation of Zn^{2+} ions and possibly small positively charged Zn cationic nanoclusters. The highly dispersed Zn species may have high mobility in the composites. In order to confirm this, we have prepared mechanical mixtures of Zn/TiO_2 with HPW/TiO_2 and performed photocatalytic conversion of methane. The activity of these mechanical mixtures (Figure 3-3) was much higher than over either Zn/TiO_2 or HPW/TiO_2. This could indicate substantial migration of zinc during the reaction and formation of the active sites with the enhanced performance of methane oxidation to CO.

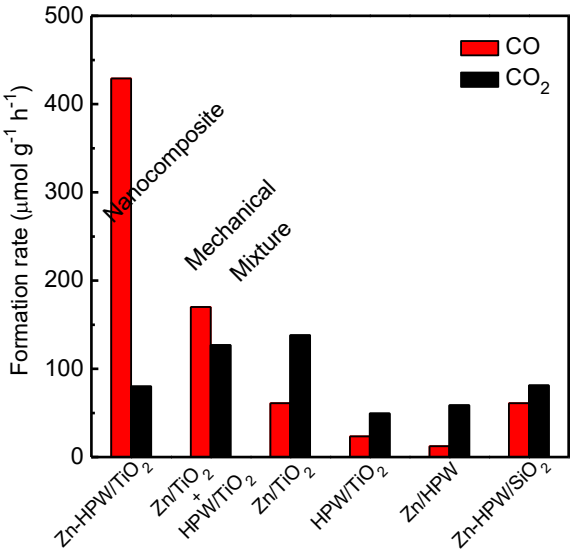

Figure 3-3 Carbon monoxide and carbon dioxide formation rate over nanocomposites and mechanical mixtures. Reaction conditions: catalyst, 0.1 g; Gas phase pressure, CH_4 0.3 MPa, Air 0.1 Mpa; irradiation time, 6h.

3.2.2 Characterization of the Zn-HPW/TiO_2 catalysts

The Zn-HPW/TiO_2 samples have shown the best catalytic performance in partial

methane photocatalytic oxidation to carbon monoxide. A combination of techniques was used for their characterization. The X-ray diffraction (XRD) patterns of Zn-HPW/TiO_2, ZnO/TiO_2, HPW/TiO_2, TiO_2 and HPW are shown in Figure 3-2. The samples containing TiO_2 exhibit XRD peaks of anatase and rutile phases, while the XRD peaks assigned to the heteropolyacid are present in HPW. Interestingly, no diffraction peaks were detected for the HPW and Zn phases in Zn-HPW/TiO_2. This can be probably due to their smaller crystallite sizes. The XRD patterns are slightly different for the Zn/TiO_2 sample. They show the presence of the hexagonal wurtzite ZnO phase (orange bar, JCPDS #36-1451), which was identified by diffraction peaks at 31.8° and 34.4° attributed to crystal face (100) and (002) respectively[9, 29]. Note that the XRD peaks of ZnO almost disappear for Zn-HPW/TiO_2 catalysts. This suggests that in the presence of HPW, zinc species are highly dispersed. No XRD zinc carbonate peaks were observed for any catalyst.

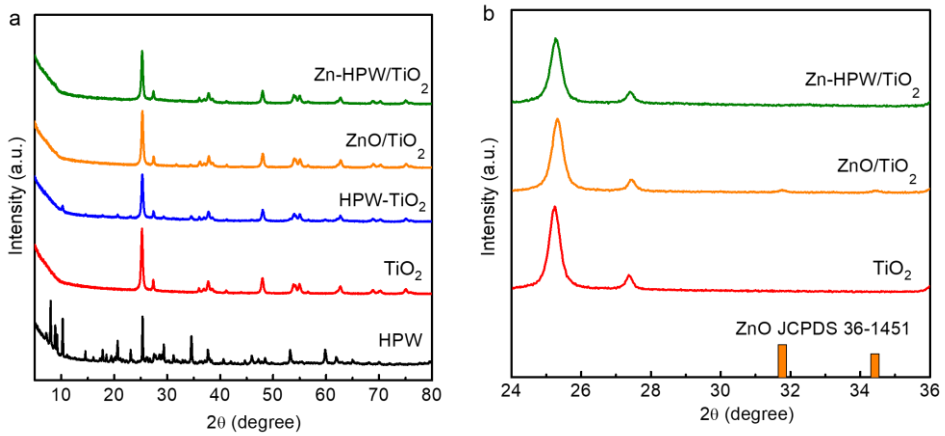

Figure 3-4 XRD patterns of different nanocomposites catalysts.

FTIR analysis has been used to identify the acidity and state of Zn in the catalyst. Figure 3-5 shows FTIR spectra of initial catalyst after evacuation at 200 °C. The catalyst shows strong bands at 1560 and 1285 cm^{-1}, which might be assigned to $\nu_{as}(CO_3)$ and $\nu_s(CO_3)$ of bidentate Zn carbonate species[30].

Adsorption of Py results in strong bands at 1621 and 1453 cm^{-1}, which might be attributed to the Py adsorption over strong Lewis acid sites[31]. The Lewis acid sites were

attributed to unsaturated Zn^{2+} ions. No Brönsted acidity associated to HPW was observed. The Zn-HPW/TiO_2 catalyst contains 0.9 mmol of Zn, while the maximum concentration of potential Brönsted acid sites associated with HPW can be only 0.3 mmol/g (assuming that Brönsted acid sites are not neutralized by zinc). Thus, in the case of full neutralization, a major part of Zn should be in the form of carbonate or oxide. The presence of carbonates might be explained by relatively high basicity ZnO, which easily adsorbs CO_2[32].

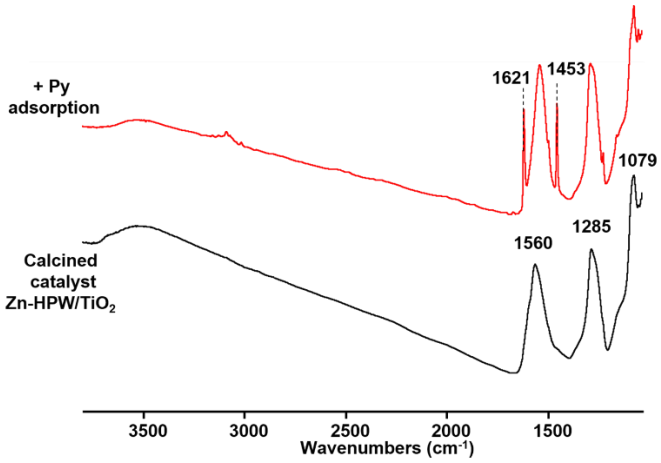

Figure 3-5 FTIR spectra of the Zn-HPW/TiO_2 catalyst before and after adsorption of pyridine and sample evacuation at 200°C.

The UV-Vis diffuse reflectance spectra of Zn-HPW/TiO_2 nanocomposite and reference compounds are displayed in Figure 3-6a. The samples exhibit intense absorption in the ultraviolet region (< 400 nm). The band gap energy estimated using Tauc's plots[20, 21, 22] varies from 3.0 eV to 3.2 eV (Figure 3-6b). Relatively small effect of the promotion with Zn is observed on the band gap. The ZnO band gap energy is a function of crystallite size and varies from 3.12 to 3.30 eV[33]. Zinc carbonate also has semiconductor properties; its band gas is situated at 3.36 eV[34]. This also is rather close to the band gap of HPW (E_g = 3.12 eV, Figure 4) and TiO_2 (E_g = 3.20 eV[35]).

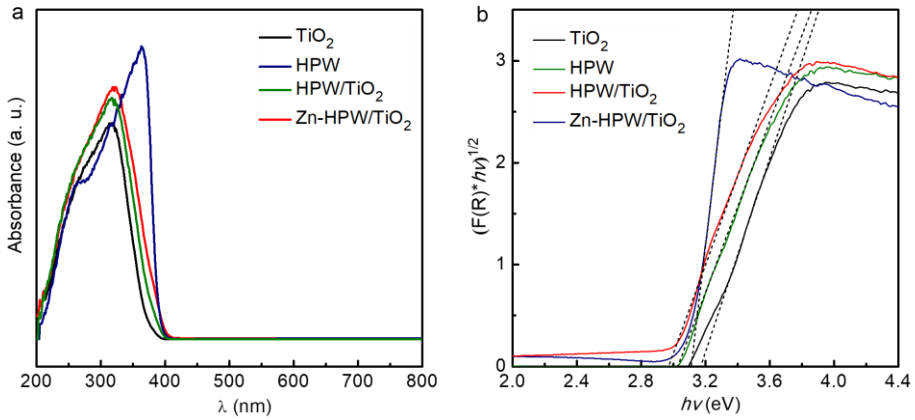

Figure 3-6 UV-visible spectra. a UV-Vis spectra, b $[F(R\infty)h\nu]^{1/2}$ versus hν for Zn-HPW/TiO_2 and reference compounds.

The TEM images of the calcined Zn-HPW/TiO_2 catalyst (Figure 3-7a) clearly show the presence of core-shell particles. The core is constituted by TiO_2 crystallites of 30-40 nm, while the shell is built by the HPW heteropolyacid (layer thickness of 1-2 nm). Small clusters of zinc, which is highly dispersed on the catalyst surface, can be also observed. Figure 3-7b shows TEM images of used Zn-HPW/TiO_2. Interestingly, the methane photocatalytic oxidation does not result in any noticeable zinc sintering. Some restructuring of the HPW shell was only observed.

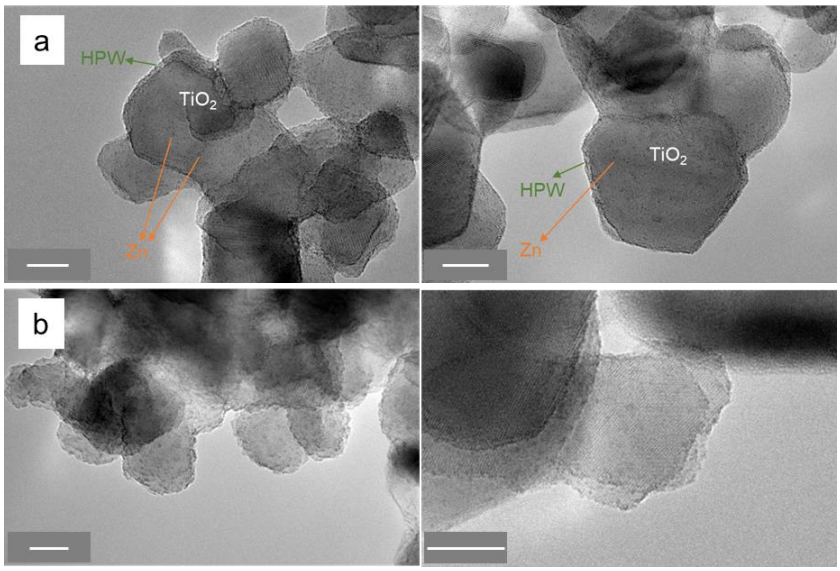

Figure 3-7 TEM images of calcined (a) and used (b) Zn-HPW/TiO_2. Scale bar: 10 nm

3.2.3 Reaction paths in methane oxidation to CO over Zn-HPW/TiO_2 composites

Additional experiments were conducted to investigate in detail the reaction paths over the Zn-HPW/TiO_2 composites. Figure 3-8a shows variations of the CO and CO_2 concentrations as functions of the reaction time over the Zn-HPW/TiO_2 catalyst, whereas the CO and CO_2 selectivity as functions of methane conversion are displayed in Figure 3-8b. The selectivity to carbon monoxide decreases and selectivity to CO_2 increases as the contact time and conversion increase. Extrapolation to zero conversion gives the selectivity of primary reactions. The primary selectivity of methane oxidation to CO is about 80%, while only about 20% of methane directly oxidizes to CO_2. Note that some small amount of CO_2 can come from decomposition of surface zinc carbonate. It can be suggested that the CH_4-O_2 mixtures may react via a combination of parallel and sequential steps. Similar reaction paths were also observed for many partial oxidation reactions[36, 37, 38, 39].

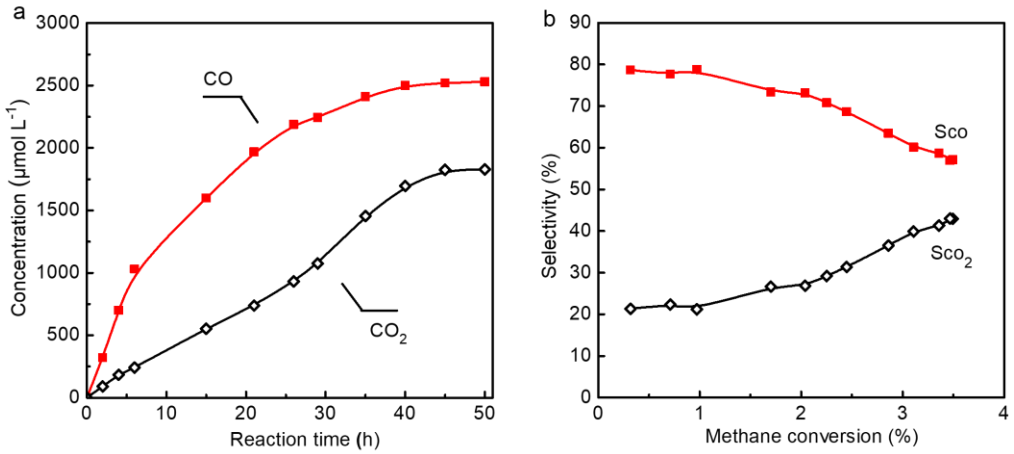

Figure 3-8 a CO and CO_2 concentrations in the reactor as function of time on stream on Zn-HPW-TiO_2 catalyst; b CO and CO_2 selectivity as functions of methane conversion. Reaction conditions: catalyst, 0.1 g; Gas phase pressure, CH_4 0.3 MPa, Air 0.1 MPa; irradiation time, 50h.

In the methane partial oxidation, CO can be formed directly from methane, while CO_2 is produced either from methane total oxidation or from CO oxidation (Figure 3-9).

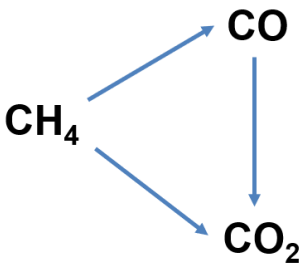

Figure 3-9 Parallel and consequent routes in methane oxidation.

Therefore, in order to increase the selectivity to CO, the catalyst should contain active sites, which are selective for methane direct oxidation to carbon monoxide. These sites should have high activity towards methane oxidation to CO and lower activity for CO oxidation to CO_2. Many reactions of partial oxidation occur with participation of oxygen atoms of the catalysts according to the Mars–van Krevelen mechanism[25]. In this mechanism, the oxygen of the catalyst first oxidizes the molecules of substrate. Oxygen vacancies are produced on the catalyst surface. Then, the oxygen vacancies react with gaseous oxygen and the catalytic structure regenerates. To confirm the relevance of the Mars–van Krevelen mechanism for methane photo-oxidation, the following experiments were conducted.

First, the Zn-HPW/TiO_2 catalyst was exposed directly to methane without adding any oxygen. Figure 3-10 shows the concentrations of CO and CO_2 produced as functions of time. The catalyst shows relatively low conversion of methane to CO and CO_2. The conversion completely stops after 20 h of reaction. This probably corresponds to exhausting oxygen in the catalyst. Assuming that the methane oxidation proceeds to carbon oxides and water with the following stoichiometry:

$$CH_4 + 3O_s \xrightarrow{h\nu} CO + 2H_2O \qquad (3)$$

$$CH_4 + 4O_s \xrightarrow{h\nu} CO_2 + 2H_2O \qquad (4)$$

Our calculation gives almost the same amount of oxygen present in ZnO in the calcined Zn-HPW/TiO_2 catalyst before conducting the reaction (6 wt. % Zn, 7.4×10^{-4} mol/g_{cat}) and amount of oxygen in the produced CO and CO_2 (7.8×10^{-4} mol/g_{cat}). This is indicative of the participation of oxygen linked to zinc in methane photocatalytic oxidation. Incorporation of

zinc oxide oxygen atoms in the produced carbon monoxide and carbon dioxide suggests that zinc is reduced to the metallic state during the reaction. Indeed, the catalyst color changes from white in the calcined catalyst to grayish (Figure 3-10, inserts). To provide further insights into the zinc oxidation state, both the calcined Zn-HPW/TiO_2 catalyst and its counterpart after exposure to methane were characterized by XPS (Figure 3-11a). The catalyst exposure to methane under irradiation results in a shift of the Zn $2p_{3/2}$ lines from 1021.9 eV characteristic for Zn^{2+} species to 1021.5 eV which corresponds to Zn^0 [40, 41], This suggests zinc reduction to the metallic state. The change in the valence state from Zn^{2+} to Zn^0 was observed even more obviously (Figure 3-11b) from the 3 eV downward shift of the binding energy of the Zn $L_3M_{4.5}M_{4.5}$ Auger peak[42, 43, 44]. In the Zn Auger peak from Zn-HPW/TiO_2 catalysts in Figure 3-12b is normalized to the peak height of the ZnO Auger feature. In the Zn Auger spectrum of Zn-HPW/TiO_2 after pretreatment in 0.3 Mpa of CH_4 under 400 W Xe lamp for 12 h, a shoulder feature appeared at the binding energy that was reduced by 3 eV. When the catalyst was regenerated in 0.1 MPa of air under 400 W Xe lamp for 12 h, the shoulder almost disappeared. Simultaneously, XPS suggests complete oxidation of Zn metal clusters after their treatment in air and under irradiation (Figure 3-11a). The Zn $2p_{3/2}$ binding energy shifts from 1021.5 eV to 1021.9 eV, which is characteristic for zinc oxide species. Thus, exposure of the Zn-HPW/TiO_2 catalyst in the presence of light results in zinc re-oxidation to the Zn^{2+} oxidation state.

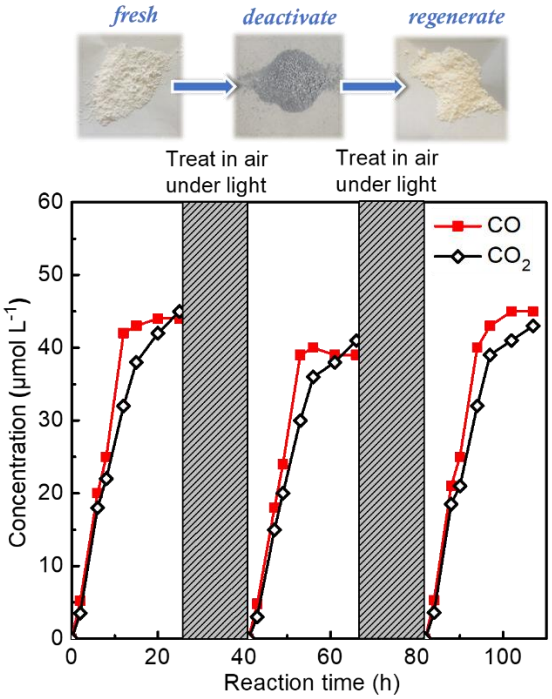

Figure 3-10 Carbon monoxide and carbon dioxide concentrations after exposure of Zn-HPW/TiO_2 to pure methane (CH_4 0.3 MPa). The catalyst was regenerated by treatment in 1 bar of air under light at ambient temperature.

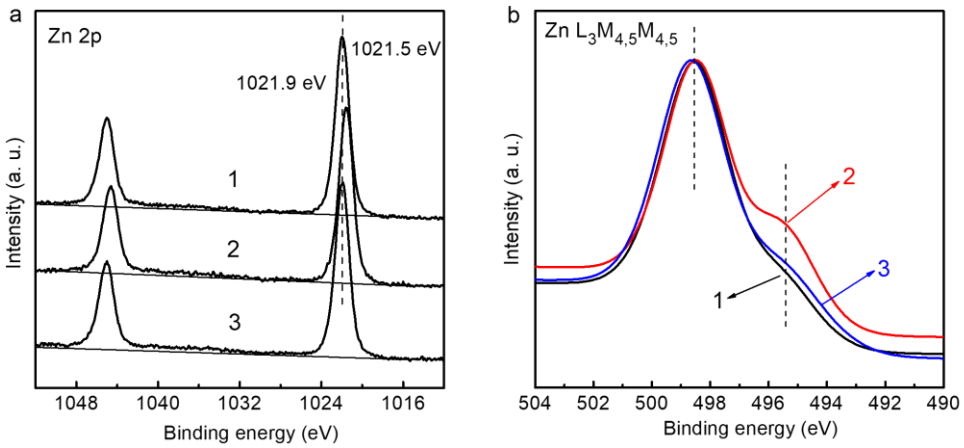

Figure 3-11 XPS (a) and Zn $L_3M_{4.5}M_{4.5}$ Auger spectra (b) of Zn-HPW/TiO_2 catalysts in the regions of Zn 2p. (1). fresh catalyst, (2). treatment in 0.3 Mpa CH_4 under 400 W Xe lamp for 12h, (3). regeneration in 0.1 Mpa air under 400 W Xe lamp for 12h.

The catalytic performance can be entirely regenerated by treatment in air at room temperature in the presence of light. Figure 3-10 shows identical methane photocatalytic conversion on the Zn-HPW/TiO_2 catalyst after exposure to 0.1 MPa of air and irradiation for 16 h. The reaction-regeneration cycle can be repeated several times. Note that after exposure to air under irradiation for 16 h, color of the used catalyst again reverted from gray to white.

The second series of experiments involves catalyst simultaneous exposure to methane and air (Figure 3-12). Exposure of the pre-calcined catalyst at the same time to methane and air results in the production of both CO and CO_2. Similarly to the exposure of the catalyst to pure methane, the catalyst changes colors from white to grey in the end of the cycle. Note that the carbon monoxide and carbon dioxide concentrations are much higher in these experiments compared to the exposure of the catalyst only to methane (Figure 3-12). This is probably due to the presence of a larger amount of oxygen in the reactor with continuous zinc oxidation-reduction cycling during the reaction. Note that the oxygen for methane oxidation can originate both from the catalyst surface and reactor gaseous phase. The production of CO and CO_2 then slows down after 12 h of reaction. Slower reaction rate is probably due to the depletion of available oxygen. The calculation again suggests that the amount of oxygen atoms in the produced CO and CO_2 (2.4 mmol, including production of water) corresponds almost exactly to the amount of oxygen atoms in the 0.25 L reactor (2.3 mmol). In the calculation, we considered both oxygen related to the ZnO species and oxygen atoms present as O_2 in the gaseous phase. The amount of the oxygen in the calcined catalysts corresponds to about 3% of the amount of the oxygen from the gaseous phase. After purging, the reactor was once again exposed to 0.3 MPa of CH_4 and 0.1 MPa of Air. Figure 3-12 shows that methane was again converted to CO and CO_2. Similar CO and CO_2 formation rates were observed in the second and third runs. Furthermore, the catalyst stability was maintained over the reaction period of 78 h, when the fresh reactants were reintroduced.

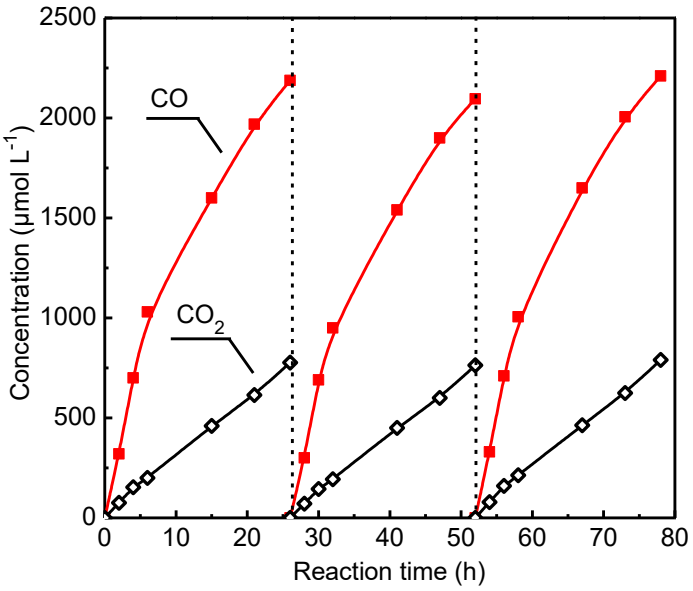

Figure 3-12 Carbon monoxide and carbon dioxide concentrations after exposure of Zn-HPW/TiO_2 to CH_4 and air.

3.2.4 In-situ FTIR study of methane photocatalytic oxidation

The structure of the Zn-HPW/TiO_2 catalyst showing higher yield of CO in methane photocatalytic oxidation was studied in detail by in-situ FTIR spectroscopy. The calcined Zn-HPW/TiO_2 catalyst pretreated in vacuum at 250 °C exhibits FTIR bands at 1560 and 1285 cm^{-1}, which correspond to bidentate surface Zn carbonates (Figure 3-14b). Then, the bidentate carbonate transforms into monodentate carbonate after 0.5 h of reaction (FTIR bands at 1510 and 1294 cm^{-1} corresponding to $\nu_{as}(CO_3)$ and $\nu_s(CO_3)$, respectively)[30, 45]. The transformation might be due to the conversion of bidentate to monodentate carbonate by water[46]. The presence of water was observed by highly intense broad IR band at 3460 and 1605 cm^{-1} related to ν(O-H) and $\delta(H_2O)$ vibrations. Subsequent exposure to light leads to the decrease in the intensity of carbonate bands with appearance of bands at 1225 and 1048 cm^{-1}, which might be assigned to ν(C-O) stretching bands in carbonate ester ($O\text{-}CO_2H^-$, Figure 3-18) and methoxy group (CH_3-O) respectively[47]. The presence of methoxy groups on the catalyst surface is also confirmed by a new FTIR band of C–H stretching at 2880 cm^{-1}

(Figure 3-13a)[47]. The bands observed at 2200 and 2300 cm^{-1} (Figure 3-13a) probably correspond to carbon monoxide adsorption on the low coordinated Zn^{2+} ions[48, 49]. It can be suggested that these unsaturated Zn^{2+} ions may play an important role in methane activation. Strong methane chemisorption over smaller clusters of zinc oxide has been observed by several groups[50, 51, 52, 53]. During the catalyst regeneration, a gradual decrease in the intensity of the bands assigned to adsorbed CO species with simultaneous increase in the intensity of the bands assigned to carbonates was observed.

FTIR analysis of the gaseous phase (Figure 3-14) clearly shows the presence of methane in the IR cell at the initial periods of the reaction (CH rotation-stretching and rotation-bending bands at around 3020 and 1300 cm^{-1}, respectively). At longer reaction time, gaseous carbon monoxide was identified by rotation - stretching bands at 2150 cm^{-1}. In agreement with the results of photocatalytic tests, the intensity of the carbon monoxide FTIR band at 2150 cm^{-1} increases with the reaction time.

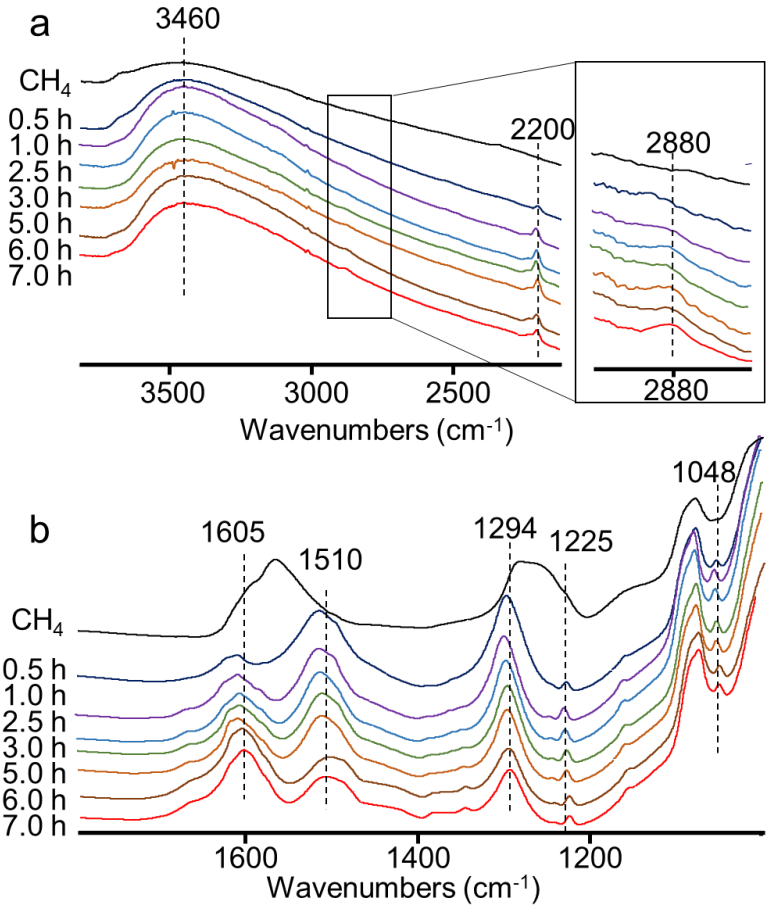

Figure 3-13 In situ FTIR spectra of the Zn-HPW/TiO_2 catalysts in the region of a 3800–2100 cm^{-1} and b 1800–1000 cm^{-1}. The spectra were measured under light at different reaction times in CH_4.

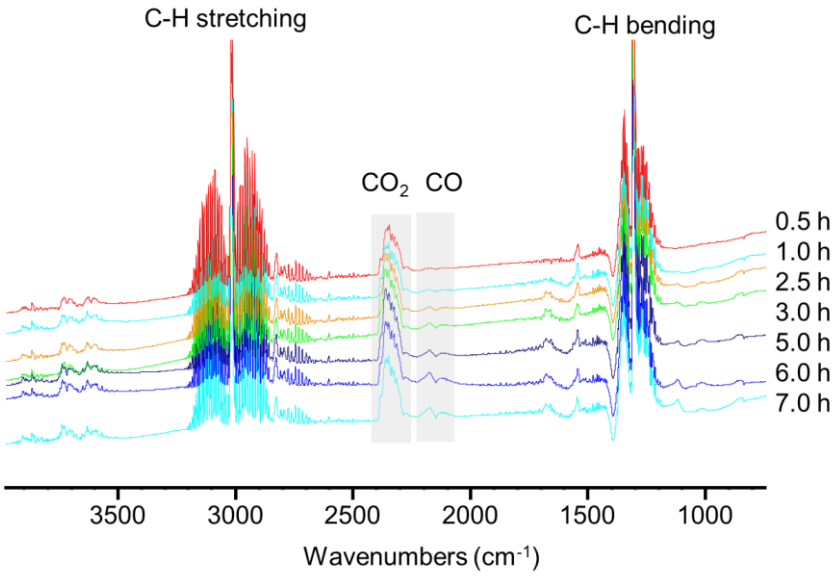

Figure 3-14 FTIR spectra of gaseous phase during methane photocatalytic oxidation over the Zn-HPW/TiO_2 catalyst as a function of reaction time.

In order to confirm the presence of zinc methyl carbonate ester in the catalyst, dimethyl carbonate [$(CH_3O)_2CO$, DMC] was adsorbed on Zn-HPW/TiO_2 with simultaneous measurements of FTIR spectra. The set of bands similar to those observed during the methane photooxidation has been observed (Figure 3-15). Treatment of the catalyst with adsorbed DMC in light leads to a gradual decrease in the intensity of the DMC bands and increase in the water bending band at 1605 cm^{-1}. FTIR analysis of gas phase shows also an increase in the intensity of CO_2 and CO bands, which indicates decomposition of DMC in the presence of light.

The Zn-HPW/TiO_2 catalyst was also exposed to the DMC vapor in the photocatalytic reactor in parallel experiments. In the absence of light, small amount of CO_2 was produced, which is probably due to the DMC hydrolysis. Interestingly, in the presence of light, photocatalytic decomposition of DMC leads to the production of mostly CO (Figure 3-16).

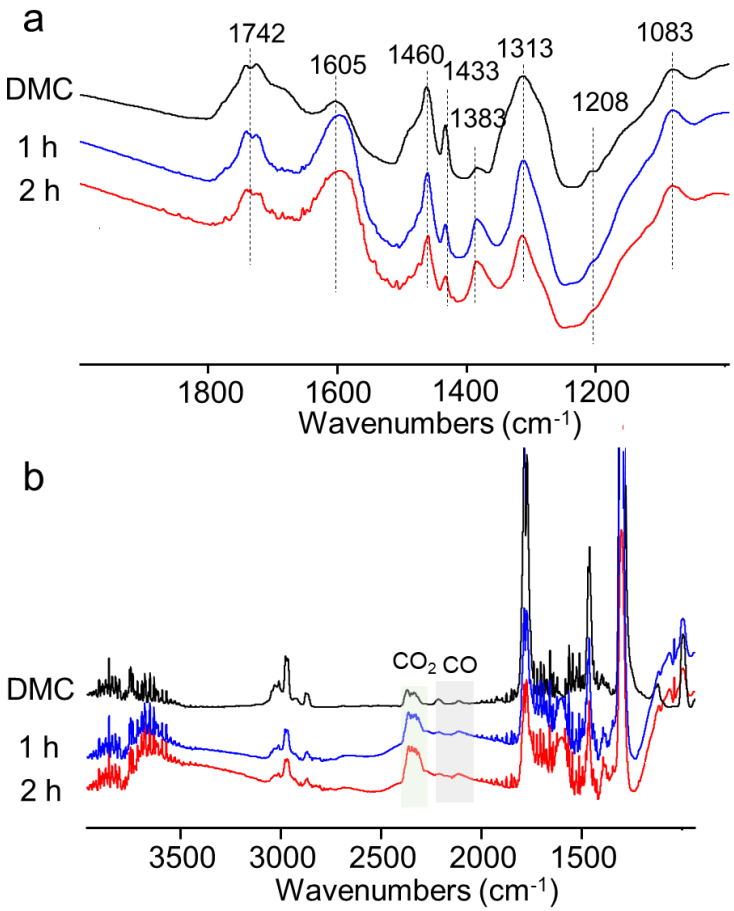

Figure 3-15 FTIR spectra of adsorbed DMC during exposure to light (a) and gas phase analysis (b).

(The bands at 1742, 1460, and 1313 cm^{-1} are attributable to C=O stretching, $\nu_{as}(CO_3)$ and $\nu_s(CO_3)$ of O–C–O stretching modes of carbonate species associated with the Zn cations. This assignment is supported by the work of DMC adsorption over cationic zeolites [*T. Beutel, J. Chem. Soc., Faraday Trans., 1998,94, 985-993; Y. Zhang, A. T. Bell, Journal of Catalysis 255 (2008) 153–161*]. The bands at 1208 and 1083 cm^{-1} might be assigned to ν(C-O) stretching bands in carbonate and methoxy groups, respectively.)

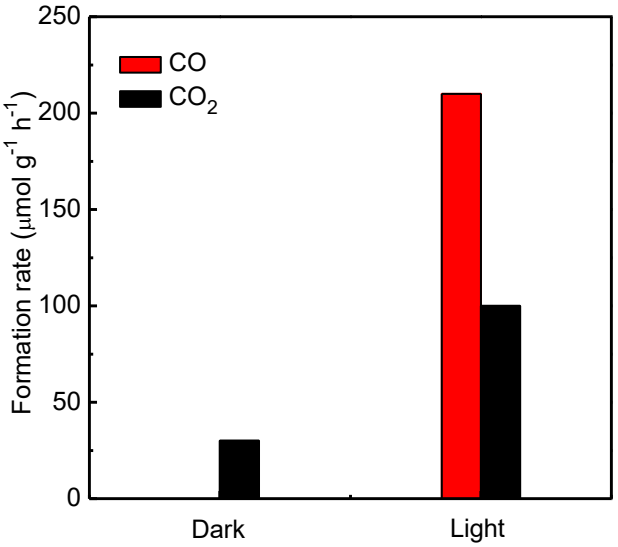

Figure 3-16 Rates of production of CO and CO_2 during decomposition of DMC over the Zn-HPW/TiO_2 catalyst. Reaction condition: Catalyst 0.1 g, Ar 0.2 Mpa; DMC 2 mL; 6 h in dark or under light.

Isotopic labelling experiments provided further information about the reaction mechanism. The goal was to elucidate if CO_2 from the gaseous phase can be involved in the reaction. Figure 3-18 presents mass spectrum recorded before and after photocatalytic reaction. The experiments were conducted under a $^{12}CH_4$, O_2 and $^{13}CO_2$ atmosphere (0.3 MPa of CH_4, 0.1 MPa of O_2 and 1% isotopic $^{13}CO_2$).

To facilitate reading, signals have been normalized to the maximum intensity of peak m/z=45. Before reaction (black curve), m/z=45 corresponding to $^{13}CO_2$ is clearly visible together with signal at m/z=29 corresponding to $^{13}CO_2$ cracking to $^{13}CO^+$ fragments in the mass spectrometer ion source. Peaks at m/z=28 represents residual N_2 in the mass spectrometer vacuum chamber or CO species generated by the ion source. m/z=44 represents residual CO_2 in the vacuum chamber and $^{12}CO_2$ impurity contained in the $^{13}CO_2$ cylinder. After reaction (red curve), m/z=28 and m/z=44 signals increase due to the production of ^{12}CO and $^{12}CO_2$ from the photocatalytic oxidation of methane. m/z=29 signal increases due to the production of ^{13}CO. Isotope labelling therefore suggests that some of added $^{13}CO_2$ is

converted to ^{13}CO. Figure 3-17b indicates a significant (+10%) increase in the (m/z=29)/(m/z=45) ratio before (black) and after (red) photocatalytic reaction. This increase could owe to the conversion of $^{13}CO_2$ to ^{13}CO under the reaction conditions.

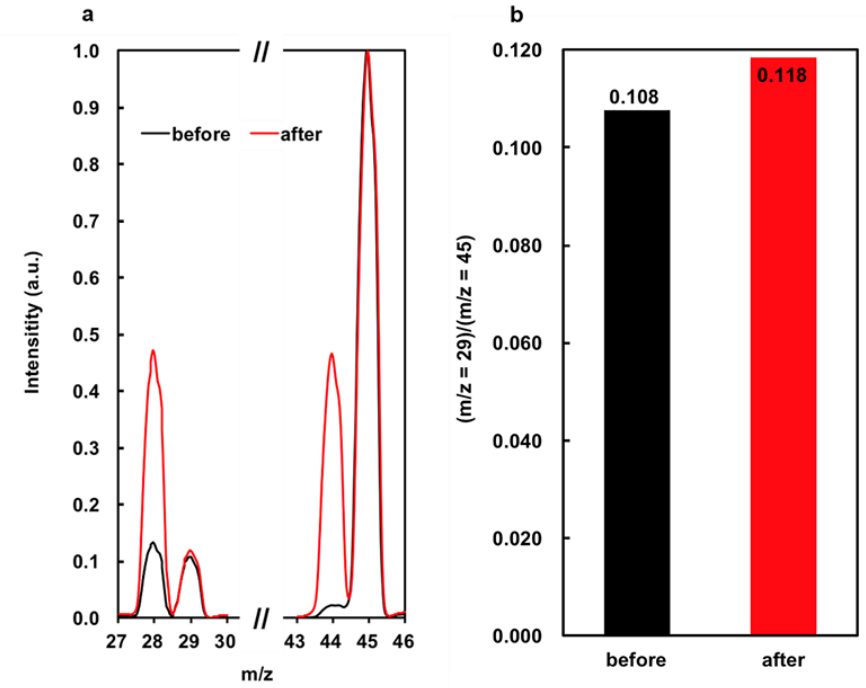

Figure 3-17 Isotopic $^{13}CO_2$ labeling experiments, (a) mass spectrum (normalized); (b) (m/z=29/(m/z=45) ratio, black = before and red = after photocatalytic reaction.

3.3 Discussion

It is well-known that the absorption of a photon corresponding to the fundamental absorption band of an oxide leads to the formation of electron and hole pairs, i.e., excitons, which undergo radiative decay[46]. For the Zn-O sites, this process is represented as

$$[Zn^{2+}\text{-}O^{2-}] \leftrightarrow [Zn^{+}\text{-}O^{-}].$$

This process corresponds to the band gap transition in zinc oxide with the energy of 3.2 eV. The photocatalytic activity of the supported metal oxides is therefore closely associated with the charge-transfer excited $[Zn^{+}\text{-}O^{-}]$ surface complex. This suggestion is also consistent with the uncovered dependence of the methane photo-oxidation rate on the irradiation wavelength. The reaction rate increases almost twenty times, when the catalyst has been

exposed to UV irradiation compared to the exposure to visible light. In the presence of the UV irradiation, the [Zn^{+}-O^{-}] complex would favor homolytic dissociation of methane molecules. Our experiments show that methane photo-oxidation occurs with participation of oxygen from the catalyst. Indeed, direct exposure of the oxidized catalysts to methane results in production of mainly CO, while the zinc is being reduced to metallic state. These reduced zinc particles can then easily re-oxidized and the catalyst regenerated.

Previously, participation of the oxygen from the catalyst lattice in the photo-oxidation of methylene blue was shown by Ali et al[26, 27] over deposited ZnO thin films. The Mars-van Krevelen type mechanism was also observed by Lee and Falconer[55] in photocatalytic decomposition of formic acid on TiO_2. Oxygen atoms for oxidation of formic acid were extracted from the TiO_2 lattice. The Mars–van Krevelen oxidation–reduction mechanism commonly operates for many reactions of selective and partial oxidation. In agreement with these previous reports, our results also indicate an important role of the Mars–van Krevelen mechanism in the reactions of methane partial photocatalytic oxidation, which target selective production of carbon monoxide instead of CO_2.

The concentration of zinc carbonate significantly decreases during the methane oxidation. The in situ FTIR data are indicative of the formation of the surface methoxy carbonate. The conducted experiments with DMC suggest that CO is a major product of decomposition of methoxy carbonates in the presence of light. The following reaction sequence (Figure 3-18) is proposed to interpret the obtained photocatalytic and spectroscopic data. The first stage of the reaction is methane dissociation over Zn-O pairs under irradiation followed by the formation of Zn-methyl species. The reaction of surface Zn-methyl species with carbonate results in surface methoxy carbonates. The surface methyl carbonates were identified by the C–O stretching bands at 1225 cm^{-1} in the carbonate ester and C–O and C–H stretching bands at 1048 and 2880 cm^{-1}, respectively, in methoxy fragments. At the same time, zinc is reduced to the metallic state. In agreement with the DMC adsorption experiments, decomposition of zinc methyl carbonate leads to carbon monoxide. The participation of zinc carbonates in the reaction is consistent with isotope tracing experiments. Indeed, addition of small amounts of $^{13}CO_2$ to the reacting medium results in the appearance

of ^{13}CO. This suggests that during methane partial photo-oxidation, CO is formed via decomposition of the surface species such as methyl carbonates produced from zinc carbonates.

Thus, the obtained results advocate in favor of the extremely important role of Zn–O pairs in the composite Zn-HPW/TiO_2 catalysts in methane photocatalytic oxidation to CO. These pairs are involved in the methane dissociation and formation of carbonate and methyl carbonate species. They can be associated either with highly dispersed ZnO clusters or with at least two Zn^{2+} ions in the cationic sites of HPW.

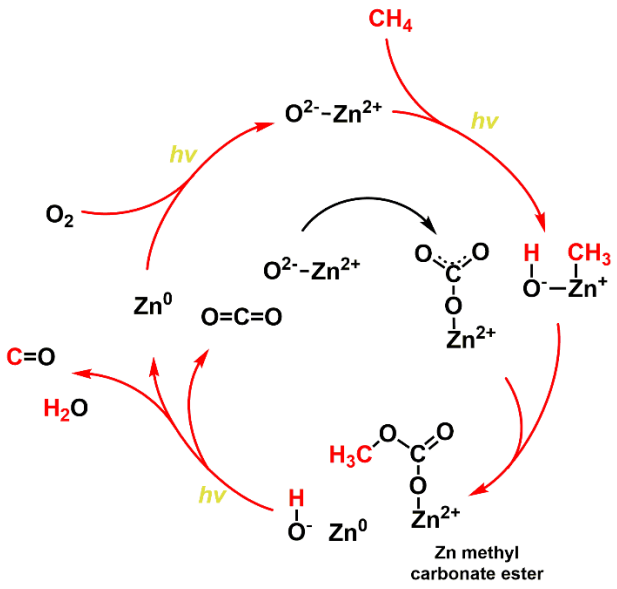

Figure 3-18 Reaction steps in methane photo-oxidation over Zn-HPW/TiO_2.

Carbon dioxide also observed in methane photo-oxidation can be produced either directly from methane or though methane consecutive oxidation to CO and then to CO_2 (Figure 3-9). On TiO_2 and HPW, a significant fraction of CO_2 is probably produced via direct methane oxidation, while over Zn-HPW/TiO_2, CO_2 seems to primarily occur via CO secondary oxidation. CO_2 is mostly produced as a secondary product of methane photo-oxidation over the zinc-containing catalysts. The mechanism of the CO total oxidation to CO_2 over TiO_2 has been investigated in several previous reports[56, 57, 58]. Linsebigler et al.[57, 58] have reported that the reaction proceeds over on vacancy defect sites on the TiO_2 surface

and involves O_2^- surface species.

3.4 Conclusion

To summarize, among metal-tungstophosphoric composite catalysts supported on titania, the zinc counterpart exhibits remarkable activity in methane photocatalytic oxidation at ambient temperature with extremely high selectivity to carbon monoxide. In the composite catalysts, tungstophosphoric acid constitutes a thin layer of 1-2 nm over titanium oxide, while zinc species are highly dispersed on the tungstophosphoric layer.

The methane photocatalytic oxidation proceeds as a combination of parallel and consecutive reactions with carbon monoxide being a primary reaction product. The carbon monoxide yield can reach 3-4 % with high QE (7.1% at 362 nm) values. The reaction is consistent with the Mars-Van Krevelen type sequence and involves formation of the surface methoxy-carbonates as intermediates and zinc oxidation-reduction cycling.

3.5 Reference

1. Nisbet, E. G., Dlugokencky, E. J. & Bousquent, P. Methane on the rise-again. *Science* **343**, 493-495 (2014).

2. Arakawa, H., Aresta, M., Armor, J.N., Barteau, M.A., Beckman, E.J., Bell, A.T., et al. Catalysis research of relevance to carbon management: progress, challenges, and opportunities. *Chem. Rev.* **101**, 953-996 (2001).

3. Gesser, H.D., Hunter, N.R., Prakash, C.B., The direct conversion of methane to methanol by controlled oxidation. *Chem. Rev*. **85**, 235-244 (1985).

4. Cargnello, M., Jaén, J.D., Garrido, J.H., Bakhmutsky, K., Montini, T., Gámez, J.C., et al. Exceptional activity for methane combustion over modular Pd@CeO_2 subunits on functionalized Al_2O_3. *Science* **337,** 713-717 (2012).

5. Gélin, P., Primet, M., Complete oxidation of methane at low temperature over noble metal based catalysts: a review. *Appl. Catal. B* **39**, 1-37 (2002).

6. Xie, S., Zhang, Q., Liu, G. & Wang, Y. Photocatalytic and photoelectrocatalytic reduction of CO_2 using heterogeneous catalysts with controlled nanostructures. *Chem. Commun.* **52**, 35–59 (2016).

7. Li, L. et al. Efficient sunlight-driven dehydrogenative coupling of methane to ethane over a Zn^+-modified zeolite. *Angew. Chem.* **123**, 8449–8453 (2011).

8. Shimura, K., Yoshida, T., Yoshida, H. Photocatalytic activation of water and methane over modified gallium oxide for hydrogen production. *J. Phys. Chem. C* **114**, 11466-11474 (2010).

9. Chen, X. et al. Photocatalytic oxidation of methane over silver decorated zinc oxide nanocatalysts. *Nat. Commun.* **7**, 12273 (2016).

10. Ward, M. D., Brazdil, J. F., Mehandru, S. & Anderson, A. B. Methane photoactivation on copper molybdate: an experimental and theoretical study. *J. Phys. Chem.* **91**, 6515–6521 (1987).

11. Wada, K., Yoshida, K., Takatani, T. & Watanabe, Y. Selective photo-oxidation of light alkanes using solid metal oxide semiconductors. *Appl. Catal. A* **99**, 21–36 (1993).

12. Shimura, K. et al. Photocatalytic steam reforming of methane over sodium tantalate. *J. Phys. Chem. C* **114**, 3493–3503 (2010).

13. Yuliati, L, Yoshida, H. Photocatalytic conversion of methane. *Chem. Soc. Rev*. **37**, 1592-1602

(2008).

14. Kaliaguine, S., Shelimov, B. & Kazansky, V. Reactions of methane and ethane with hole centers O−. *J. Catal.* **55**, 384–393 (1978).

15. In, S.-I. et al. Photocatalytic methane decomposition over vertically aligned transparent TiO2 nanotube arrays. *Chem. Commun.* **47**, 2613–2615 (2011).

16. Tavasoli, A. and Ozin, G., Green Syngas by Solar Dry Reforming, *Joule* **2,** 571-575 (2018).

17. Shimura, K., Yoshida, H. Semiconductor Photocatalysts for Non-oxidative Coupling, Dry Reforming and Steam Reforming of Methane, *Catal Surv Asia* **18**:24–33 (2014)

18. Pan, F., Xiang, X., Deng, W., Zhao, H., Feng, X. and Li, Y., A Novel Photo-thermochemical Approach for Enhanced Carbon Dioxide Reforming of Methane *ChemCatChem*, **10**, 940 – 945 (2018)

19. Chung, W.-C., Lee, Y.-E., Chang, M.-B. Syngas production via plasma photocatalytic reforming of methane with carbon dioxide, *Int. J. Hydrogen Energy* (2018), https://doi.org/10.1016/j.ijhydene.2018.01.156

20. Gondal, M.A., Hameed, A., Yamani, Z.H., Arfaj, A. Photocatalytic transformation of methane into methanol under UV laser irradiation over WO_3, TiO_2 and NiO catalysts. *Chem. Phys. Letts.* **392**, 372–377 (2004).

21. Murcia-Lopez, S., Bacariza M. C., Villa, K Lopes, J. M., Henriques C., Morante J. R. and Andreu, T. Controlled photocatalytic oxidation of methane to methanol through surface modification of Beta zeolites, *ACS Catal.* **7**, 2878−2885 (2017).

22. Murcia-Lopez, S., Villa, K., Andreu, T. and Morante, J. R. Partial oxidation of methane to methanol using bismuth-based photocatalysts, *ACS Catal.* **4**, 3013−3019 (2014).

23. Villa, K., Murcia-Lopez, S., Morante, J. R., Andreu, T., Catalonia. An insight on the role of La in mesoporous WO_3 for the photocatalytic conversion of methane into methanol. *Appl. Catal. B* **187**, 30–36 (2016).

24. Bae, K.-L., Kim, J., Lim, C. K., Nam, K. M. & Song, H. Colloidal zinc oxide-copper (I) oxide nanocatalysts for selective aqueous photocatalytic carbon dioxide conversion into methane. *Nat. Commun.* **8**, 1156 (2017).

25. Mars, P., Van Krevelen, D.W. Oxidations carried out by means of vanadium oxide catalysts. Chem. Eng. Sci. **3**, 41-59 (1954).

26. Ali, A.M., Emanuelsson, E.A., Patterson, D.A. Photocatalysis with nanostructured zinc oxide thin films: The relationship between morphology and photocatalytic activity under oxygen limited and oxygen rich conditions and evidence for a Mars Van Krevelen mechanism. *Appl. Catal. B* **97**, 168-181 (2010).

27. Ali, A.M., Emanuelsson, E.A., Patterson, D.A. Conventional versus lattice photocatalysed reactions: Implications of the lattice oxygen participation in the liquid phase photocatalytic oxidation with nanostructured ZnO thin films on reaction products and mechanism at both 254 nm and 340 nm. *Appl. Catal. B* **106**, 323-336 (2011).

28. Marcì, G., Lopez, E. I. G., Palmisano, L. Heteropolyacid-Based Materials as Heterogeneous Photocatalysts, *Eur. J. Inorg. Chem.* **1,** 21-35 (2014).

29. Zhang, J., Sun, L., Liao, C., Yan, C. A simple route towards tubular ZnO. *Chem. Commun.* 262-263 (2002).

30. Busca, G. and Lorenzelli, V. Infrared spectroscopic identification of species arising from reactive adsorption of carbon oxides on metal oxide surfaces. *Mater. Chem.* **7**, 89–126 (1982).

31. Tao, M., Xue, L., Sun, Z., Wang, S., Wang, X., Shi, J. Tailoring the synergistic Bronsted-Lewis acidic effects in heteropolyacid catalysts: applied in esterification and transesterification reactions. *Sci. Rep.* **5**, 13764 (2015).

32. Lindsay, R., Michelangeli, E., Daniels, B.G., Ashworth, T.V., Limb, A.J., Thornton, G., Gutiérrez-Sosa, A., Baraldi, A., Larciprete, R., Lizzit, S. Impact of defects on the surface chemistry of ZnO(000$\bar{1}$)−O, *J. Am. Chem. Soc.* **124**, 7117–7122 (2002).

33. Gancheva, M., Markova-Velichkova, M., Atanasova, G., Kovacheva, D., Uzunov, I., Cukeva R. Design and photocatalytic activity of nanosized zinc oxides. *Appl. Surf. Sci.* **368**, 258-266 (2016).

34. Bouibes, A., Zaoui, A., Tunega, D. Bonds, bands and elasticity of smithsonite rock, *Solid State Commun.***166**, 76–82 (2013).

35. Carp, O. Huisman, C.L. Reller A. Photoinduced reactivity of titanium dioxide. *Prog. Solid State Chem.* **32**, 33-177 (2004).

36. Blasko, T., Lopez Nieto, J.M. Oxidative dyhydrogenation of short chain alkanes on supported vanadium oxide catalysts. *Appl. Catal. A* **157**, 117-142 (1997).

37. Kung, H.H. Oxidative dehydrogenation of light (C2 to C4) alkanes, *Adv. Catal.* **40**, 1-38 (1994).

38. lbonetti, S., Cavani, F., Trifirò, F. Key aspects of catalyst design for the selective oxidation of paraffins. *Catal. Rev. Sci. Eng.* **38**, 413-438 (1996).

39. Khodakov, A., Olthof, B., Bell, A.T., Iglesia, E. Structure and catalytic properties of supported vanadium oxides: support effects on oxidative dehydrogenation reactions. *J. Catal.* **181,** 205-216 (1999).

40. Wöll, C. The chemistry and physics of zinc oxide surfaces *Prog. Surf. Sci.* **82**, 55-120 (2007).

41. Biesinger, M.C., Laua, L.W.M., Gerson, A.R., Smart, R.S.C., Resolving surface chemical states in XPS analysis of first row transition metals, oxides and hydroxides: Sc, Ti, V, Cu and Zn, *Appl. Surf. Sci*. **257,** 887-898 (2010)

42. Gao, Y., Traeger, F., Shekhah, O., Idriss, H., Wöll, C. Probing the interaction of the amino acid alanine with the surface of ZnO ($10\bar{1}0$). *J. Cool. Interf. Sci.* **338**, 16-21 (2009).

43. Kuld, S., Conradsen, C., Moses, P.G., Chorkendorff, I., Sehested, J. Quantification of zinc atoms in a surface alloy on copper in an industrial type methanol synthesis catalyst. *Angew. Chem*. **126**, 6051-6055 (2014).

44. Kuld, S., Thorhauge, M., Falsig, H., Elkjær. C.F., Helveg, S, Chorkendorff, I., et al. Quantifying the promotion of Cu catalysts by ZnO for methanol synthesis. *Science* **352**, 969-974 (2016).

45. Bordiga, S., Lamberti, C., Bonino, F., Travert, A., Thibault-Starzyk, F.Probing zeolites by vibrational spectroscopies. *Chem. Soc. Rev*. **44**, 7262-7341 (2015).

46. Evans, J.V., Whateley, T.L. Infrared study of adsorption of carbon dioxide and water on magnesium oxide, *Trans. Faraday Society* **63**, 2769-2777 (1967).

47. Jung, K. T., Bell, A.T. An in situ infrared study of dimethyl carbonate synthesis from carbon dioxide and methanol over zirconia, *J. Catal.,* **204**, 339–347 (2001).

48. Gruver, V. and Fripiat, J. J. Lewis acid sites and surface aluminum in aluminas and mordenites: an infrared study of CO chemisorption, *J. Phys. Chem.* **98**, 8549–8554 (1994).

49. Ballinger, T.H., Yates, J.T. IR Spectroscopic detection of lewis acid sites on Al_2O_3 using adsorbed co. correlation with Al-OH group removal. *Langmuir* **7,** 3041-3045 (1991).

50. Barbosa, L.A.M.M., Zhidomirov, G.M., Van Santen, R.A. Theoretical study of methane adsorption on Zn(II) zeolites. *Phys. Chem. Chem. Phys*. **2**, 3909-3918 (2000).

51. Kazansky, V.B., Serykh, A.I., Pidko, E.A. DRIFT study of molecular and dissociative adsorption

of light paraffins by HZSM-5 zeolite modified with zinc ions: Methane adsorption. *J. Catal.* **225**, 369-373 (2004).

52. Kolyagin, Y.G., Ivanova, I.I., Ordomsky, V.V., Gedeon, A., Pirogov, Y.A. Methane activation over Zn-modified MFI zeolite: NMR evidence for Zn-methyl surface species formation. *J. Phys. Chem. C*, **112**, 20065-20069 (2008).

53. Arzumanov, S.S., Gabrienko, A.A., Freude, D., Stepanov, A.G. Competitive pathways of methane activation on Zn^{2+}-modified ZSM-5 zeolite: H/D hydrogen exchange with Brønsted acid sites: Versus dissociative adsorption to form Zn-methyl species, *Catal. Sci. and Techn.* **6**, 6381-6388 (2016).

54. Anpo, M. and Kubokawa y; Photoluminescence of Zinc Oxide Powder as a Probe of Electron-Hole Surface Processes *J. Phys. Chem.* **88**, 5556-5560 (1984).

55. Lee, G.D., Falconer, J.L. Transient measurements of lattice oxygen in photocatalytic decomposition of formic acid on TiO_2, *Catal. Letts*. **70**, 145–148 (2000).

56. Dai, W., Chen, X., Zheng, X., Ding, Z., Wang, X., Liu, P., and Fu, X. Photocatalytic Oxidation of CO on TiO_2: Chemisorption of O_2, CO, and H_2, *ChemPhysChem* **10**, 411 – 419 (2009).

57. Linsebigler, A., Rusu, C., Yates, J.T. Jr., Absence of Platinum Enhancement of a Photoreaction on TiO_2-CO Photooxidation on Pt/TiO_2(110) *J. Am. Chem. Soc.* **118**, 5284– 5289 (1996).

58. Lu, G.Q., Linsebigler, A., Yates, J.T. Jr., The photochemical identification of two chemisorption states for molecular oxygen on TiO_2(110) *J. Chem. Phys.* **102**, 3005– 3008 (1995).

Chapter 4. Selective Photochemical Synthesis of Ethane from Methane at Ambient Temperature over Silver-Heteropolyacid-Titania Nanocomposites

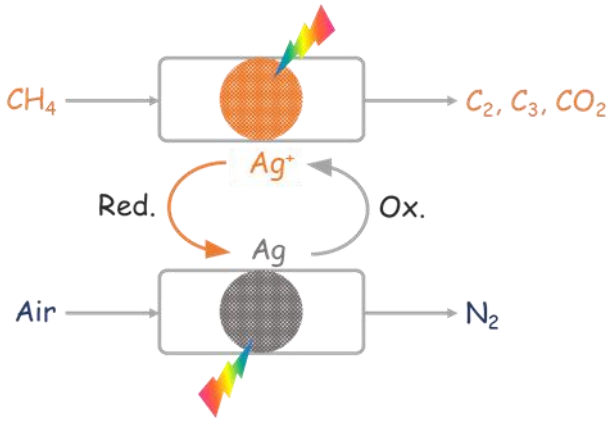

Abstract

Methane activation and utilization are among the major challenges of modern chemistry. Herein, we uncovered a highly selective (>90%) quantitative photochemical conversion of methane to ethane at ambient temperature over silver-heteropolyacid-titania nanocomposites. The strategy for methane unitization developed in this work makes use of photosensitivity of silver salts utilized in the analog photography. The ethane photochemical synthesis from methane involves stoichiometric reaction of methane under irradiation with silver cationic species highly dispersed over heteropolyacid layer over titania resulting in the formation of methyl radicals. Recombination of the generated CH_3 radicals leads to the selective and almost quantitative formation of ethane. Silver cationic species are simultaneously reduced to metallic silver. Small amounts of propane are also produced. The silver-heteropolyacid-titania nanocomposites can be regenerated in the presence of light at the ambient temperature. The ethane yield from methane reaches 9 % on the optimized materials. High selectivity, significant yield of ethane combined with high quantum efficiency, excellent stability and simple regeneration of the silver-heteropolyacid-titania nanocomposites are major advantages of ethane quantitative synthesis from methane using the photochemical looping.

4.1 Introduction

Methane is the main component of natural, shale gas, methane clathrates and biogas. Methane emission is a major source of the global warming and greenhouse effect. Although methane is the most promising alternative to crude oil as a greener and less expensive carbon feedstock for the chemical industry[1, 2], about 90% of methane currently is burnt in various combustion processes, releasing carbon dioxide into the atmosphere[3, 4, 5, 6, 7]. Methane is a highly stable molecule. It has no functional groups and a very high C-H bond enthalpy (439 kJ mol^{-1}). Methane is inert relative to the acid attack and it has very low proton affinity (544 kJ mol^{-1}) and acidity (pK_a=40). Direct chemical conversion of methane to value-added chemicals and fuels remains, therefore, a formidable challenge for modern science[8, 9, 10].

Commercial technologies of methane utilization other than combustion, are rather limited. They involve methane steam reforming, partial oxidation, autothermal reforming or Andrussow reaction[11, 12, 13]. Numerous attempts to elaborate new routes for methane conversion have described in the literature[14, 15, 16, 17]. The most portrayed non-commercial routes for methane conversion can be divided into oxidative and non-oxidative ones. The non-oxidative routes such as methane aromatization result in significant carbon deposition, while the oxidative routes such as methane thermocatalytic coupling and methane partial oxidation usually suffer from insufficient selectivity and coincide with major production of CO_2. Most of the known methane conversion reactions require very high temperatures (>800°C). All these thermochemical processes are typically accompanied by major CO_2 emissions arising from combustion of fossil fuels used to maintain the reactor at high temperatures[18, 19, 20 ,21, 22, 23].

Photocatalytic non-oxidative coupling of methane with very low quantum efficiencies was discovered in the 1980s over Mg and Ce species highly dispersed on silica-alumina[24, 25, 26]. More recently, Chen et al. reported C-H activation of methane over the Zn^{2+}/ZSM-5 and Ga^{3+}/EST-10 photocatalysts. The photocatalytic activity was attributed to the presence of the extraframework zinc cations and Ti-OH groups on titanate wires[27, 28]. Long et al. observed the photocatalytic non-oxidative coupling of methane from the surface plasmon effect of

Au[29]. Very recently, Zhang[30] et al. investigated the photo-driven non-oxidative coupling of methane over Ga and Pt photocatalysts supported on TiO_2-SiO_2. Note that very low quantum efficiency and low yield were observed over all these systems. The major challenges of methane coupling in both thermocatalytic and photocatalytic routes are insufficient selectivities and yields of ethane or ethylene, large production of CO_2 and poor catalyst stability.

In this work, we uncovered highly selective and quantitative methane conversion into ethane occurring at ambient temperature under the UV irradiation over the silver-heteropolyacid–titania nanocomposites through a photochemical looping approach. Our strategy for methane selective coupling to ethane is based on the photosensitivity of silver salts, which have been used for many decades in the analog photography. Silver species in the nanocomposites react stoichiometrically with methane under UV irradiation and generate methyl radicals. Ethane is then produced from the recombination of methyl radicals. Silver oxidized species are simultaneously reduced to small metallic silver clusters. Following the methane coupling, the nanocomposites can be reversibly regenerated in air under irradiation at ambient temperature. The ethane selectivity from methane reaches 90%. The ethane yield of 9.2% from methane has been obtained under the optimized conditions in a batch reactor. High selectivity, significant yield of C_2H_6 at ambient temperature, high quantum efficiency (QE = 3.5% at 362 nm) and excellent stability in the photochemical looping make direct ethane synthesis via methane selective coupling over silver-heteropolyacid-titania nanocomposites potentially interesting for practical applications.

4.2 Result and discussion

4.2.1 Photochemical coupling of methane over the metal HPW-TiO_2 nanocomposites

First, we investigated photochemical conversion of methane over TiO_2, HPW, HPW/TiO_2 composites containing different metals in a batch photoreactor. No methane conversion to any products was observed in the absence of light on all the solids. CO_2 was detected as the only reaction product after exposure of TiO_2, HPW and HPW/TiO_2

composites to methane at ambient temperature using the 400 W Xe lamp illumination (Figure 4-1). This suggests complete photooxidation of methane to CO_2 occurring under these conditions over TiO_2, HPW and their mixtures. Previously, complete photo-oxidation of methane to CO_2 has been observed on TiO_2 and other semiconductors[31, 32]. Note that the gaseous phase in the reactor contained only methane, no oxygen or other gases were present. This suggests that oxygen for methane oxidation to CO_2 is probably provided by the solids (TiO_2, HPW, etc) present in the reactor.

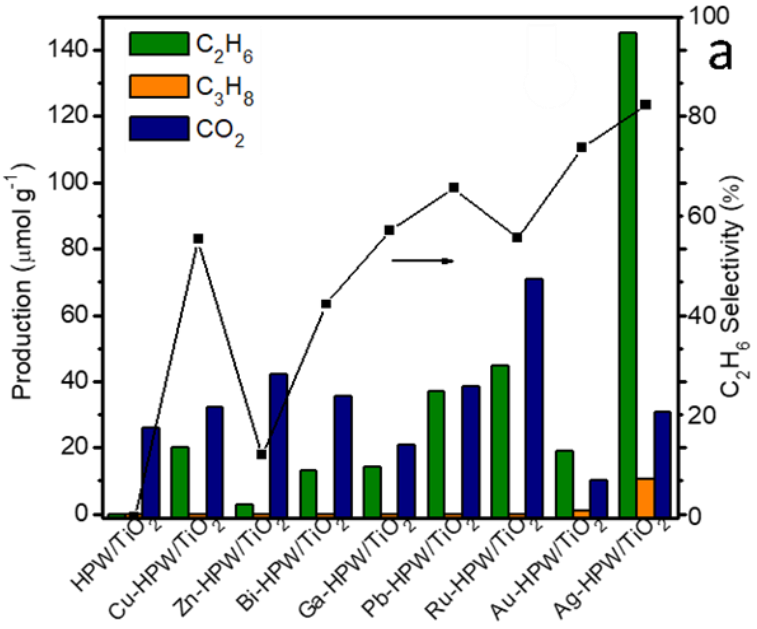

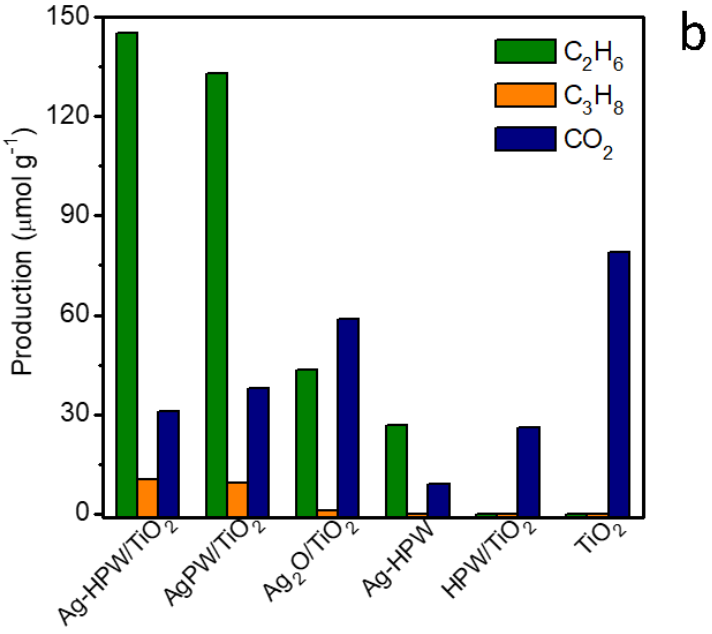

Figure 4-1 Production of ethane, propane and carbon dioxide and ethane selectivity during photocatalytic oxidation coupling of methane on different materials: (a) Metal-HPW/TiO_2 composite, (b) TiO_2, HPW, and Ag containing samples.

Interestingly, methane conversion over metal containing HPW/TiO_2 composites yields both C_2H_6 and CO_2 (Figure 4-1a). Trace amounts of CO were also observed, while no hydrogen or oxygen were detected. Lower methane coupling conversion was observed over the solids containing transition metals. Addition of noble metals (Ag, Au, Ru,) to HPW/TiO_2 strongly increases the rate of methane coupling. Higher selectivity to ethane was observed on the Au and Ag based nanocomposites. Besides ethane, small amounts of propane were detected. Remarkably, compared to the Au-based counterpart, Ag-HPW/TiO_2 demonstrated both a higher ethane selectivity and a very high methane conversion rate. The overall selectivity of methane coupling to ethane and propane is greater than 90% on the Ag-HPW/TiO_2 system.

Apart from the analysis by GC, the composition of the gaseous phase during the methane conversion on Ag-HPW/TiO_2 was followed by FTIR using an *in-situ* cell filled with methane. The FTIR spectra are shown in Figure 4-2. FTIR clearly shows the presence of methane in the FTIR cell at the initial periods of the reaction (CH rotation- stretching and

rotation-bending bands at around 3020 cm^{-1} and 1300 cm^{-1}, respectively). Gaseous carbon dioxide and water were identified in the cell at longer reaction times by rotation- stretching bands at 2350 cm^{-1} of carbon dioxide and by OH rotation-stretching and rotation-bending bands of water at around 3200 cm^{-1} and 1700 cm^{-1} respectively. Interestingly, the intensity of the H_2O IR bands noticeable increases with the reaction time. This suggests that water can be one of the products of methane coupling to ethane and methane oxidation to CO_2 over the Ag-HPW/TiO_2 nanocomposites. Among the studied materials, Ag-HPW/TiO_2 has the highest potential for selective photochemical coupling of methane to higher hydrocarbons.

After the exposure to methane in the presence of light, the Ag-HPW/TiO_2 sample becomes black. This could indicate photochemical decomposition of the silver species in the nanocomposite and appearance of the silver metallic phase, which can occur in the presence of methane. This also suggests that some of methane conversion reactions could involve oxygen of the Ag-HPW/TiO_2 nanocomposites. The evolution of the Ag chemical state during the photochemical reaction is detailed below in the manuscript.

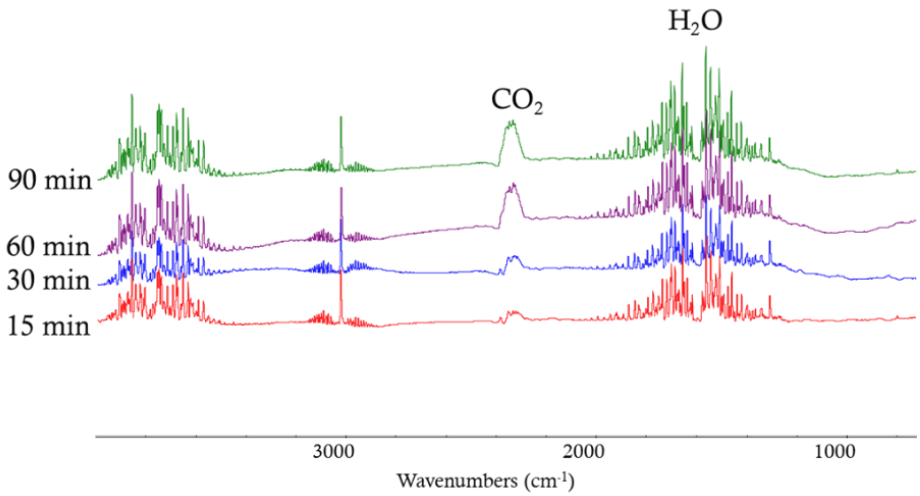

Figure 4-2 FTIR spectra of gaseous phase during photochemical coupling of methane over Ag-HPW/TiO_2 as a function of reaction time.

In order to enhance the production of ethane and propane, an attempt was made to optimize the chemical composition of Ag-HPW/TiO_2. Figure 4-3 displays methane photochemical conversion on Ag-HPW/TiO_2 with different Ag contents. No methane

coupling occurs in the absence of silver. Addition of even small amounts of silver to HPW/TiO_2 results in a major increase in the rate of methane coupling. Thus, silver species seem to be essential for ethane synthesis from methane. The highest rate of methane coupling was observed at the Ag content of 6.0 wt. %, while the coupling rate somehow decreases at higher Ag loadings. Note that the rate of methane oxidation to CO_2 also slightly increases with the increase in silver content.

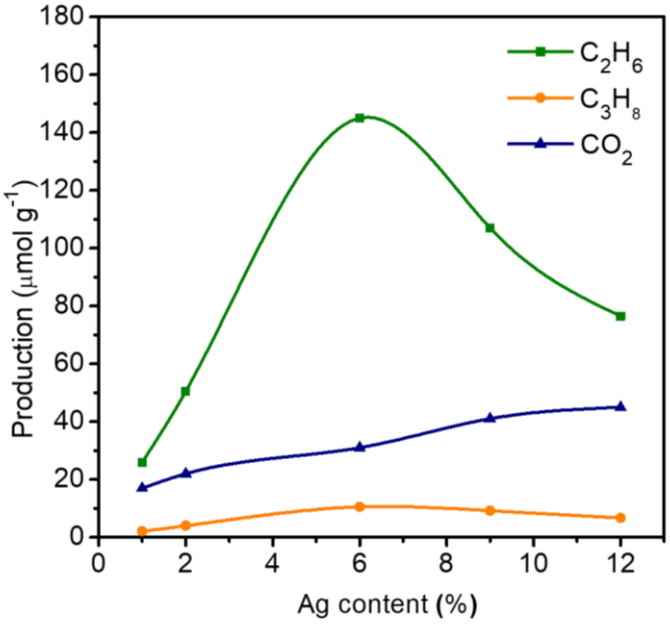

Figure 4-3 Products over Ag-HPW/TiO_2 with different Ag loadings.

Another parameter, which may affect the methane conversion, is the HPW/TiO_2 ratio in the nanocomposite. Figure 4-4 shows the performance of Ag-HPW/TiO_2 with different ratio of HPW to TiO_2, while the sliver content was maintained at 6 wt. %. The optimized performance was obtained at HPW/TiO_2 ratio of 0.6, while the methane coupling rate decreases at higher HPW/TiO_2 ratio. One of the reasons of the decrease in methane coupling rate could be the decline of the specific surface area measured by BET at high content of heteropolyacid (Table 4-1).

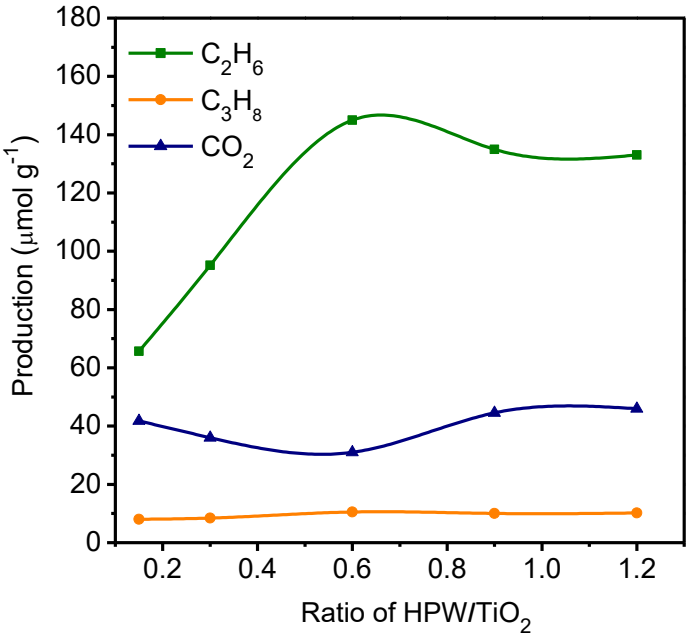

Figure 4-4 Products over Ag-HPW/TiO_2 with different ratio of HPW/TiO_2.

Table 4-1 BET specific surface area measured for the Ag-HPW/TiO_2 composites with different ratio of HPW/TiO_2.

Ag-HPW/TiO_2 (the ratio of HPW/TiO_2)	BET (m^2/g)
0.15	40
0.30	36
0.60	31
0.90	25
1.2	18

The role of silver and hetepolyacid species have been evaluated in photochemical conversion of methane using different supports, such as TiO_2, SiO_2, g-C_3N_4 and $BiVO_4$ (Figure 4-5). The methane conversion is very low on the $BiVO_4$ and g-C_3N_4 supported systems, while their silica supported counterpart produces significant quantities of carbon

dioxide. TiO_2 is therefore, the best performing nanocomposite support for methane photochemical conversion. Additionally, several heteropolyacids such as phosphotungstic acid, phosphomolybdic acid and silicotungstic acid, were used in the preparation of silver-hetepolyacid titania nanocomposites. The amounts of ethane, propane and carbon dioxide produced over these systems as a function of reaction time are shown in Figure 4-6. Interestingly, ethane and propane are produced with high selectivity only in the presence of phosphotungstic acid. The nanocomposites prepared using phosphomolybdic and silicotungstic acids display lower ethane and higher carbon dioxide selectivities.

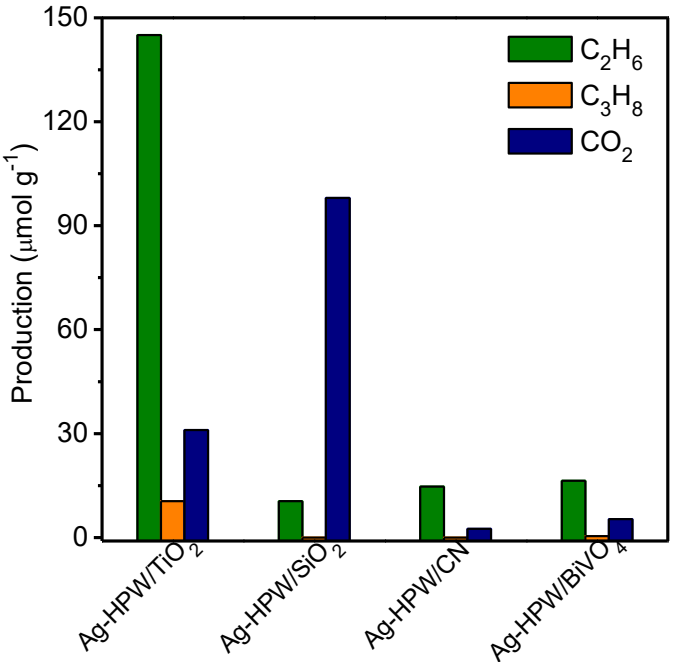

Figure 4-5 Methane conversion on silver-heteropolyacid on different semiconducting supports.

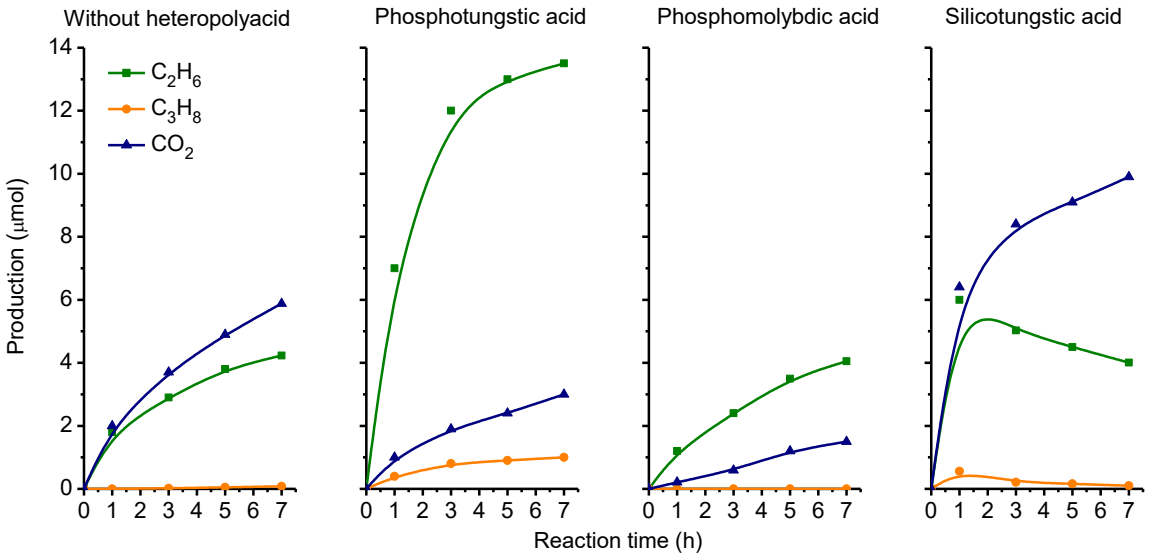

Figure 4-6 Photochemical conversion of methane on the Ag-HPW-TiO_2 nanocomposites prepared suing different heteropoly acids

Comparison of methane photochemical reaction data over the investigated solids suggests that a major increase in the C_2H_6 production from methane only occurs when the nanocomposite contains together TiO_2, phosphotungstic acid and Ag with specific ratios between these components. Phosphotungstic acid has been discovered earlier as highly efficient for transfer of holes and electrons from TiO_2. The photochemical performance of the HPW/TiO_2 nanocomposite can be enhanced by *p-n* semiconductor heterojunction, which created by adding to TiO_2 a semiconductor with lower levels of valence and conduction bands. The valence and conduction bands of phosphotungstic acid are located at a lower energy than that for TiO_2, which may result in higher electron flux from TiO_2 onto HPW[33, 34, 35, 36]. High selectivity of the Ag-HPW/TiO_2 nanocomposite in the methane conversion to ethane seems to be related to silver species. The most reactive silver species are obtained at the intermediate silver contents, ~5-6 wt.% (Figure 4-3). Interestingly, the Ag-HPW/TiO_2 nanocomposite and silver salt of heteropolyacid deposited on TiO_2 (AgPW/TiO_2*)* exhibit similar performance in methane coupling (Figure 4-1).

4.2.2 Characterization of the Ag-HPW/TiO_2 composites

A combination of techniques was used for extensive characterization of the Ag-HPW/TiO_2 samples, which have shown the best selectivity in photochemical methane coupling to ethane and propane. X-ray diffraction (XRD) patterns of the Ag-HPW/TiO_2, Ag/TiO_2, HPW/TiO_2, TiO_2 and HPW samples are shown in Figure 4-7. All the samples supported over TiO_2 (P25) exhibit intense XRD peaks of anatase and rutile phases, while the peaks assigned to the heteropolyacid are only observed in the XRD patterns of the pure HPW sample. Interestingly, no HPW diffraction peaks were detected in the Ag-HPW/TiO_2 nanocomposite. XRD peaks attributable to silver species were not observed either even at a relatively high silver content. This could be due to the high dispersion of HPW and smaller crystallite size of silver species. The TEM, STEM-HAADF and STEM-EDX elemental maps of the Ag-HPW/TiO_2 sample are shown in Figures 4-8 and 4-9. They identify irregular morphology of TiO_2 crystallites with the mean sizes of 30-40 nm. The STEM-EDX maps for tungsten indicate the formation of a thin layer of HPW (1-2 nm) embedding the TiO_2 crystals. Extremely small silver nanoparticles (probably as silver oxide species) with the mean diameter of 1.9 nm are uniformly dispersed on the surface of HPW/TiO_2. Silver oxide nanoparticles are located on the top of the HPW layer from the surface of TiO_2. Note that the Ag-HPW/TiO_2 sample can also contain isolated silver cations in the cationic sites of the heteropolyacid, which cannot be undoubtedly detected by TEM for this particular system.

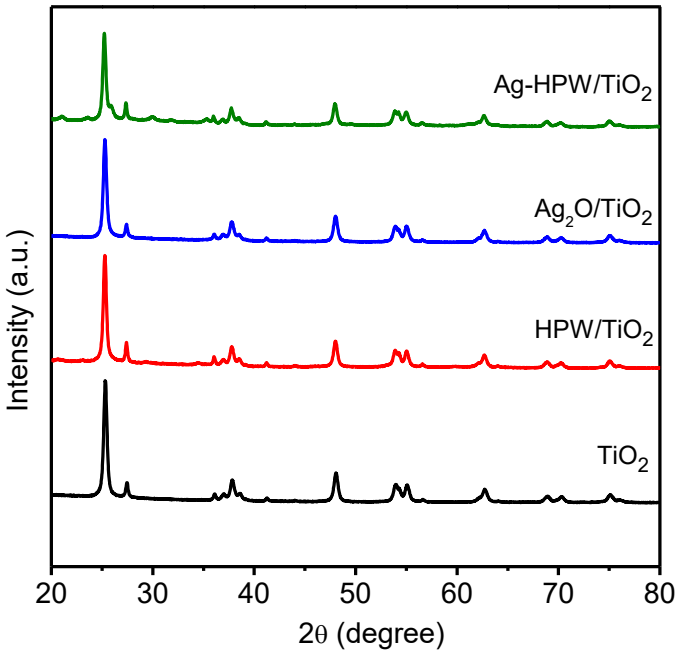

Figure 4-7 XRD patterns of different calcined nanocomposites.

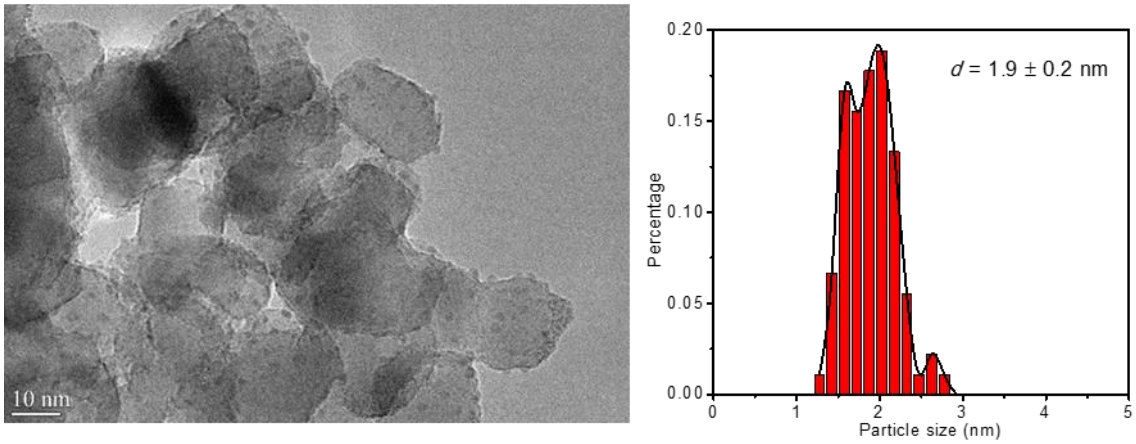

Figure 4-8 TEM images and Ag particle size distribution of Ag-HPW/TiO_2.

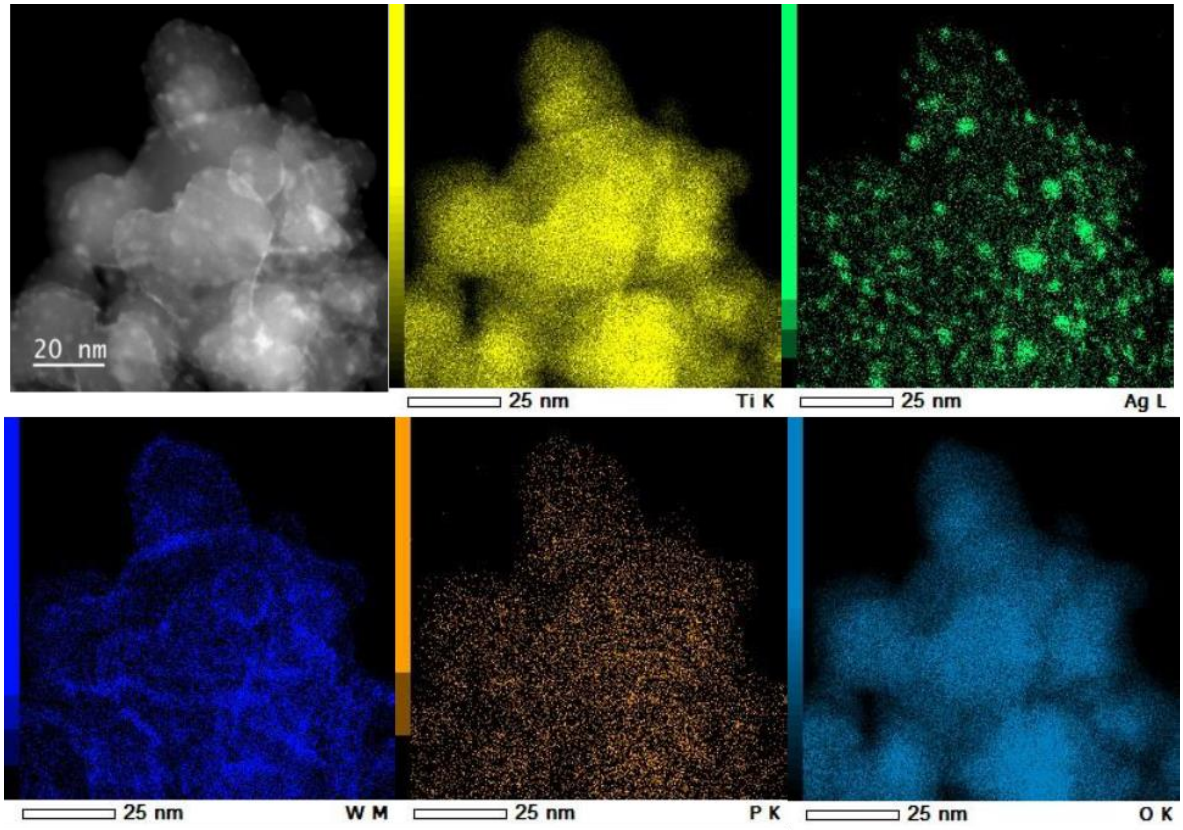

Figure 4-9 STEM-EDX images of fresh Ag-HPW/TiO_2 sample.

The TPR profiles of different based TiO_2 samples are shown in Figure 4-10. No noticeable TPR peaks were observed for TiO_2 up to temperature of 1000 K. This suggests that bulk reduction of TiO_2 does not occur under these conditions. The HPW/TiO_2 composites exhibit broad low intense peaks at 770 and 980 K. These peaks probably correspond to the reduction of the HPW heteropolyacid. The introduction of silver results in the occurrence of additional low temperature TPR peaks at 400 K, which could be attributed to the reduction of silver species. Interestingly, the position of silver reduction peaks does not depend on the support. They are observed at 400 K on both Ag/TiO_2 and Ag-HPW/TiO_2 samples. The calculated amount of hydrogen consumed in the low temperature TPR peak corresponds to 0.56 mmol of Ag. This suggests that all silver is reduced to the metallic state. The stoichiometry of silver reduction is given below:

$$2Ag^{+} + H_2 \rightarrow 2Ag^{0} + 2H^{+}$$

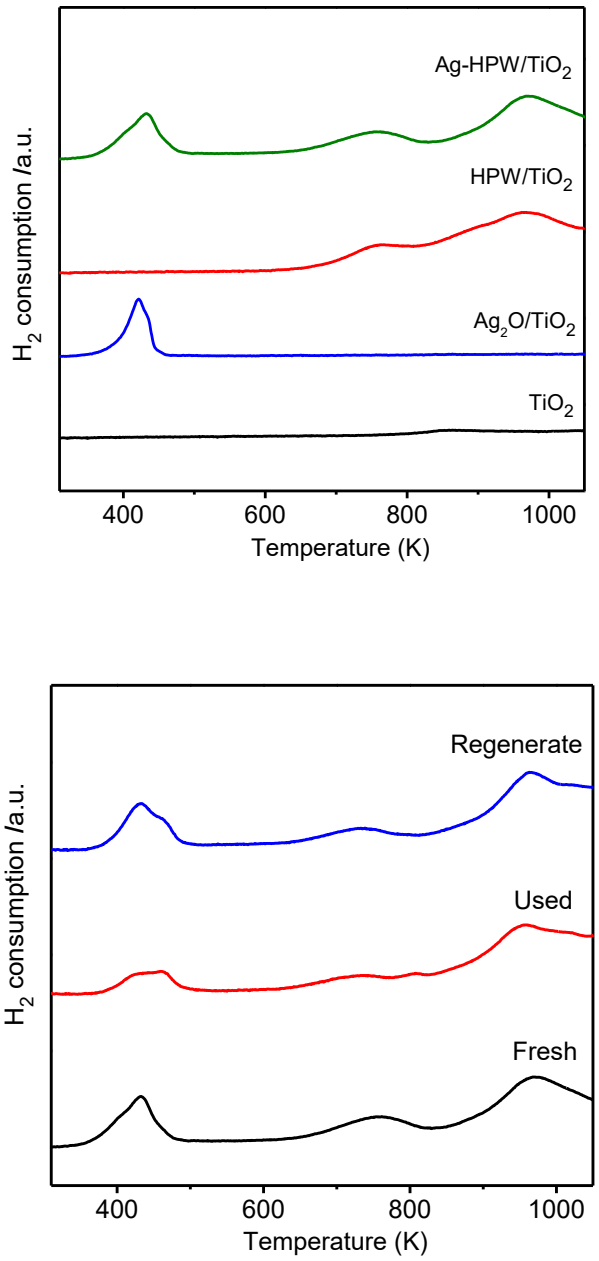

Figure 4-10 H_2-TPR profiles of TiO_2 based composites (a) and fresh, used and regenerated Ag-HPW/TiO_2.

The UV-Vis diffuse reflectance spectra of Ag-HPW/TiO_2 and reference compounds are displayed in Figure 4-11. The samples exhibit intense absorption in the ultraviolet region (< 400 nm). The band gap energy estimated using Tauc's plots varies from 2.9 eV to 3.2 eV[37, 38, 39]. Relatively small effect of the promotion with Ag is observed on the band gap. In order

to evaluate the influence of UV, visible and IR light, we conducted photochemical experiments on selected spectral ranges ($280 < \lambda < 400$ nm and $\lambda > 380$ nm, Table 4-2). The Ag-HPW/TiO_2 nanocomposite exhibits a very mild reaction rate in the methane coupling under visible irradiation, while the reaction rate increases 90 times, when the reactor is exposed to UV. This suggests that excitation of the band gap transfer in TiO_2 could be necessary for this photochemical process.

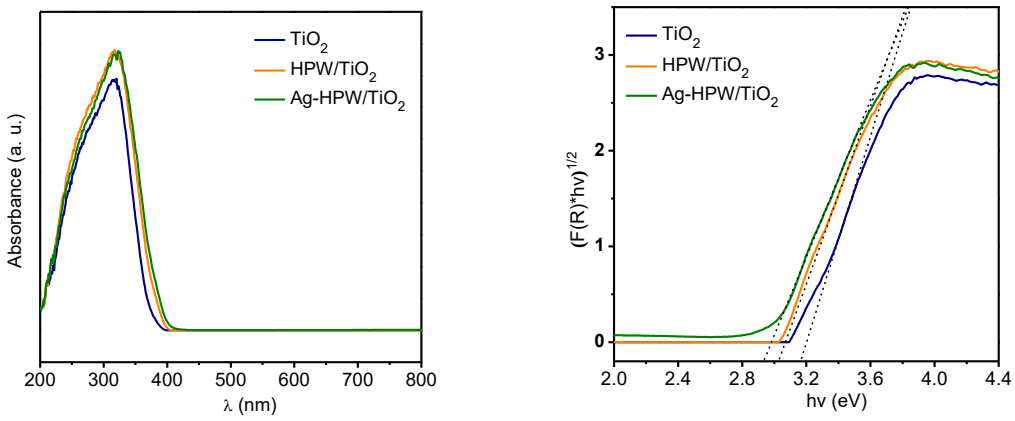

Figure 4-11 a. UV-Vis spectra of Ag-HPW/TiO_2 sample b. $[F(R\infty)h\nu]^{1/2}$ versus *hv* for Ag-HPW/TiO_2 sample.

Table 4-2 Rate of photochemical methane coupling measured under irradiation at different spectral ranges.

Spectral range of irradiation (nm)	Formation rate (μmol g^{-1} h^{-1})		Irradiance (mW cm^{-2})	Formation rate to power ratio (μmol g^{-1} h^{-1} mW^{-1} cm^2)
	C_2H_6	C_3H_8		
>382	0.7	0	94	0.0074
280-400	23	1.2	38	0.64

Reaction conditions: solid sample, 0.1 g; Gas phase pressure, CH_4 0.3 Mpa; irradiation time, 7h; light source, Hamamatsu LC8-06 Hg-Xe stabilized irradiation lamps with a spectral irradiance in the range 240-600; Cut-off filter: Vis-IR $\lambda > 382$ nm; UV light, $\lambda = 280$-400 nm.

4.2.3 Reaction pathways in photochemical coupling of methane to ethane and propane over Ag-HPW/TiO_2

In order to explore the molecular pathway of photochemical methane coupling, Ag-HPW/TiO_2 was exposed to methane, ethane or a mixture of methane and ethane under irradiation (Figure 4-12). Ethane and propane have been observed during the photochemical conversion of methane and small amounts of CO_2 have been produced. Interestingly, the exposure of Ag-HPW/TiO_2 to ethane under the Xe-lamp irradiation leads to some amounts of butane, whilst CO_2 becomes the main product of ethane photochemical conversion. When the reactor contained a mixture (95% methane, 5% ethane), ethane, propane and butane were produced under the Xe-lamp irradiation. This is indicative of simultaneous ethane self-coupling and ethane-methane cross-coupling over Ag-HPW/TiO_2, though the selectivity to higher hydrocarbons in the ethane coupling is much lower because of the competitive reactions of complete oxidation of the produced ethane and higher hydrocarbons. Interestingly, the addition of small amounts of hydroquinon results in a major decrease in the methane conversion over Ag-HPW/TiO_2. Hydroquinon is a well-known inhibitor of radical reactions[40]. Therefore, it can be suggested that the methane oxidative coupling proceeds via radical pathways (Figure 4-12). Indeed, selective formation of ethane in methane photo-oxidative coupling indicates that the CH_3 radicals can be intermediates of this reaction.

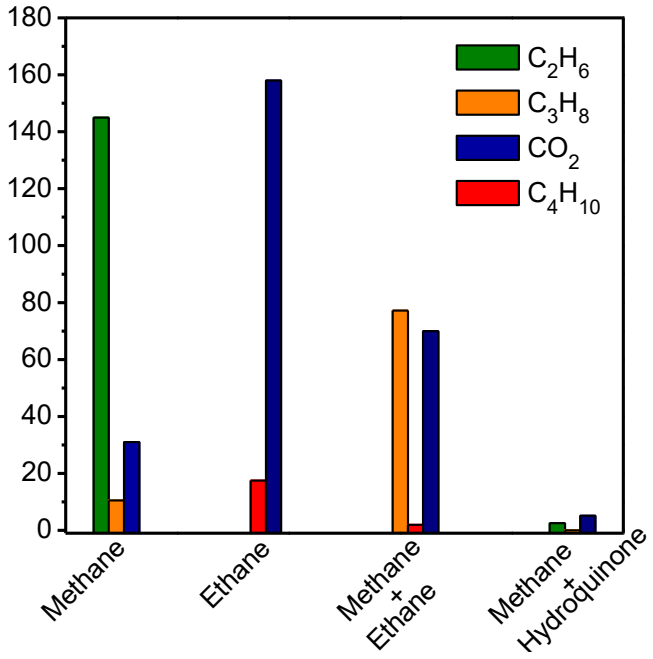

Figure 4-12 Photochemical coupling of methane and ethane on Ag-HPW/TiO_2.

The variation of ethane concentration during exposure of Ag-HPW/TiO_2 to light in the presence of methane is shown in Figure 4-13 and Figure 4-14. The ethane concentration increases sharply during the first 2 h of the reaction and reaches a plateau. In the experiments conducted with different amounts of Ag-HPW/TiO_2, the molar amount of produced ethane was always comparable with that of silver present in the reactor. During the reaction, the nanocomposite changes color, which is indicative of the formation of metallic silver species (Figure 4-13, inserts). At longer reaction time, the amounts of ethane and propane decrease, while the amount of CO_2 continuously increases. The selectivities to ethane, propane and CO_2 as a function of the reaction time are displayed in Figure 4-14b. Extrapolation to zero reaction time gives primary overall selectivity to ethane and propane higher than 90%. The ethane and propane selectivities decrease and CO_2 selectivity increases with the reaction time suggesting that some CO_2 can be produced by secondary oxidation of ethane and possibly, propane. Indeed, complete oxidation of ethane under the same conditions seems to proceed much more easily than that of methane (Figure 4-12)

After conducting the reaction for 7 h, the nanocomposite without any regeneration was

exposed again to methane under the Xe-lamp irradiation (Figure 4-13). The amount of ethane produced from methane was much lower than that in the first cycle, most probably because of the lower concentration of silver oxidized species and presence of metallic silver, which could be inactive in methane coupling.

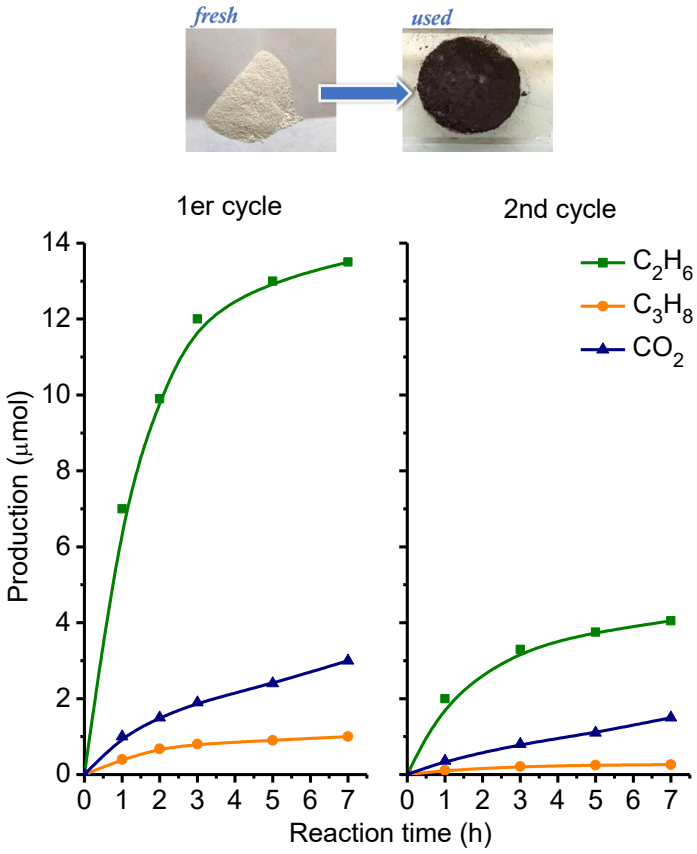

Figure 4-13 Recycle activity of photochemical coupling on Ag-HPW/TiO_2.

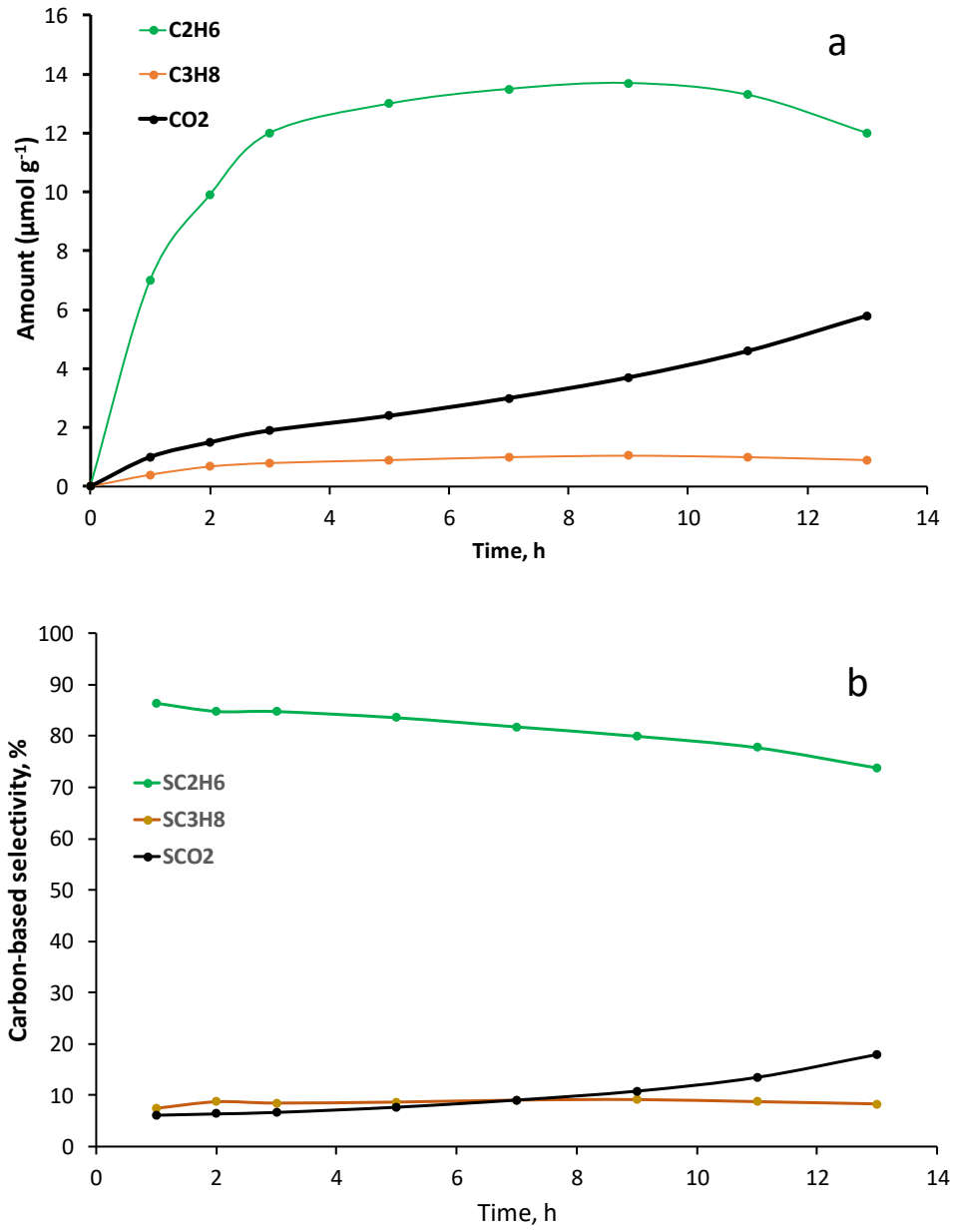

Figure 4-14 (a) Production of ethane, propane and carbon dioxide, and (b) selectivity on carbon basis as a function of the reaction time over Ag-HPW/TiO_2 nanocomposite.

To provide further insights into the variation of silver oxidation state during the reaction, both the freshly calcined Ag-HPW/TiO_2 nanocomposite and its "spent" counterpart after exposure to methane have been characterized by XRD and XPS. The nanocomposite exposure to methane under irradiation results in several new peaks in the XRD profile. These peaks at 2θ of 44.48°, 64.69° and 77.62° correspond to 200, 220, and 311 planes for silver,

respectively[41, 42]. When the solid material was regenerated in ambient air under 400 W Xe lamp for 2 h, the XRD peaks of metallic silver almost disappear (Figure 4-15). XPS characterization provided further insights into the silver oxidation state in the fresh and spent materials. The value of the Ag $3d_{5/2}$ binding energy does not allow discerning the silver oxidation state. The Ag $3d_{5/2}$ lines for metallic Ag and silver oxide are positioned at 368.2 eV and 367.8 eV, respectively[43]. Such a small difference in the binding energy is often beyond the resolution of the XPS spectrometers. The energy of Auger peaks $M_4N_{45}N_{45}$ (M_4VV) is known to be more sensitive to the oxidation state (Figure 4-16). It differs by more than 1 eV for Ag^+ vs. Ag^0 [44, 45, 46]. The positions of all Auger peaks were aligned by the C 1s peak, and a Shirley background was subtracted. In the Ag Auger spectrum of the Ag-HPW/TiO_2 material that was recorded after treatment in 0.3 MPa CH_4 under 400 W Xe lamp for 7h, the $M_4N_{45}N_{45}$ (M_4VV) peak shifts to lower binding energy by 1.9 eV. When the sample was regenerated, the peak returns to its initial position (Figure 4-15). The results obtained by XRD and Auger spectroscopy are indicative of reversible reduction and re-oxidation of highly dispersed silver species, which take place under the Xe-lamp irradiation, respectively in methane and air.

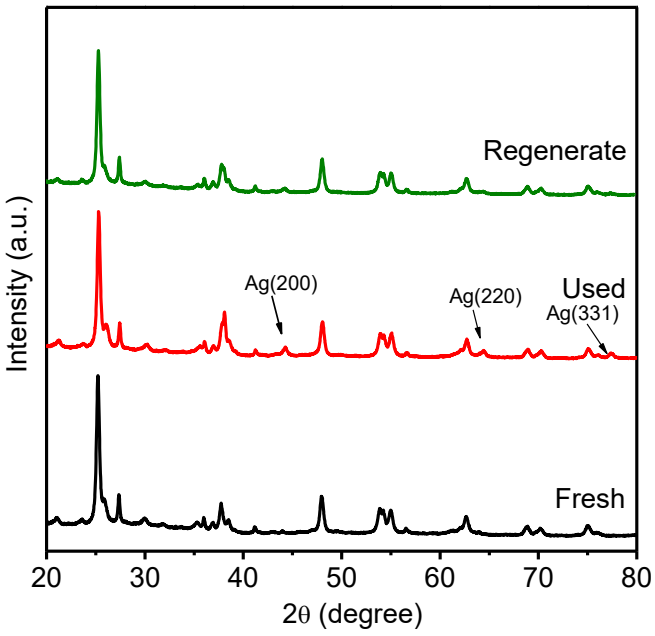

Figure 4-15 XRD spectra. fresh and used Ag-HPW-TiO_2 sample: treatment in 0.3 Mpa

CH_4 under 400 W Xe lamp for 7h, regenerate catalyst: regeneration in ambient air under 400 W Xe lamp for 2h.

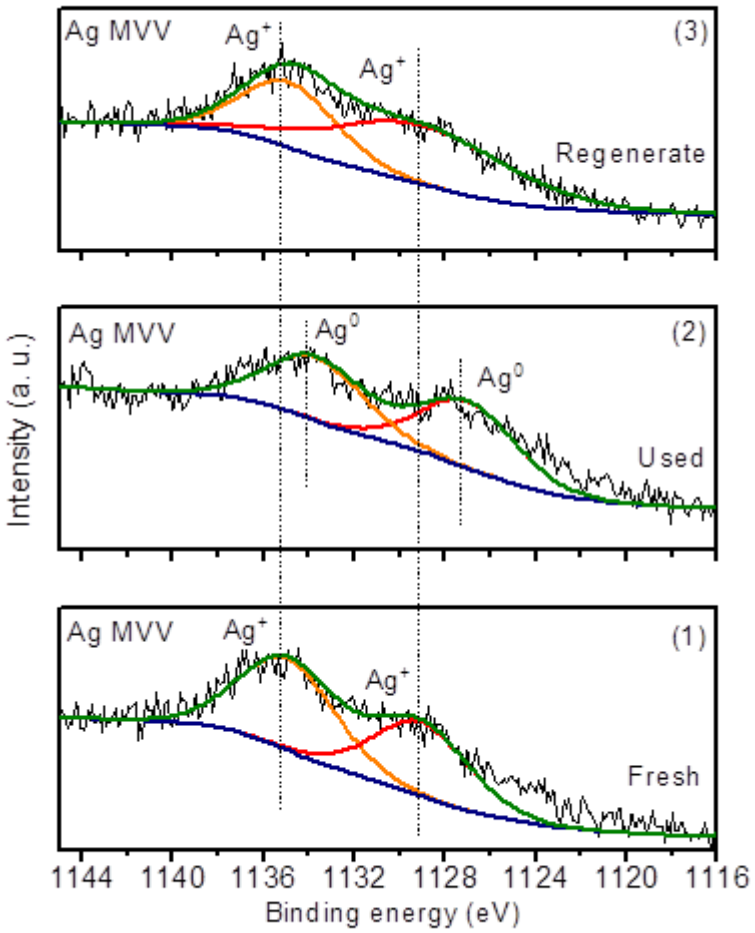

Figure 4-16 Ag M_4VV Auger spectra of Ag-HPW-TiO_2. (1). fresh sample, (2). treatment in 0.3 MPa CH_4 under 400 W Xe lamp for 7h, (3). regeneration in ambient air under 400 W Xe lamp for 2h.

The acidity of the Ag-HPW/TiO_2 nanocomposites during methane oxidative coupling was characterized by IR spectroscopy using Py adsorption. The IR spectra of the fresh oxidized Ag-HPW/TiO_2 show the FTIR bands of adsorbed Py at 1490 and 1450 cm^{-1}, which can be attributed to Py adsorption over the Lewis acid sites probably associated with unsaturated Ag^+ cations[47] (Figure 4-17). The exposure of Ag-HPW/TiO_2 to methane under irradiation results in appearance of the FTIR peak at 1540 cm^{-1}, which is assigned to Py

adsorbed over Bronsted acid sites. This suggest that silver atoms located in the cationic sites of Ag-HPW/TiO_2 are converted into metallic silver with generation of the Brønsted acid sites:

$$2Ag^{+} + CH_4 \rightarrow 2Ag^{0} + 2H^{+} + C_2H_6$$

The FTIR experiments suggest therefore, reversible photoreduction and reoxidation of isolated silver ions located in the cationic sites of HPW. These species seem to exhibit enhanced selectivity in methane coupling to ethane. Much lower ethane selectivity was observed in methane conversion over Ag/TiO_2 samples, which contains larger clusters of silver oxide. The participation of silver cations, located in HPW, in methane selective coupling to ethane is consistent with the results obtained for the silver salt of HPW deposited on TiO_2 (AgPW/TiO_2, Figure 4-1b), which was synthesized for this model experiment. The silver salt of HPW over TiO_2 shows a very high selectivity to ethane after its exposure to methane under the Xe-lamp irradiation. The experimental ratio of reacted methane to the silver amount in the nanocomposite calculated from Figure 4-3 is close to 0.6 at silver content up 6 wt. %. The suggestion about the role of isolated silver cations in the ethane production from methane is also consistent with the observed decrease in the rate of methane coupling at higher silver contents (Figure 4-3). Indeed, higher silver contents in the nanocomposites could result in the lower concentrations of isolate silver cations and an increase in the fraction of sliver oxide clusters, which are less selective in methane coupling.

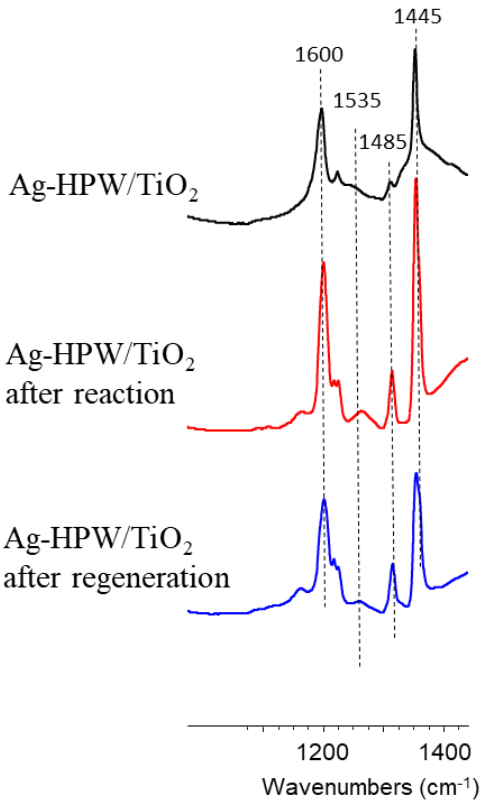

Figure 4-17 FTIR of Py adsorbed over fresh, spent and regenerated Ag-HPW/TiO_2.

4.2.3 Quantitative synthesis of ethane from methane via photochemical looping

The reaction tests and characterization suggest that stoichiometric reaction of methane with silver cationic species can selectively yield ethane. During the reaction, under irradiation silver cationic species are reduced to metallic silver, hence, the reaction eventually stops. In order to conduct ethane synthesis from methane continuously, the reduced silver species should be reversibly reoxidized, so that the spent Ag-HPW/TiO_2 nanocomposite could be regenerated. Figure 4-18 shows photochemical conversion of methane on spent Ag-HPW/TiO_2, which was regenerated via its exposure to air at atmospheric pressure and irradiation for 7 h. The rate and amounts of ethane, propane and CO_2 are the same over the fresh and regenerated Ag-HPW/TiO_2 nanocomposites. The reaction-regeneration cycle without losing the amount of produced ethane can be repeated numerous times.

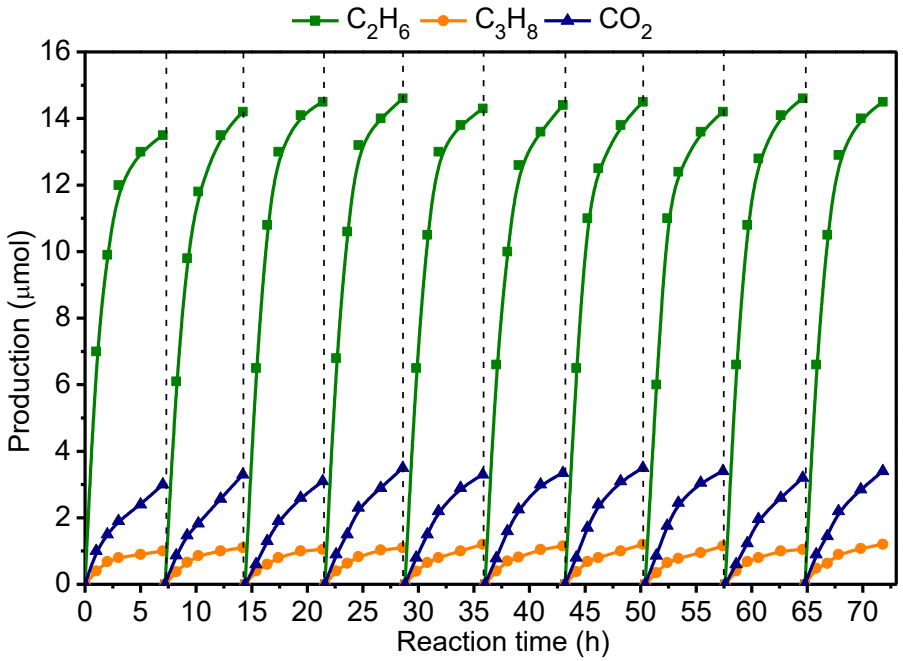

Figure 4-18 Stability of methane photochemical coupling on Ag-HPW/TiO_2.

A different response is observed (Figure 4-19) during reaction-regeneration cycles for the silver species supported on TiO_2 (Ag/TiO_2). It is worth noting that at methane conversion on Ag/TiO_2 results in mostly CO_2 and small amounts of ethane (Figure 4-1b). The lower selectivity to ethane in methane conversion over Ag/TiO_2 is consistent with the important role of silver cationic sites in achieving higher ethane selectivity. Indeed, the Ag/TiO_2 sample contain relatively large silver oxide clusters. Interestingly, the Ag/TiO_2 sample exhibits a different behavior following its regeneration. In contrast to the Ag-HPW/TiO_2 nanocomposite, the amounts of the produced CO_2 and ethane decrease as a function of the number of reaction-regeneration cycles. This is indicative of the irreversible modifications of the Ag/TiO_2 structure. It seems that the presence of the hetepolyacid stabilizes the photochemical activity of the Ag-HPW/TiO_2 nanocomposite. The effect of heteropolyacid on the stability of Ag-HPW/TiO_2 has been examined by the particle size measurements using TEM in fresh and used Ag-HPW/TiO_2 and Ag/TiO_2 (Figures 4-20). For the used Ag/TiO_2 sample, the Ag nanoparticles became noticeably larger after the reaction, a much broader particle size distribution was observed due to sintering (3.3 ± 1.3 nm, Figures 4-20b). In

contrast to Ag/TiO_2, the Ag particle size in Ag-HPW/TiO_2 was essentially unchanged after the reaction and regeneration (Figures 4-20a). This suggests that the presence of HPW stabilizes high silver dispersion, while silver sintering is a major reason for the decrease in the photochemical activity of Ag/TiO_2 after several reaction-regeneration cycles. Another role of HPW and in particular HPW/TiO_2 heterojunction can be in the efficient transfer and charge separation of electron and holes.

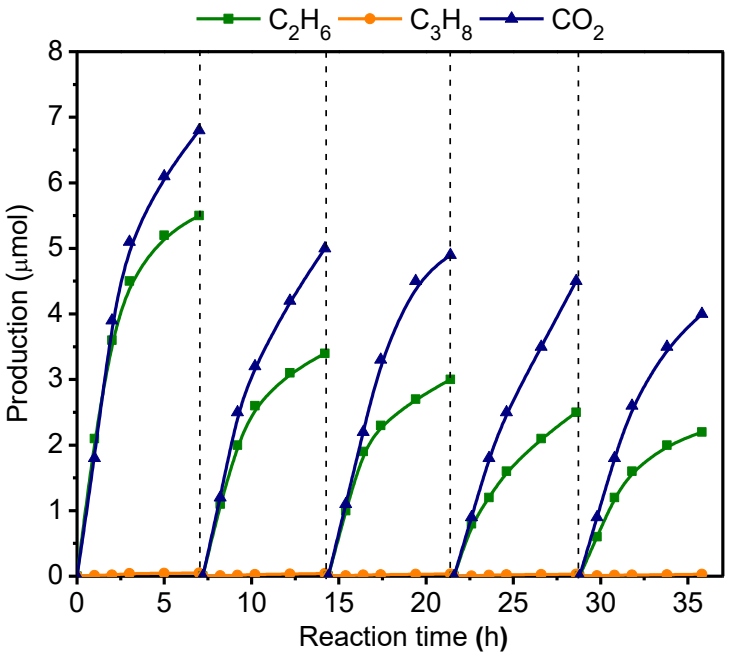

Figure 4-19 Stability of photochemical coupling of methane on Ag_2O/TiO_2.

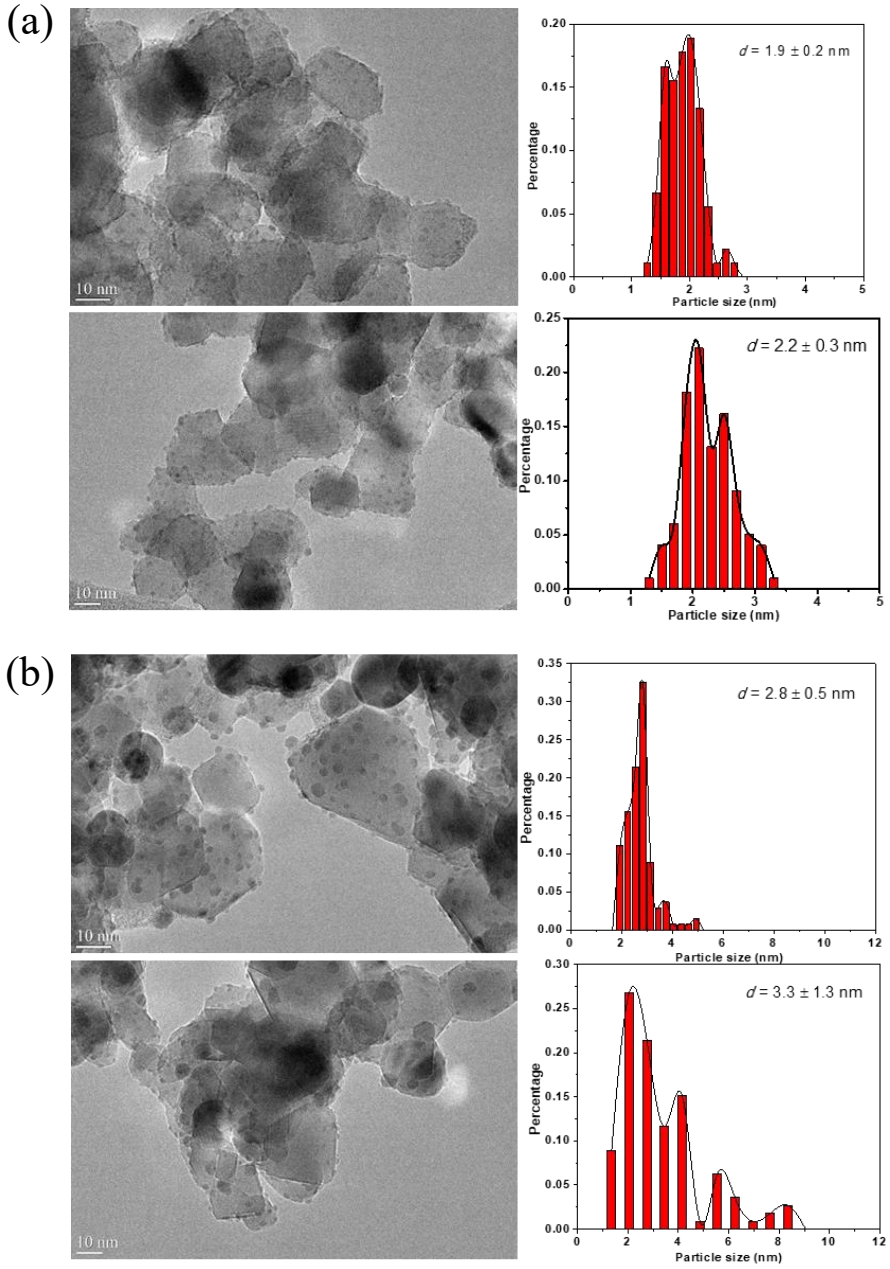

Figure 4-20 TEM images of fresh and used sample after photochemical coupling of methane, (a) Ag-HPW/TiO_2, (b) Ag/TiO_2.

The stability of the Ag-HPW/TiO_2 nanocomposite after numerous reaction-regeneration cycles suggests that methane coupling to ethane can be conducted using the chemical looping strategy. Chemical looping has been previously used for several reactions. Chemical looping combustion (CLC) is an emerging combustion technology[48, 49, 50], which facilitates CO_2 capture and sequestration. In this process, fuel is oxidized by a reducible

metal oxide, e.g. Fe_3O_4, producing selectively CO_2, which can be sequestrated and the reduced metal oxide is re-oxidized by air in a separate step. Recently, the chemical looping concept was applied for methane dry reforming[51, 52, 53]. The working principle of the "photochemical looping process" system proposed in this work for the methane photochemical coupling to ethane over Ag-HPW/TiO_2, is schematically shown in Figure 4-21. During the methane-coupling step, pure CH_4 is fed into reactor with the Ag-HPW/TiO_2 nanocomposite under irradiation. The interaction of methane with silver cationic species leads to formation of metallic silver, ethane, propane and small amount of CO_2. This reaction also generates Brønsted acidity, observed by FTIR monitoring of Py adsorption, in the spent Ag-HPW/TiO_2 sample (Figure 4-17). In the regeneration step, Ag-HPW/TiO_2 is exposed to ambient air under irradiation, which leads to re-oxidation of metallic silver. The relevant chemical reactions are specified below:

$$2CH_4 + 2Ag^+ \rightarrow C_2H_6 + 2Ag^0 + 2H^+ \qquad \text{methane coupling step}$$

$$4Ag^0 + O_2 + 4H^+ \rightarrow 4Ag^+ + 2H_2O \qquad \text{silver regeneration step}$$

In the photochemical looping strategy, Ag-HPW/TiO_2 reacts stoichiometrically with methane. The maximum amount of ethane and higher hydrocarbons produced during the photochemical conversion of methane depends on the amount of cationic silver in the reactor.

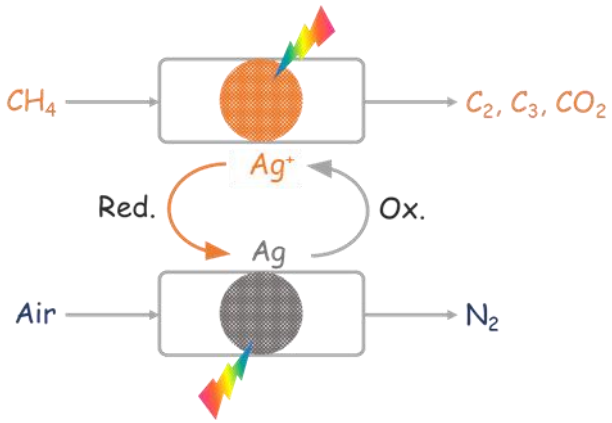

Figure 4-21 Schematic description of chemical looping process.

An attempt was made to increase the yield of ethane in the photochemical looping, since separation of methane and ethane can be prohibitively expensive if the yield and

concentration of the target product in the post-reaction mixture are low. In order to increase the methane conversion and correspondingly the yield of ethane, the ratio of photoactive Ag-HPW/TiO_2 nanocomposite to methane should be high. To achieve these goals, methane coupling was conducted in a capillary photoreactor with a reduced volume (Figure 4-22). The ratio of sliver to methane amounts in the reactor was 0.33 (3 μmol of silver and 9 μmol of methane). The yield of ethane of 9.2% (on carbon basis) was obtained after 5 h of the exposure of the capillary reactor to irradiation. Note that the maximum yield of ethane from methane assuming that all sliver atoms are involved in the methane coupling can be 30% under these conditions. Further works are in progress to design a commercially viable photoreactor and process for ethane selective synthesis from methane.

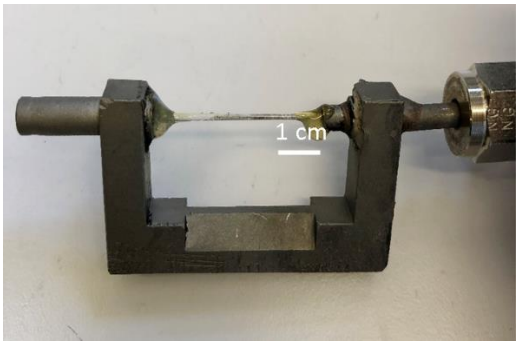

Figure 4-22 Capillary photoreactor.

4.3 Conclusion

High selectivity of methane coupling to ethane and high ethane yield were observed over silver-hetetopolyacid-titania nanocomposites in the presence of irradiation at ambient temperature. Ethane synthesis involves stoichiometric methane reaction with highly dispersed silver cationic species resulting in methyl radicals recombining to ethane. The photosensitive silver cationic species are reduced to metallic silver during the reaction. The selectivity of methane coupling to ethane of 90% can be achieved over the optimized materials. High silver dispersion essential for the methane coupling to ethane during the reaction is maintained by the thin heteropolyacid layer over titania. The nanocomposites can

be regenerated by exposure to air at ambient temperature under irradiation. The photochemical looping strategy has been demonstrated as a viable approach to attain a higher methane conversion and higher ethane yield (9%) from methane under the optimized conditions.

4.4 Reference

1. McFarland E. Unconventional chemistry for unconventional natural gas. *Science* **338**, 340-342 (2012).

2. Tang P, Zhu Q, Wu Z, Ma D. Methane activation: the past and future. *Energ. Environ. Sci.* **7**, 2580-2591 (2014).

3. Taarning E, Osmundsen CM, Yang X, Voss B, Andersen SI, Christensen CH. Zeolite-catalyzed biomass conversion to fuels and chemicals. *Energ. Environ. Sci.* **4**, 793-804 (2011).

4. Dapsens PY, Mondelli C, Pérez-Ramírez J. Biobased chemicals from conception toward industrial reality: lessons learned and to be learned. *ACS Catal.* **2**, 1487-1499 (2012).

5. Kondratenko EV, Mul G, Baltrusaitis J, Larrazábal GO, Pérez-Ramírez J. Status and perspectives of CO_2 conversion into fuels and chemicals by catalytic, photocatalytic and electrocatalytic processes. *Energ. Environ. Sci.* **6**, 3112-3135 (2013).

6. Kondratenko, E. V. Peppel, T. Seeburg, D. Kondratenko, V. A. Kalevaru, N. Martin, A. Wohlrab. Methane conversion into different hydrocarbons or oxygenates: current status and future perspectives in catalyst development and reactor operation. *Catal. Sci. Technol.* **7**, 366-381 (2017).

7. Kaygusuz K. Global energy issues, climate change and wind power for clean and sustainable energy development. *Journal of Engineering Research and Applied Science* **4**, 317-327 (2015).

8. Farrell BL, Igenegbai VO, Linic S. A viewpoint on direct methane conversion to ethane and ethylene using oxidative coupling on solid catalysts. *ACS Catal.* **6**, 4340-4346 (2016).

9. Hammond C, Conrad S, Hermans I. Oxidative methane upgrading. *ChemSusChem* **5**, 1668-1686 (2012).

10. Choudhary TV, Choudhary VR. Energy-efficient syngas production through catalytic oxy-methane reforming reactions. *Angew. Chem. Int. Ed.* **47**, 1828-1847 (2008).

11. Song H, Meng, XG, Wang ZJ, Liu HM, Ye JH. Solar-Energy-Mediated Methane Conversion. *Joule* **3**, 1606-1636 (2019)

12. Jang WJ, Shim, JO, Kim HM, Yoo SY. Roh HS. A review on dry reforming of methane in aspect of catalytic properties. *Catal. Today* **324**, 15-26 (2019).

13. Lunsford JH. Catalytic conversion of methane to more useful chemicals and fuels: a challenge

for the 21st century. *Catal. Today* **63**, 165-174 (2000).

14. Webb JR, Bolaño T, Gunnoe TB. Catalytic Oxy-Functionalization of Methane and Other Hydrocarbons: Fundamental Advancements and New Strategies. *ChemSusChem* **4**, 37-49 (2011).

15. Wang B, Albarracín-Suazo S, Pagán-Torres Y, Nikolla E. Advances in methane conversion processes. *Catal. Today* **285**, 147-158 (2017).

16. Keller G, Bhasin M. Synthesis of ethylene via oxidative coupling of methane: I. Determination of active catalysts. *J. Catal.* **73**, 9-19 (1982).

17. Zavyalova U, Holena M, Schlögl R, Baerns M. Statistical analysis of past catalytic data on oxidative methane coupling for new insights into the composition of high-performance catalysts. *ChemCatChem* **3**, 1935-1947 (2011).

18. Stansch Z, Mleczko L, Baerns M. Comprehensive kinetics of oxidative coupling of methane over the La_2O_3/CaO catalyst. *Ind. Eng. Chem. Res.* **36**, 2568-2579 (1997).

19. Lunsford JH. The catalytic oxidative coupling of methane. *Angew. Chem. Int. Ed.* **34**, 970-980 (1995).

20. Baerns M, Kondratenko EV. Oxidative coupling of methane. In: *Handbook of Heterogeneous Catalysis. 2nd Edition*. Wiley-VCH Verlag GmbH & Co. KGaA (2008).

21. Kuo J, Kresge C, Palermo R. Evaluation of direct methane conversion to higher hydrocarbons and oxygenates. *Catal. Today* **4**, 463-470 (1989).

22. Kanai M. Photocatalytic upgrading of natural gas. *Science* **361**, 647-648 (2018).

23. Yuliati L, Yoshida H. Photocatalytic conversion of methane. *Chem. Soc. Rev.* **37**, 1592-1602 (2008).

24. Yuliati L, Hamajima T, Hattori T, Yoshida H. Highly dispersed Ce (III) species on silica and alumina as new photocatalysts for non-oxidative direct methane coupling. *Chem. Commun.,* **38**, 4824-4826 (2005).

25. Yuliati L, Tsubota M, Satsuma A, Itoh H, Yoshida H. Photoactive sites on pure silica materials for nonoxidative direct methane coupling. *J. Catal.* **238**, 214-220 (2006).

26. Yuliati L, Hattori T, Itoh H, Yoshida H. Photocatalytic nonoxidative coupling of methane on gallium oxide and silica-supported gallium oxide. *J. Catal.* **257**, 396-402 (2008).

27. Li L, Li GD, Yan C, Mu XY, Pan XL, Zou XX, Wang KX, Chen JS. Efficient Sunlight-Driven

Dehydrogenative Coupling of Methane to Ethane over a Zn^{+}-Modified Zeolite. *Angew. Chem. Int. Ed.* **50**, 8299-8303 (2011).

28. Li L, Cai YY, Li GD, Mu XY, Wang KX, Chen JS. Synergistic Effect on the Photoactivation of the Methane C-H Bond over Ga^{3+}-Modified ETS-10. *Angew. Chem. Int. Ed.* **51**, 4702-4706 (2012).

29. Meng LS, Chen ZY, Ma ZY, He S, Hou YD, Li HH, Yuan RS, Huang XH, Wang XX, Wang XC, Long JL. Gold plasmon-induced photocatalytic dehydrogenative coupling of methane to ethane on polar oxide surfaces. *Energ. Environ. Sci.* **11**, 294-298 (2018).

30. Wu, SQ, Tan XJ, Lei JY, Chen HJ, Wang LZ, Zhang JL. Ga-Doped and Pt-Loaded Porous TiO_2–SiO_2 for Photocatalytic Nonoxidative Coupling of Methane. *J. Am. Chem. Soc.* **141**, 6592-6600, (2019).

31. Chen, X. et al. Photocatalytic oxidation of methane over silver decorated zinc oxide nanocatalysts. *Nat. Commun.* **7**, 12273, (2016).

32. Shimura K, Yoshida T, Yoshida H. Photocatalytic Activation of Water and Methane over Modified Gallium Oxide for Hydrogen Production. *J. Phys. Chem. C* **114**, 11466-11474, (2010).

33. H. Wang, L. Zhang, Z. Chen, J. Hu, S. Li, Z. Wang, J. Liu and X. Wang, Semiconductor heterojunction photocatalysts: design, construction, and photocatalytic performances. *Chem. Soc. Rev.* **43**, 5234-5244 (2014).

34. Z. Sun, Y. Zhang, N. Li, L. Xu and T. Wang, Enhanced photoconductivity of a polyoxometalate–TiO_2 composite for gas sensing applications. *J. Mater. Chem. C*, **3**, 6153-6157 (2015).

35. P. Meng, H. Heng, Y. Sun, J. Huang, J. Yang, X. Liu, Positive effects of phosphotungstic acid on the in-situ solid-state polymerization and visible light photocatalytic activity of polyimide-based photocatalyst. *Appl. Catal. B*, **226**, 487- 498 (2018)

36. P. D. Tran, L. H. Wong, J. Barberbcd and J. S. C. Loo, Recent advances in hybrid photocatalysts for solar fuel production. *Energy Environ. Sci.*, **5**, 5902-5918 (2002).

37. Gondal M, Hameed A, Yamani Z, Arfaj A. Photocatalytic transformation of methane into methanol under UV laser irradiation over WO_3, TiO_2 and NiO catalysts. *Chem. Phys. Lett.* **392**, 372-377 (2004).

38. Murcia-López Sn*,* Nacariza MC, Villa K, Lopes JM, Henriquess C, Morante JR, Andreu T. Controlled photocatalytic oxidation of methane to methanol through surface modification of beta

zeolites. *ACS Catal.* **7**, 2878-2885 (2017).

39. Murcia-López Sn, Villa K, Andreu T, Morante JR. Partial oxidation of methane to methanol using bismuth-based photocatalysts. *ACS Catal.* **4**, 3013-3019 (2014).

40. Nakarada Đ, Petković, M. Mechanistic insights on how hydroquinone disarms OH and OOH radicals. *Int. J. Quantum Chem.* **118**, e25496 (2018).

41. Kalishwaralal K, Deepak V, Ramkumarpandian S, Nellaiah H, Sangiliyandi G. Extracellular biosynthesis of silver nanoparticles by the culture supernatant of Bacillus licheniformis. *Mater. Lett.* **62**, 4411-4413 (2008).

42. Prieto P, Nistor V, Nouneh K, Oyama M, Abd-Lefdil M, Díaz R. XPS study of silver, nickel and bimetallic silver–nickel nanoparticles prepared by seed-mediated growth. *Appl. Surf. Sci.* **258**, 8807-8813 (2012).

43. Gaarenstroom S, Winograd N. Initial and final state effects in the ESCA spectra of cadmium and silver oxides. *J. Chem. Phys.* **67**, 3500-3506 (1977).

44. Anthony M, Seah M. XPS: Energy calibration of electron spectrometers. 1-An absolute, traceable energy calibration and the provision of atomic reference line energies. *Surf. Interface Anal.* **6**, 95-106 (1984).

45. Samokhvalov A, Nair S, Duin EC, Tatarchuk BJ. Surface characterization of Ag/Titania adsorbents. *Appl. Surf. Sci.* **256**, 3647-3652 (2010).

46. Fernández A, González-Elipe A. "In situ" XPS study of the photoassisted reduction of noble-metal cations on TiO_2. *Appl. Surf. Sci.* **69**, 285-289 (1993).

47. Laube T, Weidenhaupt A, Hunziker R. Activation of .alpha.-bromo ketones by complexation with hard and soft Lewis acids. A combined x-ray and NMR study. *J. Am. Chem. Soc.* **113**, 2561-2567 (1991).

48. Adanez J, Abad A, Garcia-Labiano F, Gayan P, Luis F. Progress in chemical-looping combustion and reforming technologies. *Prog. Energ. Combust. Sci.* **38**, 215-282 (2012).

49. Bhavsar S, Najera M, Solunke R, Veser G. Chemical looping: To combustion and beyond. *Catal. Today* **228**, 96-105 (2014).

50. Vorrias I, Atsonios K, Nikolopoulos A, Nikolopoulos N, Grammelis P, Kakaras E. Calcium looping for CO_2 capture from a lignite fired power plant. *Fuel* **113**, 826-836 (2013).

51. Galvita VV, Poelman H, Marin GB. Combined chemical looping for energy storage and conversion. *J. Power Sources* **286**, 362-370 (2015).

52. Buelens LC, Galvita VV, Poelman H, Detavernier C, Marin GB. Super-dry reforming of methane intensifies CO_2 utilization via Le Chatelier's principle. *Science* **354**, 449-452 (2016).

53. Zhang J, Haribal V, Li F. Perovskite nanocomposites as effective CO_2-splitting agents in a cyclic redox scheme. *Sci. Adv.* **3**, e1701184 (2017).

Chapter 5. Design of Core-Shell Titania-Heteropolyacid-Metal Nanocomposites for Photocatalytic Reduction of CO_2 to CO at Ambient Temperature

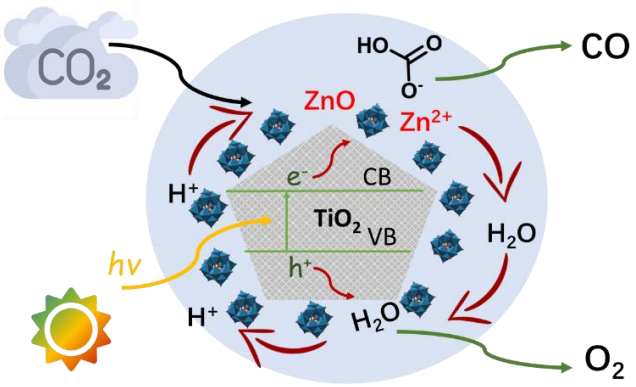

Abstract

The photocatalytic conversion of CO_2, which occurs at ambient temperature, not only reduces the greenhouse effect, but also provides value-added solar fuels and chemicals. Herein, we report design of new efficient core-shell nanocomposites for selective photocatalytic CO_2 to CO conversion. A combination of characterization techniques (TEM, STEM-EDX, XPS, XRD, photoluminescence) indicates that the CO_2 reduction occurs over zinc species highly dispersed on the heteropolyacid/titania core-shell nanocomposites. These core-shell structures create n-p heterojunction, which increases charge separation, lifetime of the charge carriers and leads to higher electron flux. In-situ FTIR investigation of the reaction mechanism uncovered that the reaction involved surface zinc bicarbonates as key reaction intermediates. In a series of catalysts containing noble and transition metals, the zinc phosphotungstic acid - titania nanocomposites exhibit high activity reaching 50 µmol CO/g·h and selectivity (73 %) in the CO_2 photocatalytic reduction to CO at ambient temperature. The competitive water splitting reaction has been significantly suppressed over the Zn sites in the presence of CO_2.

5.1 Introduction

Development of human economic activities, especially use of fossil fuel in transportation, industry and household combined with deforestation and land-use changes have led to the increase in the concentration of CO_2 in the atmosphere from 280 ppm to 390 ppm. The CO_2 concentration may reach 500-1000 ppm and cause the average temperature increase of 1.9 ºC by 2100[1, 2, 3, 4]. The carbon dioxide content in the atmosphere can be reduced using carbon capture and storage (CCS) and carbon capture and utilization (CCU)[5]. An important strategy of the CCU is the CO_2 chemical conversion into useful products[6, 7, 8, 9, 10].

Development of novel carbon dioxide utilization technologies should meet three major challenges[2]: design of efficient catalysts, surmounting unfavorable thermodynamics and achieving competitive cost of the CO_2-based fuels and chemicals. The CO_2 chemical conversion is typically an endothermic process that requires a large amount of energy input due to the CO_2 high thermodynamic stability[11]. Photocatalysis is particularly interesting for CCU, because it can overcome thermodynamic limitations typical for thermocatalytic processes.

One of the most promising technologies for the CO_2 mitigation is its photocatalytic reduction[12, 13]. Photocatalytic reduction of CO_2 may result in the formation of several compounds: carbon monoxide, formic acid, formaldehyde, methanol, methane, ethane, ethane and others. The photocatalytic process involves three steps such as (i) light harvesting, (ii) charge separation, transport and (iii) CO_2 adsorption and catalytic reaction. Major progress has been obtained in the optimization of the first two steps. Low energy efficiency, uncontrollable selectivity (because of the presence of several CO_2 reduction products and competing water-splitting reaction) and deactivation are major challenge of CO_2 photocatalytic reduction. In addition, in order to improve the yield of desired products, further information is required about the reaction mechanism and active intermediates.

Numerous semiconducting materials have been studied for the CO_2 photocatalytic reduction. TiO_2 has been so far the most studied semiconductor due to its high chemical

stability, availability and low toxicity[13, 14]. The selectivity of carbon dioxide reduction principally depends on the structure and catalytic properties of co-catalysts, which intervene at the third step of the photocatalytic process such as reduction of CO_2 or water splitting. As summarized by Ran et al[15], cocatalysts can promote separation and migration of photoexcited electron–hole pairs. The CO_2 reduction selectivity to specific products and semiconductor stability can be therefore improved and the side reactions are impeded. The photocatalytic CO_2 reduction rate is a function of several catalyst parameters such as dispersion of active phase, catalyst porosity, basicity, oxygen vacancies, and presence of functional groups.

Several groups of cocatalysts have been proposed for CO_2 photocatalytic reduction: noble metals[15], metal oxides (CuO[16, 17], ZnO[18], CeO_2[19], Zn_2GeO_4[20], $ZnGa_2O_4$[21] and $BiWO_6$[22]), metal complexes[23], metal–organic-frameworks[24], carbon nitrides[25, 26, 27, 28, 29], sulfides[30] or biological systems[31, 32]. Noble metal-based cocatalysts represent almost a half of studied systems. High price and rarity of noble metals significantly limit their possible industrial use for photocatalytic CO_2 reduction. Use of transition metal oxides as cocatalysts seems to be an interesting route for design of efficient photocatalysts for the CO_2 hydrogenation. In addition, the photocatalytic performance in the CO_2 hydrogenation can be further enhanced by p-n semiconductor heterojunction[33]. This heterojunction can be created by adding to TiO_2 a semiconductor with lower levels of valence and conduction bands. This heterojunction can be achieved by combining TiO_2 with a heteropolyacid acid ($H_3PW_{12}O_{40}$). The valence and conduction bands of phosphotungstic acid are located lower[34, 35, 36] than for TiO_2[34, 37], which may result in better charge separation and higher electron flux from TiO_2 onto HPW. Recently, we developed zinc-modified heteropolyacid - titania-nanocomposites, which exhibit selective carbon monoxide production from methane at ambient temperature[38]. In the present study, we report for the first time that the Zn-HPW/TiO_2 system exhibited high photocatalytic activity in selective conversion of carbon dioxide to carbon monoxide in the presence of water. In-situ study of the reaction mechanism by IR and XPS has provided important insights into the reaction mechanism. We uncovered that CO was produced during

the decomposition of zinc bicarbonate in the presence of H_2O under light. No change of the Zn valence state occurred from the fresh to the used catalyst.

5.2 Result and discussion

5.2.1 CO_2 conversion over titania-heteropolyacid-metal nanocomposites to CO at ambient temperature

Photocatalytic conversion of CO_2 in the presence of water vapor was investigated for a series of catalysts supported on the HPW/TiO_2 composites (Figure 5-1), which were prepared by impregnation. Carbon monoxide, oxygen, methane and hydrogen were detected as reaction products on these solids exposed to light irradiation using a 400 W Xe lamp. Note that no oxygenates (alcohols, aldehydes etc.) were observed. No CO_2 conversion and reaction products were observed in the experiments without irradiation (dark). This confirms that the CO_2 catalytic conversion is indeed driven by light. Addition of noble or transition metals including Ag, Pd, V, Fe, Ga, Ce, Co, Cu and Zn to the HPW/TiO_2 composites enhances the CO_2 and water reduction compared to the pristine HPW/TiO_2 composite (Figure 5-1). Note that the reaction selectivity and product formation rates strongly depend on the type of metal. Much higher H_2 and O_2 production rates were observed over the catalysts containing noble metals. The production of hydrogen indicates water-splitting reaction, which occurs over these catalysts alongside with CO_2 conversion to CO in the presence of light[12, 39]. The CO formation rates was higher over the catalysts containing transition metals than those with noble metals catalysts, while the formation rate of methane was higher with the latter catalysts. The Zn containing catalyst showed extremely high rate of the CO_2 reduction to CO compared to all studied transition and noble metal containing samples.

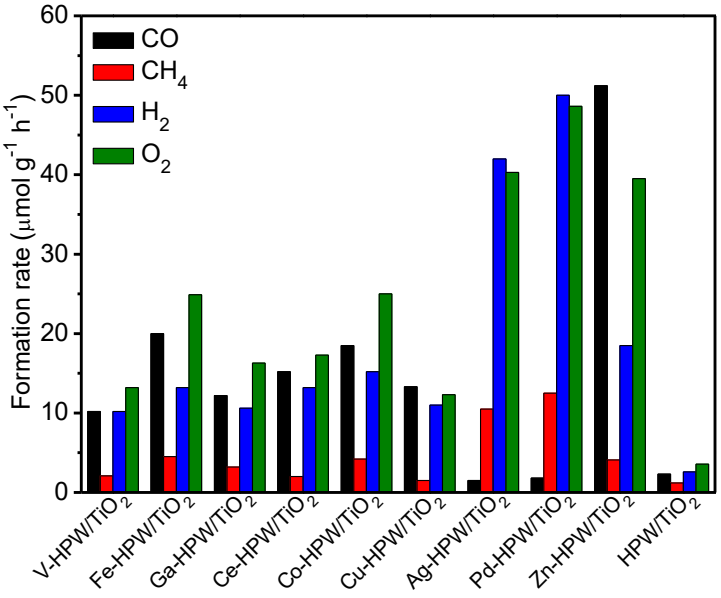

Figure 5-1 Performances of different catalysts in photocatalytic reduction of CO_2 in water. Reaction conditions: catalyst, 0.1 g; Gas phase pressure, CO_2 0.2 MPa; H_2O, 15mL; irradiation time, 6h.

In order to provide further insights into the catalytic performance of the Zn-containing catalysts, a series of catalysts with different composition were prepared from HPW and TiO_2 with and without zinc and tested in photocatalytic reduction of CO_2 (Figure 5-2). The promotion of pure TiO_2 or HPW with Zn results only in a slight increase in the CO_2 conversion rate compared to the pristine semiconductors.

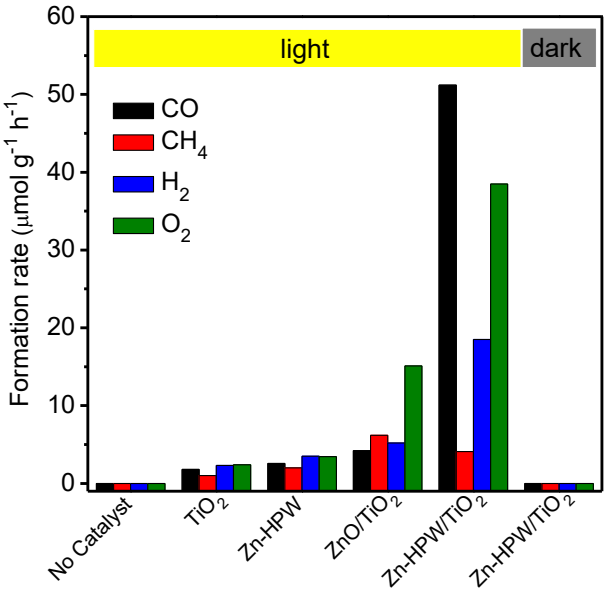

Figure 5-2 Performances of TiO_2, HPW and Zn containing catalysts in photocatalytic reduction of CO_2 in water. Reaction conditions: catalyst, 0.1 g; Gas phase pressure, CO_2 0.2 MPa; H_2O, 15mL; irradiation time, 6h.

Figure 5-3 displays the catalytic performance data of Zn-HPW/TiO_2 with different Zn contents. It is clear that higher Zn loading significantly enhances the CO, O_2 and H_2 formation rates, while the rate of methane production decreases at high zinc content. Note also that higher Zn content leads to higher selectivity to CO and lower hydrogen selectivity. This suggest that relative contribution of water splitting decreases at higher zinc content.

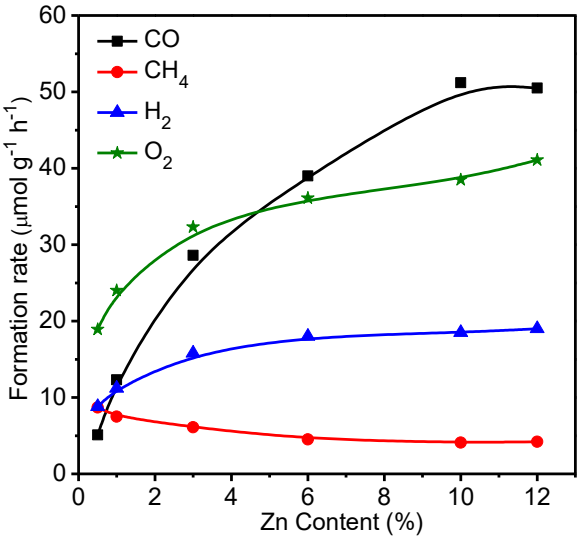

Figure 5-3 CO, CH_4 and H_2 production over Zn-HPW/TiO_2 catalysts with different Zn loadings. Reaction conditions: catalyst, 0.1 g; Gas phase pressure, CO_2 0.2 MPa; H_2O, 15mL; irradiation time, 6h.

Another catalyst parameter, which may affect the catalytic performance, is the HPW/TiO_2 ratio in the Zn-HPW/TiO_2 composite. Figure 5-4 shows the carbon monoxide, oxygen, hydrogen and methane production rates over the Zn-HPW/TiO_2 catalysts with different ratios of HPW to TiO_2. In these catalysts, the ratio of Zn to HPW was kept at 2. Note that higher HPW/TiO_2 ratio in the catalysts results in a slight increase in the rate of CO production, where the rates of formation of other products were affected to a lesser extent by the HPW/TiO_2 ratio. Furthermore, photocatalytic CO_2 reduction was investigated as a function of carbon dioxide pressure (Figure 5-5). The CO_2 pressure has a mild effect on the CO_2 conversion rate and selectivity.

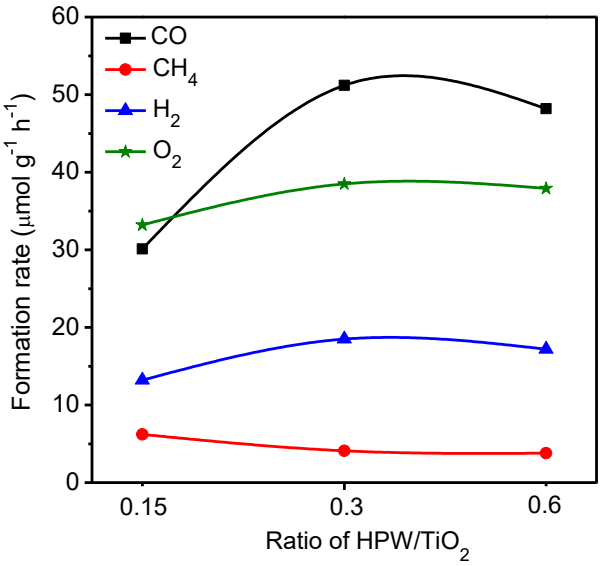

Figure 5-4 CO, O_2, CH_4 and H_2 production formation rates over Zn-HPW/TiO_2 composites with different ratio of HPW/TiO_2. Reaction conditions: catalyst, 0.1 g; Gas phase pressure, CO_2 0.2 MPa; H_2O, 15mL; irradiation time, 6h.

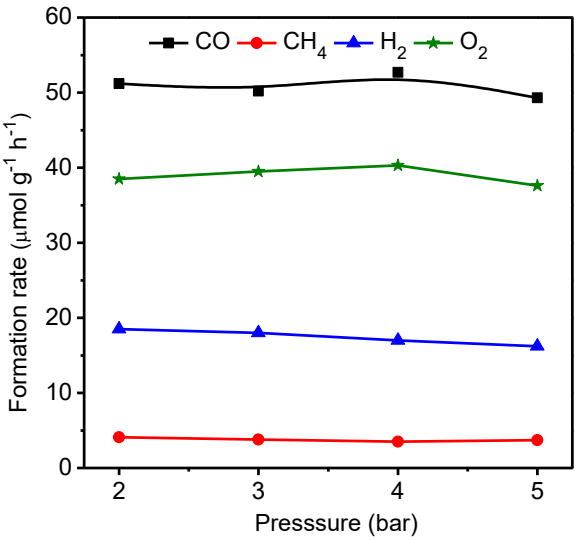

Figure 5-5 CO, O_2, CH_4 and H_2 production formation rates over Zn-HPW/TiO_2 composites with different pressure. Reaction conditions: catalyst, 0.1 g; Gas phase pressure, CO_2 0.2 ~ 0.5 MPa; H_2O, 15mL; irradiation time, 6h.

Thus, the presence of three components: TiO_2, HPW and Zn is required in order to attain a major increase in CO production from CO_2. Importantly, the selectivity were also very different over the Zn-HPW/TiO_2 three-component catalyst as compared to the binary Zn/HPW and Zn/TiO_2 systems. CO and oxygen were major products over Zn-HPW/TiO_2 composites, while the rates of CO and hydrogen production (because of water splitting reaction) were comparable over the binary catalysts (Figure 5-2). Zn^{2+} isolated ions can form because of the reaction of ZnO with the $H_3PW_{12}O_{40}$ acid.

High mobility of Zn species within the HPW-TiO_2 composites can be suggested. The mechanical mixtures of Zn/TiO_2 with HPW/TiO_2 were then prepared for CO_2 photocatalytic reduction. The activity of the Zn/TiO_2-HPW/TiO_2 mechanical mixture (Figure 5-6) was much higher than over pure Zn/TiO_2 and HPW/TiO_2. This can be assigned therefore, to significant Zn migration under the reaction conditions.

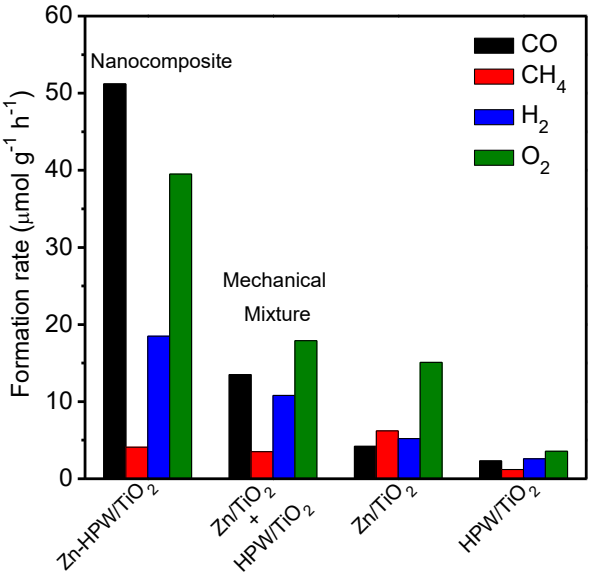

Figure 5-6 Performances of Zn-HPW/TiO_2, Zn/TiO_2, HPW/TiO_2 and mechanical mixture Zn/TiO_2 + HPW/TiO_2 photocatalytic CO_2 reduction. Reaction conditions: catalyst, 0.1 g; Gas phase pressure, CO_2 0.2 MPa; H_2O, 15mL; irradiation time, 6h

5.2.2 Catalyst characterization

The structure of Zn-HPW/TiO_2 catalysts was then investigated using several

characterizations techniques. Figure 5-7 displays XRD patterns of the Zn-HPW/TiO_2, ZnO/TiO_2, HPW/TiO_2, TiO_2 and HPW samples. The XRD peaks of anatase and rutile phases were detected in the samples containing TiO_2, while the HPW sample showed the presence of the XRD peaks assigned to the heteropolyacid. The absence of diffraction peaks attributed to the HPW and Zn phases in Zn-HPW/TiO_2 can indicate high HPW and Zn dispersion and smaller crystallite sizes. No zinc carbonate XRD patterns were observed in any sample. Hexagonal wurtzite ZnO phase (♦ symbol, JCPDS #36-1451) identified by diffraction peaks at 31.8° and 34.4° attributed to crystal face (100) and (002)[40, 41] was detected in Zn/TiO_2. The ZnO XRD peaks disappear in Zn-HPW/TiO_2 catalysts. This indicates high dispersion of zinc species in the presence of HPW are highly dispersed.

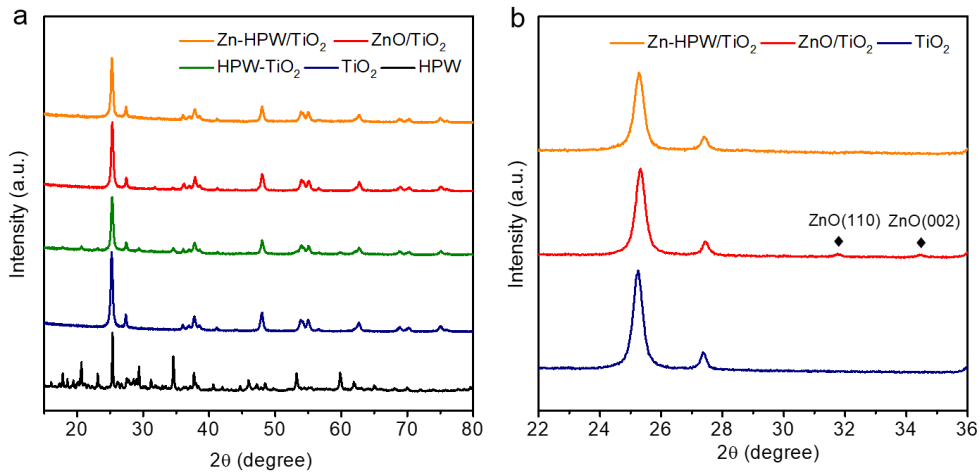

Figure 5-7 XRD patterns of different nanocomposites catalysts.

Photoluminescence (PL) spectroscopy (Figure 5-8) is a powerful tool that provides information on the surface processes involved in the recombination of photogenerated charge carriers. We observed a visible luminescence band centered at ~450nm for TiO_2[42, 43]. The intensity of the luminescence band at ~450nm, which was caused by the recombination of photogenerated electron-hole pairs, decreased in the order of TiO_2 > HPW/TiO_2 > Zn-HPW/TiO_2. This suggests that the Zn-HPW/TiO_2 composite was the most efficient for the separation of photogenerated electron-hole pairs. This can be explained by the migration of excited electrons from TiO_2 to the HPW and Zn nanoparticle, preventing the electron−hole

recombination. This effect is discussed in detail below in the manuscript. It has been observed earlier for other photocatalytic reactions in the presence of HPW[44].

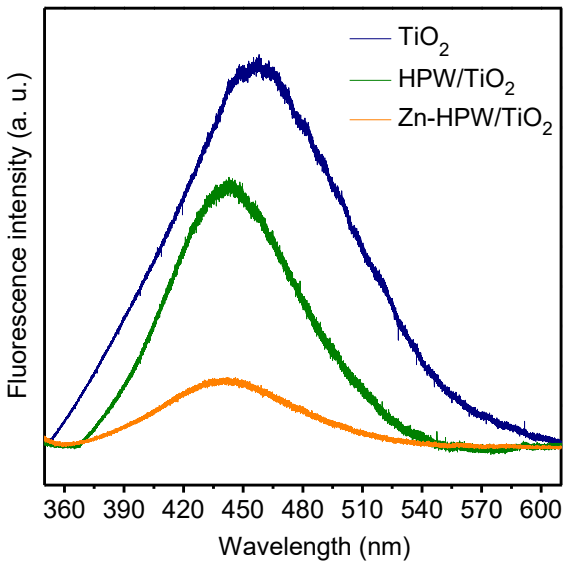

Figure 5-8 Photoluminescence spectra of TiO_2, HPW and Zn containing catalysts.

FTIR analysis has been used to identify Zn species and catalyst acidity. Figure 5-9 shows FTIR spectra of the Zn/HPW-TiO_2 composites which different Zn contents. The three strong bands at 1510, 1410 and 1320 cm^{-1} are attributed to carbonates species are observed at zinc content in the catalysts higher than 1 wt. %. In agreement with previous report[45], these bands can be attributed to mono-dentate carbonates. Interestingly at higher zinc contents, two new IR bands appear at 1634 cm^{-1} and 1390 cm^{-1}. The bands at 1634 and 1390 cm^{-1} can be assigned to the bicarbonate species (HCO_3^-)[46, 47]. The assigned of the bands at 1634 and 1390 cm^{-1} to bicarbonates is also confirmed by a significant increase in the intensity of IR band at 3300 cm^{-1} assigned to OH stretching vibrations. It can be tentatively suggested that the new species identified by the bands at 1630 and 1390 cm^{-1} correspond to zinc bicarbonates containing OH groups, though some contribution of chemisorbed water molecules to the intensity of the bands at 1634 cm^{-1} and 3300 cm^{-1} cannot be excluded.

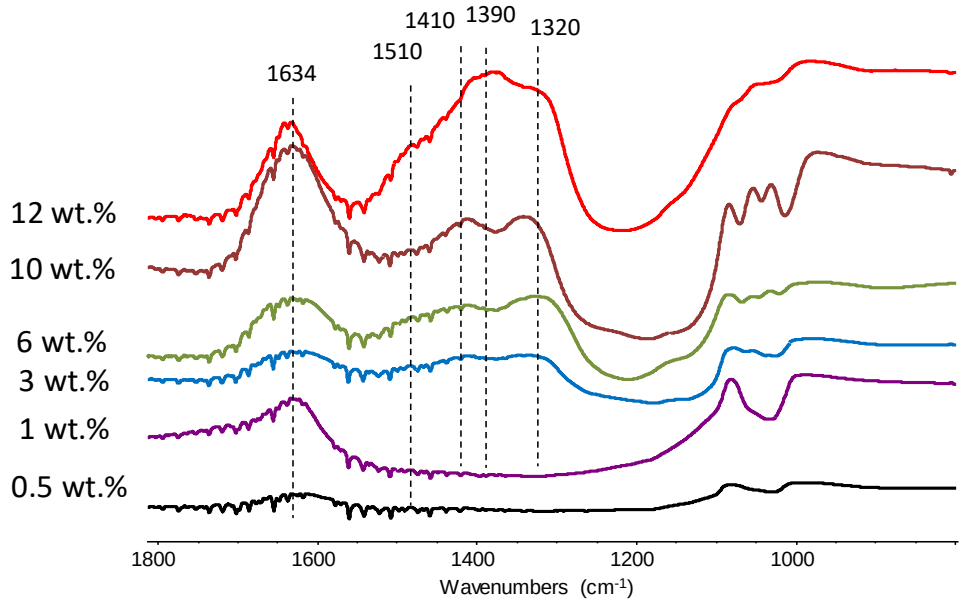

Figure 5-9 FTIR spectra of the Zn-HPW/TiO_2 catalysts with different Zn content. The spectra were recorded without preliminary pretreatment.

Two strong bands at 1621 and 1453 cm^{-1} appeared after adsorption of Py (Figure 5-10), They might be respectively attributed to the complexes of Py with strong Lewis acid sites[48]. The Lewis acidity can be related to unsaturated Zn^{2+} ions. Interestingly, no Brönsted acidity associated to HPW was observed in the samples with zinc. Thus suggests full neutralization of the HPW Brönsted acidity by Zn^{2+} ions. Indeed, in the Zn-HPW/TiO_2 catalyst (6 wt.% Zn), the maximum concentration of potential Brönsted acid sites associated with HPW is only 0.3 mmol/g, while the amount of zinc is three times higher (0.9 mmol). Thus, Zn should be mostly present as cationic Zn, carbonate, bicarbonate or oxide. It is known that ZnO has high basicity. This would favor adsorption of CO_2 from the atmosphere resulting in zinc carbonates[49]. FTIR spectra (Figure 5-9) show appearance of bicarbonate bands at 1634 and 1390 cm^{-1} in the Zn-HPW/TiO_2 catalysts starting from 1 wt. % of Zn. It should be noted as zinc content in the catalyst reaches 1 wt.%, their activity in the CO formation from CO_2 significantly increases.

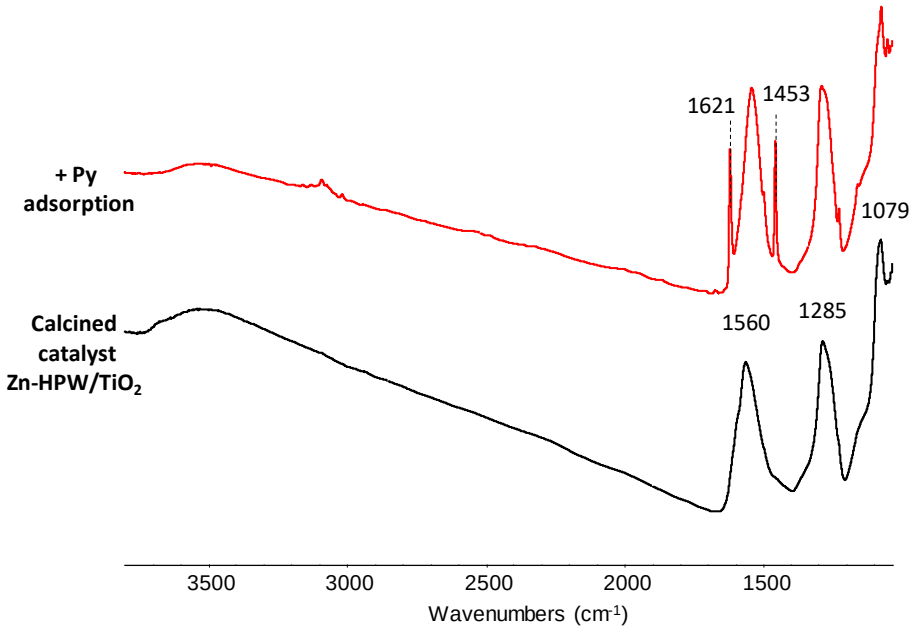

Figure 5-10 FTIR spectra of the Zn-HPW/TiO_2 (6wt.%) catalyst before and after adsorption of pyridine and sample evacuation at 200°C.

The UV-Vis diffuse reflectance spectra of Zn-HPW/TiO_2 nanocomposite and reference compounds are displayed in Figure 5-11**.** The sample exhibits intense absorption in the ultraviolet region (< 400 nm). The band gap energy for different nanocomposites estimated using Tauc's plots of UV-Vis spectra varies from 3.0 eV to 3.2 eV. Relatively small effect of the promotion with Zn is observed on the band gap of HPW (E_g = 3.12 eV) and TiO_2 (E_g = 3.20 eV[50]). Note that both zinc oxide and zinc carbonate have semiconductor properties; their band gaps vary from 3.12 to 3.36 eV[51, 52].

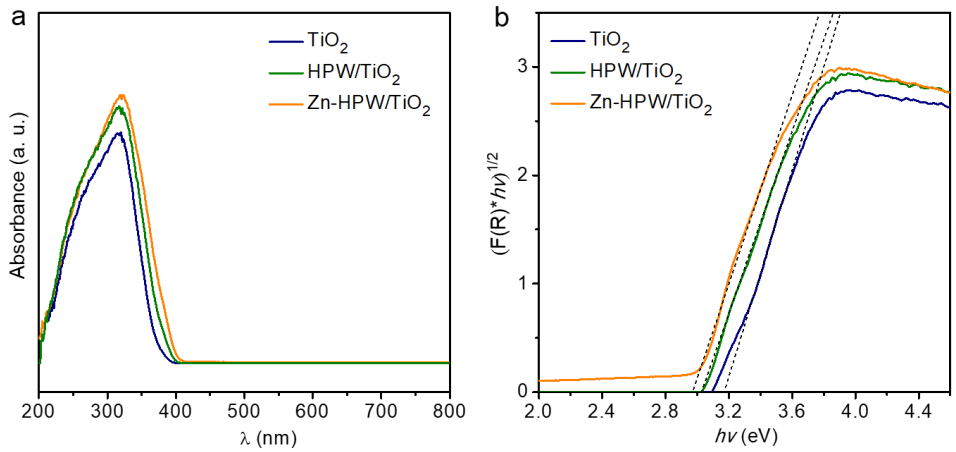

Figure 5-11 a UV-Vis spectra of Zn-HPW/TiO_2 sample; b $[F(R\infty)h\nu]^{1/2}$ versus *hv* for Zn-HPW/TiO_2 sample

The catalysts were characterized by high resolution transmission electron microscopy (HRTEM), high angle annular dark-field scanning TEM (HAADF-STEM) and EDX maps (Figure 5-12a, Figure 5-13). The Zn-HPW/TiO_2 composite shows the presence of two populations of particles: highly faceted NPs with sizes >100 nm and smaller faceted NPs with sizes between 10 and 50 nm (Figure 5-14). Figure 5-12b displays TEM images of the spent catalyst. Interestingly, the HPW shell remains almost intact after conducting CO_2 photochemical reduction and no noticeable sintering of zinc species was observed. The clearly observed separation of TiO_2 and HPW phases in the core-shell structure is indicative of a possible semiconductor heterojunction, which might affect the photocatalytic properties.

The enhanced contrast achieved in the high-resolution STEM-HAADF micrographs (Figure 5-13 and Figure 5-15) is due to the difference of the Z-atomic number of the constituents. Therefore, the presence of the lighter shell is associated to the presence of the HPW embedding the TiO_2, as anticipated by the previous TEM observations. This issue is further confirmed by the elemental maps corresponding to the Ti, O, W and Zn. Here, the Ti defines the facetted grains, whilst the TiO_2 edges appear to be covered by the W and P from the HPW heteropolyacid. The Zn is present as small nanoparticles and/or clusters highly dispersed on the catalyst surface (light-grey circular nanoparticles in the right-side image from Figure 5-13a, with a slight tendency of agglomeration at the TiO_2 rims, similar to tungsten and phosphorous.

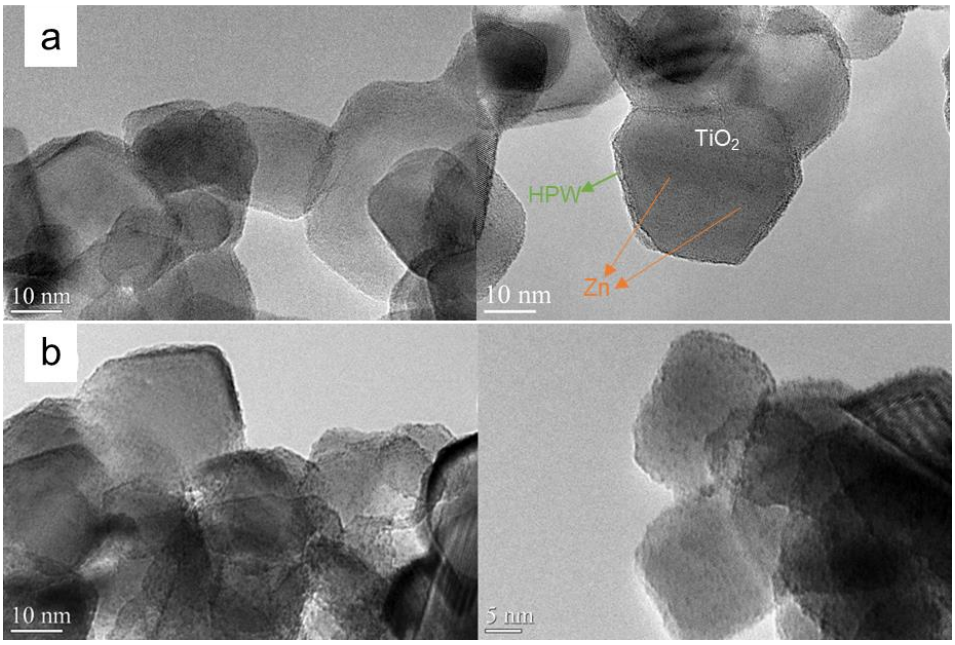

Figure 5-12 TEM images of the calcined (a) and used (b) Zn-HPW/TiO_2 catalyst.

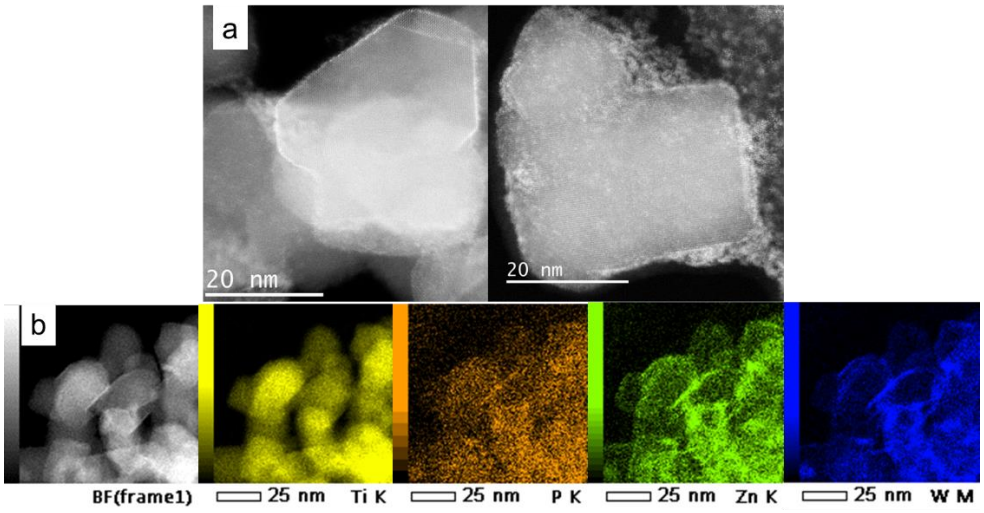

Figure 5-13 a. HAADF-STEM image; b. EDX maps of Zn-HPW/TiO_2 catalyst.

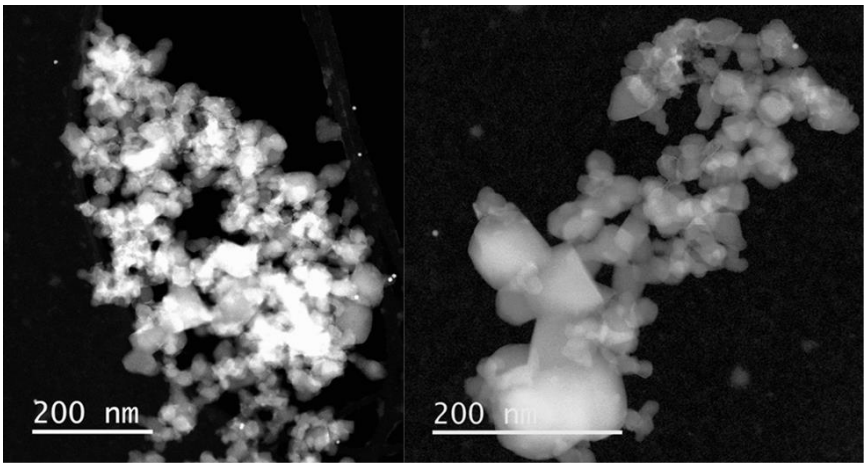

Figure 5-14 TEM images of Zn-HPW/TiO_2 composite

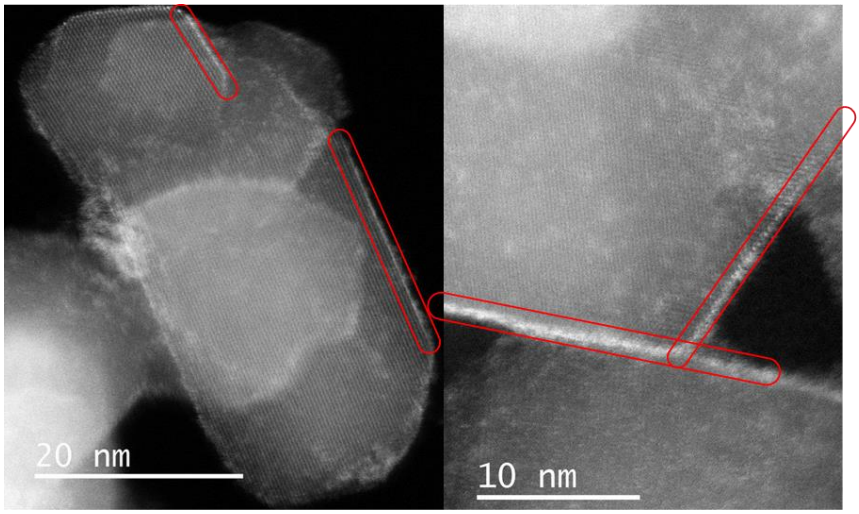

Figure 5-15 High resolution TEM images showing formation of core shell structure in Zn-HPW/TiO_2.

To provide further insights into the zinc oxidation state and its evolution during the reaction, both the calcined Zn-HPW/TiO_2 catalyst and its spent counterpart after the reaction were characterized by XPS (Figure 5-16). XPS is indicative of the presence of Zn^{2+} species in the calcined catalysts, which were identified by the Zn 2p binding energies at 1021.9 eV. No changes were noticed in the Zn $2p_{3/2}$ XPS binding energy after catalyst exposure to CO_2 and H_2O[53, 54] (Figure 5-16). It is known that Auger spectroscopy is more sensitive than the XPS binding energy to the changes in the Zn valence state (Figure 5-17). The Zn Auger peak from Zn-HPW/TiO_2 catalysts is normalized to the peak height of the ZnO Auger feature. The

positions of all Auger peaks are aligned by the C 1s peak, and a Shirley background was subtracted. Note however that the Auger peaks were similar for the fresh Zn catalyst and that after conducting the catalytic reaction. Thus, Auger spectroscopy also suggests no changes in the oxidation state of Zn during the reaction.

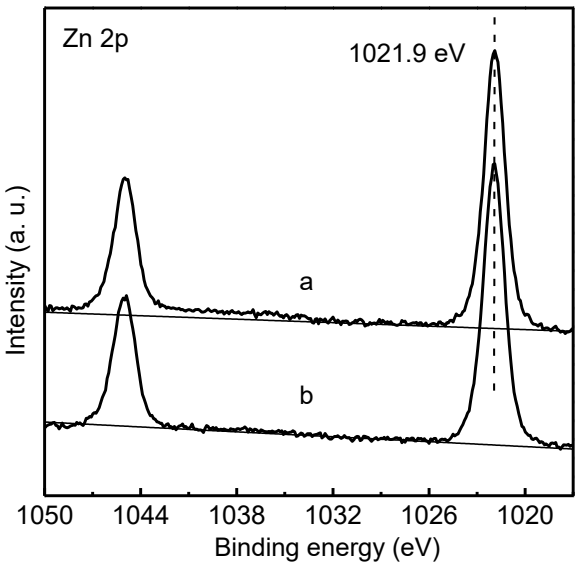

Figure 5-16 XPS spectra of Zn-HPW/TiO_2 catalysts in the regions of Zn 2p; a. fresh catalyst, b. used catalyst.

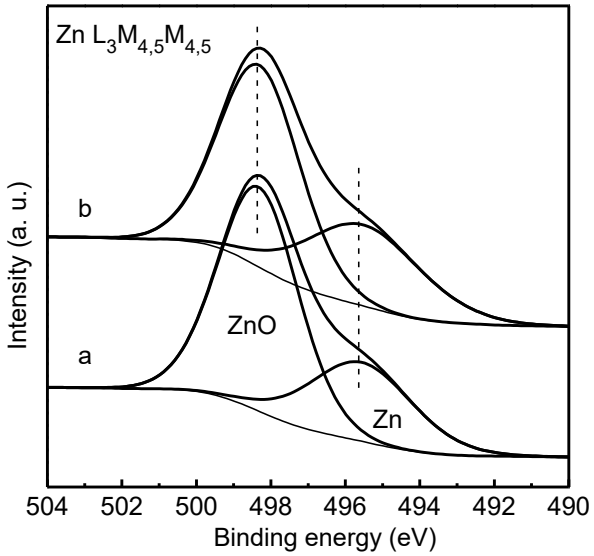

Figure 5-17 Zn $L_3M_{4.5}M_{4.5}$ Auger peaks for the Zn-HPW/TiO_2 catalysts; a. fresh catalyst,

b. used catalyst.

5.2.3 Mechanistic aspects of CO_2 photo-reduction to CO

Additional experiments were conducted to investigate in detail the reaction paths in the CO_2 photocatalytic reduction over the Zn-HPW/TiO_2 composites. Table 5-1 shows the CO, CH_4 and H_2 reaction rates measured in the CO_2 in the presence of water, in dry atmosphere and in the presence of hydrogen. Higher CO formation rate was observed in the presence of water. Note that the CO formation rates were extremely low in the absence of water; no methane was produced in the dry atmosphere even in the presence of added hydrogen. This suggests that water plays a critical role in this reaction.

Table 5-1 Catalytic behavior of Zn-HPW/TiO_2 catalyst in different reaction atmospheres.

Catalyst	Reaction atmosphere	Formation rate μmol g^{-1} h^{-1}		
		CO	CH_4	H_2
Zn-HPW/TiO_2	CO_2 + H_2O vapor [a]	51	4.1	19
	CO_2 [b]	0.42	0	0
	CO_2 + H_2 [c]	0.51	0	

Reaction conditions: catalyst, 0.1 g; [a] Gas phase pressure, CO_2 0.2 Mpa; H_2O, 15mL; [b] CO_2 pressure, 0.2 MPa; [c] H_2/CO_2 = 1/10; irradiation time, 6h.

Figure 5-18 shows variation of the product amount with the reaction time during the photocatalytic reduction of CO_2 over the Zn-HPW/TiO_2 catalyst. First, the catalyst was exposed to irradiation in nitrogen in the presence of water, but without CO_2. Mostly hydrogen, oxygen and small amounts of carbon monoxide (~2.5 μmol in 10 h) were produced. The small amounts of CO can possibly come from decomposition of surface zinc bicarbonate detected in the calcined catalysts by IR. Second, the system was degassed, and then CO_2 was introduced into the system. Figure 5-18 shows that CO_2 was converted to CO and CH_4 in the presence of H_2O vapor. Some amounts of oxygen were also produced. Note

also the production of H_2, which is probably generated from H_2O splitting. Third, after the catalytic test for 10 h, the reactor was degassed again and N_2 was reintroduced into the system. Note that the amount of CO was larger than that formed in the first step, and only a trace amount of CH_4 was detected (< 1.0 μmol in 10 h). This confirms that the surface zinc carbonate was formed on the catalyst in the presence of CO_2 and its decomposition yields CO. Finally, in the fourth step, CO_2 and water were again introduced to the reactor (Figure 5-18). Similar CO, CH_4, O_2 and H_2 formations were again observed. Interestingly, the reaction rates were similar to those in the second step. This suggests that the Zn-HPW/TiO_2 catalyst can operate with the same activity after several reaction cycles and does not deactivate after the 40 h test.

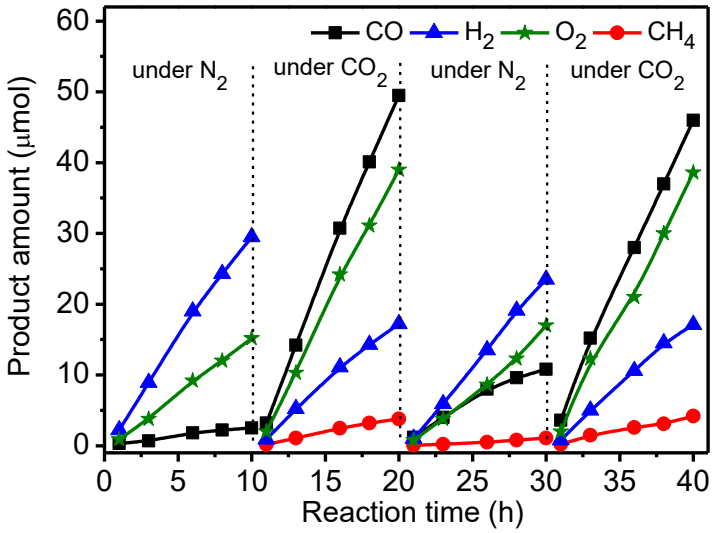

Figure 5-18 Variation of the amount of CO, CH_4 and H_2 production in the reactor with reaction time and repeated uses of the Zn-HPW/TiO_2 catalyst for photocatalytic reduction of CO_2 in the presence of H_2O vapor. Reaction conditions: catalyst, 0.1 g; Gas phase pressure, CO_2 or N_2 0.2 MPa; H_2O, 15mL; irradiation time, 10h. Initially the reactor filled with N_2 and H_2O, after 10h, the system was degassed, and the CO_2 was introduced into the reactor.

The CO_2 photoreduction in the presence of water vapor is likely to proceed via adsorption of the reactants (CO_2 and H_2O) on the catalyst surface followed by photo-induced activation by electron and hole transfer[55]. Adsorption of CO_2 onto the surface of the photo-

catalyst, which results in zinc carbonate may be an initial step in the CO_2 reduction. Single electron transfer to form surface-bound $CO_2/CO_2^{\cdot -}$ is thought to trigger a series of chemical reactions [Eq. (1)]. However, this process is highly thermodynamically unfavorable because of the high negative redox potential of 1.85 V (vs NHE at pH=7)[56, 57]. In contrast, an alternative and more favorable process to reduce CO_2 can occur through the proton-assisted multi-electron transfer with relatively lower redox potential, as shown in Eqs. (1) – (5). The interaction of CO_2 with protons and electrons lowers to some extent the reaction redox potential. This transfer was already suggested for many CO_2 photo-reduction systems[56, 57, 58, 59, 60, 61].

$$CO_2 + e^- \rightarrow CO_2^{\cdot -} \quad (1)$$

$$CO_2 + 2e^- + 2H^+ = CO + H_2O \quad (2)$$

$$CO_2 + 6e^- + 6H^+ = CH_3OH + H_2O \quad (3)$$

$$CO_2 + 8e^- + 8H^+ = CH_4 + 2H_2O \quad (4)$$

$$2H^+ + 2e^- = H_2 \quad (5)$$

It is interesting to note that the rate of water splitting reaction slows down in the presence of CO_2 in comparison with the test under inert atmosphere. This suggests some competition between water and CO_2 for the catalyst active sites, which can produce either hydrogen or CO.

The TEM and STEM EDX indicate the presence of core shell structures with the shell formed by HPW and core, which contains TiO_2. These core-shell structures are expected to create n-p heterojunction (Figure 5-19, band levels from Ref. 34), which would increase charge separation and lifetime of the charge carriers[33]. This could also build up the electrical potential. In the presence of irradiation and electric field, the electrons are transferred to the conduction band of the p-type semiconductor (HPW) and the holes to valence of the n-type semiconductors (TiO_2). This will increase electron concentration over HPW and hole concentration in TiO_2. Consequently, the HPW ability for electron transfer and carbon dioxide reduction will be enhanced. Water oxidation will be enhanced by higher

concentrations of holes on the surface of TiO_2 (Figure 5-19). The characterization techniques did not reveal the presence of ZnO phase. Indeed, XRD and imaging techniques indicate the presence of isolated Zn^{2+} species and possibly extremely small clusters. These highly dispersed zinc species do not have any semiconductor band structure. Zinc located on the surface of HPW seems to play a role of cocatalyst by providing active sites for fixing CO_2 on the surface and facilitating subsequence reduction.

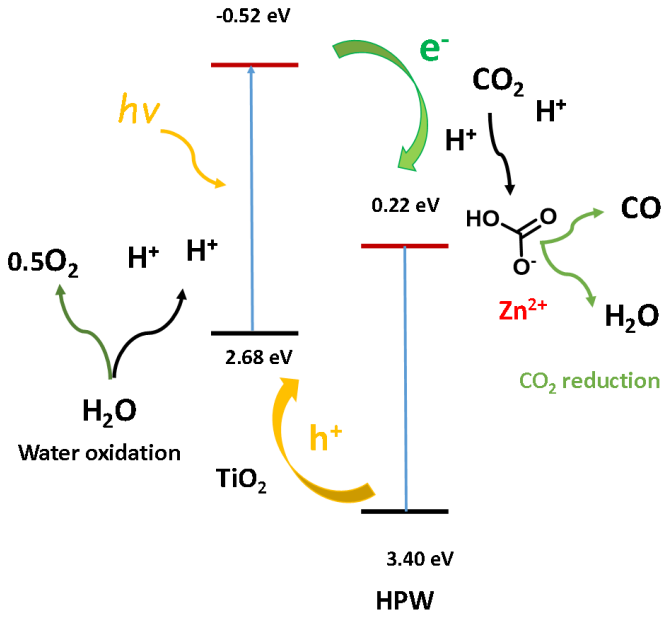

Figure 5-19 Elementary steps in the CO_2 photocatalytic reduction to CO.

Further information about the catalytic role of Zn species in the CO_2 reduction was obtained using in-situ IR spectroscopy (Figure 5-20**)**. The experiments were conducted in a Pyrex cell in the presence of carbon dioxide and water with catalyst exposure to the irradiation through Pyrex and KBr windows. The Zn-HPW/TiO_2 catalyst pellet has been saturated by water vapors and the cell has been filled by CO_2. The pretreated sample exhibits IR bands at 1634, 1510, 1410, 1390 and 1320 cm^{-1}. The bands at 1320 and 1510 cm^{-1} might be assigned to mono-dentate carbonates (Figure 5-20)[62, 63]. The bands at 1634 and 1390 cm^{-1} correspond to bicarbonate (Figure 5-20). Interestingly, the intensity of the band at 1634 cm^{-1} always correlates with the intensity of the bands at 1390 cm^{-1}.

Catalyst exposure to light during 3 h leads to gradual decrease in the intensity of the

bands at 1634 and 1390 cm^{-1} assigned to the bicarbonates containing OH groups. The intensity of the band of OH stretching vibration decreases simultaneously with the bands attributed to bicarbonate. Indeed, the concentration of the bicarbonate containing hydroxyl groups decrease during the reaction. Similar correlation between the intensity of bicarbonate IR band and that of the hydroxyl groups was observed in previous report[46].

The intensities of the bands at 1510 and 1320 cm^{-1} corresponding to mono-dentate carbonates are affected to a lesser extent by the reaction. This indicates higher reactivity of the zinc bicarbonates compared to monodentate carbonates. One of the reasons of the higher reactivity of bicarbonates can be due to localization of protons in a close proximity to the carbonates fragments. The decomposition of these bicarbonates under irradiation provides carbon monoxide and oxygen. The analysis of the gas phase during the in-situ experiments (Figure 5-21) shows the presence of P (<2140 cm^{-1}) and R (>2140 cm^{-1}) branches of gas phase CO[64]. The intensity increases with increase of the time of the treatment of the sample. Thus, these results clearly show that the observed decomposition of carbon bicarbonates results in the carbon monoxide production. The performance of the developed catalyst can further improve by optimization of the reaction conditions and catalyst promotion.

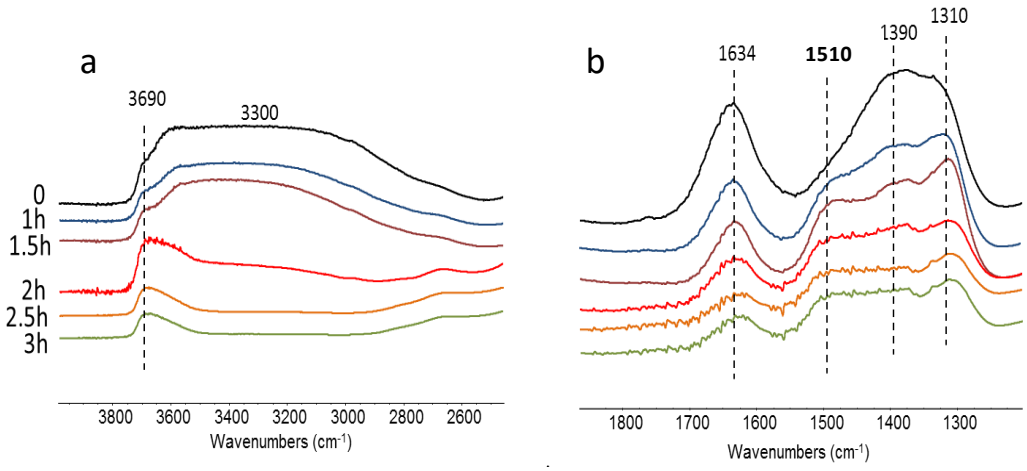

Figure 5-20 In situ FTIR spectra of the Zn-HPW/TiO_2 catalyst in the region of stretching vibrations of hydroxyl groups (a) and carbonates (b) measured under light at different reaction times in CO_2 and H_2O vapor.

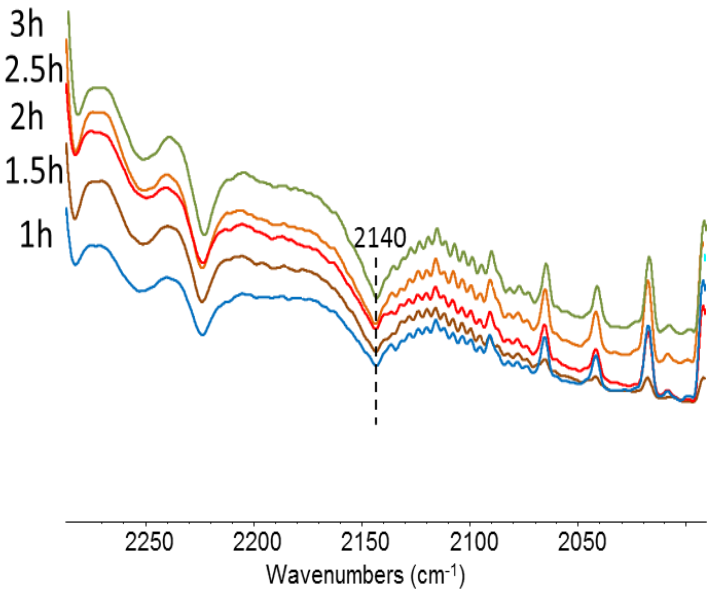

Figure 5-21 In situ FTIR spectra of and gas phase over the Zn-HPW/TiO_2 catalyst measured under light at different reaction times in CO_2 and H_2O vapor.

5.3 Conclusion

Among a series of metal catalysts supported on the composite materials on the basis of TiO_2 and phosphotungstic acid, the zinc-containing counterparts showed the extremely high activity and selectivity in the carbon dioxide reduction to carbon monoxide. The reaction requires the presence of water vapor. The heteropolyacid forms a thin layer over titania nanoparticles. The enhanced activity in photocatalytic reduction of carbon dioxide to carbon monoxide was attributed to the formation of p-n heterojunction, which slows down charge recombination and facilitates electron transport to Zn species highly dispersed over HPW. The CO_2 reduction to CO proceeds via formation of zinc bicarbonate species over the heteropolyacid. No visible deactivation was observed, the catalyst was stable after conducting several reaction cycles for more than 40 h of reaction. No changes of zinc oxidation state or zinc sintering were observed under the reaction conditions. The in-situ IR experiments suggest that reaction involves zinc bicarbonates containing hydroxyl groups. The decomposition of these zinc bicarbonate species under irradiation leads to the selective production of carbon monoxide, while water oxidation leading to O_2 takes place over TiO_2.

5.4 Reference

1. M. Aresta, A. Dibenedetto A. Utilisation of CO_2 as a chemical feedstock: opportunities and challenges. *Dalton T.* **28**, 2975-2992 (2008).

2. V. V. Ordomsky, A.-B. Dros, R. Schwiedernoch and A. Y. Khodakov, Challenges and Role of Catalysis in CO_2 Conversion to Chemicals and Fuels, Nanotechnology in Catalysis: Applications in the Chemical Industry, Energy Development, and Environment Protection, First Edition. Edited by Bert Sels and Marcel Van de Voorde. 2017 Wiley-VCH Verlag GmbH & Co. KGaA.

3. J. Vergara, C. McKesson, M. Walczak, Sustainable energy for the marine sector. *Energy Policy* **49**, 333-345 (2012).

4. Z. Sun, N. Talreja, H. Tao, J. Texter, M. Muhler, J. Strunk. J. Chen. Catalysis of Carbon Dioxide Photoreduction on Nanosheets: Fundamentals and Challenges. *Angew. Chem.* **57**, 7610-7627 (2018).

5. A. El Mekawy, H.M. Hegab, G. Mohanakrishn, A.F Elbaz, M. Bulut, D. Pant, Technological advances in CO_2 conversion electro-biorefinery: A step toward commercialization, *Bioresource Technology*, **215**, 357-370 (2016).

6. M. Mikkelsen, M. Jørgensen, F.C. Krebs, The teraton challenge. A review of fixation and transformation of carbon dioxide. *Energy Environ. Sci.*, **3**, 43-81 (2010).

7. S. Xie, Q Zhang, G. Liu, Y. Wang, Photocatalytic and photoelectrocatalytic reduction of CO_2 using heterogeneous catalysts with controlled nanostructures, *Chem. Commun.*, **52**, 35-59 (2016).

8. W. Tu, Y. Zhou, Z. Zou, Photocatalytic conversion of CO_2 into renewable hydrocarbon fuels: state-of-the-art accomplishment, challenges, and prospects. *Adv. Mater.* **26**, 4607-4626 (2014).

9. A. Corma, H. Garcia, Photocatalytic reduction of CO_2 for fuel production: Possibilities and challenges. *J.Catal.* **88**, 168-175 (2013).

10. Y. Ma, X. Wang, Y. Jia, X. Chen, H. Han, C. Li, Titanium dioxide-based nanomaterials for photocatalytic fuel generations. *Chem. Rev.,* **114**, 9987-10043 (2014).

11. M. Marszewski, S. Cao, J. Yu, M. Jaroniec. Semiconductor-based photocatalytic CO_2 conversion. *Materials Horizons*, **2**, 261-278 (2015).

12. X. Chang, T. Wang, J. Gong, CO_2 photo-reduction: insights into CO_2 activation and reaction on surfaces of photocatalysts, *Energy Environ. Sci.* **9**, 2177–2196 (2016).

13. S. N. Habisreutinger, L. Schmidt-Mende and J. K. Stolarczyk Photocatalytic Reduction of CO_2 on TiO_2 and Other Semiconductors, *Angew. Chem. Int. Ed.,* **52**, 7372 – 7408 (2013).

14. N. Shehzada, M. Tahir, K. Joharia, T. Murugesan, M. Hussaind, A critical review on TiO_2 based photocatalytic CO2 reduction system: Strategies to improve efficiency, *J. CO_2 Util.* **26**, 98–122 (2018).

15. J. Ran, M. Jaroniec and S.Z. Qiao, Cocatalysts in Semiconductor-based Photocatalytic CO2 Reduction: Achievements, Challenges, and Opportunities, *Adv. Mater.* **30**, 1704649 (2018).

16. M. Edelmannová, K.-Y. Lin, J. C.S. Wu, I. Troppová, L. Čapek, K. Kočí, Photocatalytic hydrogenation and reduction of CO_2 over CuO/TiO_2 photocatalysts, *Appl. Surf. Sci.* **454**, 313–318 (2018).

17. H. Jiang, K.-I. Katsumata, J. Hong, A. Yamaguchi, K. Nakata, C. Terashima, N. Matsushita, M. Miyauchi, A. Fujishima, Photocatalytic reduction of CO_2 on Cu_2O-loaded Zn-Cr layered double hydroxides, *Appl. Catal. B* **224**, 783–790 (2018).

18. L.-Y. Lin, S. Kavadiya, B. B. Karakocak, Y. Nie, R. Raliya, S. T. Wang, M. Y. Berezin, P. Biswas, ZnO_{1-x}/carbon dots composite hollow spheres: Facile aerosol synthesis and superior CO_2 photoreduction under UV, visible and near-infrared irradiation, *Appl. Catal. B* **230**, 36-48 (2018).

19. P. Li, Y. Zhou, Z. Zhao, Q. Xu, X. Wang, M. Miao, Z. Zou, Hexahedron prism-anchored octahedronal CeO_2: crystal facet-based homojunction promoting efficient solar fuel synthesis, *J. Am. Chem. Soc.* **137**, 9547–9550 (2015).

20. Q. Liu, Y. Zhou, J. Kou, X. Chen, Z. Tian, J. Gao, S. Yan, Z. Zou, High-yield synthesis of ultralong and ultrathin Zn_2GeO_4 nanoribbons toward improved photocatalytic reduction of CO_2 into renewable hydrocarbon fuel, *J. Am. Chem. Soc.* **132**, 14385–14387 (2010).

21. S.C. Yan, S. Ouyang, J. Gao, M. Yang, J.Y. Feng, X.X. Fan, L.J. Wan, Z.S. Li, J.H. Ye, Y. Zhou, Z.G. Zou, A room-temperature reactive-template route to mesoporous $ZnGa_2O_4$ with improved photocatalytic activity in reduction of CO_2, *Angew. Chem. Int. Ed.* **49**, 6400–6404 (2010).

22. H. Cheng, B. Huang, Y. Liu, Z. Wang, X. Qin, X. Zhang, Y. Dai, An anion exchange approach to Bi_2WO_6 hollow microspheres with efficient visible light photocatalytic reduction of CO_2 to methanol, *Chem. Commun.* **48**, 9729–9731 (2012).

23. C. Cometto, R. Kuriki, L. Chen, K. Maeda, T.-Chu Lau, O. Ishitani and M. Robert, A Carbon Nitride/Fe Quaterpyridine Catalytic System for Photostimulated CO_2-to-CO Conversion with Visible Light, *J. Am. Chem. Soc.* **140**, 7437−7440 (2018).

24. R. Li, W. Zhang and K. Zhou, Metal–Organic-Framework-Based Catalysts for Photoreduction of CO_2, *Adv. Mater.* **30**, 1705512 (2018).

25. J. Fu, B. Zhu, C. Jiang, B. Cheng, W. You, J. Yu, Hierarchical Porous O-Doped g-C_3N_4 with Enhanced Photocatalytic CO_2 Reduction Activity, *Small* **13**, 1603938–1603947 (2017).

26. S. Bai, X. Wang, C. Hu, M. Xie, J. Jiang, Y. Xiong, Two-dimensional g-C_3N_4: an ideal platform for examining facet selectivity of metal co-catalysts in photocatalysis, *Chem. Commun.* **50**, 6094–6097 (2014).

27. S. Ye, R. Wang, M.-Z. Wu, Y.-P. Yuan, A review on g-C_3N_4 for photocatalytic water splitting and CO_2 reduction, *Appl. Surf. Sci.* **358**, 15–27 (2015).

28. P. Xia, B. Zhu, J. Yu, S. Cao, M. Jaroniec, Ultra-thin nanosheet assemblies of graphitic carbon

nitride for enhanced photocatalytic CO_2 reduction, *J. Mater. Chem. A* **5**, 3230–3238 (2017).

29. J. Yu, K. Wang, W. Xiao, B. Cheng, Photocatalytic reduction of CO_2 into hydrocarbon solar fuels over g-C_3N_4–Pt nanocomposite photocatalysts, *Phys. Chem. Chem. Phys.* **16**, 11492-11501 (2014).

30. J. Yu, J. Jian, B. Cheng, M. Jaroniec, A noble metal-free reduced graphene oxide–CdS nanorod composite for the enhanced visible-light photocatalytic reduction of CO_2 to solar fuel, *J. Mater. Chem. A* **2**, 3407–3416 (2014).

31. K. K. Sakimoto, A. B. Wong, P. Yang, Self-photosensitization of nonphotosynthetic bacteria for solar-to-chemical production, *Science* **351**, 74-77 (2016).

32. Y. S. Chaudhary, T. W. Woolerton, C. S. Allen, J. H. Warner, E. Pierce, S. W. Ragsdale, F. A. Armstrong,Visible light-driven CO_2 reduction by enzyme coupled CdS nanocrystals, *Chem. Commun.* **48**, 58 (2012).

33. H. Wang, L. Zhang, Z. Chen, J. Hu, S. Li, Z. Wang, J. Liu and X. Wang, Semiconductor heterojunction photocatalysts: design, construction, and photocatalytic performances, *Chem. Soc. Rev.* **43**, 5234-5244 (2014).

34. Z. Sun, Y. Zhang, N. Li, L. Xu and T. Wang Enhanced photoconductivity of polyoxometalate–TiO_2 composite for gas sensing applications, *J. Mater. Chem. C,* **3**, 6153-6157 (2015).

35. P. Meng, J. Huang, X. Liu, In-situ solid phase thermal transformation of self-assembled melamine phosphotungstates produce efficient visible light photocatalysts, *J. Colloid Interf. Sci.* **551**, 208–218 (2019).

36. P. Meng, H. Heng, Y. Sun, J. Huang, J. Yang, X. Liu, Positive effects of phosphotungstic acid on the in-situ solid-state polymerization and visible light photocatalytic activity of polyimide-based photocatalyst, *Appl. Catal. B* **226**, 487–498 (2018).

37. P. D. Tran, L. H. Wong, J. Barberbcd and J. S. C. Loo, Recent advances in hybrid photocatalysts for solar fuel production, *Energy Environ. Sci.* **5**, 5902-5918 (2002).

38. Yu X, De Waele V, Löfberg A, Ordomsky V, Khodakov AY. Selective photocatalytic conversion of methane into carbon monoxide over zinc-heteropolyacid-titania nanocomposites. *Nat. Commun.,* **10**, 700 (2019).

39. W. Tu, Y. Zhou and Z. Zou, Photocatalytic Conversion of CO_2 into Renewable Hydrocarbon Fuels: State-of-the-Art Accomplishment, Challenges, and Prospects, *Adv. Mater.,* **26**, 4607-4626 (2014).

40. X. Chen, Y. Li, X. Pan, D. Cortie, X. Huang, Z. Yi,. Photocatalytic oxidation of methane over silver decorated zinc oxide nanocatalysts. *Nat. Commun.,* **7**, 12273 (2016).

41. J. Zhang, L. Sun, C. Liao, C. Yan, A simple route towards tubular ZnO. *Chem. Commun.* **12**, 262-263 (2002).

42. Shi J, et al. Photoluminescence characteristics of TiO_2 and their relationship to the photoassisted

reaction of water/methanol mixture. *J. Phys. Chem. C* **111**, 693-699 (2007).

43. Xie S, Wang Y, Zhang Q, Deng W, Wang Y. MgO-and Pt-promoted TiO_2 as an efficient photocatalyst for the preferential reduction of carbon dioxide in the presence of water. *ACS Catal.* **4**, 3644-3653 (2014).

44. H. Shi, T. Zhang, T. An, B. Li, X. Wang, Enhancement of photocatalytic activity of nano-scale TiO_2 particles co-doped by rare earth elements and heteropolyacids. *J. Colloid Interf. Sci.* **380**, 121-127 (2012).

45. H. Li, X. Jiao, L. Li, N. Zhao, F. Xiao, W. Wei, Y. Sun and B. Zhang, Synthesis of glycerol carbonate by direct carbonylation of glycerol with CO_2 over solid catalysts derived from Zn/Al/La and Zn/Al/La/M (M = Li, Mg and Zr) hydrotalcites, *Catal. Sci. Technol.,* **5**, 989-1005 (2015).

46. E.-M. Köck, M. Kogler, T. Bielz, B. Klötzer and S. Penner, In Situ FT-IR Spectroscopic Study of CO_2 and CO Adsorption on Y_2O_3, ZrO_2, and Yttria-Stabilized ZrO_2, *J. Phys. Chem. C* **117**, 17666−17673 (2013).

47. G Busca, V Lorenzelli, Infrared spectroscopic identification of species arising from reactive adsorption of carbon oxides on metal oxide surfaces, *Materials Chemistry* **7**, 89-126 (1982).

48. M. Tao, L. Xue, Z. Sun, S. Wang, X. Wang, J. Shi, Tailoring the synergistic Bronsted-Lewis acidic effects in heteropolyacid catalysts: Applied in esterification and transesterification reactions. *Sci. Rep*. **5**, 13764 (2015).

49. R. Lindsay, E. Michelangeli, B.G. Daniels, T.V. Ashworth, A.J. Limb, G. Thornton G, A. Gutiérrez-Sosa, A. Baraldi, R. Larciprete, and S. Lizzit, Impact of Defects on the Surface Chemistry of ZnO (000$\bar{1}$)$^{-}$ O. *J. Am. Chem.Soc.* **124**, 7117-7122 (2002).

50. O. Carp, C.L. Huisman, A. Reller, Photoinduced reactivity of titanium dioxide. Prog. *Solid State Chem.,* **32**, 33-177 (2004).

51. A. Bouibes, A. Zaoui, D. Tunega, Bonds, bands and elasticity of smithsonite rock. *Solid State Commun.,* **166**, 76-82 (2003).

52. M. Gancheva, M. Markova-Velichkova, G. Atanasova, D. Kovacheva, I. Uzunov, R. Cukeva, Design and photocatalytic activity of nanosized zinc oxides. *Appl. Surf. Sci.,* **368**, 258-266 (2016).

53. C. Wöll, The chemistry and physics of zinc oxide surfaces. *Prog. Surf. Sci.* **82**, 55-120 (2007).

54. M.C. Biesinger, L.W.M. Laua, A.R. Gerson, R.S.C. Smart, Resolving surface chemical states in XPS analysis of first row transition metals, oxides and hydroxides: Sc, Ti, V, Cu and Zn, *Appl. Surf. Sci.* **257**, 887-898 (2010).

55. P. Kar, S. Zeng, Y. Zhang, E. Vahidzadeh, A. Manuel, R. Kisslinger, K. M.Alama, U. K. Thakur, N. Mahdi, P. Kumar, K. Shankar, High rate CO_2 photoreduction using flame annealed TiO_2 nanotubes, *Appl. Catal. B* **243**, 522-536 (2019).

56. S.N. Habisreutinger L. Schmidt-Mende, J.K. Stolarczyk, Photocatalytic reduction of CO_2 on TiO2 and other semiconductors. *Angew. Chem. Int. Ed.,* **52**, 7372-7408 (2013).

57. J. Lee, D.C. Sorescu, X. Deng, Electron-induced dissociation of CO_2 on TiO_2 (110). *J. Am. Chem. Soc.* **133**, 10066-10069 (2011).

58. L. Yuan, Y.-L. Xu, Photocatalytic conversion of CO_2 into value-added and renewable fuels. *Appl. Surf. Sci,* **342**, 154-167 (2015).

59. S. Nahar, M. Zain, A.A.H. Kadhum H.A. Hasan, M.R. Hasan, Advances in photocatalytic CO_2 reduction with water: a review. *Materials* **10**, 629 (2017).

60. Q. Xiang, B. Cheng, J. Yu, Graphene-based photocatalysts for solar-fuel generation. *Angew. Chem. Int. Ed.,* **54**, 11350-11366 (2015).

61. Y. Izumi, Recent advances in the photocatalytic conversion of carbon dioxide to fuels with water and/or hydrogen using solar energy and beyond. Coord. *Chem. Rev.,* **257**, 171-186 (2013).

62. C. Su, D.L. Suarez, In situ infrared speculation of adsorbed carbonate on aluminum and iron oxides. *Clays and Clay Minerals,* **45**, 814-825 (1997).

63. R.L. Frost, W.N. Martens, D.L. Wain, M.C. Hales, Infrared and infrared emission spectroscopy of the zinc carbonate mineral smithsonite, *Spectrochim. Acta Part A* **70**, 1120–1126 (2008).

64. E. Garrone, B. Fubini, B. Bonelli, B. Onida, C.O. Areán, Thermodynamics of CO adsorption on the zeolite Na-ZSM-5 A combined microcalorimetric and FTIR spectroscopic study, *Phys. Chem. Chem. Phys.* **1**, 513-518 (1999).

Chapter 6. Selective Deposition of Cobalt and Copper Oxides on $BiVO_4$ Facets for Enhancement of CO_2 Photocatalytic Reduction to Hydrocarbons

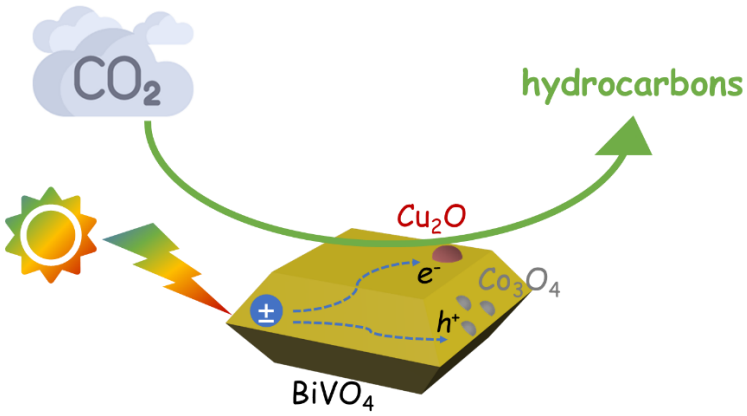

Abstract

The nanostructure of a semiconductor is a crucial parameter for efficient photocatalytic performance. Hereby, we have synthesized monoclinic bismuth vanadate ($BiVO_4$) crystals with controlled ratio of {010} and {110} facets. The selective deposition of CuO_x and CoO_x over {010} and {110} facets has been performed using photo-reduction and photo-oxidation methods, respectively. It resulted in a highly efficient charge separation of photogenerated electrons and holes and enhancement of the photocatalytic reduction of CO_2 by H_2O into hydrocarbons, including CH_4, C_2H_6 and C_3H_8. The controlled cocatalyst deposition different semiconductor facets provide a strategy for the synthesis of hydrocarbons from CO_2 and H_2O by efficient charge separation.

6.1 Introduction

Carbon dioxide is widely recognized as a major greenhouse gas that causes global environmental problems[1]. Worldwide consumption of limited fossil fuels not only accelerates their depletion but also results in production of excessive atmospheric CO_2. In this regard, transformation of CO_2 to the fuels is a promising method for simultaneous solution of energy and environmental problems[2]. In 1979, Japanese researcher Fujishima and Honda reported [3] for the first time the photocatalytic reduction of CO_2 into organic compounds using semiconductor catalysts such as SiC, GaP, and TiO_2. Since then, numerous works have focused on the development of new semiconductor materials for reduction of CO_2 [4, 5, 6, 7]. Various semiconductors were proven to be effective in photocatalytic reduction of CO_2, for example: TiO_2 [8, 9], Ga_2O_3 [10, 11], Zn_2GeO_4 [12, 13], WO_3 [14], Bi_2WO_6 [15, 16] and so on. The main products of photocatalytic reduction of CO_2 by water are usually methane, higher hydrocarbons, methanol, ethanol, formaldehyde, formic acid or CO [7].

Although a lot of progress has been made in this field, the activity of photocatalytic reduction of CO_2 is still insufficient due to poor charge separation and low quantum efficiency. In addition, photocatalytic transformation of CO_2 is limited due to low adsorption over the catalyst and difficulties in the activation of the stable CO_2 molecule.

In the photocatalytic reaction, the difference in the morphology of the catalyst often has a significant impact on the photocatalytic performance[17]. The difference in catalyst morphology is mainly reflected by the exposure of different crystal facets, or the proportion of exposed crystal facets. In recent years, more and more reports have addressed the effects of exposed crystals on photocatalytic properties. It is generally believed that photocatalysts exhibit better catalytic properties when more active crystal facets are exposed to reacting molecules [18, 19]. In many classical photocatalytic semiconductors, it has been shown that controlling the exposure of a suitable crystal facets is an effective strategy to improve photocatalytic performance, for example: TiO_2 [20, 21], $BiVO_4$ [22, 23, 24], Cu_2O [25, 26] and CeO_2 [27]. In photocatalytic reactions, the high recombination rate of photogenerated electrons and holes is a major factor limiting its photocatalytic performance. The recombination rate of

photogenerated electrons and holes can be greatly reduced with increase of activity by deposition of co-catalysts over semiconductors. In general, the role of co-catalyst can be relevant to the following processes: (1) better charge separation, (2) higher activity and selectivity of CO_2 reduction by suppression of side reactions and (3) enhanced stability of photocatalyst[28].

Bismuth vanadate ($BiVO_4$) is a promising visible light-driven semiconductor photocatalyst with low production cost, low toxicity, high stability and narrow band gap (2.4 eV) with good response to visible light excitation. $BiVO_4$ has demonstrated as efficient catalyst for the reduction of CO_2 into methanol and ethanol [29, 30]. However, the photocatalytic efficiency of $BiVO_4$ is low because of relatively low visible-light utilization and inefficient charge separation. The formation of Z-scheme photocatalytic systems that mimic natural photosynthesis with photocatalytic systems and electron mediator is a promising strategy to improve charge separation [31]. According to a few reports, the photocatalytic efficiency can be improved by Z-scheme on the $BiVO_4$ catalyst [32, 33, 34].

Herein, the separation of electrons and holes in bismuth vanadate ($BiVO_4$). is improved by control of the semiconductor morphology. The photocatalytic reduction of CO_2 under irradiation is significantly enhanced by selective photo-deposition of Cu and Co co-catalysts over different facets providing Z-scheme charge flow.

6.2 Result and discussion

6.2.1 Monoclinic $BiVO_4$ crystal with designable facets

Uniform truncated tetragonal bipyramidal morphology $BiVO_4$ with designable exposed facets has been prepared using hydrothermal method with variation of NaCl content [24]. XRD measurements indicate that these samples exhibit a monoclinic structure [23, 35] (Figure 6-1). The intensity of the (040) diffraction peak at 30.5 2θ depends on the concentration of NaCl. Increase of NaCl concentration from 0.04 to 0.5 M leads to increase of intensity with subsequent rapid decrease when the concentration reaches 2 M, indicating that NaCl affects the morphology of $BiVO_4$.

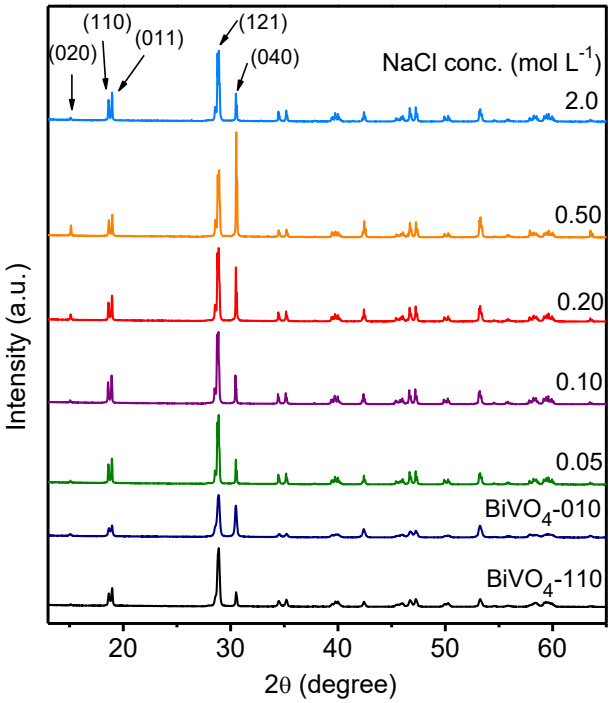

Figure 6-1 XRD patterns of the monoclinic $BiVO_4$ samples with different concentration of NaCl and $BiVO_4$ with predominately exposed {010} and {110} facets.

The SEM images show that the $BiVO_4$ crystals were composed of uniformed single crystal with truncated tetragonal bipyramidal shape (Figure 6-2b-e) when the concentration of NaCl is between 0.04 - 0.50 M. However, the $BiVO_4$ crystals has an irregular morphology (Figure 6-2a, f) when NaCl was not included or if the concentration is too high. Interestingly, the morphology of monoclinic $BiVO_4$ crystals changed gradually with the concentration of NaCl. Crystal model of monoclinic $BiVO_4$ crystals with truncated tetragonal bipyramidal shape contains two {010} facets on the top and bottom and eight {110} facets on the edges (Figure 6-3). The fraction of {010} facets has been calculated by the crystal model equation. The percentages of {010} facets can be calculated as follows [21, 24].

$S_{010} = 2a^2$,

$S_{110} = 8 * 0.5 * (a + b) * L_{DE}$, $L_{DE} = L_{CE} – L_{CD}$, $L_{CE} = 0.5b / \cos\theta$, $L_{CD} = 0.5a / \cos\theta$,

$S_{110} = 2 * (b^2 – a^2) / \cos\theta$,

$F_{010\%} = S_{110} / (S_{110} + S_{010}) = 2a^2 / 2 * (b^2 – a^2) / \cos\theta = \cos\theta / (\cos\theta + b^2 / a^2 –1)$

Here θ is the theoretical value (66.07°) for the angle between the {010} and {110} facets of monoclinic $BiVO_4$ crystal. Note that the fraction of {010} facets increases significantly with the increase of NaCl concentration from 26 % to 75 % (Table 6-1).

$BiVO_4$-010 and $BiVO_4$-110 samples with predominantly {010} and {110} facets have been synthesized. The SEM images confirm that the $BiVO_4$ crystals have {010} and {110} facets predominantly exposed (Figure 6-2). XRD measurements also confirm synthesis of $BiVO_4$-010 and $BiVO_4$-110 samples with predominantly {010} and {110} facets (Figure 6-1).

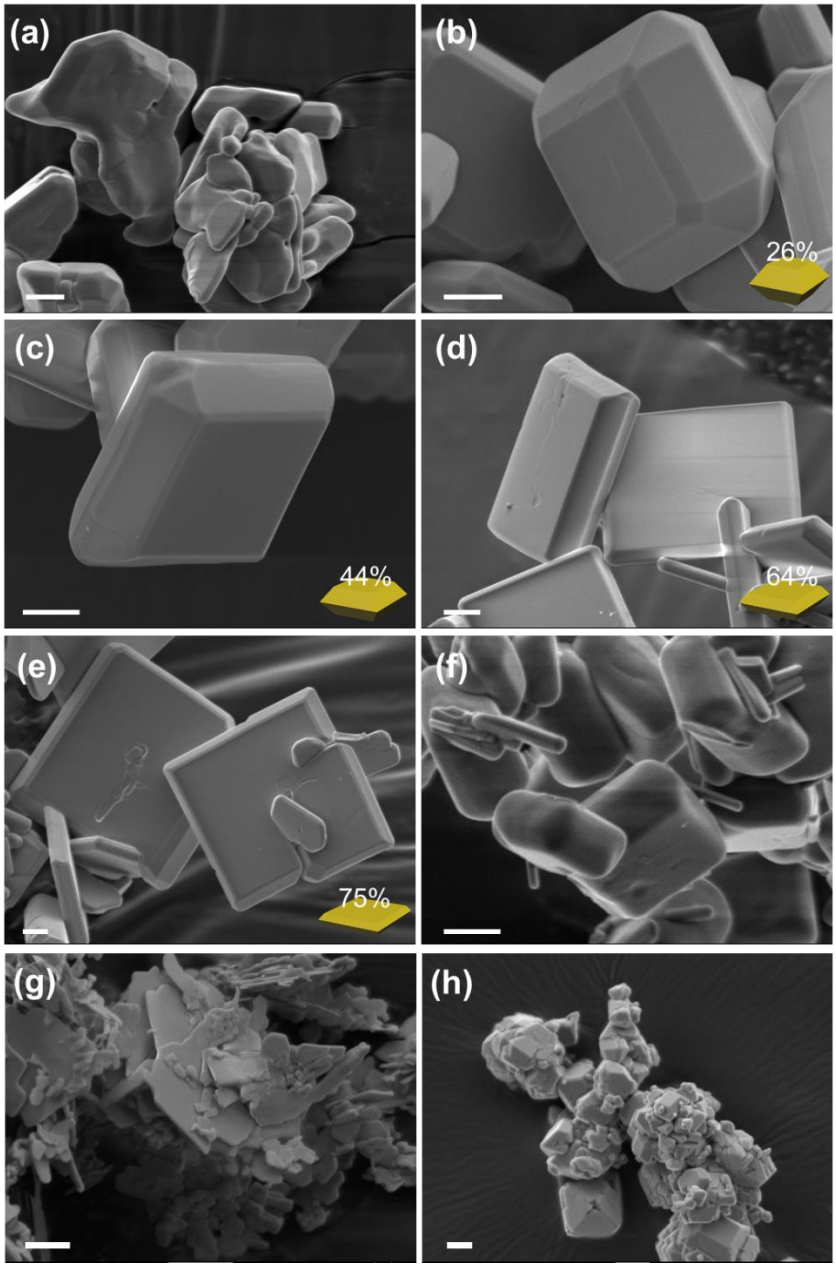

Figure 6-2 SEM images of $BiVO_4$ samples synthesized with different concentration of NaCl. NaCl concentration: (a) 0 M, (b) 0.04 M, (c) 0.10 M, (d) 0.20 M, (e) 0.50 M, (f) 2.0 M, (g) $BiVO_4$-010, (h) $BiVO_4$-110. Scale bar: 1.0 μm.

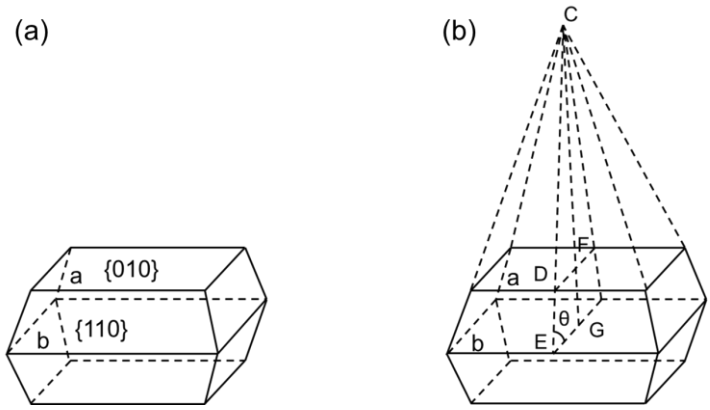

Figure 6-3 Crystal model of monoclinic $BiVO_4$ crystals with truncated tetragonal bipyramidal shape.

The UV-Vis diffuse reflectance spectra of the $BiVO_4$ crystals with different concentration of NaCl is shown in Figure 6-4. The samples exhibit intense absorption in the ultraviolet region (< 400 nm) as well as visible light region (< 500 nm). The band gap energy for different morphology samples estimated using Tauc's plots of UV-Vis spectra is the same, being 2.3 eV (Table 6-1).

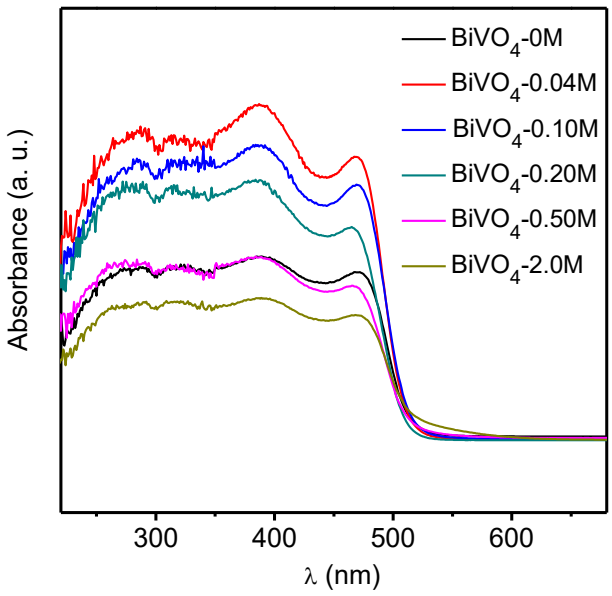

Figure 6-4 UV-Vis spectra of $BiVO_4$ samples synthesized with different concentration of NaCl.

Photoluminescence spectroscopy has been used to evaluate the recombination of holes and electrons of different $BiVO_4$ catalysts. A luminescence band centered at 620 nm was observed for monoclinic $BiVO_4$ crystals (Figure 6-5). It is generally accepted that photoluminescence is produced by the recombination of photogenerated carriers on a semiconductor, and therefore the higher intensity of the luminescent band means that the probability of photogenerated carrier recombination is higher [36]. For the series of $BiVO_4$ samples, the intensity of the luminescence band decreases in the order of $BiVO_4$-0.04M > $BiVO_4$-0M > $BiVO_4$-2.0M > $BiVO_4$-0.50M > $BiVO_4$-0.10M > $BiVO_4$-0.20M, indicating that $BiVO_4$-0.20M with 64 % of {010} facet has the lowest ability of electron-hole recombination. Note that the irregular $BiVO_4$ crystals show a higher ability of electron-hole recombination. In other words, truncated tetragonal bipyramidal shape is good for electron-hole separation.

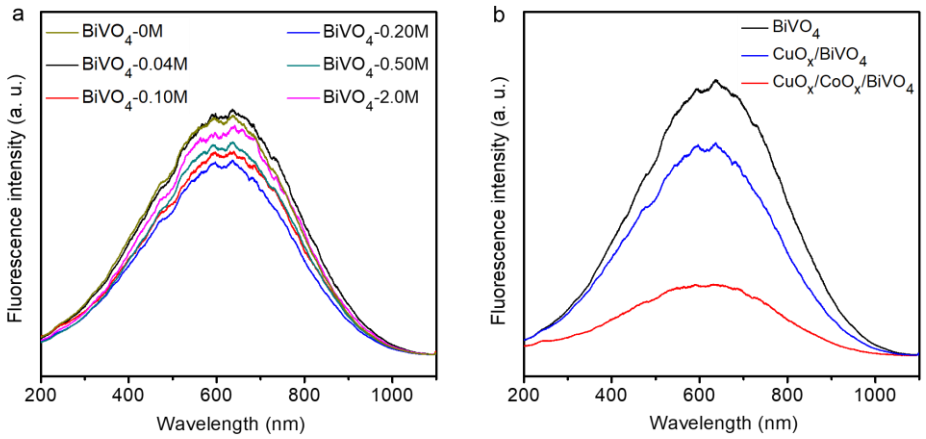

Figure 6-5 (a) Photoluminescence spectra of $BiVO_4$ samples synthesized with different concentration of NaCl. (b) Photoluminescence spectra of $BiVO_4$-0.20M crystal with selective photo-deposited the metal oxides.

Table 6-1 Fraction of {010} facets, specific surface areas, bandgap energies of $BiVO_4$ samples with different NaCl concentration.

Sample	Fraction of {010} facets (%)	Surface area ($m^2\ g^{-1}$)	Bandgap energy (eV)
$BiVO_4$-0M	/	1.3	2.3
$BiVO_4$-0.04M	26	2.2	2.3
$BiVO_4$-0.10M	44	2.8	2.3
$BiVO_4$-0.20M	64	2.9	2.3
$BiVO_4$-0.50M	75	2.6	2.3
$BiVO_4$-2.0M	/	1.4	2.3

ZnO_x, WO_x, FeO_x and CuO_x were loaded onto series of $BiVO_4$ samples through photo-reduction deposition technique (Figure 6-6). SEM images show that CuO_x nanoparticles were selectively deposited onto the {010} facets of $BiVO_4$ crystal (Figure 6-7b). Several oxide co-catalysts MnO_x, PbO_2 and CoO_x have been deposited by photo-oxidation using $NaIO_3$ as sacrificial agent on the surface of $CuO_x/BiVO_4$ catalyst. SEM analysis demonstrates that these oxides are located on the {110} facets of $BiVO_4$ crystal (Figure 6-6, 6-7c).

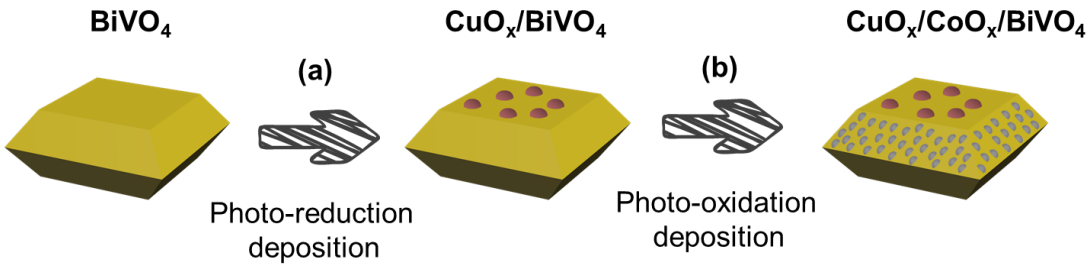

Figure 6-6 Schematic of the synthesis of $CuO_x/CoO_x/BiVO_4$ catalyst.

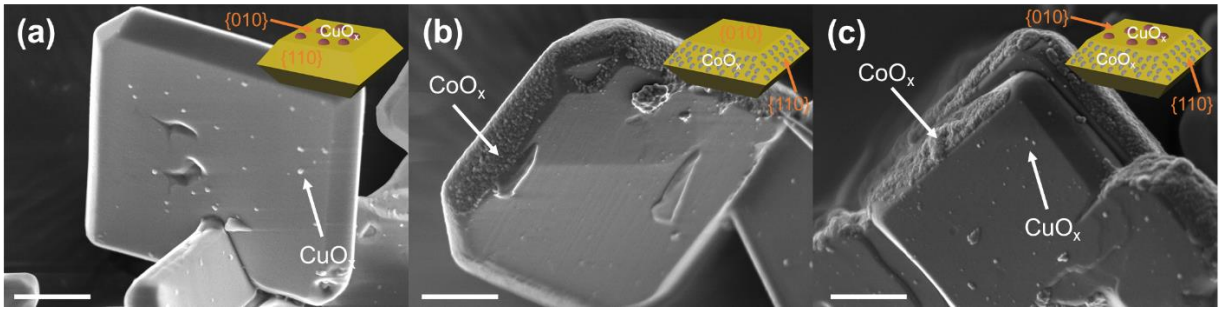

Figure 6-7 SEM images of $BiVO_4$-0.20M sample with selective photo-deposited metal oxides: (a) $CuO_x/BiVO_4$, (b) $CoO_x/BiVO_4$, (c) $CuO_x/CoO_x/BiVO_4$.

To provide further insights into the copper and cobalt state in $CoO_x/CuO_x/BiVO_4$ catalyst was characterized by XPS (Figure 6-8). The binding energies of Cu $2p_{3/2}$ for the catalyst was about 932.7 eV, which could be attributed to either Cu^0 or Cu^I [37, 38, 39]. The positions of the Cu L_3VV Auger lines for these samples were centered at 916.7 eV, corresponding to that of Cu^I in Cu_2O [40]. Figure 6-8 represents the Co 2p XPS spectra of the catalyst. Co $2p_{3/2}$ binding energies at 781.5 eV, absence of the satellite structure and $2p_{3/2}$-$2p_{1/2}$ spin-orbit splitting (ΔE) of 15.1 eV indicates on the presence of Co_3O_4 phase [41, 42, 43].

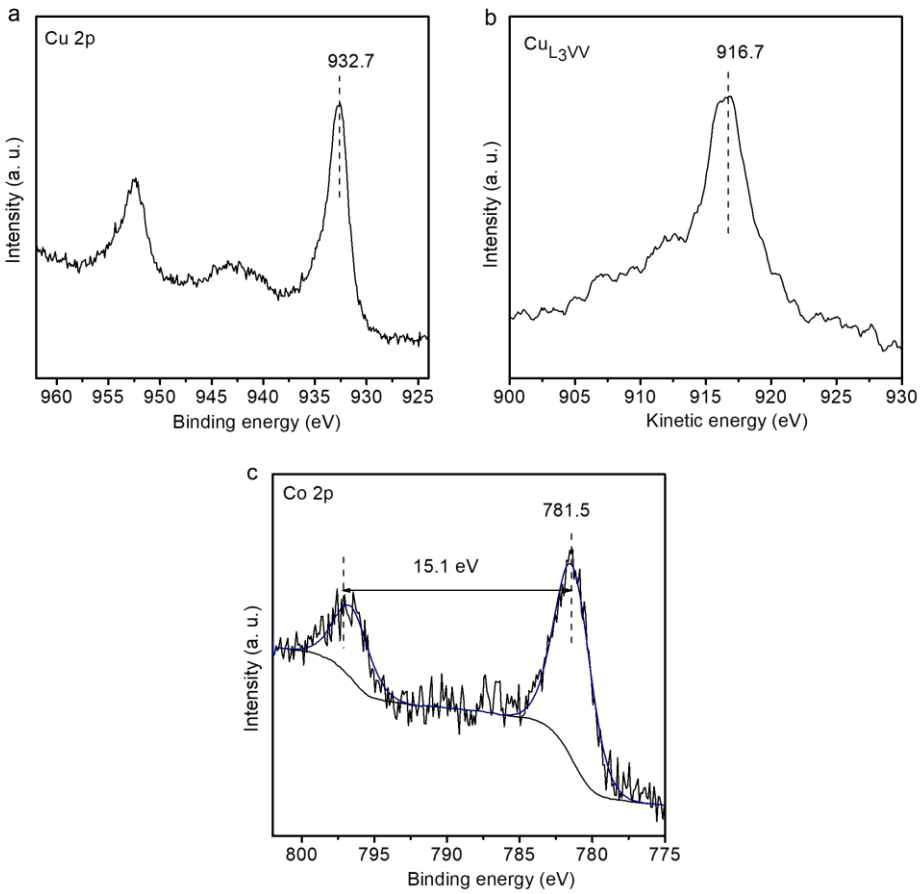

Figure 6-8 XPS spectra for the CuO_x/CoO_x /$BiVO_4$ catalyst. (a) Cu 2p spectra, (b) Cu L_3VV Auger spectra and (c) Co 2p spectra.

6.2.2 Catalytic performance

Figure 6-9 demonstrates the effect of photo-reductive deposition of different metal oxides over $BiVO_4$-0.20M sample, which according to our characterization study demonstrates the most efficient charge separation. Methane, ethane, propane, formaldehyde and methanol were formed as the products of the reaction of CO_2 reduction by H_2O. The deposition of W and Fe does not lead to significantly improve of the catalytic performance in comparison with the parent $BiVO_4$-0.20M which is almost inactive. The main products of the reaction were CO and methane. In the presence of ZnO_x activity significantly increases to 2 $\mu molg^{-1}h^{-1}$ with increase of the contribution of methane in the products in comparison with CO. The highest activity (6.8 $\mu molg^{-1}h^{-1}$) has been observed over $CuO_x/BiVO_4$-0.20M

with formation of broad range of hydrocarbons (methane, ethane and propane) and oxygenates (formaldehyde and methanol).

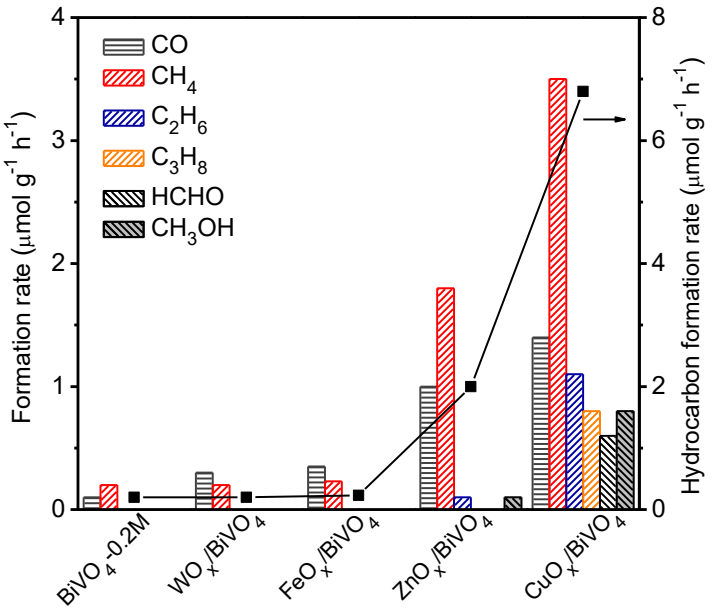

Figure 6-9 Effect of metal oxides on the performance of $BiVO_4$-0.20M for photocatalytic reduction CO_2 with H_2O.

Further we have studied effect of CuO_x deposition over $BiVO_4$ catalyst with systematically changed fraction of {010} facets (Figure 6-10). As compared to $BiVO_4$ with an irregular morphology, which was synthesized without addition of NaCl, $CuO_x/BiVO_4$ catalysts with a uniform truncated tetragonal bipyramidal morphology exhibited higher formation rate of hydrocarbon fuels. Interestingly, the photocatalytic performance depends on the fraction of {010} facets. The formation rate of hydrocarbons has bell shaped curve with maximum at the fraction of exposed {010} facets 64 % with formation rate 6.8 $\mu molg^{-1}h^{-1}$. $CuO_x/BiVO_4$-010 and $CuO_x/BiVO_4$-110 with predominantly {010} and {110} facets demonstrate lower formation rate of hydrocarbons in comparison with catalysts containing both facets.

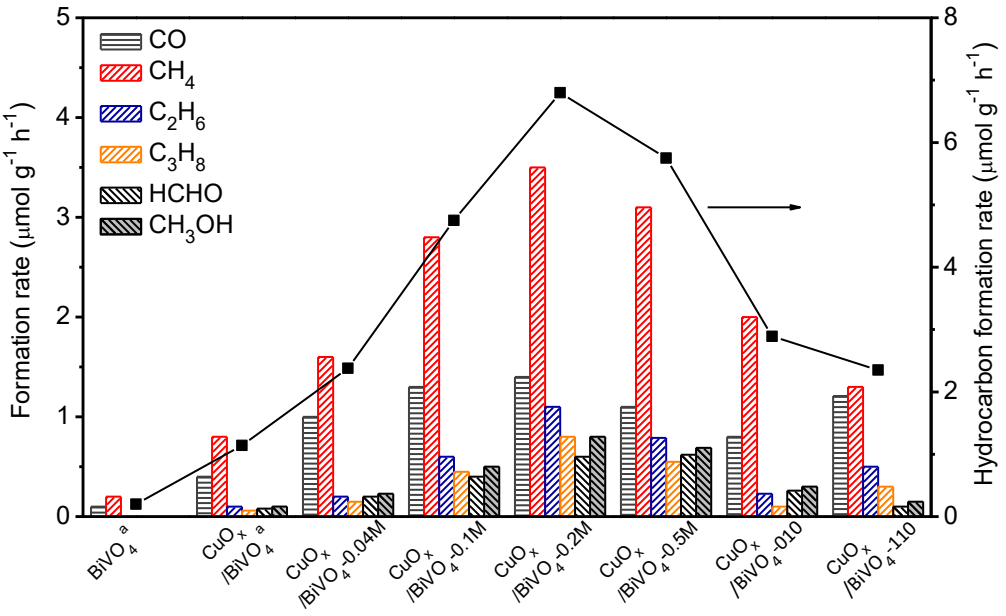

Figure 6-10 Effect of the fraction of {010} facets on the photocatalytic performance of $CuO_x/BiVO_4$ catalyst for reduction CO_2 with H_2O. [a] $BiVO_4$ with an irregular morphology (NaCl concentration: 0M).

Recent studies have demonstrated that photogenerated electrons and holes in monoclinic $BiVO_4$ crystals will migrate to the {010} and {110} facets respectively [23]. Li and coworker [44] evaluated the energy levels of {010} and {110} facets of $BiVO_4$ crystals by DFT calculation method. They observed a slight difference in energy of the valence and conductive band between the {010} and {110} facets which suggested that the electron transfer from {110} to {010} facets is feasible thermodynamically. Thus, it can be expected that the coexistence of the {010} and {110} facets with the appropriate ratio will favor the separation of photogenerated electrons and holes. This order fits well with obtained photoluminescence measurement, confirming that the {010} and {110} facet coexistence and appropriate ratio facilitates the separation of electron-hole pairs. Furthermore, the order of the efficiency of electron-hole pairs separation is the same as that of the formation rate of hydrocarbon fuels for the photocatalytic reduction of CO_2 with H_2O (Figure 6-10). Therefore, we believe that the ability of electron-hole pairs separation is a key factor in determining the catalytic behavior of $CuO_x/BiVO_4$ with different fraction of {010} facets.

Table 6-2 displays the photocatalytic performance data of $CuO_x/BiVO_4$ with different CuO_x contents over $BiVO_4$-0.20M. Note that the increase in Cu content from 1 to 5 wt% enhances the formation rate of hydrocarbons with further stabilization at 8 wt%. The surface area of $BiVO_4$ is quite low and saturation of {010} facets takes place already at relatively low Cu content.

Table 6-2 Effect of Cu content on the performance of $CuO_x/BiVO_4$-0.20M for photocatalytic reduction CO_2 with H_2O.

Catalyst	Product formation rate ($\mu mol\ g^{-1}\ h^{-1}$)						Hydrocarbon formation rate ($\mu mol\ g^{-1}\ h^{-1}$)
	CO	CH_4	C_2H_6	C_3H_8	HCHO	CH_3OH	
1% $CuO_x/BiVO_4$	0.51	0.73	0	0	0	0	0.73
3% $CuO_x/BiVO_4$	0.82	2.5	0.61	0.42	0.35	0.55	4.4
5% $CuO_x/BiVO_4$	1.4	3.5	1.1	0.80	0.60	0.82	6.8
8% $CuO_x/BiVO_4$	1.3	3.3	1.0	0.63	0.51	0.60	6.0

The catalytic properties after deposition of co-catalysts by photo-oxidation over $CuO_x/BiVO_4$ have been studied by catalytic tests at the same conditions (Figure 6-11). The catalytic activity was gradually increasing in the row: $CuO_x/BiVO_4$<$MnO_x/CuO_x/BiVO_4$ <$PbO_2/CuO_x/BiVO_4$ <$CoO_x/CuO_x/BiVO_4$. Afterwards the catalytic performance of $CoO_x/CuO_x/BiVO_4$ has been optimized by variation of CoO_x content. The catalytic behavior is similar to those of Cu with increase of the catalytic activity till 5 wt% of CoO_x and stable performance at higher loading (Table 6-3). Thus, the highest catalytic activity for CO_2 reduction by water is achieved for the $CuO_x/CoO_x/BiVO_4$ catalyst with selective photo-deposited CuO_x and CoO_x nanoparticles over {010} and {110} facets, respectively. For comparison, the $CuO_x/CoO_x/BiVO_4$ (imp) synthesized by impregnation method with non-selective loading of CuO_x and CoO_x demonstrates much lower catalytic activity (Figure 6-11). This result indicates that the photocatalytic performance can be significantly enhanced when the reduction/oxidation co-catalysts were selectively deposited on the corresponding

reduction/oxidation reaction facets, which can minimize electron-hole pairs recombination. This assumption has been confirmed by the fact that intensity of photoluminescence band decreased significantly by loading CuO_x and CoO_x onto the $BiVO_4$-0.20M crystal (Figure 6-5).

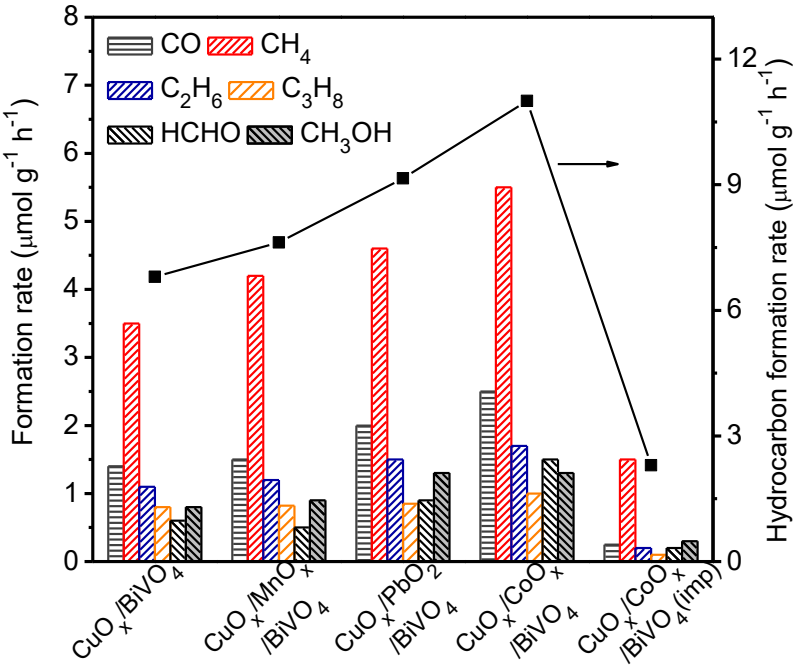

Figure 6-11 Effect of cocatalyst on the performance of $CuO_x/BiVO_4$-0.20M for photocatalytic reduction CO_2 with H_2O.

Table 6-3 Effect of CoO_x cocatalyst content on the performance of $CuO_x/CoO_x/BiVO_4$-64% for photocatalytic reduction CO_2 with H_2O.

Catalyst	Product formation rate (μmol g^{-1} h^{-1})						Hydrocarbon formation rate (μmol g^{-1} h^{-1})
	CO	CH_4	C_2H_6	C_3H_8	HCHO	CH_3OH	
5% CuO_x/ 1% $CoO_x/BiVO_4$	1.9	4.0	1.2	0.81	0.92	0.90	7.8
5% CuO_x/ 3% $CoO_x/BiVO_4$	2.2	5.0	1.6	0.80	1.0	1.1	9.5
5% CuO_x/ 5% $CoO_x/BiVO_4$	2.5	5.5	1.7	1.0	1.5	1.3	11
5% CuO_x/ 8% $CoO_x/BiVO_4$	2.6	5.2	1.5	0.81	1.5	1.1	10

The stability of optimized catalyst containing 5 wt% Cu and 5 wt% Co over $BiVO_4$-0.20M has been studied by repeated tests with degassing and CO_2 reintroduction after 7 h of reaction. Similar activities for the formations rate of hydrocarbon fuels were observed after five cycles (Figure 6-12).

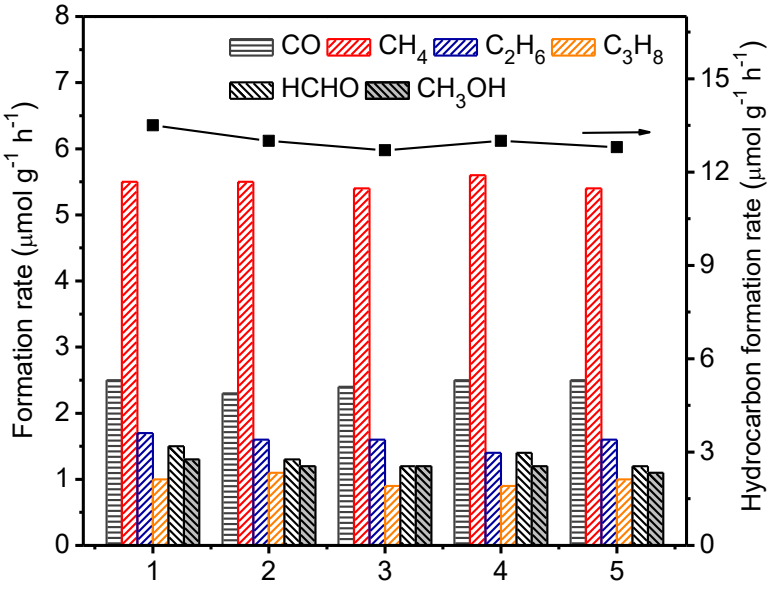

Figure 6-12 Repeated uses of the 5 wt% CuO_x/5 wt% CoO_x /$BiVO_4$-0.20M catalyst for photocatalytic reduction of CO_2 with H_2O.

Table 6-4 shows that the formation rate of the CO_2 reduction over $CoO_x/CuO_x/BiVO_4$ catalyst under visible light range (382-600 nm) is only slightly lower compared to the results with light range before filtration (240-600 nm). The main advantage of $BiVO_4$ as semiconductor in comparison with TiO_2 is its ability to work under visible light irradiation.

Table 6-4 Performances of the 5wt%CuO_x/5wt%CoO_x/$BiVO_4$-64% catalyst for photocatalytic reduction CO_2 with H_2O measured under irradiation at different spectral ranges.

Spectral range of irradiation (nm)	Product formation rate (μmol g^{-1} h^{-1})[a]						Hydrocarbon formation rate (μmol g^{-1} h^{-1})
	CO	CH_4	C_2H_6	C_3H_8	HCHO	CH_3OH	
dark	0	0	0	0	0	0	0
240-600	1.5	3.8	1.1	0.50	1.1	0.81	7.3
382-600	0.60	2.0	0.52	0.21	0.30	0.41	3.1

[a] Reaction conditions: catalyst, 0.1 g; Gas phase pressure, CO_2 0.2 Mpa; H_2O 15 mL; irradiation time, 7h; light source, Hamamatsu LC8-06 Hg-Xe stabilized irradiation lamps with a spectral irradiance in the range 240-600 nm; Cut-off filter: visible light, $382 < \lambda < 600$ nm.

6.2.3 Z-scheme mechanism of the CuO_x/CoO_x /$BiVO_4$-0.20M catalyst for photocatalytic reduction CO_2 with H_2O

The valence band (VB) of Cu_2O is very close to the conduction band (CB) of $BiVO_4$. This fact suggests a possibility of construction of the Z-scheme photocatalysis system for reduction of CO_2 similar to the previous reports [34, 45, 46, 47]. The significant enhancement of photocatalytic CO_2 reduction can be explained by Z-scheme charge-transfer mechanism (Figure 6-13).

In summary, when both Cu_2O and $BiVO_4$ were excited by the irradiation, the photogenerated electrons in the CB of $BiVO_4$ recombine with the photogenerated holes in the VB of Cu_2O owing to their close band position. Finally, the photogenerated electrons in the CB of Cu_2O are used for the reduction of CO_2 produce hydrocarbon fuels, while the photogenerated holes in the VB of $BiVO_4$ transfer to Co_3O_4 of oxidation co-catalyst, which used for the oxidation reaction of water (Figure 6-13).

The effect of close position of CB of $BiVO_4$ and VB of Cu_2O has been verified by deposition of other metal oxides (WO_x, FeO_x and ZnO) by photo-reduction technique with different band positions instead of CuO_x (Figure 6-9). The activity correlates well with band position on the Figure 6-13. Thus, FeO_x and WO_x almost did not affect catalytic activity of pure $BiVO_4$ due to low CB potential in comparison with the CO_2/CH_4 reduction potential However, ZnO with higher reduction potential results in significant increase of the catalytic activity.

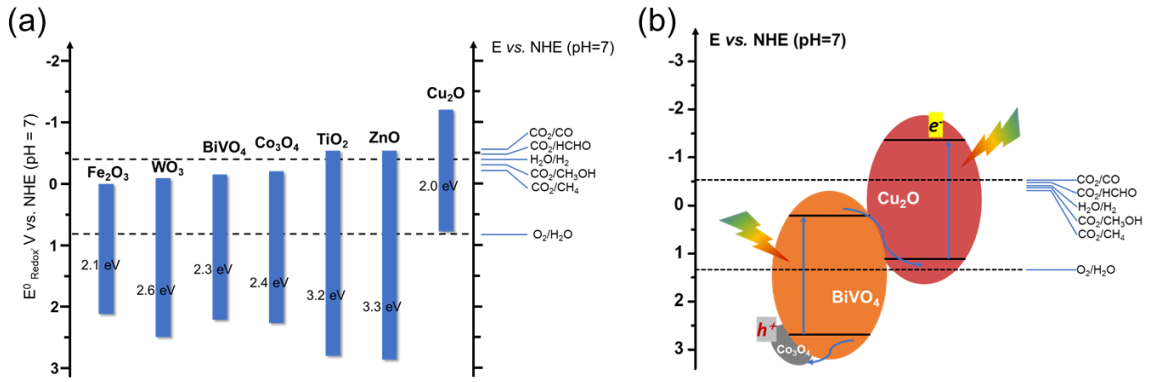

Figure 6-13 (a) Comparison of the band structures of various semiconductor with respect to the redox potentials of reduction of CO_2; (b) Schematic of the Z-scheme of CuO_x/CoO_x /$BiVO_4$-0.20M catalyst.

6.3 Conclusion

The present work focuses on the design efficient photocatalyst construction for the preferential photocatalytic reduction of CO_2 with H_2O. The monoclinic $BiVO_4$ crystals with truncated tetragonal bipyramidal morphology and controllable exposed {010} and {110} facets ratios have been synthesized. The fraction of {010} facets could be varied in the range from 26 to 75 %. The facet-selective photo-deposition of the metal oxides can significantly enhance the photocatalytic reduction of CO_2. $BiVO_4$ crystals containing 64% of {010} facets fraction with Cu_2O and Co_3O_4 nanoparticles photo-deposited onto {010} and {110} facets, respectively, were the most efficient for the separation of photogenerated electron-hole pairs. This catalyst demonstrated the highest stable catalytic activity toward production of hydrocarbons even under visible light irradiation. The construction of Z-scheme for CO_2 reduction by water using oxidation and reduction co-catalysts played a key role in enhancing of the efficiency of charge separation.

6.4 Reference

1. Worrell E, Price L, Martin N, Hendriks C, Meida LO. Carbon dioxide emissions from the global cement industry. *Ann. Rev. Environ. Resour.* **26**, 303-329 (2001).

2. Barber J. Photosynthetic energy conversion: natural and artificial. *Chem. Soc. Rev.* **38**, 185-196 (2009).

3. Xie S, Zhang Q, Liu G, Wang Y. Photocatalytic and photoelectrocatalytic reduction of CO_2 using heterogeneous catalysts with controlled nanostructures. *Chem. Commun.* **52**, 35-59 (2016).

4. Indrakanti VP, Kubicki JD, Schobert HH. Photoinduced activation of CO_2 on Ti-based heterogeneous catalysts: Current state, chemical physics-based insights and outlook. *Energy Environ. Sci.* **2**, 745-758 (2009).

5. Roy SC, Varghese OK, Paulose M, Grimes CA. Toward solar fuels: photocatalytic conversion of carbon dioxide to hydrocarbons. *ACS Nano.* **4**, 1259-1278 (2010).

6. Corma A, Garcia H. Photocatalytic reduction of CO_2 for fuel production: Possibilities and challenges. *J. Catal.* **308**, 168-175 (2013).

7. Habisreutinger SN, Schmidt-Mende L, Stolarczyk JK. Photocatalytic reduction of CO_2 on TiO_2 and other semiconductors. *Angew. Chem. Int. Ed.* **52**, 7372-7408 (2013).

8. Liu L, Zhao H, Andino JM, Li Y. Photocatalytic CO_2 reduction with H_2O on TiO_2 nanocrystals: Comparison of anatase, rutile, and brookite polymorphs and exploration of surface chemistry. *ACS Catal.* **2**, 1817-1828 (2012).

9. Jiao W, Wang L, Liu G, Lu GQ, Cheng H-M. Hollow anatase TiO_2 single crystals and mesocrystals with dominant {101} facets for improved photocatalysis activity and tuned reaction preference. *ACS Catal.* **2**, 1854-1859 (2012).

10. Park H-a, Choi JH, Choi KM, Lee DK, Kang JK. Highly porous gallium oxide with a high CO_2 affinity for the photocatalytic conversion of carbon dioxide into methane. *J. Mater. Chem.* **22**, 5304-5307 (2012).

11. Tsuneoka H, Teramura K, Shishido T, Tanaka T. Adsorbed Species of CO_2 and H_2 on Ga_2O_3 for the Photocatalytic Reduction of CO_2. *J. Phys. Chem. C* **114**, 8892-8898 (2010).

12. Liu Q*, et al.* High-yield synthesis of ultralong and ultrathin Zn_2GeO_4 nanoribbons toward

improved photocatalytic reduction of CO_2 into renewable hydrocarbon fuel. *J. Am. Chem. Soc.* **132**, 14385-14387 (2010).

13. Zhang N*, et al.* Ion-exchange synthesis of a micro/mesoporous Zn_2GeO_4 photocatalyst at room temperature for photoreduction of CO_2. *Chem. Commun.* **47**, 2041-2043 (2011).

14. Chen X, Zhou Y, Liu Q, Li Z, Liu J, Zou Z. Ultrathin, single-crystal WO_3 nanosheets by two-dimensional oriented attachment toward enhanced photocatalystic reduction of CO_2 into hydrocarbon fuels under visible light. *ACS Appl. Mater. Inter.* **4**, 3372-3377 (2012).

15. Cheng H*, et al.* An anion exchange approach to Bi_2WO_6 hollow microspheres with efficient visible light photocatalytic reduction of CO_2 to methanol. *Chem. Commun.* **48**, 9729-9731 (2012).

16. Zhang N, Ciriminna R, Pagliaro M, Xu Y-J. Nanochemistry-derived Bi_2WO_6 nanostructures: towards production of sustainable chemicals and fuels induced by visible light. *Chem. Soc. Rev.* **43**, 5276-5287 (2014).

17. Chen X, Mao SS. Titanium dioxide nanomaterials: synthesis, properties, modifications, and applications. *Chem. Rev.* **107**, 2891-2959 (2007).

18. Liu G, Jimmy CY, Lu GQM, Cheng H-M. Crystal facet engineering of semiconductor photocatalysts: motivations, advances and unique properties. *Chem. Commun.* **47**, 6763-6783 (2011).

19. Huang Z-F, Pan L, Zou J-J, Zhang X, Wang L. Nanostructured bismuth vanadate-based materials for solar-energy-driven water oxidation: a review on recent progress. *Nanoscale* **6**, 14044-14063 (2014).

20. Han X, Kuang Q, Jin M, Xie Z, Zheng L. Synthesis of titania nanosheets with a high percentage of exposed (001) facets and related photocatalytic properties. *J. Am. Chem. Soc.* **131**, 3152-3153 (2009).

21. Yu J, Low J, Xiao W, Zhou P, Jaroniec M. Enhanced photocatalytic CO_2-reduction activity of anatase TiO_2 by coexposed {001} and {101} facets. *J. Am. Chem. Soc.* **136**, 8839-8842 (2014).

22. Xi G, Ye J. Synthesis of bismuth vanadate nanoplates with exposed {001} facets and enhanced visible-light photocatalytic properties. *Chem. Commun.* **46**, 1893-1895 (2010).

23. Li R*, et al.* Spatial separation of photogenerated electrons and holes among {010} and {110} crystal facets of $BiVO_4$. *Nat. Commun.* **4**, 1432 (2013).

24. Xie S, Shen Z, Zhang H, Cheng J, Zhang Q, Wang Y. Photocatalytic coupling of formaldehyde

to ethylene glycol and glycolaldehyde over bismuth vanadate with controllable facets and cocatalysts. *Catal. Sci. Technol.* **7**, 923-933 (2017).

25. Huang W-C, Lyu L-M, Yang Y-C, Huang MH. Synthesis of Cu_2O nanocrystals from cubic to rhombic dodecahedral structures and their comparative photocatalytic activity. *J. Am. Chem. Soc.* **134**, 1261-1267 (2011).

26. Wang L*, et al.* Designing p-type semiconductor–metal hybrid structures for improved photocatalysis. *Angew. Chem. Int. Ed.* **126**, 5207-5211 (2014).

27. Li P*, et al.* Hexahedron prism-anchored octahedronal CeO_2: crystal facet-based homojunction promoting efficient solar fuel synthesis. *J. Am. Chem. Soc.* **137**, 9547-9550 (2015).

28. Ran J, Jaroniec M, Qiao SZ. Cocatalysts in Semiconductor-based Photocatalytic CO_2 Reduction: Achievements, Challenges, and Opportunities. *Adv. Mater.* **30**, 1704649 (2018).

29. Liu Y*, et al.* Selective ethanol formation from photocatalytic reduction of carbon dioxide in water with $BiVO_4$ photocatalyst. *Catal. Commun.* **11**, 210-213 (2009).

30. Dai W*, et al.* Photocatalytic reduction of CO_2 into methanol and ethanol over conducting polymers modified Bi_2WO_6 microspheres under visible light. *Appl. Surf. Sci.* **356**, 173-180 (2015).

31. Zhou P, Yu J, Jaroniec M. All-solid-state Z-scheme photocatalytic systems. *Adv. Mater.* **26**, 4920-4935 (2014).

32. Wei Z-H, Wang Y-F, Li Y-Y, Zhang L, Yao H-C, Li Z-J. Enhanced photocatalytic CO_2 reduction activity of Z-scheme CdS/$BiVO_4$ nanocomposite with thinner $BiVO_4$ nanosheets. *J. CO2 Util.* **28**, 15-25 (2018).

33. Sommers JM, Alderman NP, Viasus CJ, Gambarotta S. Revisiting the behaviour of $BiVO_4$ as a carbon dioxide reduction photo-catalyst. *Dalton T.* **46**, 6404-6408 (2017).

34. Kim C, Cho KM, Al-Saggaf A, Gereige I, Jung H-T. Z-scheme photocatalytic CO_2 conversion on three-dimensional $BiVO_4$/carbon-coated Cu_2O nanowire arrays under visible light. *ACS Catal.* **8**, 4170-4177 (2018).

35. Park Y, McDonald KJ, Choi K-S. Progress in bismuth vanadate photoanodes for use in solar water oxidation. *Chem. Soc. Rev.* **42**, 2321-2337 (2013).

36.Wang X*, et al.* Trap states and carrier dynamics of TiO_2 studied by photoluminescence spectroscopy under weak excitation condition. *PCCP* **12**, 7083-7090 (2010).

37. Espinós J, Morales J, Barranco A, Caballero A, Holgado J, González-Elipe A. Interface effects for Cu, CuO, and Cu_2O deposited on SiO_2 and ZrO_2. XPS determination of the valence state of copper in Cu/SiO_2 and Cu/ZrO_2 catalysts. *J. Phys. Chem. B* **106**, 6921-6929 (2002).

38. Park J-Y, Jung Y-S, Cho J, Choi W-K. Chemical reaction of sputtered Cu film with PI modified by low energy reactive atomic beam. *Appl. Surf. Sci.* **252**, 5877-5891 (2006).

39. Ghodselahi T, Vesaghi M, Shafiekhani A, Baghizadeh A, Lameii M. XPS study of the $Cu@Cu_2O$ core-shell nanoparticles. *Appl. Surf. Sci.* **255**, 2730-2734 (2008).

40. Zhai Q*, et al.* Photocatalytic conversion of carbon dioxide with water into methane: platinum and copper (I) oxide co-catalysts with a core–shell structure. *Angew. Chem. Int. Ed.* **125**, 5888-5891 (2013).

41. Riva R, Miessner H, Vitali R, Del Piero G. Metal–support interaction in Co/SiO_2 and Co/TiO_2. *Appl. Catal., A* **196**, 111-123 (2000).

42. Qian K, Huang W, Jiang Z, Sun H. Anchoring highly active gold nanoparticles on SiO_2 by CoOx additive. *J. Catal.* **248**, 137-141 (2007).

43. Yuan C*, et al.* Flexible hybrid paper made of monolayer Co_3O_4 microsphere arrays on rGO/CNTs and their application in electrochemical capacitors. *Adv. Funct. Mater.* **22**, 2560-2566 (2012).

44. Liu T, Zhou X, Dupuis M, Li C. The nature of photogenerated charge separation among different crystal facets of $BiVO_4$ studied by density functional theory. *PCCP* **17**, 23503-23510 (2015).

45. Zhou C, Wang S, Zhao Z, Shi Z, Yan S, Zou Z. A Facet-Dependent Schottky-Junction Electron Shuttle in a $BiVO_4${010}–Au–Cu_2O Z-Scheme Photocatalyst for Efficient Charge Separation. *Adv. Funct. Mater.* 1801214 (2018).

46. Deng Y*, et al.* Plasmonic resonance excited dual Z-scheme $BiVO_4/Ag/Cu_2O$ nanocomposite: synthesis and mechanism for enhanced photocatalytic performance in recalcitrant antibiotic degradation. *Environ. Sci-Nano* **4**, 1494-1511 (2017).

47. Zhu M, Sun Z, Fujitsuka M, Majima T. Z-Scheme Photocatalytic Water Splitting on a 2D Heterostructure of Black Phosphorus/Bismuth Vanadate Using Visible Light. *Angew. Chem. Int. Ed.* **57**, 2160-2164 (2018).

Chapter 7. General Conclusions and Perspectives

In the past few decades, considerable attention has been paid to energy conversion and environment. Semiconductor photocatalysis has attracted considerable attention because it is a promising way to deal with the global energy scarcity, environmental degradation and modern organic synthesis. Over the past few decades, numerous strategies have been put forward to improve the visible-light absorption and decrease the electron–hole recombination of semiconductor photocatalysts. This thesis mainly focuses on the progress in morphology and the structure design of heterostructure based semiconductor photocatalysts. In addition, the photocatalytic performance of semiconductor systems discussed mainly involves the environmental and energy application, including the methane photocatalytic oxidation to carbon monoxide, photochemical coupling to upgrading products and photocatalytic reduction of carbon dioxide.

7.1 General Conclusion

7.1.1 Photocatalytic conversion of methane

We developed a new system on the basis of metal, tungstophosphoric acid and titania which exhibits exceptional performance for the photocatalytic conversion of methane. Interestingly, different metal-heteropolyacid-titania catalysts can lead to different reaction pathways (Figure 7-1).

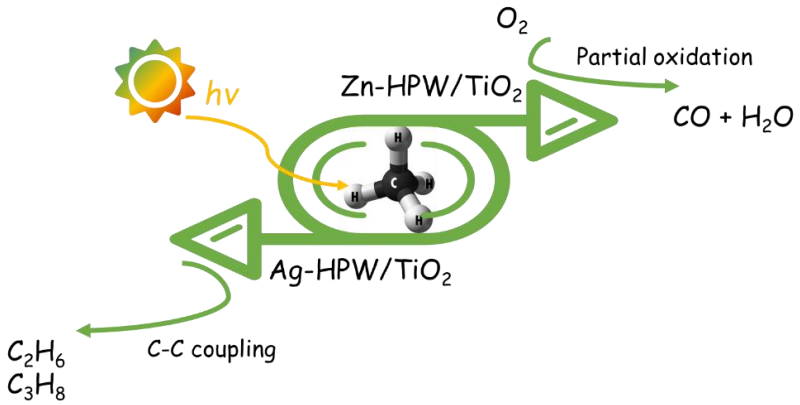

Figure 7-1 Reaction pathways of photoactivation of methane over different metal-

heteropolyacid-titania nanocomposites

A simple way to prepare metal-heteropolyacid/TiO_2 composite catalysts is the direct loading of a different noble or transition metal onto the heteropolyacid /TiO_2 composite via impregnation. The composite catalysts show the presence of core-shell particles. The core is constituted by TiO_2 crystallites of 30-40 nm, while the shell is built by the HPW heteropolyacid (layer thickness of 1-2 nm), while metal species are highly dispersed on the tungstophosphoric layer.

The Zn-HPW/TiO_2 system exhibits extremely selective photocatalytic methane partial oxidation to CO at ambient temperature. The methane photocatalytic oxidation proceeds as a combination of parallel and consecutive reactions with carbon monoxide being a primary reaction product. The carbon monoxide yield from methane can reach 3-4 % and give high quantum efficiency (7.1% at 362 nm) values under the optimized reaction conditions. In-situ FT-IR and XPS uncover that the catalytic performance can be attributed to zinc species highly dispersed on tungstophosphoric acid/titania, which undergo reduction and oxidation cycles during the reaction according to the Mars-Van Krevelen sequence. Surface methoxy carbonates were identified as reaction intermediates

The Ag-HPW/TiO_2 system exhibited high selectivity of methane coupling to ethane and high ethane yield in the presence of irradiation at ambient temperature. The reaction involves stoichiometric reaction of methane with silver oxidized species highly dispersed over heteropolyacid layer over titania resulting in methyl radicals. The recombination of the generated CH_3 radicals leads to selective and almost quantitative formation of ethane. The ethane yield from methane reaches 9 % on the optimized materials. The photochemical looping strategy has shown to be viable to attain higher methane conversion and higher and stable ethane yield from methane under the optimized conditions.

7.1.2 Photo-reduction of carbon dioxide

The photocatalytic conversion of CO_2, which occurs at ambient temperature, not only reduces the greenhouse effect, but also provides value-added solar fuels and chemicals. We

developed zinc modified the heteropolyacid-titania nanocomposites which exhibit exceptional photocatalytic activity in selective carbon monoxide production from methane at ambient temperature. Interestingly, we report for the first time that the Zn-HPW/TiO_2 composite system exhibited extremely high photocatalytic activity reaching 50 μmol CO/g·h and selectivity (73 %) in the CO_2 photocatalytic reduction to CO in the presence of water. A combination of characterization techniques indicates that the heteropolyacid forms a thin layer over titania nanoparticles. The activity in photocatalytic reduction of carbon dioxide to carbon monoxide was attributed to zinc bicarbonate species highly dispersed over heteropolyacid. No visible deactivation was observed, the catalyst was stable after conducting several reaction cycles for more than 40 h of reaction. In-situ FTIR investigation uncovered that the reaction involved surface zinc bicarbonates species as key reaction intermediates. HPW transfers photo-energy from TiO_2 to zinc bicarbonate with its reduction to carbon monoxide. The water splitting has been significantly suppressed over the Zn sites in the presence of CO_2. In addition, the photocatalytic performance in the CO_2 hydrogenation can be further enhanced by p-n semiconductor heterojunction. This heterojunction can be created by adding to TiO_2 a semiconductor with lower levels of valence and conduction bands. This heterojunction can be achieved by combining TiO_2 with a heteropolyacid acid ($H_3PW_{12}O_{40}$), which may result in better charge separation and higher electron flux from TiO_2 onto HPW.

To date, most of research has been focused on titanium dioxide (TiO_2) photocatalyst for energy and environmental applications owing its outstanding photocatalytic activity, non-toxicity and high photostability. However, TiO_2 is only sensitive under UV-light and utilizes only 4% of available solar energy, which highly restricts its potential application. Hence, there is a need to develop new strategies to improve the use of solar energy.

Bismuth vanadate is a promising visible light-driven semiconductor photocatalyst with low production cost, low toxicity, high stability and narrow band gap (2.4 eV) with good response to visible light excitation. we successfully designed efficient photocatalyst construction for the preferential photocatalytic reduction of CO_2 with H_2O. The formation of Z-scheme photocatalytic systems that mimic natural photosynthesis with photocatalytic

systems and electron mediator is a promising strategy to improve charge separation. Herein, the separation of electrons and holes in bismuth vanadate is improved by control of the semiconductor morphology. The photocatalytic reduction of CO_2 to hydrocarbons under irradiation is significantly enhanced by selective photo-deposition of Cu and Co co-catalysts over different facets providing Z-scheme charge flow. The activity of $Cu_2O/Co_3O_4/BiVO_4$ increases up to 100 times in comparison with the parent $BiVO_4$.

7.2 Perspectives

Semiconductor photocatalysts have been widely applied to solve environmental pollutions and convert solar energy into renewable fuels, which represents a promising way to achieve sustainable society. Nevertheless, the photocatalytic process is a complex reaction, which still exists some problems for future studies, such as exploiting novel photocatalytic materials, better understanding the mechanism of heterogeneous photocatalysts and the charge transportation way on the interface.

7.2.1 Photocatalytic conversion of methane

The catalytic conversion of methane to value-added chemicals and fuels by a sustainable method is a highly attractive goal that still has significant challenges in catalysis. Solar energy can be employed with photocatalysts to activate methane and drive methane conversions. Although very impressive progress has been achieved in photocatalytic conversion of methane, there are still a number of challenges that have to be solved, as discussed in the following. First, although photocatalytic methane conversion can proceed under mild conditions, the efficiencies of the reported processes remain low. One solution is to efficiently utilize solar light (such as UV, visible, and infrared light) through the development of photocatalysts. Second, the selectivity of photocatalytic methane oxidation to desired liquid products such as methanol and formic acid remains challenging since the reactivity of oxygenates is higher than that of methane under reaction conditions. Finally, at present, the mechanism investigations of methane activation and conversion both on

semiconductors and plasmonic metal nanoparticles remain in the preliminary stages due to the complicated reaction pathways and the limited characterization techniques for photocatalytic reaction systems.

7.2.2 Photocatalytic carbon dioxide reduction

Photocatalytic reduction of CO_2 into hydrocarbon fuels is a challenging, yet promising avenue for achieving a sustainable alternative to conventional fossil fuels with advantages as follows: (1) it can be carried out in relatively mild conditions – room temperature and pressure, (2) this process uses a mass of abandoned CO_2 as the starting carbon source driven by inexhaustible and clean solar energy, (3) the photoreduction of CO_2 can directly generate short-chain hydrocarbon fuels such as CH_4, CH_3OH, C_2H_6 and so on, which can alleviate increasingly tense energy crisis, (4) the realization of this technology will make it possible to replace fossil fuels by CO_2 as C source in chemical industry. Therefore, photocatalytic reduction of CO_2 with H_2O into hydrocarbon fuels would be like killing two birds with one stone in terms of saving supplying energy and our environment.

The pathways to improve the performance of photocatalytic operation are either by enhancing the photocatalyst activity or improving the design configuration of photoreactor. To enhance the photocatalyst efficiency, light harvesting, charge excitation, preventing charge recombination and photocatalytic reduction and oxidation steps must be enhanced. Although a lot of progress has been made in this field, it is clear that the existing techniques are not sufficient to make them applicable for industrial production of fuels. A deep understanding of engineering aspects of CO_2 reduction is still required for the development of highly efficient photoreactor designs. In order to achieve high conversion efficiency, photoreaction system designs must take into account: (1) The material of construction and thickness of reactor chosen is constricted by the necessity of light transmission and reflectance. (2) The collectivity of photons which depends on the geometry (length, volume etc.) of photoreactor vessel, light intensity, and operating wavelength, catalyst and substrate should be optimized. (3) Mixing and flow characteristics must be designed properly to attain high contact between the reactants and catalyst by reducing mass transfer limitations. (4)

Moreover, the CO_2 photo-reduction system must be designed with high stability, cycle-ability, nontoxicity that has very critical significance.

Author Introduction

Xiang Yu was born in June 1991 in Wuhan City, Hubei Province, China. He received his master's degree in physical chemistry from Xiamen University in 2016 under the supervision of Prof. Ye Wang and Prof. Qinhong Zhang focused on the metal nanoparticles supported on carbon nanotubes for catalyzing syngas into diesel fuel products with the impact of hydrogenolysis. In 2016, he started the PhD programs which was sponsored by China Scholarship Council to study at Unité de catalyse et de chimie du solide (UCCS), Université de Lille, France. His PhD thesis was supervised by Dr. Vitaly Ordomsky and Dr. Andrei Khodakov. His PhD research focuses on the photocatalytic conversion of methane and reduction of CO_2 with H_2O.

List of Published Papers

1. **Yu X**, De Waele V, Löfberg A, Ordomsky V, Khodakov AY. Selective photocatalytic conversion of methane into carbon monoxide over zinc-heteropolyacid-titania nanocomposites. *Nat. Commun.,* **10**, 700 (2019).

2. **Yu X**, Moldovan S, Ordomsky V, Khodakov AY. Design of core-shell titania-heteropolyacid-metal nanocomposites for photocatalytic reduction of CO_2 to CO at ambient temperature. *Nanoscale Adv.,* DOI: 10.1039/c9na00398c.

3. **Yu X**, Ordomsky V, Khodakov AY. Selective deposition of cobalt and copper oxides on $BiVO_4$ facets for enhancement of CO_2 photocatalytic reduction to hydrocarbons. *ChemCatChem*, Under review.

4. **Yu X**, Moldovan S, Zholobenko VL, Ordomsky V, Khodakov AY. Selective photochemical synthesis of ethane from methane at ambient temperature over silver-heteropolyacid-titania nanocomposites. *Nat. Energy*, Under review.

Conference Papers

1. **Yu X**, Ordomsky V, Khodakov AY. Highly efficient photocatalytic methane oxidation to CO over Zn-solid acid-TiO_2 nanocomposites. *Le Groupement de Recherche (GDR) Solar Fuels*, France, **2018**, poster.

2. **Yu X**, Ordomsky V, Khodakov AY. Selective carbon monoxide production from methane under mild conditions using photocatalysis. *Le Groupe d'Etude en Catalyse (GECat)*, France, **2018**, oral presentation.

3. **Yu X**, Ordomsky V, Khodakov AY. Metal-heteropolyacid-titania nanocomposites for enhanced photocatalytic reduction of CO_2 to CO in the presence of water. *European Materials Research Society*, France, **2019**, oral presentation.

4. **Yu X**, Ordomsky V, Khodakov AY. Selective photocatalytic conversion of methane into carbon monoxide over zinc-heteropolyacid-titania nanocomposites. *12th Natural Gas Conversion Symposium*, USA, **2019**, oral presentation.

5. **Yu X**, Löfberg A, Ordomsky V, Khodakov AY. Selective methane photocatalytic oxidation to carbon monoxide and coupling to C_{2+} hydrocarbons over metal-heteropolyacid-titania nanocomposites. *Europacat*, Germany, **2019**, oral presentation.

Acknowledgement

The completion of the thesis is attributed to many peoples support and encouragement. First and foremost, I want to extend my heartfelt gratitude to my supervisor, Dr. Vitaly Ordomsky and Dr. Andrei Khodakov whose patient guidance, valuable suggestions and constant encouragement make me successfully complete this thesis. His conscientious academic spirit and modest, open-minded personality inspire me both in academic study and dailylife. He gives me much help and advice during the whole process of my writing, which has made my accomplishments possible.

Also, I would like to express my sincere gratitude to all the professors who have taught me in this university. Their instructions have helped broaden my horizon and their enlightening teaching has provided me with a solid foundation to accomplish this paper and will always be of great value for my future career and academic research.

Last but not least, I would like to express my special thanks to my parents and girlfriend, whose care and support motivate me to move on and make me want to be a better person.

Thanks to all my friends!!!